Gdańsk University of Technology
Faculty of Civil and Environmental Engineering

mgr inż. Jarosław Florczuk

Numerical model of innovative solar collector

Doctoral thesis

Supervisor: dr hab. inż. Marek Krzaczek

Gdańsk, 2014

Summary

The doctoral thesis presents results of comprehensive numerical investigations of an innovative solar collector performance during a year-round operation under Polish climate conditions. The proposed solar collector, so-called hidden solar collector, consists of the polypropylene pipe system with the flowing fluid as the energy carrying medium located inside a ventilated roof's structure. Hence, it is characterized by a relatively low-investment cost (about 36 pln/m^2). Cost-effectiveness and completely non-affecting building aesthetics are the main advantages over conventional solar collectors, which make the hidden solar collector an attractive solar device to supply low-temperature residential building applications. The aim of the study is to evaluate the hidden solar collector's performance and capability to supply space-heating systems based on low-temperature heat sources dedicated for residential detached houses characterized by a low heat demand and to support domestic hot water systems.

The Finite Element Method is applied to solve the problem of the three-dimensional heat transfer in a hidden solar collector. Since the unsteady simulation of year-round solar collector operation is required to analyze the system performance, the objective of thermal modeling is to reach a compromise between the complexity of a numerical model, accuracy of its results and time of calculations. The three-dimensional FE model, developed using the software package ABAQUS v.6.10, is able to simulate the convective/diffusive heat transfer within the flowing fluid as well as to consider the influence of the natural convective heat transfer in the air layer on the heat exchange within the air-cavity without a direct use of computationally-time-expensive CFD methods. The latter is achieved through modeling the air layer as an orthotropic solid body with the time-varying convective-equivalent thermal conductivity coefficients. Further improvement of the model for heat transfer in the fluids is achieved by modification of convective heat transfer coefficients on both inner and outer pipes' surfaces. All the relationships for time-varying parameters in function of climate and operating conditions are determined by means of additional CFD steady-state simulations conducted in ANSYS CFX 15.0. The FE analysis is

supported by a number of several existing and several new subroutines implemented in FORTRAN to simulate real-working conditions and control convective-equivalent thermal parameters at each time increment of transient simulation. The CFD model used to determine the relationships was positively validated against the results of analytical solutions, thus it can be stated that the FE model of HSC is close to reality.

The evaluation of the collector performance during the year-round operation was preceded by parametric steady-state simulations aiming at a verification of the FE model and providing some recommendations for the design of a collector structure and an operation control strategy in order to maximize the performance. Results of the unsteady simulation of a year-round collector operation indicate that application of HSC under Polish climate conditions to support domestic hot water systems may be effective only during spring and summer, especially from May to August. During this time period, with the appropriate absorber surface area (corresponding to a typical roof surface area) the total hot water requirements could be provided on average 81 %. The annual averaged solar energy conversion efficiency of the collector applied to supply space-heating systems slightly exceeds 0.09 [-], whereas the amount of thermal energy collected by HSC from June to December is over 3 times lower as compared to the energy collected by flat plate collectors during the same time period. As expected, the performance of the hidden solar collector is significantly lower than conventional solar collectors. Nevertheless, the hidden solar collector with the 60 m^2 absorber area is able to collect during a year-round operation approximately 3 times more energy than it is required to satisfy annual space-heating loads in a residential detached house of the 250 m^2 heated area, which meets standards of passive houses. Therefore, it can be concluded that there is a great potential of hidden solar collector to supply space-heating systems based on low-temperature heat sources dedicated for residential buildings characterized by a low heat demand. The obtained results are in accordance with the literature findings related to experimental investigations of building integrated solar collectors dedicated for low-temperature applications.

Contents

List of Figures

List of Tables

List of important symbols

Latin symbols

b	–	characteristic length measure [m]
C	–	Courant number [−]
$C_{c,f}$	–	fluid heat capacity per unit area [J/(m^2·K)]
$C_{c,g}$	–	glass cover heat capacity per unit area [J/(m^2·K)]
$C_{c,i}$	–	insulation layer heat capacity per unit area [J/(m^2·K)]
$C_{c,p}$	–	absorber plate heat capacity per unit area [J/(m^2·K)]
$C_{c,r}$	–	roof heat capacity per aperture unit area [J/(m^2·K)]
C_l	–	log-layer constant [−]
C_p	–	specific heat of material [J/(kg·K)]
$C_{p,f}$	–	specific heat of fluid [J/(kg·K)]
$C_{\varepsilon 1\mathrm{RNG}}$	–	RNG $k-\varepsilon$ turbulence model constant equal to $1.42 - f_\eta$ [−]
$C_{\varepsilon 2\mathrm{RNG}}$	–	RNG $k-\varepsilon$ turbulence model constant equal to 1.68 [−]
$C_{\mu\mathrm{RNG}}$	–	RNG $k-\varepsilon$ turbulence model constant equal to 0.085 [−]
d_{ACH}	–	air-cavity dimension in main direction of airflow [m]
d_{ACV}	–	height of air-cavity [m]
d_i	–	inside pipe diameter [mm]
d_o	–	outside pipe diameter [mm]
e	–	internal energy [J/kg]
E	–	specific energy of fluid [J/kg]

$E_{diff,tilt}$	–	diffuse irradiance on a tilted surface $\left[\mathrm{W/m^2}\right]$
$E_{dir,tilt}$	–	direct irradiance on a tilted surface $\left[\mathrm{W/m^2}\right]$
$E_{G,tilt}$	–	global irradiance on a tilted surface $\left[\mathrm{W/m^2}\right]$
$E_{refl,tilt}$	–	ground reflected irradiance on a tilted surface $\left[\mathrm{W/m^2}\right]$
f_η	–	RNG $k-\varepsilon$ turbulence model coefficient [−]
F_1	–	surface area of body with temperature T_1 [m^2]
F_2	–	surface area of body with temperature T_2 [m^2]
F'	–	collector efficiency factor [−]
g	–	gravity acceleration [m/s^2]
$\mathbf{g}$	–	gravity vector [m/s^2]
G	–	solar irradiation on external collector surface [J/m^2 per time unit]
Gr	–	Grashof number [−]
Gz	–	Graetz number [−]
h	–	static enthalpy [J/kg]
h_{ag}	–	heat transfer coefficient of ambience-cover [W/(m^2·K)]
h_{ac}	–	average convective heat transfer coefficient of external pipe surface computed by solver [W/(m^2·K)]
h_{ae}	–	empirical convective heat transfer coefficient of external pipe surface [W/(m^2·K)]
h_e	–	convective heat transfer coefficient of external collector surface [W/(m^2·K)]
h_{fr}	–	heat transfer coefficient of fluid-roof [W/(m^2·K)]
h_{gp}	–	heat transfer coefficient of cover-plate [W/(m^2·K)]
h_i	–	convective/radiative heat transfer coefficient of internal collector surface [W/(m^2·K)]
h_{ia}	–	heat transfer coefficient of insulation-ambience [W/(m^2·K)]
h_{pf}	–	heat transfer coefficient of plate-fluid [W/(m^2·K)]
h_{pi}	–	heat transfer coefficient of plate-insulation [W/(m^2·K)]
h_{ra}	–	heat transfer coefficient of roof-ambience [W/(m^2·K)]
h_{sf}	–	heat transfer coefficient surface-fluid [W/(m^2·K)]
h_{tot}	–	total enthalpy [J/kg]
$\bar{h}_{wc}$	–	average convective heat transfer coefficient of internal pipe surface computed by solver [W/(m^2·K)]

h_{we}	–	empirical convective heat transfer coefficient of internal pipe surface [W/(m^2·K)]
ip	–	integration point [−]
$\mathbf{i}$, $\mathbf{j}$, $\mathbf{k}$	–	unit vectors in Cartesian coordinate system
I	–	solar irradiance $\left[\mathrm{W/m^2}\right]$
I_e	–	solar irradiance on external collector surface $\left[\mathrm{W/m^2}\right]$
k	–	turbulent kinetic energy [J/kg]
$k_{a-p,down}$	–	convective heat transfer coefficients of external down-pipe surface [W/(m^2·K)]
$k_{a-p,up}$	–	convective heat transfer coefficients of external up-pipe surface [W/(m^2·K)]
$k_{w-p,down}$	–	convective heat transfer coefficients of internal down-pipe surface [W/(m^2·K)]
$k_{w-p,up}$	–	convective heat transfer coefficients of internal up-pipe surface [W/(m^2·K)]
K	–	kinetic energy [J/kg]
l_{abs}	–	length of absorber tube [m]
l_c	–	cavity length in the flow direction [m]
l_p	–	pipe length [mm]
L	–	characteristic length scale [m]
L_b	–	cube root of buidling volume [m]
L_{eh}	–	thermal entrance length [m]
$\dot{m}$	–	water mass flux [kg/(m^2·s)]
$(\mathrm{mc})_e$	–	effective heat capacity of the collector per unit area [J/(m^2·K)]
$(\mathrm{Mc})_{\Delta X}$	–	total thermal capacity of the element whose length is ΔX [J/K]
$\mathbf{n}$	–	vector normal to surface [−]
N^N	–	shape function
N_c	–	number of collector nodes [−]
N_i	–	shape function for node i
N_{node}	–	number of nodes in element [−]
$\mathrm{Nu_w}$	–	Nusselt number for water flow [−]
$\bar{\mathrm{N}}\mathrm{u}_{dp}$	–	Nusselt number for airflow [−]
p	–	thermodynamic pressure [Pa]

p'	–	modified pressure [Pa]
p_{abs}	–	absolute pressure [Pa]
p_{ref}	–	reference pressure [Pa]
Pr	–	Prandtl number [−]
$\mathrm{Pr_p}$	–	Prandtl number evaluated at mean bulk temperature [−]
$\mathrm{Pr_s}$	–	Prandtl number evaluated at mean wall temperature [−]
$\mathrm{Pr_t}$	–	turbulent Prandtl number [−]
q	–	heat flux per unit area [W/m^2]
q_{Hflux}	–	heat flux at outlet cavity plane $S_{a,po}$ [W/m^2]
q_V	–	internal heat source [W/m^3]
q_{Vflux}	–	heat flux at inlet cavity plane $S_{a,pb}$ [W/m^2]
Q	–	useful heat per time unit provided by the collector [W]
Q_{1-2}	–	radiation heat flux between the bodies '1' and '2' [W]
Q_d	–	daily amount of collected energy [J]
Re	–	Reynolds number [−]
$\mathrm{Re_{dp}}$	–	Reynolds number far enough from pipe [−]
$S_{a,a}$	–	adiabatic surface of air-cavity layer [m^2]
$S_{a,b}$	–	bottom air-cavity surface [m^2]
$S_{a,e}$	–	air-cavity surface being adjacent to solid bodies surface $S_{c,i}$ [m^2]
$S_{a,i}$	–	air-cavity surface being adjacent to external pipe surface $S_{p,e}$ [m^2]
$S_{a,in}$	–	inlet air-cavity surface [m^2]
$S_{a,out}$	–	outlet air-cavity surface [m^2]
$S_{a,pb}$	–	bottom air-cavity plane [m^2]
$S_{a,pi}$	–	inlet air-cavity plane [m^2]
$S_{a,po}$	–	outlet air-cavity plane [m^2]
$S_{a,pu}$	–	upper air-cavity surface [m^2]
$S_{a,u}$	–	upper air-cavity surface [m^2]
$S_{c,i}$	–	solid bodies surface being adjacent to air-cavity surface $S_{a,e}$ [m^2]
S_e	–	external collector surface [m^2]
S_f	–	fraction of solar radiation absorbed by the plate [W/m^2]
S_i	–	internal collector surface [m^2]
$S_{p,e}$	–	external pipe surface [m^2]
$S_{pe,down}$	–	external surface of lower pipe [m^2]

$S_{pe,up}$	–	external surface of top pipe [m^2]
$S_{p,i}$	–	internal pipe surface [m^2]
$S_{pi,down}$	–	internal surface of lower pipe [m^2]
$S_{pi,up}$	–	internal surface of top pipe [m^2]
$S_{s,1}$, $S_{s,2}$	–	surface of solid body being adjacent to other solid body [m^2]
$S_{s,a}$	–	adiabatic surface of solid body [m^2]
$S_{w,a}$	–	surface of additional water segment [m^2]
$S_{w,in}$	–	inlet water surface [m^2]
$S_{w,out}$	–	outlet water surface [m^2]
$S_{w,s}$	–	surface of water layer beinng adjacent to pipe [m^2]
$\mathbf{S_E}$	–	energy source [W/m^3]
$\mathbf{S_M}$	–	momentum source [kg/ (m$^2 \cdot$ s^2)]
$\mathbf{S_{M,buoy}}$	–	momentum source [kg/ (m$^2 \cdot$ s^2)]
t	–	time [s]
T	–	temperature [°C]
T^N	–	nodal temperature [°C]
T_1, T_2	–	absolute temperatures of bodies between which heat exchange occurs [°C]
T_a	–	average air temperature out of the pipe surface [°C]
$T_{a,in}$	–	indoor air temperature [°C]
$T_{a,out}$	–	outdoor air temperature [°C]
T_C	–	temperature of external pipe surface [°C]
T_f	–	temperature of fluid [°C]
$T_{f,i}$	–	fluid temperature of the ith collector segment [°C]
T_g	–	temperature of glass cover [°C]
T_i	–	temperature of insulation [°C]
T_p	–	temperature of absorber plate [°C]
T_r	–	temperature of roof [°C]
T_{sky}	–	equivalent sky temperature [°C]
T_S	–	temperature of central water segment surface [°C]
T_{S_e}	–	temperature of external collector surface [°C]
T_{S_i}	–	temperature of internal collector surface [°C]
T_w	–	average water temperature along the centerline [°C]

$T_{w,in}$	–	inlet water temperature [°C]
$T_{w,out}$	–	outlet water temperature [°C]
$\bar{T}_{w,out}$	–	hourly averaged outlet water temperature [°C]
$\bar{u}$	–	average fluid velocity [m/s]
$u_{a,c}$	–	air velocity in the dominant flow direction [m/s]
u_i	–	time varying velocity component [m/s]
$u_{a,\infty}$	–	air velocity out of the pipe in the dominant flow direction [m/s]
u_w	–	water flow velocity [m/s]
$u_{w,in}$	–	water flow velocity at inlet surface [m/s]
u_x, u_y, u_z	–	velocity vector component on x, y, z direction [m/s]
u^+	–	mean dimensionless velocity [-]
u^*	–	alternative velocity scale used instead of u_τ [m/s]
u_τ	–	shear (or friction) velocity [m/s]
$\mathbf{U}$	–	velocity vector [m/s]
U_L	–	overall collector heat loss coefficient [W/(m^2·K)]
U_t	–	near-wall velocity [m/s]
$\bar{U}_i$	–	time-averaged velocity component [m/s]
U^+	–	dimensionless velocity [-]
V	–	volume of element [m^3]
w	–	molecular weight of air [kg/kmol]
w_s	–	wind speed [m/s]
w_n	–	component of wind speed vector in direction normal to surface [m/s]
R_0	–	universal gas constant [J/(mol · K)]
y^+	–	dimensionless distance from wall [-]
y^*	–	dimensionless distance from wall [-]
$\tilde{y^*}$	–	dimensionless distance from wall [-]

Greek symbols

α	–	absorptivity coefficient of material [−]
β	–	thermal expansion coefficient [1/K]
β_{opt}	–	optimum tilt angle of solar collector [deg]
β_{RNG}	–	RNG $k-\varepsilon$ turbulence model constant equal to 0.012 [−]
γ	–	angle between velocity and gravity vectors [deg]

ϵ	–	emissivity coefficient of material [−]
ϵ_{1-2}	–	emissivity between bodies '1' and '2' [−]
ε	–	turbulence dissipation rate [m^2/s^3]
ε_{eff}	–	effective emittance of absorber surface [−]
η	–	solar collector efficiency [−]
$\bar{\eta}_d$	–	daily averaged solar collector efficiency [−]
$\bar{\eta}_h$	–	hourly averaged solar collector efficiency [−]
κ	–	Von Karman constant equal to 0.41 [−]
λ	–	thermal conductivity of material [$W/(m \cdot K)$]
λ_{Heqv}	–	convective-equivalent horizontal thermal conductivity coefficient [$W/(m \cdot K)$]
λ_{Veqv}	–	convective-equivalent vertical thermal conductivity coefficient [$W/(m \cdot K)$]
μ	–	dynamic viscosity [Pa·s]
μ_{eff}	–	effective viscosity [Pa·s]
μ_t	–	turbulent viscosity [Pa·s]
ν	–	kinematic viscosity [m^2/s]
ρ	–	density of material $\left[kg/m^3\right]$
ρ_{ref}	–	reference density of material $\left[kg/m^3\right]$
σ	–	Stefan-Boltzmann constant equal to $5.670373 \times 10^{-8}\, W/\left(m^2 \cdot K^4\right)$
$\sigma_{k\mathrm{RNG}}$	–	turbulence model constant equal to 0.7179 [−]
σ_p	–	turbulence Schmidt number [−]
$\sigma_{\varepsilon\mathrm{RNG}}$	–	turbulence model constant equal to 0.7179 [−]
$\boldsymbol{\tau}$	–	stress tensor [Pa]
τ_ω	–	wall-shear stress [$kg/\left(m \cdot s^2\right)$]
$(\tau\alpha)_e$	–	effective transmittance absorptance product [−]
ϕ	–	energy dissipation [W/m^3]
ϕ_{1-2}	–	view factor [−]
ϕ_{2-1}	–	view factor [−]
ϕ_l	–	latitude of specified location [deg]
φ	–	general scalar variable [−]
Γ_t	–	turbulent diffusivity [Pa·s]
$\Delta\dot{m}$	–	water mass flux change [$kg/(m^2 \cdot s)$]

Δt	–	time increment [s]
ΔT	–	temperature difference [°C]
$\triangle X$	–	element length along the flow direction [m]
Δy	–	distance from near-wall point to wall [m]
ΔY	–	element width [m]
Φ	–	additional variable $\left[\mathrm{kg/m^3}\right]$

Abbrevations

BC	–	boundary condition
BIPV/T	–	building integrated photovoltaic-thermal
BTCS	–	Backward Time Centered Space
CFD	–	computational fluid dynamics
CPC	–	compound parabolic collector
DBT	–	dry bulb temperature
DHW	–	domestic hot water
DNS	–	Direct Numerical Simulation
EAHE	–	earth to air heat exchanger
ETC	–	evacuated tube collector
FDM	–	Finite Difference Method
FEM	–	Finite Element Method
FPC	–	flat plate collector
FTCS	–	Forward Time Centered Space
FVM	–	Finite Volume Method
GHS	–	ground heat storage
HS	–	heat storage
HSC	–	hidden solar collector
LES	–	Large Eddy Simulation
PCM	–	Phase Change Material
PI	–	Proportional-Integral
PV	–	photovoltaic
RANS	–	Reynolds-averaged Navier-Stokes
RES	–	renewable energy sources
RMS	–	root mean square

RNG	–	Re-Normalization Group
SDHW	–	solar domestic hot water
TB	–	Thermal Barrier
TMY	–	Typical Meteorological Year

Chapter 1

Introduction

1.1 Background

In this century, the strongly limited energy sources are widely recognized as the major issue the mankind will have to face and solve. In the next few decades the availability of fossil fuels will be very limited. It is not, however, yet clear which source of energy will replace them. This problem especially refers to the oil whose domination era in energy supplying systems is undoubtedly going to end, as the half of available global conventional oil resources has already been consumed [22]. According to the recent estimation of the world oil reserve, the average figure amounts to 1200 billion barrels [24]. Taking into consideration the heavily increasing consumption that currently is 88 million of barrels per day (over 32 billion of barrels per year) [98], the time span is evidently less than 40 years. In the case of gas, the proved reserves at the current rate of consumption would be adequate to meet the demand for another 60 years [91]. Continuous decreasing reserves of fossil fuels will be reflected by the acceleration of their prices, hence influencing the global economy. The alternative primary energy sources like nuclear energy or coal are also very problematic. The coal reserves are adequate for at least the next 250 years [91]. Nevertheless, the usage of coal as a primary energy source has an impact on climate changes, since it is responsible for emissions of CO_2 into the atmosphere [134]. The nuclear energy, on the other hand, meets with a lot of protests in many parts of the world against its waste products. What is more, reserves of fissionable uranium are also limited. A growing consciousness of the problem with the availability of conventional energy sources together with environmental harms, such as acid rains [51], ozone layer depletion [52, 53] and global climate change [51], caused by the conventional power sector entail that more and more consideration is paid to technologies of the energy manufacturing.

The balance between the industrialization growth and environmental preservation can be accomplished through the sustainable development. The widely accepted definition of the sustainable development is: *development that meets the needs of the present without compromising the ability of future generations to meet their own needs* [91]. In this respect, the usage of renewable energy sources (RES) appears to be the most reasonable, efficient and effective solution. Based on two distinctive qualifications pointed by Erdodgu [59], it can be assumed that each source of the renewable energy should be carbon neutral and derived from natural, mechanical, thermal and growth processes that repeat themselves within our lifetime. There are such renewable sources as: geothermal, wind, hydro, solar and bioenergy sources. An important turning point in efforts to promote the worldwide use of the renewable energy was marked in The Kyoto Protocol to the United Nations Framework Convention on Climate Change [107], agreed in December 1997. Besides the legally binding emissions limits for industrial countries, this pact includes a promotion of the renewable energy as a key strategy for reducing green-house gas emissions. In general, there are many environmental friendly technologies, based on RESs, that can be used to meet various energy needs, including electricity, heating buildings, fueling vehicles and providing process heat for industrial facilities [68]. The usage of RESs has a significant contribution to the world electricity production as the total renewable energy is accounted for 20 % of the total power generation [14]. This achievements prevents to release CO_2 emissions into the atmosphere each year.

The environmental benefits provided by the use of RESs are self-evident. However, besides the use of RESs, the efforts should be also targeted at decreasing the global energy consumption. According to the recent data from European Union [15] and United States of America [189] buildings are responsible for approximately 40 % of the total energy demand. Most of this energy comes from non-renewable energy sources. Therefore, the main objective of RES is to provide solutions that would improve the life quality, while reducing the energy consumption in the building sector.

Recently, more attention is paid to investigate and develop new sustainable building technologies based on environmentally clean energy sources. In general, all the energy demands, including heating, ventilation and air-conditioning can be fully satisfied directly with the use of various RES-based technologies: the geothermal energy can be applied with the usage of ground source heat pump systems [127], subsequently the biomass energy with the usage of combined heat and power systems [56], and the solar energy with the use of flat plate collectors [175] and photovoltaic (PV) panels [71, 187]. The electricity can be provided with the use of all aforemen-

tioned renewable energy sources [1, 150, 187], but the most common are the district or central grids based on wind [78] or hydro [85] energy sources, which provides the electricity to buildings.

The aforementioned approaches to use RESs in buildings have a great influence on a decrease of the non-renewable energy consumption as well as CO_2 emissions into the atmosphere. However, it is estimated that about 57 % (in Polish households is even higher – 70 %) of the total energy consumption in residential buildings is used for space-heating purposes [42]. Therefore, from the environmental point of view it is desirable to reduce the energy demand for heating in residential buildings with a simultaneous use of technologies based on RESs.

The well-known methods for a heat loss reduction in buildings usually increase the thermal resistance of the building's envelope. Unfortunately, there are limitations in a decrease of heat losses in this simple way. The buildings still demand the energy for heating and cooling. However, the reduced thermal loads can be fully satisfied with the use of technologies based on environmentally clean and renewable energy sources, especially those using the solar energy, which is the most attainable [22].

In the past 20 years, the interest has been growing up to develop new sustainable building technologies based on the solar energy and passive solutions. One of the most effective approaches to the energy management in buildings is the idea of the passive solar heating and cooling, also known as the solar design [165]. In this approach, the solar radiation is absorbed by the building envelope and stored in structure components. The stored energy can be further extracted, e.g. to preheat ventilation air without using any appliances. There are several technologies based on a concept of passive heating and cooling such as Trombe Wall [31], Water Wall [13] or Roof Ponds [95]. However, according to Chan et al. [31], the solar designs have a number of limitations and might not be sufficient to provide the indoor thermal comfort, particularly in regions having extreme climates. Moreover, this approach does not enable to supply the energy to warm up the domestic hot water, whose contribution to the energy consumption in residential buildings may be up to 25 % [42]. Thus, the solar radiation driven passive techniques should be considered together with active solar energy collecting systems [12].

1.2 Problem

The active solar energy collecting systems can be used to supply space-heating and domestic hot water (DHW) systems. Moreover, they can also be used to provide

electricity. The main feature of active solar energy systems is the use of plants, so-called solar collectors and PV collectors, that collect the solar energy and convert it into the useable heat [12] or electricity [71, 187]. The active solar energy systems can be installed separately outside the building's outline or roof-mounted. However, due to the limited area surrounding buildings, they are usually located on the roof top.

Since the problem of this thesis refers to an active solar energy system used to supply heating systems in residential buildings, the further discussion deals with solar collectors only.

During the last two decades, a number of investigations have been performed to develop new and more efficient solar collectors or improving existing ones [70]. Most of the efforts were made to improve the thermal performance by increasing the characteristics of the absorber plate [5, 105, 106], reducing the collector heat losses [174], extending the heat transfer area [81] or optimizing the design parameters [114, 162]. In consequence, the efficiency of the solar energy conversion higher than 50 % is typical for conventional solar collectors [9]. Thus, solar collectors have a great potential to become a main stream in renewable energy supply technologies.

However, according to disadvantages of conventional solar collectors, including high investment costs and a crucial influence on the building aesthetics [25, 31, 168], there is still a barrier to widespread a deployment of solar collectors. Moreover, the performance of space- and water-heating technologies using the solar energy is limited according to the nature of its source. The solar energy is characterized by a strongly variable availability. A maximum energy demand for the space-heating systems occurs when its availability is minimum or none. On the other hand, the peak of the solar energy availability occurs in summer when there is no need for heating. Hence, the heat storage, preserving and extraction for a further use, makes the Heat Storage (HS) a key technology in an efficient use of the solar energy. This problem especially concerns high latitude countries, e.g. Poland [43].

In general, there are several available methods for a seasonal storage of the solar energy for the purpose of residential applications. They are usually based on a large heat capacitance of building materials [73], ground [39, 55, 63, 145, 172, 186], water [135] or on the latent heat of Phase Change Materials (PCM) [143]. The use of solar energy storage systems, however, does not enable to cover all energy demands in residential buildings. Schmidt et al. [146] presented the results from central solar heating plants with a seasonal HS in Germany. The authors reported that by the integration of the seasonal HS, slightly more than 50 % of the annual heating demand for space-heating and domestic hot water can be supplied by the solar energy.

Generally, the problem is related to the operational temperature of conventional heating systems, such as floor heating or radiators, whose operating temperatures are about 35 °C and 60 °C, respectively. The maintenance of such temperatures in the seasonal solar HS system during the winter season is impossible. Hence, conventional heating systems have to be still supported by appliances, e.g. heat pumps and electrical heaters which increase the operational temperature.

Fortunately, recent improvements of building technologies and new international [54] and local requirements [171] significantly reduced the heat demand in residential buildings. This led to the development of new heating technologies based on low-temperature heat sources with the temperature much less than 50 °C, such as air-conditioning systems basing on the earth to air heat exchanger (EAHE) for supply the air pre-heating [129]. One of the most recent technology, known as the Thermal Barrier (TB), was presented by Krzaczek and Kowalczuk [103]. TB (more extensively described in Section 3.3.2.4) is a technique of the indirect heating and cooling driven by the solar energy stored in a ground heat storage (GHS) system of a very-low-temperature but at least 25 °C. This temperature in a seasonal HS system can be successfully maintained during the entire year, when the solar energy is collected with the use of conventional solar collectors. The recent advances in buildings heating technologies enable to implement a new generation of solar collectors which are characterized by a reduced performance but are cheap and easy to mount and are still able to fulfill requirements of very-low temperature heating systems.

In this study, a concept of the innovative solar energy hidden collector is presented and investigated numerically. The collector, later named as the hidden solar collector (HSC), consists of a solar energy collection pipe system located under the roofing. Therefore, it does not affect the aesthetics of buildings and is very cheap in manufacturing, mounting and maintaining. These are the great advantages of the concept. The solar energy is collected with the help of the fluid flowing through a simple system of polypropylene pipes. Opposite to conventional solar collectors, HSC enables to fit the size of the collection area in dependence on heating loads, without any impact on the building aesthetics and is limited by the roof area, only. It is expected that during a year-round operation, HSC is able to collect the sufficient amount of the solar energy to supply space-heating systems based on very-low-temperature heat sources dedicated for residential, single- and multi-family, detached houses characterized by a low heat demand and to support DHW systems.

1.3 Aims

The main objective of the thesis is to determine the performance of a hidden solar collector during a year-round operation under Polish climate conditions. The present study was performed using a numerical approach. Thus, attention was paid to develop a numerical model of the hidden solar collector which enables a reliable simulation of the complex multidimensional unsteady heat transfer. Results of a simulation of the year-round operation are crucial to evaluate the potential of the proposed solar collector to supply space-heating systems based on very-low-temperature heat sources dedicated for residential detached houses characterized by a low heat demand and to support DHW systems. The study also aims at giving some recommendations to design hidden solar collectors and an operation control strategy in order to maximize the performance of the entire system. Hence, comprehensive parametric analyses using a model of the steady-state heat transfer in a hidden solar collector were carried out.

Conclusions of this thesis would contribute to realization of the ongoing research project "Innovative comprehensive and solution system for the energy-efficient, characterized by a high-class comfort, house building in a unique prefabrication technology, and installation of composite panels" financed by the National Centre for Research and Development (in Poland). The project inter alia aims at implementation of the TB heating/cooling technology (Section 3.3.2.4) in the house building sector, which is supplied by the solar energy collected by the hidden solar collector. The main stage of the project is the experimental investigation of the performance of the TB technology and its ability to maintain the designed thermal comfort conditions. For this purpose, a full-scale test building will be built. An active solar energy system for supplying the TB technology in the test building will be composed of the hidden solar collector and ground heat storage system with horizontal heat exchangers. The implementation of the test building must be preceded by numerical analyses of its key components (including a wall with TB, hidden solar collector and ground heat storage system) aiming at operation optimization of the entire system. Within the project, the author of this thesis is responsible for the implementation of the active solar energy system.

1.4 Outline

The thesis consists of 7 chapters. Chapter 2 focuses on the availability of the solar energy and the current state of solar systems' applications in Poland. A characteristics of the solar radiation as an energy source is also discussed. This Chapter clearly

indicates the importance of the problem considered in the thesis.

Chapter 3 describes the recently available technologies driven by the solar energy for applications in residential buildings. The advantages and limitations of solar technologies, and possible improvements are also discussed.

Chapter 4 presents a basic characteristics of the proposed hidden solar collector including structure, efficiency and possible applications of the collector. The problem of the heat transfer in a hidden solar collector is discussed. Available solution methods and literature review of approaches for a thermal modeling of heat transfer mechanisms identified for a hidden solar collector, are also presented.

Chapter 5 presents thermal models of the hidden solar collector developed for numerical investigations. All assumptions of thermal models and a strategy of the fluid flow control in the collector are discussed. The efficiency and performance indices are defined and discussed.

Chapter 6 presents results of numerical investigations. The investigations are divided into two main stages: (1) an analysis of the impact of environmental, optical and operational parameters on the performance (2) and unsteady simulations to investigate the performance of the proposed solar collector during a year-round operation applied to supply space-heating systems and to support domestic hot water systems.

Chapter 7 lists the final conclusions and describes the future work plan.

1.5 Novelties

The integration of solar collectors with the roof structure of residential buildings is presently an object of interest to researchers. Both structure and operation principle (the simplest structure and cheapest in maintaining) of the solar collector investigated in this thesis have never been an object of any theoretical and experimental analysis. There is a lack of data concerning the efficiency and possibility of its application to supply the low-temperature-based thermal systems in residential buildings. The novelty of this doctoral thesis is the research undertaken to determine the performance of hidden solar collector applied to supply space-heating systems based on very-low-temperature heat sources dedicated for residential houses characterized by a low heat demand and to support DHW systems.

Results of this study contributed to the realization of the experimental building, in a full scale, equipped with a hidden solar collector, ground heat storage system and Thermal Barrier technology. The use of a solar collector to supply the Thermal Barrier technology has not been an object of any experimental research yet.

Chapter 2

Energy profile and use of solar energy in Poland

In this chapter, the characteristics of the solar radiation as the energy source and the current state of solar systems are presented.

2.1 Solar energy

Solar radiation is emitted by nuclear fusion reactions in the sun core. According to the brief explanation by Kalogirou [91], the sun is a sphere of the intensely hot gaseous matter with the diameter of 1.39×10^9 m, whose effective blackbody temperature is 5762 K. The temperature in the central region is, however, higher $8 \times 10^6 - 40 \times 10^6$ K. In consequence, the sun is a reactor of the continuous fusion, in which the hydrogen is turned into the helium. The sun emits the energy in all directions at the rate of 3.8×10^{23} kW [165] but only a small part of this energy reaches the earth's surface.

In general, the amount of the extraterrestrial solar radiation falling on top of the atmosphere can be predicted with a high precision. This amount depends essentially on the astronomical geometric parameter, such as the actual distance from sun to earth. Since the earth moves around the sun on an elliptical orbit, the sun-earth distance is a function of the day. With regard to the mean value of the earth-sun distance, the amount of the energy per unit area received from the sun outside the earth's atmosphere, termed as the solar constant, equals 1367 W/m^2 [58]. Taking into account the earth's cross-section of 127400000 km^2, the total power for the earth is approximately 1.75×10^{14} kW.

The prediction of the solar radiation reaching the earth's surface is more difficult because of the interaction with the atmosphere, and with different soil surfaces.

The mean solar radiation is a function of various statistical data which cannot be predicted with a high precision. While passing through the atmosphere, a large part of the incident energy is suppressed by reflection, scattering or absorption by air molecules, clouds and particulate matter (usually called aerosols). As a consequence, only 60 % (approximately 1.05×10^{14} kW) of sunlight striking the earth's atmosphere reaches the earth's surface [92]. Nevertheless, the total annual solar radiation falling on the earth's surface is more than 7500 times the world's total annual primary energy consumption of 450 EJ [165].

The radiation part that is not reflected or scattered, and reaches a defined surface straight from the sun is called the direct or beam radiation. The scattered radiation which reaches a defined surface from all directions is called the diffuse sky radiation. Various components of solar radiation on intercepting surfaces are illustrated in Fig. 2.1.

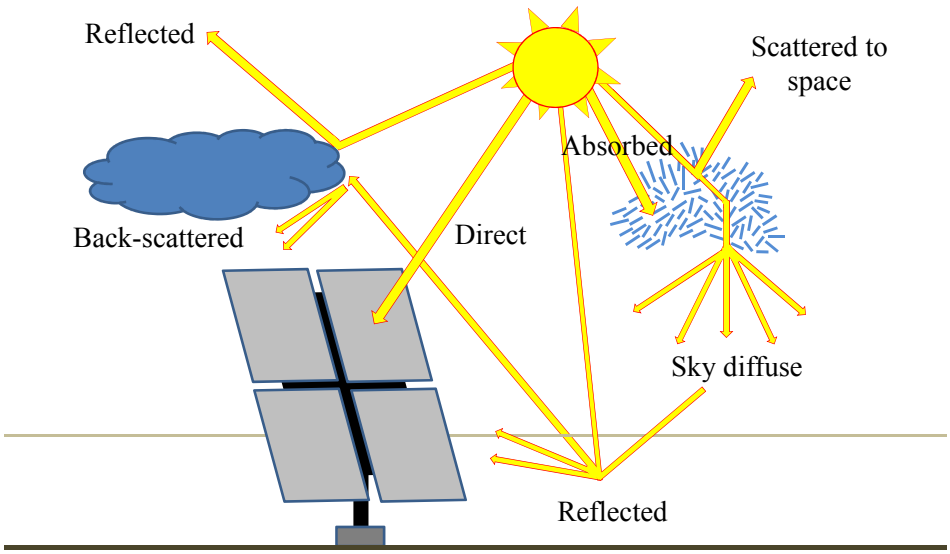

Figure 2.1: Solar radiation components (based on [8])

The total radiation flux on a horizontal surface in the presence of the diffuse sky and direct radiation is called the global or total horizontal radiation. The total radiation flux on a non-horizontal (tilted) surface is a combination of the direct radiation, diffuse sky radiation, and additional radiation that is reflected from the ground surface, and is called the global tilted radiation. The relationship between the components of global tilted radiation can be described as [144]:

$$E_{G,tilt} = E_{dir,tilt} + E_{diff,tilt} + E_{refl,tilt}, \tag{2.1.1}$$

where $E_{G,tilt}$ is the global irradiance on a tilted surface, $E_{dir,tilt}$ is the direct irradiance on a tilted surface, $E_{diff,tilt}$ is the diffuse irradiance on a tilted surface and $E_{refl,tilt}$

is the ground reflected irradiance on a tilted surface.

In general, a fundamental factor that determines the availability of the solar radiation in specific locations are climate conditions formed by geographical factors including: latitude, size of lands and seas, sea tides, height above sea level and land formation. Especially the latitude is of a great importance since the angle of the incidence of the solar radiation results in the lower irradiance at higher latitudes (Fig. 2.2). Kjellson [99] pointed two reasons for this. One refers to the distance through which the solar radiation has to travel in the atmosphere before reaching the earth. At higher latitudes the distance is longer, resulting in the increased absorption and reflection of the solar radiation before reaching the earth. The other one is that the higher angle of incidence results in the lower irradiance on the horizontal ground surface.

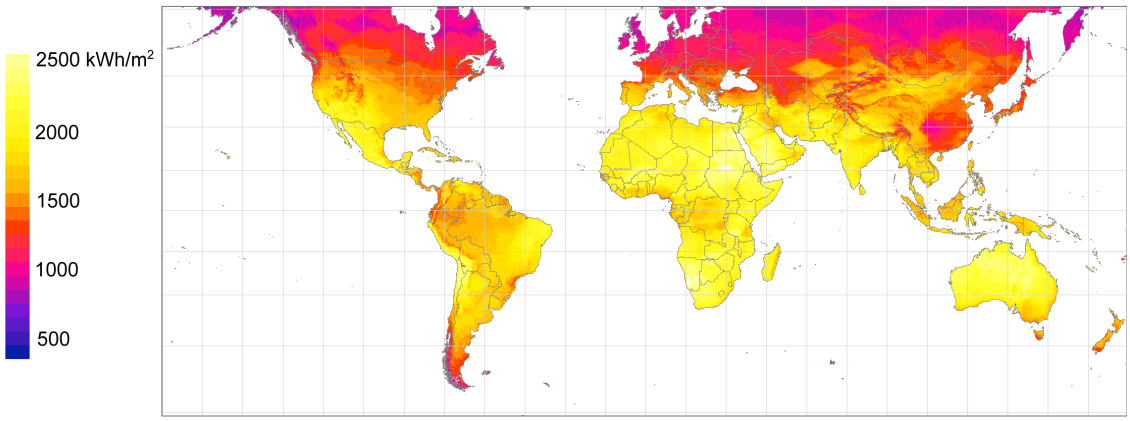

Figure 2.2: Annual global solar irradiation in world on horizontal surface [99]

2.2 Availability of solar energy in Poland

The use of solar technologies for thermal applications in residential buildings is crucially dependent on the availability of the solar radiation, its distribution in time and structure. As it was aforementioned, the climate formed by geographical factors is a fundamental factor determining the availability of the solar radiation for specific locations.

Poland is located at the Northern European Plain. It is bordered by the Baltic Sea in the north and Carpathian Mountains in the south, and lies open to the east and west. The country is located between 49 °N and 54.5 °N latitudes in a moderate climate zone that is influenced by both the Atlantic and Continental climate. According to its location, Poland is continuously affected by different atmospheric fronts resulting in frequent heavy cloud formations that have a significant impact on

the structure of the solar radiation. In general, the availability of the solar energy in Poland is similar to the most of European countries. As shown in Fig. 2.3, the quantity of the average annual solar irradiation on the horizontal plane in Poland is in range from 950 up to 1150 kWh/m^2 per year [21]. To compare, it is 898 and 1025 kWh/m^2 per year for London and Berlin, respectively [144]. Basically, the smallest quantities of the average annual irradiation on the horizontal plane are observed in the highly industrialized area located at the border of three countries: Czech Republic, Germany and Poland, and in the coastal region - coastal zone, except the West Coast. The rest of the country is characterized by a relatively high level of the average annual irradiation.

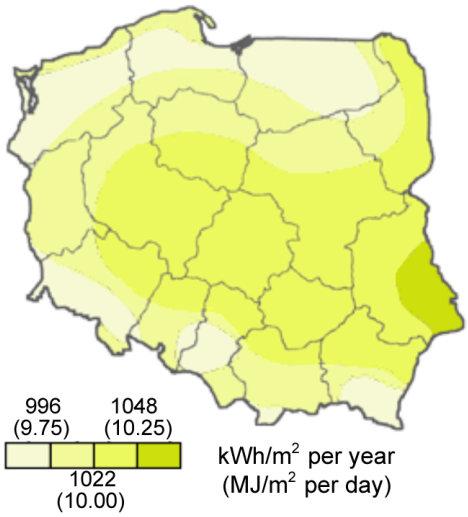

Figure 2.3: Distribution of average annual solar irradiation in Poland [179]

The structure of the solar radiation is characterized by a very high share of the diffuse radiation, especially during the winter season. An average annual percentage of the diffuse radiation is equal to 55 % [43]. In December it reaches the level up to 70 % [35]. In the summer season, the share of the direct radiation is smaller and is 56 %. The number of solar operation hours is very close throughout the country (Fig. 2.4). The average number of solar operation hours can be estimated as 1600 hours [67].

Fig. 2.5 presents the total solar irradiance on a horizontal surface based on the representative and averaged hourly solar radiation model for Elbląg, North-East Poland. The model is based on the 30-year period of measurements series of the hourly total and diffuse radiation for an actinometrical station in Elbląg [164]. The distribution of the available solar irradiance during the whole year is very irregular. It is estimated that only 23 % of the annual solar irradiation is available in the period from October to March. The highest and lowest solar irradiation for the specified

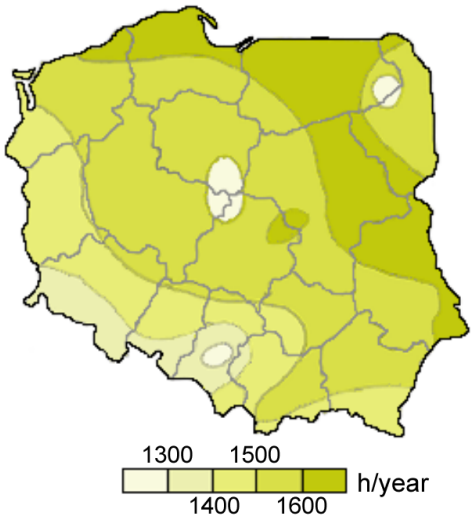

Figure 2.4: Distribution of annual solar hours in Poland [179]

location occurs in May and December, respectively. Taking into account the total surface area of Poland (about 312678 km^2) and the average annual solar irradiation on the horizontal plane (1050 kWh/m^2 per year), the approximated annual amount of the available solar energy is 1181926 PJ. With regard to 3000 PJ of the heat that is used for annual heating purposes in Poland [41], it can be concluded that there is a great potential for solar systems in the Polish building sector.

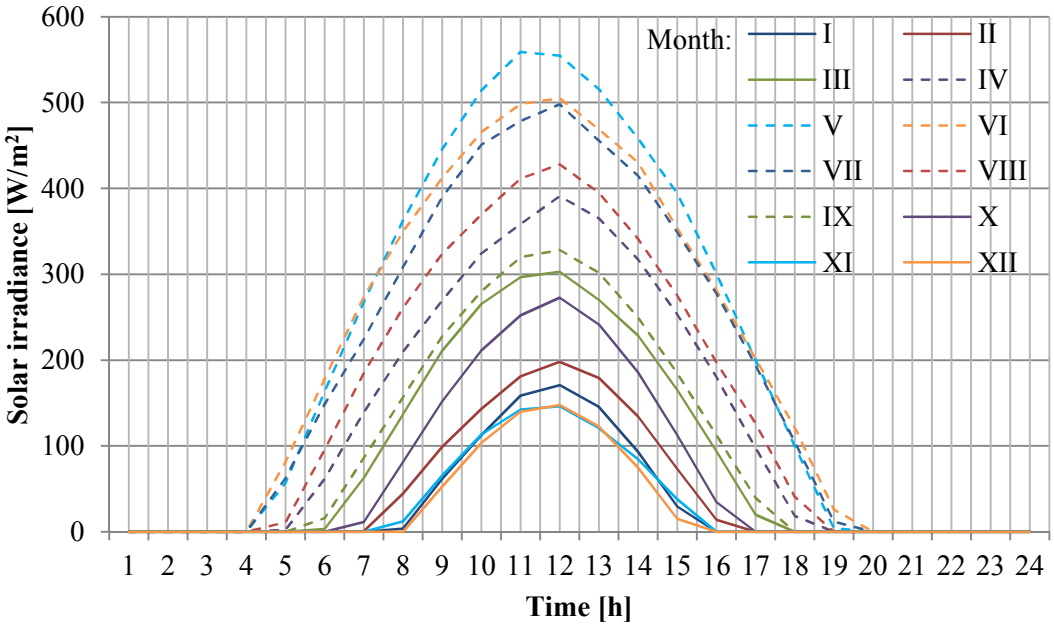

Figure 2.5: Distribution of total solar irradiance during averaged days for every month of year for horizontal surface in Elbląg

2.3 Use of solar energy in Poland

Reserves of solar energy in Poland are generally sufficient to supply solar technologies [41]. Nevertheless, according to a stochastic nature of the solar radiation and its periodic availability, the implementation of solar technologies in Polish buildings needs an employment of additional or specific solutions.

The first solution concerns a discrepancy between the thermal loads and solar energy availability, especially during the winter season. An application of the solar energy for space heating purposes, usually, requires active solar systems in a combination with seasonal HS systems [135]. The use of solar systems enable to reduce in 30 % the heat consumption for the space heating (in comparison with a traditional heating system) [38]. The reduced thermal requirements cannot be, however, fully satisfied with the energy collected by active solar systems. Under Polish climate conditions, these systems must be additionally equipped with auxiliary heaters. The auxiliary heaters are turned on when the useful solar energy cannot meet heating requirements.

Another solution refers to a structure of the solar radiation. The high share of the diffuse radiation determines the need of applying solar collectors that are able to collect both the diffuse and direct solar radiation. Active solar systems applying only the direct radiation cannot operate effectively under Polish climatic conditions. In general, a very attractive solution from the standpoint of the solar radiation structure is the use of vacuum tube collectors (Section 3.3.1). However, it is worth to notice that glass tubes of vacuum collectors may be easily destroyed when they are covered with snow and ambient temperatures vary around 0 °C. Such climate conditions are typical for Poland, hence, the use of vacuum tube collectors is problematic.

Last solutions that should be considered in order to implement a particular solar technology in Poland are related to a proper orientation and angle of inclination of each element of solar systems. The general recommendations to maximize the collection of the solar energy under Polish conditions are given by Chwieduk [38]. In the case of passive solar systems (Section 3.2), it is suggested to expose the living area, sun glass spaces, main part of a building envelope to the south west. The components should be tilted at angles not less than 60 °. The horizontal and tilted (at small angle) glass surfaces are not recommended since they may give a high solar heat gain effect in summer, that is undesired in the Polish climate. In the case of active solar systems (Section 3.3) which are expected to operate only in warm months (i.e. from May to the end of September) the optimum inclination angle for the solar collector surface is suggested to be in range from 20 ° up to 25 °. If an

active solar system is expected to operate only during the heating season (i.e. from October to April), the optimum inclination angle for solar collector surface should be in range from 55 ° up to 60 °. According to Wisniewski et al. [180] a surface of the solar collector should be tilted at the angle of 40 °, when an active solar system is expected to operate continuously throughout the year. Moreover, to maximize the performance of solar collectors, it is recommended to move the absorbing surface slightly to the south east (10–15 °) in warm months and to the south west (10 °) during the heating season.

The present state of the solar energy use in the Polish building sector is disproportional to an existing potential for solar heat applications; less than 8 PJ of about 3000 PJ of the heat used for annual heating purposes is produced by active solar heating systems [41]. The total surface area of solar collectors under operation in 2010 in Poland was only 655890 m^2. At the same time, the area of 13824000 m^2 was under operation in Germany [60]. A significant limitation in the state of the development of solar technologies as compared to countries with similar solar radiation conditions, is a consequence of the coal energy lobby, standards of architecture designs, investment costs and common opinion that solar technologies are not efficient under Polish climate conditions. Among the above-mentioned limitations, the reasonable barriers are, however, the interference into the building aesthetics and investment costs. The application of solar collectors is not aesthetically acceptable in many cases [25, 168]. The economic efficiency expressed by the payback time of active solar heating system investments can be equal up to 16 years [41]. Nevertheless, the Polish market of solar technologies grows over recent time [60]. The forecast (assuming a realization of the solar energy promotion scenario) for 2020 and 2030 of the use of solar active heating systems in Poland is given in Table 2.1.

Table 2.1: Forecast for active solar thermal system use in Poland [36]

Solar thermal energy use				
Year	Installed capacity [GW]	Area of solar collectors [10^6 m^2]	Area per person [m^2/person]	Annual energy [PJ]
2020	112	160	2	160
2030	224	320	4	320

In general, the use of the solar energy in Poland concerns mainly the solar active systems in the form of a stand-alone or roof-mounted flat plate or vacuum solar collectors, in which the fluid flow is forced by mechanical device. These systems are

mostly used to heat the water for domestic purposes. Chwieduk [41] indicated that the use of solar collectors in Poland to support DHW systems is effective during spring and summer, especially from May to the end of August. In this time, the total hot water demands can be fulfilled on average of 80–100 %. The use of the solar energy in Poland should be, however, more focused on the space-heating systems since there are already available technologies, such as the floor and wall heating, which require a much lower operating temperature than the operating temperature of DHW systems. Moreover, due to a radical decrease of the heat demand in residential buildings, many new heating technologies based on very-low-temperature heat sources, e.g. Thermal Barrier (Section 3.3.2.4), were developed. These technologies give an opportunity to develop and implement novel, very cheap and of simple structure solar collectors which overcomes above-mentioned limitations to widespread the use of solar technologies. The promotion and implementation of such solar collectors should be a major target in the future.

2.4 Summary

The availability of the solar energy in Poland is similar as in most of European countries. The approximated annual amount of the available solar energy in the entire country is almost 400 times more than the total amount of the heat energy used for annual heating purposes. Hence, it can be concluded that there exist a great potential for solar systems in the Polish building sector. One should notice, that the solar energy availability and heat demand for the space heating are opposite in time. Therefore, the use of the solar energy for the space heating under Polish climate conditions requires a seasonal HS system.

The total surface area of solar collectors in operation in 2010 in Poland was over 21 times lower as compared to Germany. The use of the solar energy in Poland is related mainly to active solar energy technologies dedicated to support DHW systems. Less than 0.3 % of the heat used for annual space-heating purposes is provided by active solar technologies. A disproportion between the existing potential and use of the solar energy is a consequence of the strong coal energy lobby, standards in architectural designing, high investment costs and common opinion that solar technologies are not efficient under Polish climate conditions. Except of the last argument (which is wrong) the interference into the building aesthetics and high investment costs are real barriers for solar technologies in Poland. Therefore, an implementation of novel, cheap and simple solar collectors should be a major target in the future.

The concept of HSC (Chapter 4) is characterized by a low cost and lack of interference into the building aesthetics. In view of these advantages over stand-alone or roof-mounted conventional solar collectors, it can be concluded that there is a great potential for applications of HSC to supply space-heating systems based on very-low-temperature heat sources dedicated for residential houses characterized by a low heat demand and also to support DHW systems. Therefore, the evaluation of the HSC performance during a year-round operation under Polish climate conditions is desired.

Chapter 3

Solar energy technologies in residential buildings

There exist several technologies to collect the solar energy to be implemented in residential buildings to provide comfortable living conditions and protect the natural environment. This chapter provides a brief history of the solar energy application and description of available solar energy technologies. The advantages and limitations of technologies are discussed.

3.1 Historical background

Sun was always considered as a common source of light and warmth. Thus, the solar energy had a great influence on building design and urban planning methods since ages. The relationship between buildings and surrounding environment was taken into account by ancient architects of Egypt, Greek and roman cities. They believed that a proper location, orientation, shape and construction of buildings could provide some benefits from the solar energy in cold seasons [2]. Ancient buildings were constructed such that the sun rays provided light and heat for indoor spaces. The Greek philosopher Socrates was the first who mentioned the issues associated with solar-heated houses, as he wrote: *In the house that looks toward the south, the sun penetrates the entrance in winter.* The Romans improved this early form of the solar architecture by covering south-facing openings with transparent materials such as glass. The introduction of glass covers represented a significant step forward in the performance of a solar technology. Such a simple solution, allowed the short-wave solar radiation to penetrate the building interior without an undesired impact of external environmental factors (e.g. wind, rain or snow). The improvement of the solar architecture also met the legislation form. The Romans passed sun-right laws

that forbade other builders from blocking a solar-designed structure's access to the winter sun. The use of the solar architecture evolved through the centuries and nowadays, it is well known as the solar design.

The history's turning point of the solar energy application, that led to a development of active solar energy technologies, dates from 1776 when the Swiss scientist Horace-Benedict de Saussure built a device which concentrated the sunlight for the use as a heat source. He built a small rectangular wooden box of the black painted interior, with the external insulation, the multi-layer glass cover at the top, and placed it inside of a bigger wooden box (Fig. 3.1). When exposed to the sun, the bottom box heated to 110 °C [155]. De Saussure was the first who demonstrated that temperatures exceeding the boiling point of water could be produced in a glass-covered box. His invention, called *solar hot box*, attracted the interest among many scientist and became the prototype for the late 19th and 20th century solar collectors that were able to supply the warm up hot water for houses and power for machines.

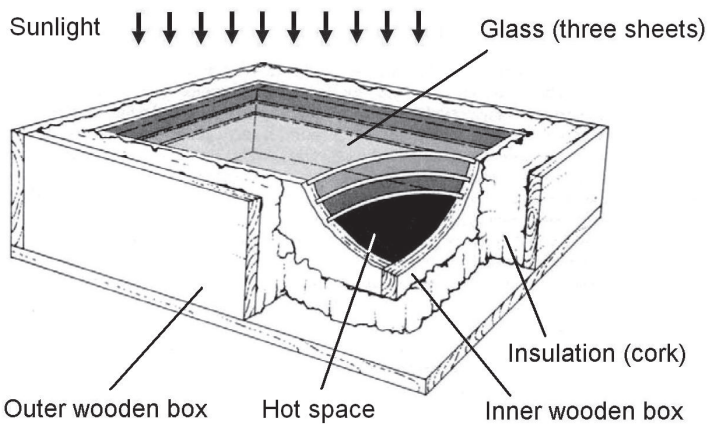

Figure 3.1: The hot box of Horace de Saussure [32]

In 1891, Clarence Kemp patented a method to combine the old practice of exposing metal tanks to the sun with the scientific principle of the *solar hot box*, by increasing the tank capability to collect and retain the solar heat [96]. It was the world first commercial solar water heater, which was manufactured under the trade name the *Climax Solar-Water Heater*. The unit of the solar water heater was made from four heavy galvanized iron cylindrical vessels (each of 29 l capacity), painted as dull black and mounted in a wooden box insulated with the felt paper, under a single-glazed aperture. Smyth et al. [155] reported that the *Climax Solar-Water Heater* could be used from April to October in the state of Maryland in the eastern USA, producing the water hotter than 38 °C during sunny days even, it was claimed,

during early spring and in late autumn when daytime temperatures sometimes approached freezing. The heating and the storage unit of the Climax system were the same. Due to a direct exposure to the cold night air, the water heated by the sun before the night never stayed hot enough to be used next morning.

In 1909, William J. Bailey patented a solar water heating system that dealt with the aforementioned problem. He separated the solar water heater into two parts: a heating element exposed to the sun and an insulated storage tank located in a house. Hence, the heated water was available all day and night and early next morning. Bailey reduced the volume of water exposed to the sun at any moment. The water passed through narrow copper pipes attached to a black-painted metal sheet placed in a glass-cover box. Therefore, the water heated up faster. The system was able to achieve the temperature of the heated water between 100–150 °C [26]. This concept forever changed the solar hot water industry and is still in a widespread use throughout the world.

The first attempts to convert solar energy into useful power date for the second part of the 19th century. In 1861, a mathematics lecturer at the Lyce de Tours, August Mouchout developed a steam engine powered entirely by the sun. It was the earliest known record of a direct conversion of the solar radiation into the mechanical power. The invention was, however, very expensive and it could not be reproduced [153].

Another big milestone in the solar energy conversion into the useful power were the photovoltaic (PV) devices that directly converted the solar radiation into the electricity without an intermediate thermal conversion process. The discovery of the PV effect can be prescribed to the French physicist Edmond Becquerel's finding (in 1839) that the electricity generation in an electrolytic cell made up of two metal electrodes increased when exposed to the light [152]. In 1883, the American inventor Charles Fritts presented first solar cells made from selenium wafers. His solar cell had a conversion rate of only 1–2 % [152]. This invention proved that a solid material could convert light into electricity without heat or moving parts. In 1953, Calvin Fuller, Gerald Pearson and Daryl Chaplin of Bell Laboratories discovered the use of silicon as a semi-conductor in a solar cell [155]. It enabled to construct a solar panel with the efficiency rate of 6 %. It was the first silicon solar cell capable of generating an electric current. Two years later, first commercial PV cells were available at the market. Later improvements increased the efficiency rate to 11 %, although the cost was prohibitively high (about $1000/W) [91]. The first practical application of solar cells was in sites where no other source of power was available and the cost was not a barrier.

After the 1960s, the public's consciousness of a need to decrease the energy demand in buildings and to increase the use of the renewable energy grew up significantly. This caused many investigations and developments of solar energy technologies. A continuous demand for an alternative power source due to decreasing reserves of fossil fuels, rising energy prices and a need to reduce greenhouse gases emissions in the building sector was its driving force.

Recent solar energy technologies are capable to collect, convert and store the solar energy efficiently. There are many solar systems that can be used to meet space- and water-heating needs and to generate the electricity. The use of the solar energy in the building sector could be divided into passive and active solar energy systems. First technologies are related to the building's envelope design while active technologies are related to the use of solar collectors to heat the fluid. Both technologies should be, however, combined together in order to efficiently use the solar energy in residential buildings.

An extensive study concerning the use of solar energy in buildings is given by Chwieduk [37]. The objective of the following sub-sections is to review the solar energy technologies which can be implemented in residential buildings to provide comfortable living conditions while protecting natural environment at a low cost.

3.2 Passive solar energy systems

A proper design of buildings with regard to building materials, building structure and heat distribution in the buildings, can significantly reduce the heat demand of buildings during winter. An additional reduction can be, however, achieved through a rational use of the solar energy by means of passive solar energy systems. A proper design of the building including a passive system, also known as a solar design, is a simple form of providing comfortable living conditions in residential buildings, since it can be used for both heating and cooling purposes.

This approach relies upon an appropriate building orientation and a design that takes advantage of local climate conditions. The general idea is to use the building itself either to gain as much solar energy as possible and release it into the building interior when the sun is not shining, or to protect from the solar radiation, in dependence on specific climate conditions and a year season. This idea can be realized by introducing passive solar energy systems at the south part of the building and applying the additional thermal insulation at north walls. A strategy of the passive solar heating can be applied to any existing building. However, it is the least expensive and the most effective when it is implemented into the design of a

new building.

The implementation of a solar design strategy can be performed by several ways with regard to the type of a passive solar energy system. In general there are three basic passive solar systems such as: direct solar heat gain system, indirect solar heat gain system and isolated solar heat gain system. All systems, however, demand an incorporation of five components of a solar design (Fig. 3.2) including the aperture, absorber, thermal mass, distribution and control system.

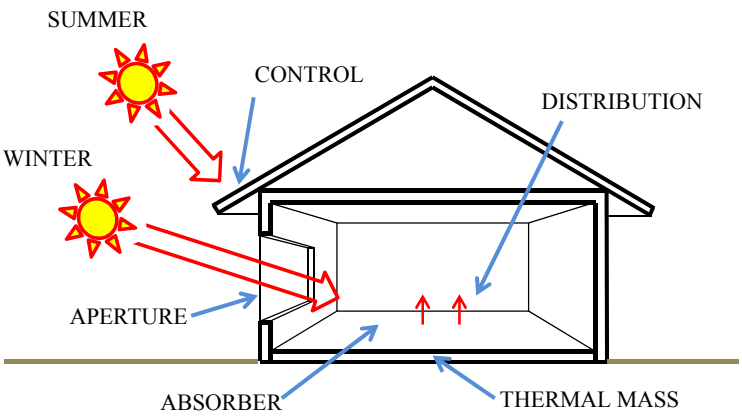

Figure 3.2: Fundamental elements of solar design

According to a brief description by Tian and Qin [166], the most common form of an aperture are windows. Its large glazing surface through which the sunlight enters the building should be south-facing. Moreover, it should be free of shading by other buildings or trees during the heating season. Another essential component, related to the surface of the thermal mass, is the absorber. This usually darkened component, situated along the path of sunlight, absorbs the solar radiation. It is possible to improve the absorption by using materials with the appropriate color and roughness. First of the factors influences the absorptive ratio of the short-wave radiation, while second one has a significant impact on the absorptive ratio of the long-wave radiation. The thermal mass is a material that is always arranged behind the absorber's exposed surface. It has to retain or store the solar energy in the form of the specific heat. The most common material of the thermal mass is represented by stone walls, floors, PCM and water containers. However, the integration of water containers into a building design is very difficult. The distribution system is the method by which the heat circulates from collection and storage points to different house areas. In the case of a standard design, the gained energy is transferred by natural heat transfer modes – conduction, convection, and radiation. In some applications, this process is supported by fans, ducts and blowers. The control

system is applied with the aim of avoiding the overheating the building interior. The most popular devices are the roof overhang (to shade the aperture surface during summer), blinds, operable vents and dampers (to allow for or restrict heat flow), and electronic sensing devices (to turn on fans). Each of aforementioned fundamental components plays a clear function. However, to realize a complete and successful solar design, all of them have to work together.

Besides heating and cooling purposes, passive solar energy systems can be also applied to meet DHW requirements. Such systems are based on solar collectors, a storage tank, and an energy carrying medium, usually fluids (later named as the operating fluids) that circulates through a pipe system between those components. In contrast to active solar energy systems, the circulation of the fluid occurs by the natural convection. The most common passive solar energy system applied to meet DHW requirements is the thermosyphon system. This system will be briefly described in Section 3.3.2 to emphasize the difference between a passive and an active approach for solar water-heating systems.

3.2.1 Direct solar heat gain system

A direct solar heat gain system is the simplest form of a solar design technique that evolved through centuries. The essence of the system is the use of the solar energy without interferences. Moreover, the heat collection, storage and distribution systems occur in the same space. According to its principle of operation (Fig. 3.3a), the sunlight directly enters the house through the south-facing windows (the rate of the solar radiation transmitted through the window depends on optical properties of windows resulted from materials used for glazing and construction of windows). Then it is absorbed and stored in the form of heat by interior walls, floors and other components inside. The surface of the wall is usually dark to absorb more solar radiation. At night, as the indoor air cools, the heat stored in walls and floors is released into rooms by natural heat transfer modes (Fig. 3.3b).

During summer the direct solar gain system helps to cool the living space due to a reverse process. With the use of shading devices the massive wall is prevented from the direct sunlight. Thus, the heat is absorbed by the thermal mass and the temperature inside the room becomes lower.

The efficiency of this system depends on the surface area and properties of glazing, the size of the thermal mass and climate conditions. The size of a glazing surface determines how much the solar radiation can be collected while the size of the thermal mass determines how much of the heat can be stored. This system is significantly vulnerable for temperature fluctuations and there is a great risk of

overheating the building during summer. On the other hand, the system might not be sufficient to provide the indoor thermal comfort during winter, particularly in regions having extreme climates.

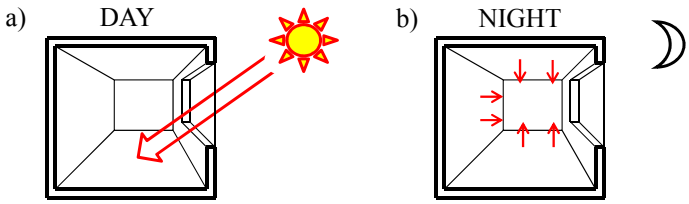

Figure 3.3: Schema of direct heat gain system operation during: (a) daytime and (b) night

3.2.2 Indirect solar heat gain system

Indirect solar heat gain systems are based on the same building materials and design principles as the direct heat gain system. The only difference is the location of the thermal mass. In this system, the thermal mass is located between the aperture and living space. Thus, the solar radiation is intercepted by the thermal mass directly behind the glazing surface of the aperture. There are various indirect solar gain systems. The most popular are the Trombe Wall, Water Wall, and Roof Pond.

Trombe Wall

The Trombe Wall system [31], also known as a solid wall solar system, was developed and patented in 1956 by Felix Trombe and is one of the most typical examples of indirect solar gain systems. It consists of a south-facing glass skin externally covering a massive wall (usually made from concrete or masonry) with vents, and the narrow air-cavity left between these layers. According to its principle of operation, during the day of winter (Fig. 3.4a), the sunlight passes through the glazing surface. The heat converted from the sunlight is collected and trapped in a narrow air-cavity between the glazing and a massive wall. The warmed air rises and flows into a living space through vents located at the wall top. Simultaneously, the cooler air in a living space flows out through vents at the wall bottom to exchange the warmer air in the air-cavity. Thus, the warmed air circulates throughout the building interior providing comfortable living conditions during a day. At the same time, the thermal mass absorbs and stores the heat to release it into the air by natural heat transfer modes when the sun disappears. To keep the warm air in a living space during a night (Fig. 3.4b), dampers should be placed in vents.

During summer the Trombe Wall system helps to cool a living space due to a reverse process. With the use of shading devices, a massive wall is prevented from the direct sunlight. Thus, the internal heat is absorbed by a massive wall and the temperature inside the room becomes lower.

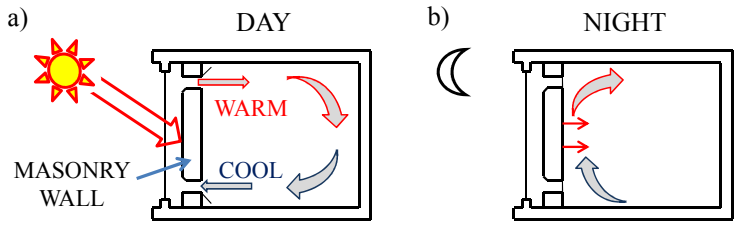

Figure 3.4: Schema of Trombe Wall system operation during: (a) daytime and (b) night

Water Wall

The Water Wall system [13] is based on the same principles as the Trombe Wall. However, it employs a different material as the thermal mass. Instead of a massive wall made from masonry or concrete, there is a water-filled container (Fig. 3.5). According to the principle of operation, the sunlight passing through the glazing surface is intercepted by a water storage mass. Subsequently, it is converted into the usable heat and distributed by natural heat transfer modes into a living space.

The use of water as a thermal mass provides benefits in efficiency and economy. The water is characterized by a high thermal capacity and a high heat conduction coefficient. Hence, the entire volume of the thermal mass gets warm much faster and thermal losses in the system are reduced significantly. In general, a large volume of the water container provides a higher and longer-term heat capacity, whereas a water container of a small volume provides a faster heat distribution. The use of this system is limited due to an interference into the building aesthetics.

Roof Pond

The Roof Pond system [95] is characterized by a different location of the thermal mass. Unlike the aforementioned solar systems, it is relocated from the wall and floor into the roof. The horizontal thermal mass of water is usually stored in plastic containers with a glazed upper layer located in the roof. This system requires a moveable external insulation to cover and uncover the water container when necessary. According to the principle of operation, during a winter day (Fig. 3.6a), the water container is uncovered and exposed to the direct solar radiation to absorb and

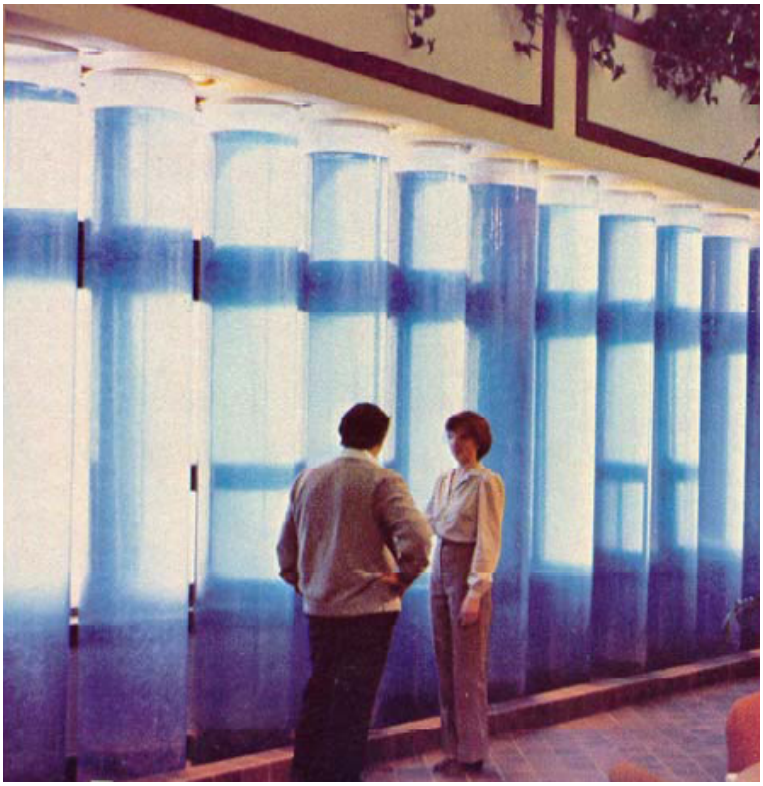

Figure 3.5: Transparent Water Wall [13]

store the energy. The accumulated heat is transferred to the ceiling under sunny and cloudy weather conditions. After the sunset, the container is covered by the insulation and a living space is warmed by the ceiling which radiates the heat, thus providing comfortable conditions.

The Roof Pond system can operate in a cooling mode as a result of a heat transfer direction reverse. During a summer day (Fig. 3.6b), the water container is covered by the insulation to prevent the water heating from the sunlight. At the same time, the ceiling mass absorbs the undesired heat from a living space and transfers it to the water container. After the sunset, the uncovered water container cools down by the exposure to the air.

The implementation of the Roof Pond system demands an appropriate design of a building structure to deal with additional loads from the water container. This system is suitable for one-store buildings located in regions where the temperature rarely drops below 0 °C and a position of the sun is relatively high during winter.

3.2.3 Isolated solar heat gain system

The isolated solar heat gain system integrates features of direct and indirect solar heat gain systems. However, the ability to isolate components that are responsi-

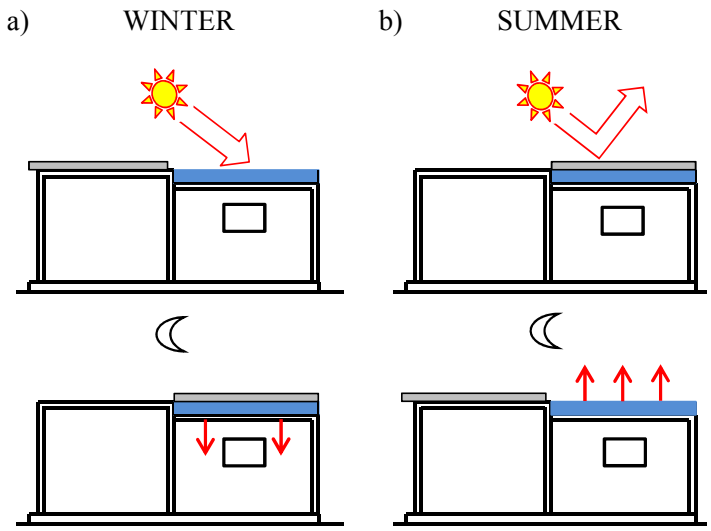

Figure 3.6: Schema of Roof Pond system operation under: (a) winter and (b) summer conditions

ble for a collection and storage of the solar energy from a primary living space of the building is the point of distinction for this system. These components work independently of the building. The most common examples of this system are the sunrooms.

During a clear sky day (Fig. 3.7a), the sunroom receives a lot of sunlight which is converted into the usable heat and stored in a massive separating wall. The heat excess retained in the air can be transferred by convection into a living space through vents, that is similar to indirect solar heat gain systems. After the sunset (Fig. 3.7b), the vents stay closed and the heat stored in a massive wall is transferred into a living space by means of natural heat transfer modes. This system possesses highly desirable architectural features as it provides to the building an additional usable space. The disadvantage is the relatively high cost and low efficiency as compared to direct and indirect solar heat gain systems.

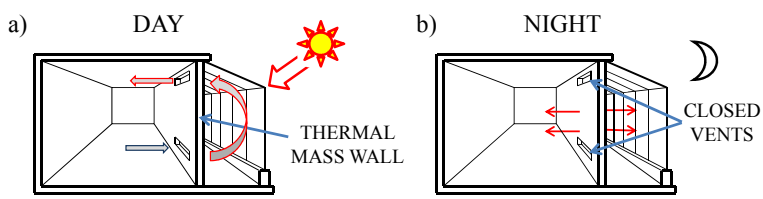

Figure 3.7: Schema of sunroom isolated solar heat gain system during: (a) daytime and (b) night

3.2.4 Summary

The use of passive solar energy systems, undoubtedly, provides environmental and financial benefits since it reduces the heat consumption for the space heating in residential buildings [38]. The solar design, however, has a number of limitations and might not be sufficient to provide the indoor thermal comfort, particularly in regions having extreme climates [31]. Moreover, this approach is not capable to satisfy any part of DHW requirements, whose contribution to the energy consumption in residential buildings may amount up to 25 % [42]. Thereby, passive solar systems should be implemented together with active solar energy systems.

3.3 Active solar energy systems

Active solar energy systems are an effective way to use the solar energy for various residential building applications. They can be used to supply space- and water-heating systems. Moreover, they can also be used to provide the electricity (PV collectors). In contrast to a passive approach, active solar heating systems employ an additional equipment in order to collect, store and distribute the solar energy. The major component of any active solar energy system is the solar collector. It is a device that absorbs the incoming solar radiation, converts it into the usable heat, and subsequently transfers the energy to the fluid flowing through the solar collector. Dependent upon the type of the fluid, there are liquid-based and air-based active solar heating systems. The heat carried by the fluid flowing out from the solar collector can be directly transferred to the domestic hot water or space-heating systems, or to the storage system with the use of heat exchangers. The heat from the storage system can be further extracted and distributed if needed.

To improve the efficiency of the heat collection and distribution, active solar energy systems comprise pumps, valves, temperature sensors and controllers. Moreover, due to the nature of the solar energy, the auxiliary energy systems should be implemented in order to meet the heating load when the solar energy is not available for a longer time period with a simultaneously depleted HS system.

3.3.1 Solar collectors

Solar collectors are a specific kind of heat exchangers that convert the solar energy to the usable heat and next transfer it to the fluid which is an energy carrier. These devices can be roof-mounted or installed separately outside the building. Therefore, they are not aesthetically acceptable in many cases. This is a great disadvantage

of conventional solar collectors, which may often limit the implementation of active solar energy systems in residential buildings.

Recently, several solar collectors are available on the market. Basically, they can be divided into two groups: non-concentrating or stationary, and concentrating solar collectors [91]. The solar collectors of the first group are characterized by a permanently fixed position and the use of the same area for intercepting and absorbing the solar radiation. The concentrating solar collectors are equipped with a single- or two-axes sun-tracking mechanism that enables the collector to be continuously positioned towards the sun. Moreover, these collectors usually have concave reflecting surfaces to intercept and focus the direct radiation to a smaller receiving area, hence increasing the radiation flux. The concentrating solar collectors are generally used for high-temperature applications (e.g. solar thermal power systems), thus they are not described in this sub-section, whereas the stationary solar collectors are mainly used for applications in residential buildings.

In general, there are three types of stationary solar collectors, including flat plate collectors (FPCs), compound parabolic collectors (CPCs) and evacuated tube collectors (ETCs). The most common forms of applications of each solar collector in residential buildings are depicted in Table 3.1.

Table 3.1: Applications of solar collectors in residential buildings [91]

Application	System category	Type of solar collector
Solar water heating		
Thermosyphon system	Passive	FPC
Direct water heating systems	Active	FPC, CPC, ETC
Indirect water heating system	Active	FPC, CPC, ETC
Air systems	Active	FPC
Solar space heating and cooling		
Space heating and service hot water	Active	FPC, CPC, ETC
Air systems	Active	FPC
Water systems	Active	FPC, CPC, ETC
Heat pump systems	Active	FPC, CPC, ETC
Absorption systems	Active	FPC, CPC, ETC

Flat Plate Collectors

The flat plate collectors (FPCs) are the most common type of solar collectors used to supply space- and water-heating systems that require temperatures below 100 °C [76], as the indicative temperature range of operating fluid in FPCs is 30–80 °C [91]. The efficiency index higher than 0.5 [−] is typical for recently available flat plate

collectors [9].

A typical FPC (Fig. 3.8) is a box that consists of an absorber plate, transparent cover, fluid, heat insulation and collector housing. According to the principle of operation, the sunlight passing through the glazing cover strikes the absorber plate. In the thick outer layer of the absorber plate, the solar radiation is converted into the usable heat and next transferred via its inner surface to the fluid passing through the collector. Subsequently, the fluid carries the energy away from the collector for a direct use or storage.

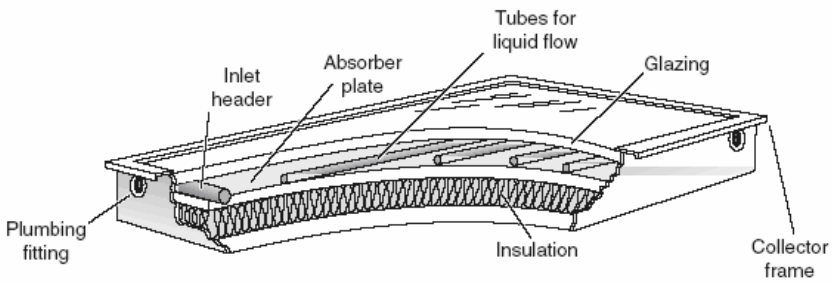

Figure 3.8: Schema of flat plate collector [88]

The absorber plate is made from a thin (flat, corrugated or grooved) high thermal conductivity metal sheet (usually cooper, steel or aluminum). In order to maximize the efficiency of a solar collector, the surface of the absorber plate is usually of the black color (high absorptivity). The flow tubes can be either an integral part of the absorber plate, or just attached to its surface. These tubes are connected at both ends by header tubes which serve as a supply or return pipe. The transparent cover, usually made from glass or other radiation transparent material, is used to reduce convection heat losses from the absorber plate. The glass is, however, transparent to the short-wave radiation received from the sun, and nearly opaque to the long-wave radiation emitted by the absorber plate, hence it also reduces radiation heat losses. The conduction heat losses are reduced by an insulation layer placed at the bottom and sides of the collector. The collector housing is usually plastic, metal or wooden. The whole structure of the collector must be properly sealed in order to reduce heat losses and protect from dirt or moisture.

FPCs are recently used to be implemented in a wide variety of designs and made from many different materials. All of them can be, however, divided into two main groups. Dependent upon the fluid type heated in solar collectors, there are liquid-based (water or water plus antifreeze additive) and air-based FPCs. Due to the low thermal conductivity of air, the air-based collectors are characterized by a significantly lower efficiency as compared to liquid-based ones. Due to the low

thermal conductivity of air, the main requirement for a structure of air-based FPCs is a large contact area between the absorbing surface and energy carrying medium. In general, air-based FPCs are used to supply space-heating systems, whereas liquid-based are used to supply both the water- and space-heating systems.

Since FPCs are installed in a permanently fixed position, the efficiency of collectors significantly depends on the appropriate orientation and inclination angle. According to Kalogirou [93], FPCs should be oriented directly towards the equator, facing south in the northern hemisphere and north in the southern hemisphere. The optimum tilt angle for FPCs is equal to the latitude of the location with the angle variations of 10–15 °.

The lifetime of FPC is limited due to adverse effects of the sun's ultraviolet radiation, corrosion and clogging as a result of acidity, alkalinity or hardness of the operating fluid, water freezing (especially in high latitude countries), or deposition of dust or moisture on the glazing, and breakage of the glazing due to thermal expansion, hail, vandalism or other causes [91].

Evacuated tube collectors

The evacuated tube collectors (ETCs) are characterized by a higher efficiency but a significant increase of investment costs as compared to FPCs. These collectors can be successfully used to supply both space- and water-heating systems, as the indicative temperature range of the operating fluid in ETCs is 50–200 °C [91]. The capability of ETCs to achieve the temperature exceeding the water boiling point can, however, cause significant problems when implemented in aforementioned systems.

The basic ETC consists of parallel rows of transparent glass tubes that are connected to a header pipe (Fig. 3.9). Each glass tube contains components with a selective coating, that absorb the solar radiation energy. These components are additionally separated from the environment by a vacuum formed in glass tubes during the manufacturing process. Such a vacuum envelope serves as a thermal insulation that diminishes heat losses through the convection and conduction. As a consequence, ETCs are able to operate with a high performance even during cloudy and windy days.

Depending upon the operation and structure of absorbing components, the ETCs can be divided into two main groups:

- direct-flow evacuated-tube collectors,
- heat-pipe evacuated-tube collectors.

Figure 3.9: Evacuated tube collector [88]

The direct-flow evacuated tube collector consists of a group of glass tubes. Each glass tube (Fig. 3.10) contains a flat or curved aluminum plate that is attached to a metal (usually made from copper) or glass absorber pipe. The aluminum plate is generally covered with a selective coating that absorbs the solar radiation. The water is used as the operating fluid that circulates through two pipes. One pipe is destined for the inlet fluid, while the other for the outlet fluid. According to the principle of operation, the sunlight passes through the outer glass tube, and strikes the surface of the aluminum plate and absorber tube. The solar radiation energy converted into the heat is subsequently transferred to the liquid flowing through the absorber tube.

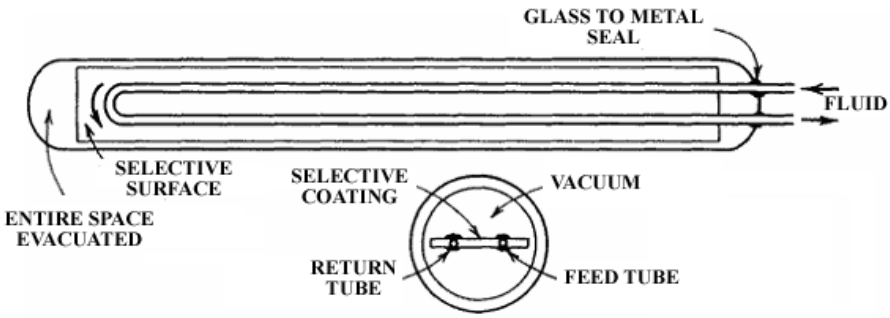

Figure 3.10: Schematic diagram of direct-flow evacuated tube collector [88]

Heat-pipe evacuated-tube collectors, similarly to direct-flow collectors, consist of glass tubes. Each vacuum-sealed solar tube (Fig. 3.11) contains a metal (usually made from copper) heat-pipe which is attached to a black copper plate (absorber)

that fills the tube. A metal tip that protrudes from the top of each tube is a heat-pipe condenser. There is a small quantity of the liquid (alcohol or purified water with some special additives) inside heat-pipes. The phase-change from liquid to vapor is the key mechanism of operation. In order to intensify this process, the air from the hollow of the heat-pipe is evacuated. The vacuum inside the heat-pipe enables the liquid to boil at the lower temperature than at the typical atmospheric pressure. The sunlight passes through the outer glass tube and strikes the absorber surface. When the absorber heats the heat-pipe above the liquid boiling point, the liquid within the pipe starts to vapor. The hot vapor travels to the heat sink region where it condenses and releases its latent heat. The condensed liquid flows back to the bottom of the heat-pipe and the cycle is repeated. At the same time, the water or glycol flows through the heat exchanger pipe (manifold) and extracts the heat from the metal tips (condenser). The operating fluid from the manifold circulates through another heat exchanger to give off the heat for a direct use or storage purposes. A great advantage of the heat-pipe evacuated tube collectors is a self-limiting temperature control, since neither evaporation nor condensation above the phase-change temperature are possible. It provides an inherent protection from freezing and overheating [91].

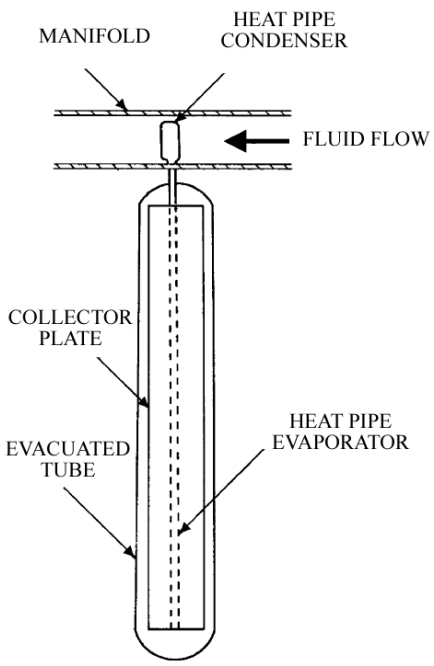

Figure 3.11: Schematic diagram of heat-pipe evacuated tube collector [91]

Compound parabolic collectors

The stationary compound parabolic collectors (CPCs) are characterized by a capability of accepting the incident radiation over a relatively wide range of angles. It is possible due to the use of a trough with two sections of parabolic reflectors facing each other (Fig. 3.12). Any solar radiation that is entering the aperture is reflected to the surface of the absorber that is located at the bottom of the collector. Most radiation reaching the absorber surface is, however, reflected by the lower portion of parabola reflectors (AB and AC). Thereby, the upper portion is usually cut off forming a short version of CPC. Such a collector hence indicates lower costs. There are various configurations of the absorber. It can be flat, bifacial, wedge or cylindrical (Fig. 3.12). The glass cover at the top of collector is usually used to protect the surface of reflectors against the dust and other contaminants that can worsen the performance.

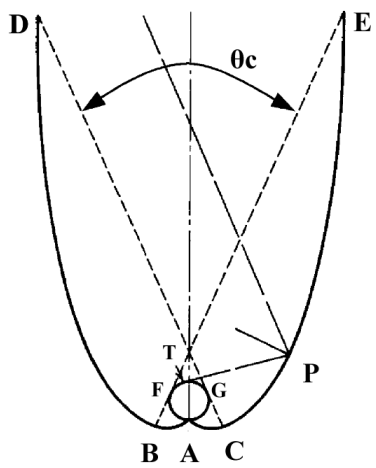

Figure 3.12: Schematic diagram of compound parabolic collector [91]

The indicative temperature range of the operating fluid in CPCs is 60–240 °C [91], hence they can be successfully used to supply both space- and water-heating systems. CPCs are recently available as a one unit or as a panel constructed from small units of truncated parabola reflectors (Fig. 3.13). The latter looks like a flat plat collector hence it is easier to be integrated into the architectural design.

A concentrator of CPCs can be oriented with its long axis along either east-west or north-south. The latter configuration requires, however, the tracking mechanism so as the concentrator faces the sun continuously. In the other way, the solar radiation will be received only during hours when the sun is in the acceptable angle of the collector. In the case of stationary CPCs oriented with its long axis along east-west, the aperture should be tilted directly towards the equator at the angle equal to the

local latitude. For this orientation, the minimum acceptance angle should be equal to the maximum incidence angle projected in a north-south vertical plane when the output is needed from the collector [91]. In general, CPCs with tracking mechanism are used for applications of a higher temperature.

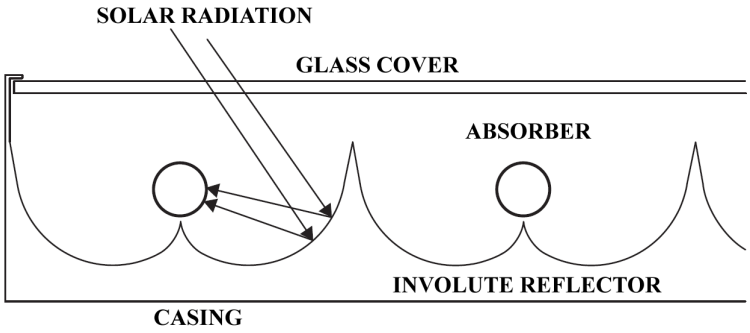

Figure 3.13: Schematic diagram of CPC panel with cylindrical absorbers [92]

3.3.2 Application of solar collectors

The solar collectors can be used in a variety of applications including water- and space-heating, cooling, solar refrigeration, industrial process heat, solar desalination, and solar thermal power systems. Since the main objective of this thesis is to evaluate the potential for application of HSC to supply space-heating systems dedicated for low-energy residential buildings and to support DHW systems, these application fields will be discussed in the following sub-sections only.

3.3.2.1 Solar water-heating systems

The domestic water heating is probably the most common application of solar systems. Such systems, also known as solar domestic hot water (SDHW) systems, can be a cost-effective way to provide residential buildings with a large portion of their hot water needs. The efficiency of the SDHW system depends on type and size of the system, and climate conditions. It is estimated that small scale SDHW systems are characterized by the annual share of the solar energy in the range of 50–70 % [41].

A design of each SDHW system can significantly differ. Nevertheless, there are three basic components in all systems: solar collector, energy transfer system and HS system in the form of e.g. storage tank. The most important part is, obviously, the solar collector that absorbs the solar radiation and converts it into the usable heat. Three types of solar collectors including FPC, ETC, and CPS are used at present for SDHW applications.

In general, SDHW systems can be divided into two categories. Whether the potable water is heated directly in solar collectors or through the use of a heat exchanger, there are direct (or open-loop) and indirect (or closed-loop) systems. Depending upon the mechanism of the operating fluid circulation, SDHW systems are also classified as passive and active systems. In the case of passive systems, also known as thermosyphon solar water heaters, the operating fluid circulates between the collector and storage tank by the natural convection. Whereas, active systems employ pumps or fans to force the circulation of the operating fluid in the system. Since there is no need for the storage tank to be located above or close to the collector, active systems are more attractive from the aesthetics point of view.

Direct SDHW systems

The direct SDHW systems represent the category of active systems. The direct systems, also known as the open-loop systems, use a pump to circulate the potable water itself between collectors and water storage tank (Fig. 3.14). The water flows from city water mains into a water storage tank. When the temperature in collectors is higher than the temperature in the water storage tank, a controller activates the pump to move the water into collectors. After heating, it leaves the collectors and returns to the water storage tank. From there, the hot water can be pumped into houses when needed. The optimum flow rate in such systems is about 0.015 l/m^2 of the collector area [91].

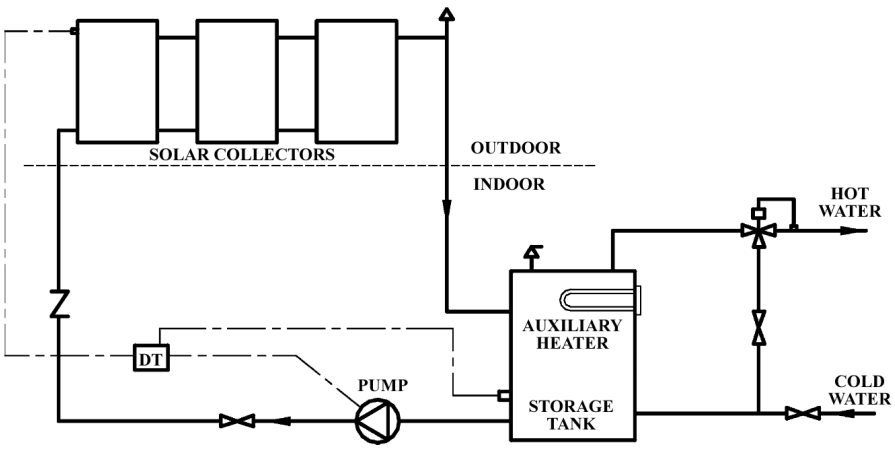

Figure 3.14: Schematic diagram of direct (open-loop) SDHW system [91]

The open-loop systems are usually used in regions where the temperature rarely drops below 0 °C. During extreme weather conditions, the protection against freezing can be provided by recirculating hot water from the storage tank. It may provide, however, heat losses from a system. Thereby, the storage tanks are often equipped with an auxiliary water heater or a two-tank storage system. At the power failure, when the water cannot be recirculated in the system, the freezing protection can be provided by the installation of a dump valve at the bottom of solar collectors. Another limitation of the use of direct systems is the hard or acidic water. In such cases, deposits may clog or corrode solar collectors [91]. The aforementioned disadvantages related to extreme weather conditions can be overcome by a variation of direct systems, known as drain-down system (Fig. 3.15). The general operation principle is the same. However, during freezing weather conditions or power failure, the circulation stops and the water from solar collectors and exterior piping systems is removed automatically using two open valves. It is worth noting that both solar collectors and exterior pipe systems should be adequately sloped in order to drain completely [92].

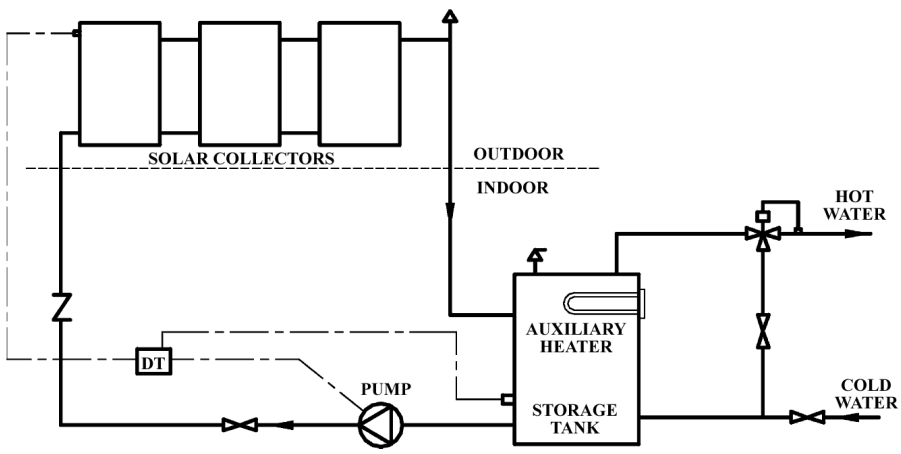

Figure 3.15: Schematic diagram of direct (open-loop) drain-down SDHW system [91]

Indirect SDHW systems

The indirect SDHW systems represent the category of active systems. The indirect systems, also known as the closed-loop systems, use a non-freezing fluid and a heat exchanger to transfer the heat to the potable water. A typical closed-loop system (Fig. 3.16) consists of solar collectors, circulation system including a pump, storage system with a heat exchanger and controller.

According to the operation principle, the non-freezing fluid is pumped into collectors when the temperature inside collectors is higher than the temperature of water in the storage tank. The most often used operating fluids are water-ethylene glycol mixtures or silicone oils. The heat drawn from collectors is transferred to the water located in the storage tank with the use of a heat exchanger. The heat exchanger is a coil that can either be inside or outside the storage tank. If the operating fluid is toxic, a double walled heat exchanger should be used to prevent the potable water from being contaminated. The pump stops fluid flow in the closed-loop system when the fluid temperature in collectors is lower than the water temperature in the storage tank or when the water in the storage tank has already reached its maximum temperature. The closed-loop systems are popular in climates prone to temperatures often dropping below 0 °C since they are based on a non-freezing operating fluid. These systems are, however, expensive to construct and operate, as a non-freezing solution needs to be checked every year, and changed every few years. Moreover, the fluid circulation in a closed-loop requires the installation of an expansion tank and a pressure relief valve [92].

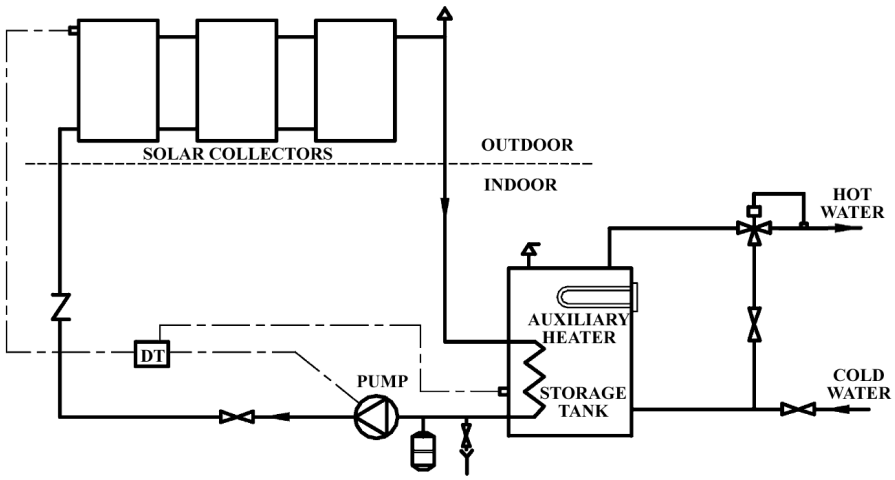

Figure 3.16: Schematic diagram of indirect (closed-loop) SDHW system [91]

A variation of the indirect SDHW system is the air system. In this case, the air circulates through the pipe system between a solar air collector (e.g. air-based flat plate collector) and an air-to-water heat exchanger. The potable water circulates between the heat exchanger and storage tank. The most often used air SDHW systems are based on a double tank storage system (Fig. 3.17). In this case, one tank is used to preheat the potable water, while the other is equipped with an auxiliary heater.

According to Kalogirou [92], the main advantage of the air SDHW system is that there is no need to protect the operating fluid from extreme weather conditions since the air neither freezes nor boils. Moreover, the air as an operating fluid is non-corrosive. The system is also more cost-effective since no safety valves or expansion vessels are required. The disadvantages are related to a bigger space that is required for the installation of air-handling ducts and fans, problems with a detection of leakages, and energy consumption (energy used for the fans operation) that is significantly higher than in liquid-based systems.

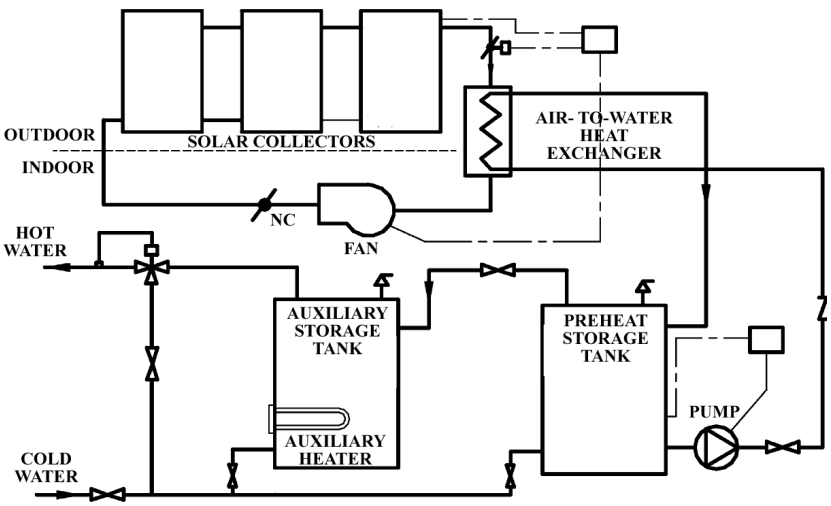

Figure 3.17: Schematic diagram of indirect (closed-loop) air SDHW system [91]

Thermosyphon systems (passive solar energy systems)

The thermosyphon solar water heaters (Fig. 3.18) represent the category of passive systems. These systems are characterized by a non-electricity-consuming mechanism of the fluid circulation that is caused by the natural convection.

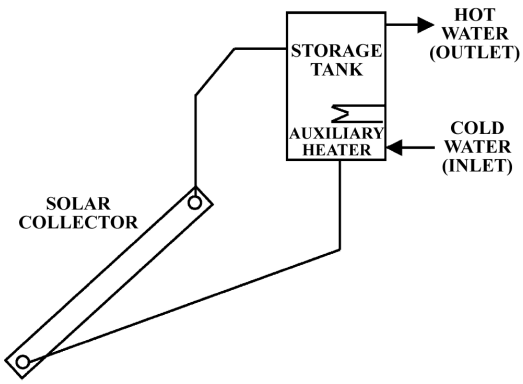

Figure 3.18: Schematic diagram of thermosyphon solar water heater [91]

The fluid in a solar collector becomes less dense at each temperature rise caused by a heat transfer from the surface of the absorber. As a consequence, the hot water rises up to the storage tank that is placed above the collector. At the same time, the cooler water from the bottom of the storage tank flows down to the collector in order to replace the hot water. The process of a fluid circulation caused by the natural convection occurs as long as the sun shines. The fluid flow mechanism, however, requires bigger than normal pipe sizes in order to reduce a negative influence of the pipe friction. Moreover, the whole system must be sealed and sloped in order to prevent the formation of air pockets which may stop the fluid circulation. During the night or periods when the fluid in a solar collector is cooler than the fluid in a storage tank, the direction of the fluid circulation reverses. Thus, the bottom part of the storage tank should be placed about 30 cm above the top of the solar collector [91]. Kalogirou [92] reported that thermosyphon systems are more reliable (since they do not rely on pumps and controllers) and have a longer life than forced circulation systems. They are, however, aesthetically non-attractive especially when a cold water storage tank is installed on the top of the solar collector to supply the hot water cylinder and to meet the current cold water needs. The thermosyphon systems are usually used in regions where the temperature rarely drops below 0 °C. In mild freeze areas, the protection from freezing can be provided by dump valves or heaters placed in the bottom of the collector header that sustains the natural circulation in the entire system [92].

3.3.2.2 Solar space-heating systems

Application of solar collectors in space-heating systems dedicated for residential buildings meets with an increasing interest in recent years due to a significant reduction of heating requirements. A typical solar space-heating system consists of a solar collector, HS system, auxiliary heat sources, devices such as pumps and fans which enable to transfer the heat to/from the HS system, and equipment such as ducts and controllers to distribute the heat in building spaces. The most common operating fluids are water, water-ethylene glycol solution and air. Depending upon the type of the operating fluid, there are air- and water-based active solar space-heating systems.

According to the principle of operation, during sunny days the solar radiation is absorbed and converted by the collector into the usable heat. The heat is then transferred by a fluid to the HS system. When needed, the stored heat is extracted and supplied to heating systems to provide the thermal comfort in the building's interior. During the winter season, the protection against freezing of a solar collector

and exterior pipe system is provided by a recirculation of the operating fluid from the HS system or by the drain-down system.

In general, active solar-space heating systems are very similar to solar water-heating ones. Thereby, they are often combined together forming so-called solar combi systems. Nevertheless, the efficiency of solar space-heating systems to a greater extent depends on climate conditions as compared to solar water-heating systems, as there is a half-year shift between peaks of heating demands and the available solar radiation. The need for long-term storing of the solar energy makes the HS system a key technology in an efficient use of the solar energy. A brief description of available methods for a seasonal storage of the solar energy in residential applications is given by Pinel et al. [135]. According to Duffie and Beckamn [58], active solar-space heating systems can operate in five basic modes in dependence on the solar radiation availability, heating loads and amount of the stored energy that all occur at a particular time. These modes are described as follows:

- solar radiation is available; however, there is no need for heating in the house. In such a case, the collected energy is given to the HS system,
- solar radiation is available; simultaneously, there is a need for heating in the house. In such a case, the collected energy is transferred directly to meet heating loads,
- solar radiation is not available; simultaneously, there is a need for heating in the house; the solar energy is available from the HS system. In such a case, the necessary heat is extracted from the heat storage system to meet heating loads,
- solar radiation is not available; simultaneously, there is a need for heating in the house; the solar energy is not available from the HS system. In such a case, the auxiliary energy system is used to meet heating loads,
- solar radiation is available; however, there is no need for heating in the house; the HS system is fully charged. In such a case, the collected energy is discarded.

Energy discarding in the last mode can be achieved with the use of pressure relief valves or by turning off fluid flow. The latter approach, however, should comply with properties of materials used in the collector, since too high temperatures may cause the undesired damage. In the case of combi systems, the energy excess is used to supply DHW systems [91]. There are air- and water-based active solar-space heating systems. A description of systems and their combination in residential buildings is

given below. The active space-heating systems can be also combined with other technologies, such as heat pumps [92] and Thermal Barrier [103]. These approaches are presented and discussed in Sections 3.3.2.3 and 3.3.2.4.

Air-based solar space-heating systems

The warm-air heating systems are in common use in residential buildings [91], hence there is a great potential for a solar space-heating systems based on air as an operating fluid. A schematic diagram of the system with a pebble bed [151] as storage unit is depicted in Fig. 3.19.

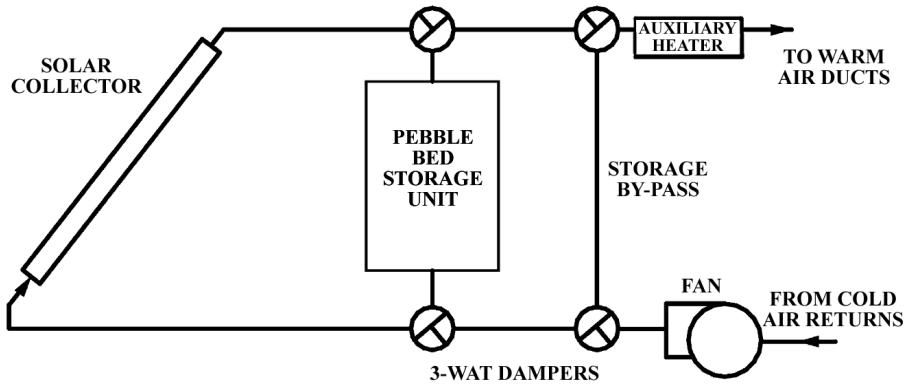

Figure 3.19: Schematic diagram of air-based solar space-heating system [91]

Air-based active solar space-heating systems can operate in several modes in dependence on a position of dampers. The warmed air stream from the collector can be used directly for heating purposes or can pass through the storage unit. According to Kalogirou [92], it is not practical to combine modes of a supplying energy to or removing from a storage unit at the same time. In cases when the energy from the collector or storage unit is not sufficient to meet current heating requirements, the auxiliary heat source can be applied. It is also possible to cover all heating loads by an auxiliary heat source, with the use of a collector bypass and storage unit.

The advantages of air-based solar space-heating systems are related to the use of the air as an operating fluid. This was outlined during description of indirect SDHW systems (Section 3.3.2.1). Other advantage pointed by Kalogirou [92] refers to a high stratification degree in the pebble bed as a storage unit that enables to decrease air temperatures at the collector inlet. The most important disadvantages are the high cost of a storage system and noisy operation.

A schematic diagram of the exemplary air-based active solar space-heating system that incorporates a subsystem to supply the DHW system is presented in Fig. 3.20. The subsystem consists of an air-to-water heat exchanger, preheat and storage tanks, auxiliary heat source and control system. Both systems operate independently from each other. Hence, thermal loads of space- and water-heating can be provided simultaneously.

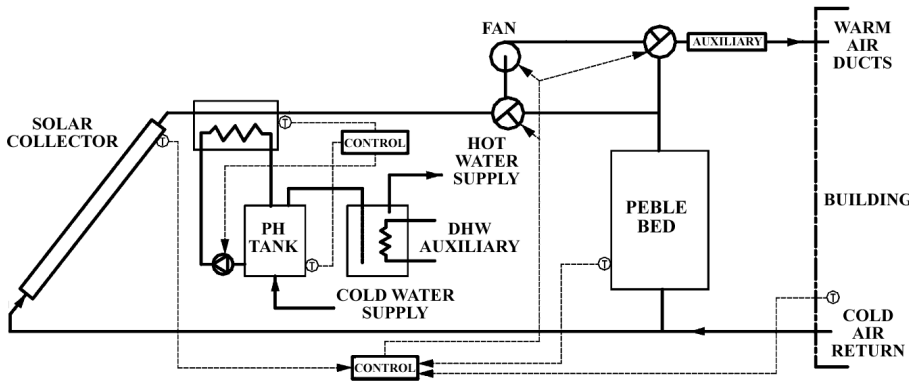

Figure 3.20: Schematic diagram of air-based active solar space- and water-heating system [91]

Liquid-based solar-space heating systems

Most liquid-based solar space-heating systems incorporate a subsystem for the heating of the domestic water. This can be achieved in many variations. The basic configuration, however, is very similar as in active solar water-heating systems (Section 3.3.2.1). A schematic diagram of the water-based active solar space- and water-heating system is shown in Fig. 3.21.

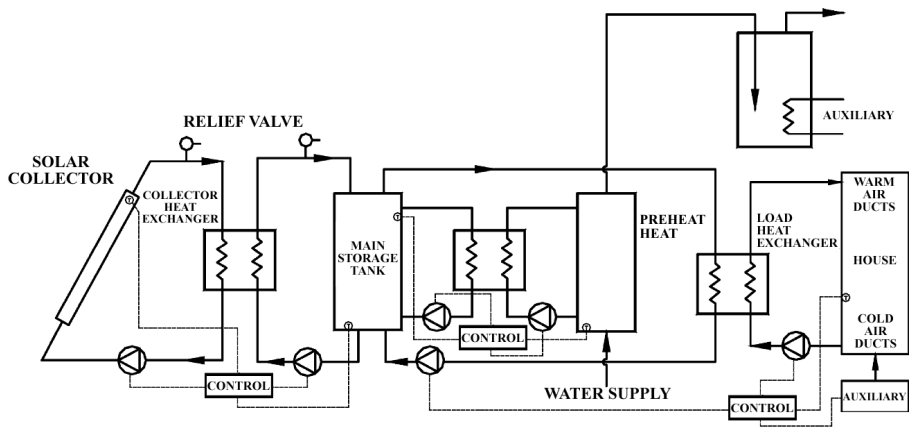

Figure 3.21: Schematic diagram of water-based active solar space- and water-heating system [91]

The operation of liquid-based systems, in contrast to air-based solar space-heating systems, combines the modes of supplying the energy into and removing the energy from the storage unit at the same time. It is due the use of a heat exchanger located between the solar collector and main storage tank. Such an approach enables to use a non-freezing operating fluid hence providing the protection against freezing during winter. Another way to protect the solar collector is the use of drain-down system (Section 3.3.2.1). The both subsystem of water-heating and space-heating can operate independently at the same time. This may, however, require the use of auxiliary heat sources for both subsystems. If the energy stored in the main storage tank is not sufficient to meet the current water-heating or space-heating loads, the control system activates an auxiliary heater.

The advantages of liquid-based systems are the high heat removal factor of the solar collector, small volume of a storage system, and potential to supply air-conditioning systems for cooling purposes.

3.3.2.3 Heat pump technology

A heat pump is one of common technologies that can be combined with active solar energy systems to meet both the water-heating and space-heating requirements in residential buildings. According to a brief description given by Kalogirou [92], a heat pump is a device that uses the mechanical energy to transfer the heat from a low-temperature source to a sink at a higher temperature. These devices are usually vapor compression refrigeration machines, where the evaporator takes the heat into the system at low temperatures and the condenser rejects the heat from the system at higher temperatures. This technology can be used to increase the performance of DHW systems as well as operates as an auxiliary heat source to meet space-heating loads when the solar energy is not available.

A schematic diagram of a common combination of a heat pump system with the active solar system is illustrated in Fig. 3.22. Such an arrangement, known as a series configuration, is based on the use of a water-to-air heat pump. When the water temperature in the storage unit is high enough, the energy from the storage unit is directly used to take on the thermal loads in the building and the heat pump is kept off. In the case when the temperature in the storage tank is not sufficient to directly carry the thermal loads, the heat pump uses the solar-heated water from the storage unit as the evaporator energy source and hence operates as an auxiliary heat source. The heat pump can also operate as an independent auxiliary source of energy for the solar system (Fig. 3.23). This configuration, known as a parallel arrangement, is based on the use of a water-to-water heat pump. The series configuration of a heat

pump system is, however, more popular. It enables to use the entire energy from the storage unit during one day hence the solar collector can operate more effectively during the next day.

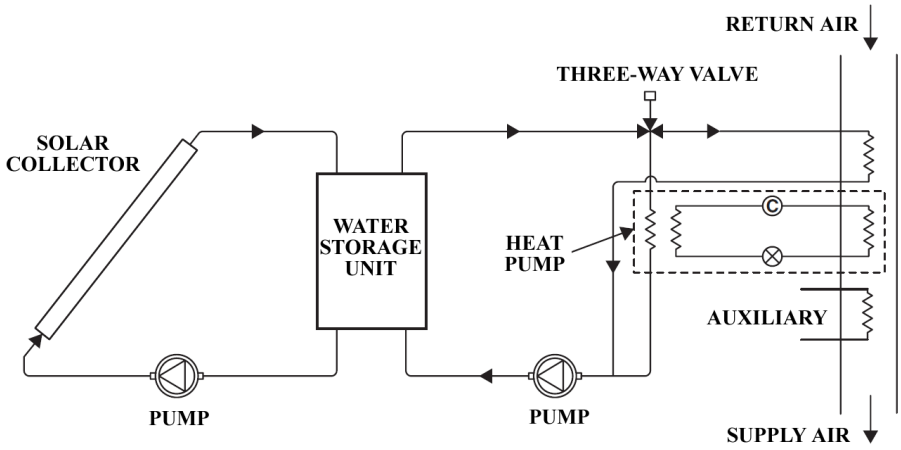

Figure 3.22: Schematic diagram of water-to-air heat pump system [92]

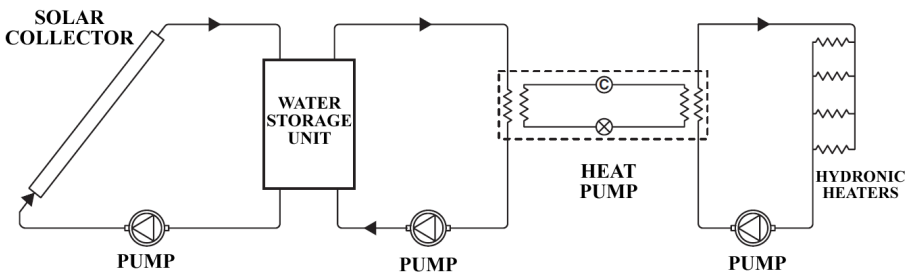

Figure 3.23: Schematic diagram of water-to-water heat pump system [92]

3.3.2.4 Thermal Barrier technology

The Thermal Barrier technology (TB technology) is an indirect heating and cooling technique of residential buildings driven by the solar thermal radiation [103]. This technique is based on an idea of supplying heat from a very-low-temperature ground heat storage (GHS) system to a polypropylene U-pipes system located inside external walls. According to its principle of operation, the energy carrying medium flows through the pipes system with time-varying velocity and temperature so as to stabilize and reduce the heat flux normal to a wall surface and, what is crucial, to maintain its direction from the internal air out to the ambient air during the entire year. The authors reported that with the use of an appropriate control strategy for the operating parameters a volume averaged temperature of the external wall is almost constant during a year-round operation and equals, approximatelly, to 17 °C.

This concept can provide comfortable living conditions with heat sources of temperature in range from 8 to 25 °C. According to low temperatures needed to implement this heating technique, it is possible to apply a very simple and low-performance solar energy collection system and a very-low-temperature seasonal HS system.

A schematic presentation (Fig. 3.24) of TB with the low-performance solar collector as the energy supplying system and multi-zone GHS system clearly shows the layout of each component and its role in the operating process. The solar collector absorbs the solar radiation energy, converts into the heat, and transfers the heat to the fluid that flows through polypropylene pipes. Next, the collected solar energy is transmitted down through a pipe system located in the core layer of external walls to the GHS system located underneath the building basement. Transmission heat losses are reduced to a minimum due to highly-effective insulation layers on both sides of the core layer and operating features of TB. The temperature distribution in ground naturally divides the GHS system into three temperature zones:

- high temperature zone with the temperature not less than 20 °C,
- medium temperature zone with the temperature not less than 15 °C,
- low temperature zone with the temperature not higher than 8 °C.

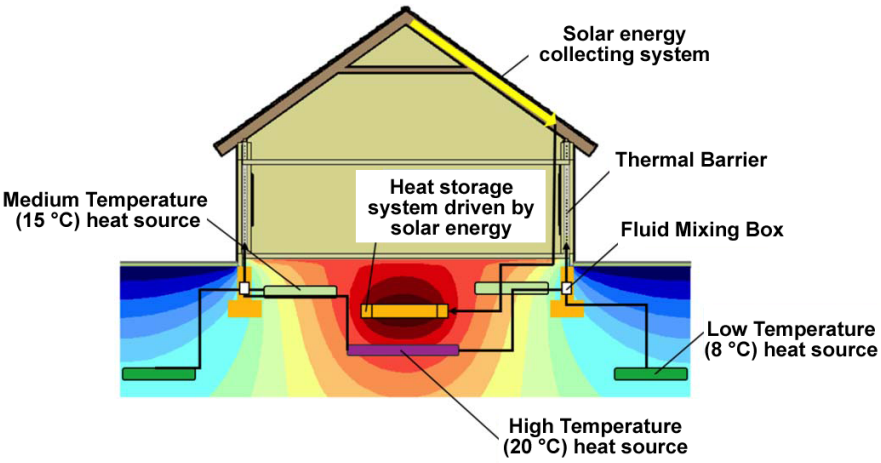

Figure 3.24: Location of Thermal Barrier components [103]

The performance of this multi-zone GHS system can be easily improved with the use of PCM, which changes between a liquid and a solid at temperatures typically between 15 °C and 45 °C [18]. The GHS system can be also used to preheat the ventilation air supplied to buildings.

3.4 Summary

The use of passive solar energy systems, undoubtedly, provides environmental and financial benefits since it reduces the energy consumption from non-renewable energy sources for the space-heating in residential buildings. The application of a solar design, however, has several limitations and might not be sufficient to provide the indoor thermal comfort, particularly in regions having extreme climates [31]. Moreover, the implementation of a solar design does not provide the DHW demand. Therefore, passive solar energy systems should be implemented together with active solar energy systems.

The active solar technology, whose main component is a solar collector, is an effective way to use the solar energy for residential buildings. Basically, three types of solar collectors including a flat plate, compound parabolic and evacuated tube collectors can be installed in residential buildings. These devices, characterized by efficiency values higher than 0.5 [−] [9], can be roof-mounted or installed separately outside the building. Therefore, they are not aesthetically acceptable in many cases [25, 168]. This is a great disadvantage of conventional solar collectors, which may often limit the implementation of active solar energy systems in residential buildings. The most common applications of active solar technologies are water- and space-heating systems.

In the case of the solar water-heating application, the efficiency of the active solar energy system is limited due to the type and size of the system, and climate conditions. Nevertheless, it is estimated that small scale SDHW systems indicate an annual share of the solar energy in the range of 50–70 % [41].

In the case of the space-heating application, the efficiency of the active solar energy system is mainly limited due to the nature of its source. The need for long-term storing of the collected energy, due to a significant discrepancy between peaks of the maximum demand and availability of the solar energy, makes the seasonal HS system a key technology in the efficient operation of the active solar energy system. It was reported [146] that by the integration of seasonal HS, more than 50 % of the annual heating demand for the space-heating in residential buildings and DHW can be supplied by the solar energy. When the energy from the collector or storage unit is not sufficient to meet current heating requirements, the auxiliary heat source must be applied. In general, a source of the problem refers to the operating temperature of conventional heating systems, such as floor heating and radiators, whose operating temperatures are 35 °C and 60 °C, respectively. The maintenance of such temperatures in the seasonal HS system during the winter season is hardly impossible. Hence, conventional active solar space-heating systems

have to be supported by auxiliary electrical heaters that may increase the total building energy consumption.

An alternative to auxiliary electrical heaters is the use of the heat pumps technology. This technology can be used to increase the performance of SDHW systems as well as operates as an auxiliary heat source to carry space-heating loads when the solar energy is not available. Such a combination contributes to the maximization of the solar energy use for the purpose of the space-heating in residential buildings. On the other hand, it does not agree with the general idea of the energy consumption reduction in residential buildings, since pumps are powered by electricity increasing the total energy consumption.

An attractive solution for problems of active solar space-heating systems, including the interference of solar collector into building aesthetics as well as high operational temperatures of heating devices, is the Thermal Barrier technology [103]. It is a representative of techniques of the indirect heating and cooling driven by the solar energy stored in the GHS system of a very-low-temperature but not smaller than 25 °C. Such a temperature in the seasonal HS system can be successfully maintained during the whole year operation, when the solar energy is collected with the use of conventional solar collectors. On the other hand, it enables to develop and implement new, very cheap and of simple structure solar collectors characterized by the lower performance than classic ones, which do not affect the building aesthetics.

Chapter 4

Hidden solar collector

This chapter provides a general characteristic of the hidden solar collector concept. A heat transfer problem for HSC is formulated. The solution methods and various approaches for the thermal modeling of the formulated heat transfer problem are reviewed.

4.1 General concept

4.1.1 Structure

The hidden solar collector uses the existing roof surface of a building in order to absorb the solar radiation. The basis of HSC is to use a very cheap solar energy collection system made from polypropylene pipes with a water as the energy carrying medium and hide it inside the structure of a ventilated roof (Fig. 4.1). The energy carrying medium is the water with an antifreeze solution. In dependence on climatic

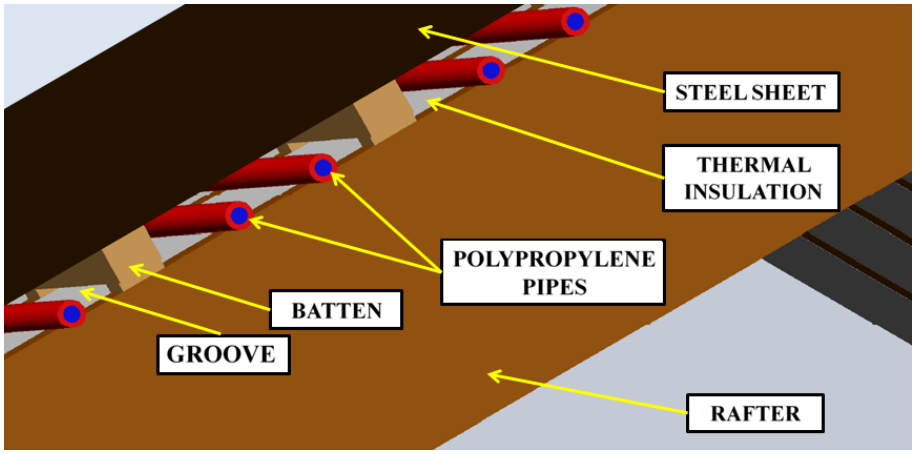

Figure 4.1: Cross-section of ventilated roof with HSC

conditions the energy carrying medium is to be either water with an antifreeze solution or pure water.

Due to a non-transparent roofing material, the solar heat is transmitted to a solar energy collection pipe system by convection rather than by radiation. The solar radiation absorbed by the roofing surface increases the air temperature in the air-cavity and enforces the natural convective heat exchange between the air and pipe system. This is a different mechanism when compared to conventional solar collectors, e.g. flat plate collectors (Section 3.3.1). The natural convection in a typical ventilated roof can be, however, disturbed by wind gusts which are a factor that forces the air movement in the air-cavity, hence increasing the amount of the heat removed from the roof to the environment [64]. This would have a negative influence on the collector efficiency. In order to reduce the negative wind effect, there are three basic technical solutions for a structure of a ventilated roof containing a solar energy collection pipe system. First refers to the roofing material. The use of a metal roof sheeting instead of ceramic/concrete roof tiles increases the roof air-tightness. This enables to reduce the air infiltration through the roofing surface caused by wind. A further reduction of heat losses from a collector caused by wind is achieved by a decrease of the air-cavity height. Taking into account the diameter of pipes (from 25 mm to 40 mm), the height of ventilation channels in HSC should not exceed 6 cm. This approach is reasonable since it is stated that the optimum height of the air-cavity in ventilated roofs in which an intensive heat removal is the target, must be in the range of 6–10 cm [176]. The last requirement concerns an additional reduction of the air movement in ventilated channels. In general, it can be achieved through the use of battens [44]. In case of HSC, the special type of battens, that possess grooves along the length (Fig. 4.1), are used. The height of the grooves should range between 5 mm and 15 mm in order to ensure that water drains off the roof. With such a shape of battens, there is no need to apply counter battens in the roof structure thus decreasing the size of air channels what results in an additional reduction of airflow. Nevertheless, despite the implementation of abovementioned roof structure improvements, the performance of HSC is expected to be lower as compared to conventional solar collectors. The layout of solar energy collection pipes in the roof structure may correspond to either serpentine or Tichelmann schema. In the serpentine layout, the solar energy collection system consists of a one long continuous flexible pipe as presented in Fig. 4.2a. In case of serpentine schema, with an increase of pipe length flow resistance in the system may significantly increase. On the other hand, the advantage of a serpentine layout is an ease of construction. In case of the Tichelmann system, the fluid has a multiple

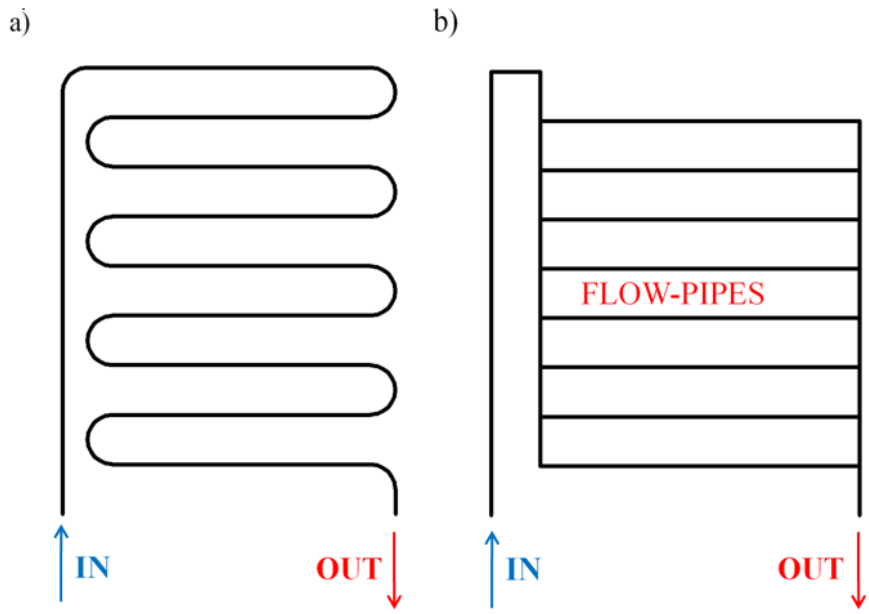

Figure 4.2: Schema of pipes layout in HSC: a) serpentine and b) Tichelmann

pipes (flow-pipes) to travel through (Fig. 4.2b). Both supply and return pipes are routed in such a way that whichever flow-pipe water flows through, it always takes the same distance. In consequence, the Tichelmann pipe layout is a self-balancing system reducing any pressure losses. When compared to the serpentine system, employing the Tichelmann-layout results in slightly higher material consumption. According to Oszczak [128], the Tichelmann-layout applied to typical FPCs results in higher efficiency of solar energy conversion when compared to serpentine-layout.

In this study, the Tichelmann-layout-based HSC is considered. An exemplary implementation of the collector into the building structure is shown in Fig. 4.3. The system of parallel polypropylene pipes running along the ridge of building is located in the air-cavity between battens. The inlet of each flow-pipe is connected to a common supply system, whereas the outlet is connected to a common return system. Both the supply and return pipes, so-called header pipes, are connected with the seasonal HS system forming a closed-loop active solar energy system. Among available methods for a seasonal storage of the solar energy [135], the GHS system has a great potential to be implemented into the HSC system.

According to the structure, the concept of HSC has several advantages over conventional solar collectors. These are:

- HSC doesn't influence aesthetics of the building,
- low investment and maintenance cost. The investment cost represents the difference between the cost of HSC and the cost of the conventional roofing

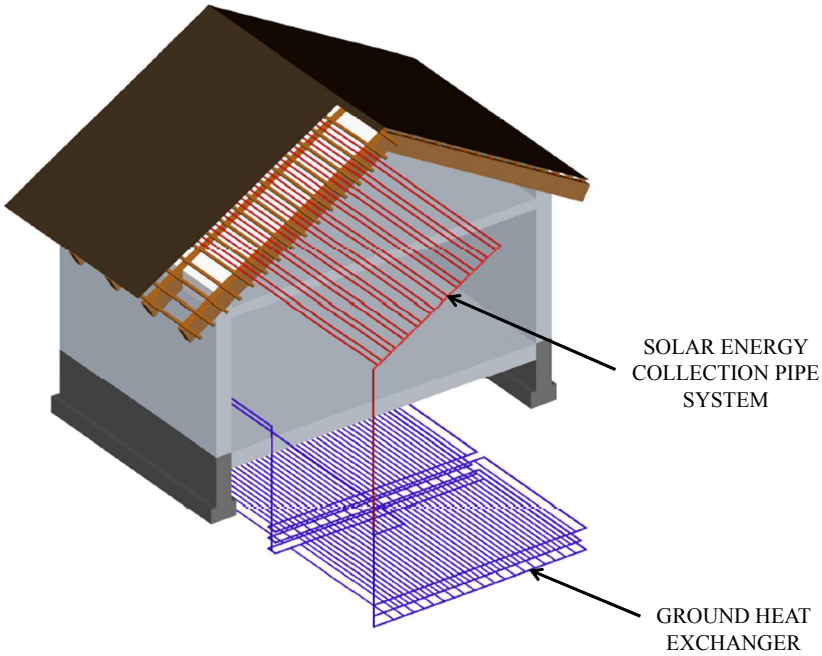

Figure 4.3: Perspective view of HSC installed in roof structure

for the same area. Hence, the initial cost of HSC includes only a purchasing of pipes for the solar energy collection system. In contrast to conventional solar collectors, the installing cost is not included in the initial cost, since the cost of the pipe mounting is the same as for the ordinary roofing. The estimated initial cost of HSC is 36 pln/m^2. To compare, the average cost of the aperture (without mounting costs) is 2182 pln/m^2 and 889 pln/m^2 [156] for an evacuated tube and flat plate collector, respectively,

- size of the system can be determined and designed as needed to satisfy the building's water- and space-heating demand, limited only by the roof area,
- layout of a solar energy collection system, protected from the weather exposure (especially ultraviolet radiation), guarantees the longer lifetime of the collector,
- solar energy collection system in the form of polypropylene pipes is not subjected to corrosion,
- reduction of summer cooling loads; According to Gagliano et al. [64] only the ventilated roof structure can reduce heat fluxes during summer up to 50 %. With the implementation of a solar energy collection system into the structure of a ventilated roof, the reduction is expected to be significantly bigger. This may provide additional benefits in the form of a decrease of the building energy consumption.

In general, the structure of HSC is in good agreement with conclusions reported by Munari Probst and Roecker [124]. The authors suggest that a solar collector should be conceived as the part of a construction system which provides active and solar benefits, flexible enough to be adapted to different buildings.

4.1.2 Efficiency

According to its structure, the presented solar collector is a type of a reduced performance solar collector. Both the fluid temperature and amount of the collected energy are expected to be significantly lower, as compared to a single unit of conventional solar collectors. The efficiency of HSC depends on the following factors:

- ambient climate conditions,
- orientation and inclination of the roofing surface. Unlike the standard solar collectors, HSC cannot follow the solar radiation with the usage of tracking mechanism. Hence, the orientation and inclination of the roofing surface should correspond to the value of maximum solar irradiance for a particular location,
- operational parameters including the inlet fluid temperature and fluid mass flux. In order to maximize the efficiency of HSC, it is reasonable to implement the system to control the operational parameters. The value of inlet fluid temperature should correspond to a minimum temperature in the HS system, whereas the value of fluid mass flux should vary in dependence on climate conditions,
- properties of the roofing material, its thickness, texture and color. In general, the darker the color, the higher is the efficiency.

4.1.3 Application

The concept of a hidden solar collector is a reduced-performance but cost-effective solar device suitable for low-temperature applications. The collector can be implemented into closed-loop active solar energy systems primarily used to supply low-temperature space-heating systems (in which the operating temperature is less than 30 °C) dedicated for residential buildings characterized by a low heat demand, e.g. TB technology [103] (Section 3.3.2.4).

In some regions, it can be additionally used for preheating the domestic water (as the required temperature of the hot water is 50 °C [169]) or water-heating for

swimming pools. These applications are used especially in regions with hot climates, such as Mediterranean countries, where roofs receive a large amount of the solar radiation during summer and their superficial temperature can be between 75 °C and 80 °C [64]. In such cases, while producing the hot water, HSC can simultaneously reduce cooling loads that is a great advantage of the collector application.

4.2 Heat transfer problem

4.2.1 Heat transfer in hidden solar collector

A reliable performance analysis of HSC requires the formulation of a heat transfer problem. In order to properly formulate the heat transfer problem, it is necessary to identify appropriate heat transfer mechanisms with respect to the structure and operation principles of the collector.

The hidden solar collector is a type of roof-integrated solar collector, in which a sheet steel roofing is employed as an absorber of the solar radiation. As compared to solar collectors with a glazing, the absence of a protective transparent cover contributes to the reduction of optical losses. On the other hand, a direct exposure of the absorber to ambient climate conditions increases thermal losses by convection and long wave radiation. The convection heat losses are mainly driven by wind forces. The absorbed solar radiation is influenced by the effect of dust and dirt. The shading of the absorber surface, if exists, should be also taken into account. The difference between the absorbed radiation and losses to the ambient is the useful energy transferred into the air-cavity. The concept of HSC is based on a ventilated roof structure. The heat is exchanged between surfaces forming an air-cavity and surfaces of polypropylene pipes through radiation, conduction and convection. The conduction has, however, a negligible effect on the heat exchange as compared to other heat transfer mechanisms [178]. The radiative heat exchange rate decreases by the air attenuation. The natural and forced convection creates airflow, hence intensifying the heat exchange in the air-cavity. The natural convection occurs as a result of buoyancy forces. The solar radiation increases the roofing temperature which heats up the air in ventilated channels. The resulted differences in air density force an upward airflow circulation. Besides the temperature differences, the buoyancy effect is also influenced by gravity forces, hence the bigger the collector tilt angle, the stronger is the buoyancy effect [30]. In turn, the forced convection is driven by wind entering the air-cavity channels through intake vents, which are located at the down-slope edge of the roof. In general case of ventilated roofs, the airflow due to the wind-driven forced convection increases the heat removed from

the roof to the environment [64], contributing at the same time to heat losses from the collector. The concept of HSC, however, employs few structural solutions (Section 4.1.1) to reduce the airflow in channels of the air-cavity. Nevertheless, the effect of the wind-driven convection should be considered in the performance analysis of HSC. The solar energy collection system in HSC is made from polypropylene pipes with water as an energy carrying medium. Depending upon a control system, the fluid flow is either stopped or turned on. In latter case, the heat is transferred into the flowing fluid mainly due to the forced convection. In case of laminar fluid flow there is a thin layer near the pipe surface where the fluid velocity decreases to zero. In this thin layer, the heat is transferred mostly by the diffusion. When the fluid flow is stopped, the heat is transferred into the fluid due to the natural convection. The bottom layer of HSC is composed of an insulation layer. The heat is exchanged between the bottom surface of the insulation layer and the indoor environment due to the radiation and forced convection. These phenomena are, however, of a little influence on the collector thermal performance since the insulation layer is characterized by relatively low magnitudes of heat conductivity and thermal capacity. In all solid layers of HSC the heat is transferred due to the conduction. The thermophysical parameters of materials should be considered as temperature-dependent. All the relevant heat transfer mechanisms that should be considered for a proper formulation of the heat transfer problem in HSC are illustrated in Fig. 4.4. To sum up the formulation of a heat transfer problem in the investigated type of solar collector, it is a complex problem that comprises all heat transfer mechanisms. A fundamental influence on the collector performance have both airflow in ventilated channels and fluid flowing through pipes. Therefore, a special attention must be given to phenomena driving the heat transfer in these medias.

4.2.2 Solution methods

The reliable performance analysis of solar collectors involves an understanding of the nature of heat transfer processes occurring in a particular system and choosing an appropriate methodology to predict them quantitatively. A prediction can be obtained by carrying out experimental investigations or theoretical calculations.

In general, the most reliable information about the thermal performance of solar collectors are given by actual in-situ measurements. Therefore, experimental investigations found an application in many analyses of solar thermal systems. The investigations can be accomplished with the use of full-scale devices or alternatively small-scale models. Conducting investigations using full-scale devices may be, however, prohibitively expensive and often impossible. On the other hand, small-scale

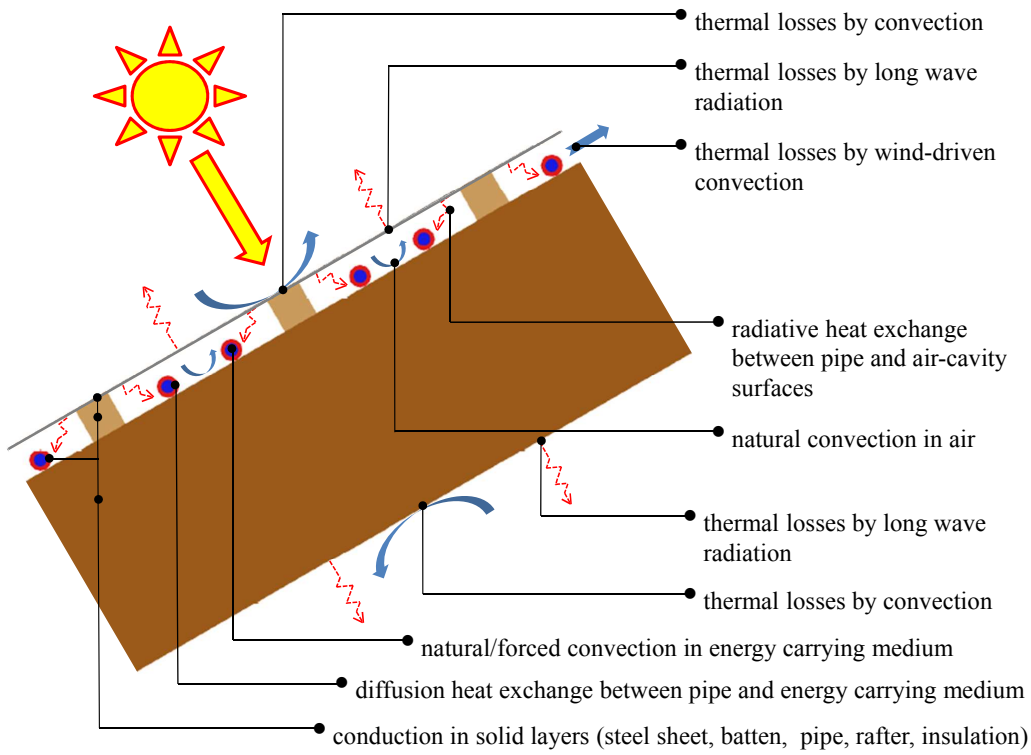

Figure 4.4: Heat transfer modes in hidden solar collector

experiments require an extrapolation of results to a full scale that may be also problematic. Furthermore, small-scale models may not be capable to simulate all relevant features of full-scale ones. Therefore, the obtained results are often not useful in order to carry out performance analyses of solar collectors. It is also worth to notice that measuring instruments are not free from errors and that unexpected difficulties, e.g. power failure, may occur during taking measurements.

A prediction of heat transfer processes in solar collectors carried out on the basis of theoretical calculations is a consequence of mathematical models, rather than a consequence of actual physical models. In general, mathematical models consist of a set of differential equations that govern heat transfer processes in a considered solar thermal system. The solution of these equations can be obtained with analytical or numerical methods.

Analytical methods provide an exact solution of differential equations, which allows for the temperature determination at any point of the considered domain, that is an advantage of the method. There are several analytical methods for solving particular heat transfer problems [27, 130]. Nevertheless, the application of analytical methods to solve a heat transfer problem in solar collectors is often limited due to complexity of a collector's geometry and boundary conditions. In such cases, the

solution does need a numerical method.

Numerical methods provide an approximate solution of heat transfer equations, which govern the heat exchange in solar collectors. Among the various numerical methods, the most commonly used are the Finite Difference Method (FDM) [130], Finite Volume Method (FVM) [133] and Finite Element Method (FEM) [110].

The FDM is a well-established and conceptually simple method. FDM replaces all partial derivatives in differential equations by approximation, using the truncated Taylor series [133]. The difference equations are written for an array of mesh points, called nodes. The system of nodes represents a discretized domain of the problem. An increasing number of nodes increases the solution accuracy. FDM can be employed to solve many heat transfer problems. However, the application of this method is difficult in problems characterized by irregular geometries or complex boundary conditions [110]. FDM is probably the most commonly used numerical method to solve the problems of one-dimensional heat conduction. The Forward Time Centered Space (FTCS) scheme, Backward Time Centered Space (BTCS) scheme and Crank-Nicolson scheme are the most widely used solution schemes.

In FVM, the solution domain is divided into a number of finite (control) volumes. The term of finite volume refers to a small volume surrounding each node point in a mesh. The Finite Volume Method is conservative, since the flux entering a given volume is identical to flux leaving an adjacent volume. In the method, the equations are presented in an integral form. The divergence term in each equation is expressed as surface integral, based on a Green's divergence theorem [133]. The surface integral represents flux at a finite volume surface. The FVM has a wider application than the FDM since finite volumes can have an arbitrary shape, making the method applicable for complex geometry. In the case of a uniform Cartesian mesh, FVM can be regarded as FDM [28]. On the other hand, Mora et al. [122] reported the vertex-centered FVM to be very similar to the linear FEM.

FEM is the most versatile numerical method among the mentioned methods. However, it is also the most difficult method to be implemented. In FEM, the solution domain is divided into many small elements which are connected to each other. The method gives a piecewise approximation to governing equations. The approximation is obtained through a reduction of complex partial differential equations to linear or non-linear equations. As a consequence, the procedure of FE discretization reduces a continuum problem, characterized by an infinite number of unknowns, to one characterized by a finite number of unknowns at nodes of the mesh. The method was originally developed to be applied in structural analyses of solids [16]. However, the method applicability was extended also to other fields including fluid

dynamics and heat transfer. FEM allows for forming elements in an arbitrary sense, hence enabling to solve the problems of complex domain geometries [110]. Similarly to FVM, it enables to use irregular meshes which are finer in the regions of a special interest and coarser in other regions. The concept of FEM is precisely described in works of Bathe [16] or Zienkiewicz and Morgan [188]. The application of FEM to problems of the heat transfer and fluid flow is discussed by Lewis et al. [110].

As compared to experimental investigations, the prediction of heat transfer processes occurring in solar collectors carried out with the use of aforementioned numerical methods offers a number of advantages. The most important advantage of numerical predictions is its low cost [133]. In many practical problems, the computing cost is much lower than the cost of corresponding experiments. The importance of this advantage increases when the physical problem to be investigated becomes larger or more complex. There are no difficulties in having large or small dimensions, in treating high or low temperatures, etc., as numerical methods enable to easily simulate realistic conditions. Another advantage is a remarkable performance speed of numerical calculations for some heat transfer problems. They enable to investigate many configurations of the considered thermal system in a relatively short-time. Alternatively, corresponding experimental investigations would last much longer. This advantage of numerical methods, however, refers to simple problems for which an adequate mathematical model can be easily defined. For complex problems involving unsteady conditions, complex geometry, strong nonlineartities, etc., a numerical solution can be also as time-expensive as experiments. In general, many unsteady heat transfer problems are still beyond practical applications. The ability of giving detailed and complete information about heat transfer processes is a further advantage. The values of most variables influencing the heat transfer problem can be determined in any point of the considered discrete domain at any time of simulations. Moreover, in contrast to experimental investigations, numerical methods enable to study basic phenomena rather than complex engineering applications. This is achieved by simulating ideal conditions such as two-dimensionality, constant density or adiabatic surfaces, that can be easily prescribed. Numerical methods are consequences of mathematical models. Even the best numerical method will provide useless results if an insufficient mathematical formulation of heat transfer problem is employed. In contrast, experimental investigations refer to the reality. Therefore, the validity of mathematical models often limits the usefulness of numerical methods. For complex heat transfer problems, when there is an uncertainty about the extent to which numerical solutions would agree with the reality, some experimental backup is highly desirable. For relatively simple problems there is no better way of

checking the validity of numerical solutions than a comparison with exact analytical solutions.

A reliable evaluation of a solar collector presented in this study requires the annual performance analysis based on experimental investigations. The development of an experimental building equipped with a solar energy collection system, seasonal heat storage, fluid flow control system and measuring instruments is, however, impossible at the recent stage of the research. On the other hand, a small-scale model of the considered collector is not capable to sufficiently simulate the heat exchange in the ventilated air-cavity. Therefore, numerical methods must be employed. As described in the previous sub-section, the heat transfer problem for a hidden solar collector involves conduction, radiation, natural and forced convection. Since all these physical phenomena are significantly influenced by time-varying weather conditions, an unsteady analysis must be carried out to achieve the main objective of the thesis. A reliable numerical solution for the formulated heat transfer problem may be, however, very-time-expensive. Thus, a mathematical model needs to be simplified.

4.2.3 Thermal modeling of solar collectors - literature review

Theoretical heat transfer investigations in solar collectors require a development of a mathematical model that is detailed enough to be able to deal with all important physical phenomena, and simple enough to give reliable results in the short runtime. In order to achieve a compromise between the complexity of the model and the accuracy of results, the set of governing equations addressing the conservation of physical quantities must be simplified. A review of mathematical models for simplified performance analysis of solar systems is presented by Chwieduk [40] and Smolec [154]. As a result of the ongoing research, a significant number of numerical models for heat transfer in conventional solar collectors, especially flat plate collectors, are described in the literature.

A standard and widely used model for a design and performance prediction of FPC was presented by Duffie and Beckmann [58]. Their approach assumes a one-dimensional heat transfer and is based on the determination of heat transfer coefficients from the absorber to the surrounding and determination of a fin efficiency factor to obtain the heat conducted from the absorber plate to the tube. The temperatures at the absorber, back plate and covers are calculated under steady-state conditions from an analogy between an one-dimensional heat transfer and electrical grids.

In general, models allowing to consider the heat transfer under steady-state conditions, so-called stationary models, are simple, that is reflected by a short run-time required for computations. However, solar collectors hardly ever reach a steady state during operation, mainly due to their large time constants and the variability of driving forces. Moreover, stationary models lead to an overestimation of the energy delivered by collectors [147]. Therefore, many efforts have been done to improve the one-dimensional steady-state heat transfer model proposed by Duffie and Beckman [58]. Later works attempted to develop dynamic (unsteady) models to include a heat thermal capacitance of solar collector components.

Amer and Nayak [3] presented a dynamic single-capacitance model for a performance prediction of FPC under unsteady climate conditions. The developed model of the one-dimensional heat transfer assumed that thermal capacities of the absorber plate, headers, risers, fluid and insulation are lumped together in one temperature node referenced to the mean fluid temperature. For this node, a dynamic heat balance equation was formed. The heat loss from the collector were expressed in terms of an overall loss coefficient comprising losses from top, bottom and sides. It was assumed to be a linear function of the temperature difference between the fluid and ambient. The overall heat loss coefficient and specific heat of the fluid were assumed to be temperature-independent. The fluid flow rate was assumed as constant, distributed uniformly in tubes. The energy conservation equation of the solar collector is written for the fluid domain, in the fluid flow direction of the solar collector over a length Δx and width Δy as:

$$\begin{aligned} \dot{m}C_{p,f}\left[T_f\left(x+\triangle X,t\right)-T_f\left(x,t\right)\right] &= F'\left(\tau\alpha\right)_e I_e\left(t\right)\triangle Y\triangle Xx \\ &\quad -F'U_L\left[T_f\left(x,t\right)-T_{a,out}\left(t\right)\right]\triangle Y\Delta X \\ &\quad -\left(\mathrm{Mc}\right)_{\Delta X}\frac{\mathrm{d}T_f\left(x,t\right)}{\mathrm{d}t}, \end{aligned} \tag{4.2.1}$$

where $\dot{m}$ is the fluid mass flux through a one collector tube, $C_{p,f}$ is the specific heat of fluid, T_f is the fluid temperature, x axial co-ordinate along the flow direction, $\triangle X$ is the element length along the flow direction, ΔY is the element width, t is time, F' is the collector efficiency factor, $(\tau\alpha)_e$ is the effective transmittance absorptance product, I_e is the solar irradiance on tilted plane, U_L is the overall collector heat loss coefficient, $T_{a,out}$ is the ambient air temperature, and $(\mathrm{Mc})_{\Delta X}$ is the total thermal capacity of the element whose length is ΔX.

As compared to measured data, theoretical predictions of the outlet fluid temperature by the proposed method were within 0.3 °C of measured values. However, this

test method requires many tests and complex math calculation [101]. Some previous studies of single-capacitance models were presented by Close [46] and Klein et al. [100]. In general, single-capacitance dynamic models are not able to predict the spatial temperature profile inside the collector because they do not consider the distributed heat capacitance of collectors. This may result in errors in a prediction of heat losses and time-dependent outlet fluid temperatures [79].

An alternative was provided by distributed-character dynamic models which try to describe the time-dependent spatial temperature distribution inside collectors. Most of distributed-character models, however, consider a time-dependent profile in the flow direction only. One method to represent the temperature profile is to divide the collector into M nodes perpendicular to the flow direction, e.g. fluid and absorber, and N nodes in the flow direction. Such approach provides a $M \times N-$node model. In consequence, a system of $M \times N$ ordinary differential equations has to be solved.

Muschawek and Spirkl [125] presented a dynamic method for a performance testing of FPC under unsteady conditions. The method is based on a $1 \times N-$node model with a heat capacitance of the absorber, risers, and fluid lumped together and referenced to the mean temperature of the fluid. According to the method, the collector is divided into $N-$segments along the flow direction. The $1 \times N-$node model composed of connected nodes, each one representing a separate segment, allows for determining the overall collector behavior. A power balance on each segment leads to an ordinary differential equation for the fluid temperature in a one segment, and the average of this temperature serves as an input for the next segment in the same time step of a simulation. The energy conservation equation for each segment is [101]:

$$\frac{(\mathrm{mc})_e}{N_c}\frac{\mathrm{d}T_f}{\mathrm{d}t} = \frac{F'}{N_c}\left[(\tau\alpha)_e I_e - U_L\left(T_{f,i} - T_{a,out}\right)\right] - \dot{m}C_{p,f}\left(T_{f,i+1} - T_{f,i}\right), \qquad (4.2.2)$$

where $(\mathrm{mc})_e$ is the effective heat capacity of the collector per unit area, N_c is the number of collector nodes, T_f is the fluid temperature, $T_{f,i}$ is the fluid temperature of the ith collector segment, t is the time, F' is collector efficiency factor, $(\tau\alpha)_e$ is the transmittance absorptance product at normal incidence, I_e is the solar irradiance on tilted plane, U_L is the overall collector heat loss coefficient, $T_{a,out}$ is the ambient air temperature, $\dot{m}$ is the fluid mass flux through one collector tube, $C_{p,f}$ is the specific heat of the fluid.

FDM was used to solve a system of equations (Eq. 4.2.2). The presented approach considers arbitrary variations of irradiance, ambient temperature, inlet fluid temper-

ature and fluid flow during tests. The results of the method, however, showed some inconsistencies in the determination of the effective thermal capacity of collectors.

Another method was to represent the temperature profile in a flow direction by a continuous time function and a coordinate in a flow direction for each node. This approach results in a system of partial differential equations.

A model with only one temperature node, so-called $1n-$ model, was described by Isakson [89]. In the model, the partial differential equation is transformed to an ordinary one to be solved analytically. Such a simplification is achieved due to the assumption that the fluid temperature profile in the collector moves with an effective velocity. The temperature of each fluid portion, that enters the collector one by one at each time step of a simulation and flows with the effective velocity, increases according to ambient conditions. This approach allows for obtaining an accurate solution. The method, however, does not work with a varying fluid mass flux [79].

The $1n-$ model described by Meaburn and Hughes [117] considers variations of a fluid mass flux. However, the method is inadequate to analyze solar systems characterized by rapid changes of a fluid mass flux [79].

More complex methods are based on models with more than one temperature node, for example glass cover, absorber plate and fluid. Such a $3n-$ model was described by Kamminga [94]. The general idea of the model is to treat the collector as a single fluid duct in which the fluid is flowing at a given velocity u along the $x-$ axis. The glass cover, absorber plate and fluid are considered as separate components, each characterized by a heat capacity per unit collector area and a temperature. The temperatures in the collector are treated as functions of x as the only parameter. A heat transfer in the flow direction occurs only by fluid flow. No conduction in a flow direction is considered. With the fraction of solar radiation absorbed by the plate S_f and the ambient temperature $T_{a,out}$ the described approach results in the following set of linear partial differential equations [147]:

$$C_{c,g}\frac{\partial}{\partial t}T_g = h_{ag}\left(T_{a,out} - T_g\right) + h_{gp}\left(T_p - T_g\right), \tag{4.2.3}$$

$$C_{c,p}\frac{\partial}{\partial t}T_p = S_f + h_{gp}\left(T_g - T_p\right) + h_{pf}\left(T_f - T_p\right), \tag{4.2.4}$$

$$C_{c,f}\left[\frac{\partial}{\partial t} + u_x\frac{\partial}{\partial x}\right]T_f = h_{pf}\left(T_p - T_f\right), \tag{4.2.5}$$

where $C_{c,g}$, $C_{c,p}$ and $C_{c,f}$ is the heat capacity per unit collector area of the glass cover, absorber plate and fluid, respectively, T_g, T_p, and T_f is the temperature of the glass

cover, absorber plate and fluid, respectively, h_{ag}, h_{gp} and h_{pf} is the ambience-cover, cover-plate and plate-fluid heat transfer coefficient, respectively, u_x is the velocity of fluid flowing along the $x-$ axis.

Based on a similar approach, Hilmer et al. [79] described the $4n$-model for flat plate collectors, in which the nodes of the glass cover temperature $T_g(x,t)$, absorber plate temperature $T_p(x,t)$, fluid temperature $T_f(x,t)$ and temperature of the insulation $T_i(x,t)$ are considered. The set of linear partial differential equations is:

$$C_{c,g}\frac{\partial T_g(x,t)}{\partial t} = h_{ag}\left(T_{a,out} - T_g(x,t)\right) + h_{gp}\left(T_p(x,t) - T_g(x,t)\right), \tag{4.2.6}$$

$$\begin{aligned} C_{c,p}\frac{\partial T_p(x,t)}{\partial t} &= S_f + h_{gp}\left(T_g(x,t) - T_p(x,t)\right) \\ &\quad + h_{pi}\left(T_i(x,t) - T_p(y,t)\right) + h_{pf}\left(T_f(x,t) - T_p(x,t)\right), \end{aligned} \tag{4.2.7}$$

$$C_{c,f}\frac{\partial T_f(x,t)}{\partial t} + u_x C_f\frac{\partial T_f(x,t)}{\partial y} = h_{pf}\left(T_p(x,t) - T_f(x,t)\right), \tag{4.2.8}$$

$$C_{c,i}\frac{\partial T_i(x,t)}{\partial t} = h_{pi}\left(T_p(x,t) - T_i(x,t)\right) + h_{ia}\left(T_a(x,t) - T_i(x,t)\right), \tag{4.2.9}$$

where $C_{c,g}$, $C_{c,p}$, $C_{c,f}$ and $C_{c,i}$ is the heat capacity per unit collector area of the glass cover, absorber plate, fluid and insulation, respectively, T_g, T_p, T_f and T_i is the temperature of the glass cover, absorber plate, fluid and the insulation, respectively, h_{ag}, h_{gp}, h_{pi}, h_{pf} and h_{ia} is the ambience-cover, cover-plate, plate-insulation, plate-fluid and insulation-ambience heat transfer coefficient, respectively, u_x is the velocity of fluid flowing along the $x-$ axis.

De Ron [50] described the $2n-$model, in which the heat capacity of glass cover and insulation are neglected. A comparison between several above-described solar collector dynamic models in terms of the energy yield was conducted by Schnieders [147]. The author concluded that the $2n-$model provided the best description of the actual collector behavior. The presented approaches provide an approximate solution for the fluid temperature at the certain time. The models, however, do not take into account the thermal capacitance of the air layer. Moreover, the methods used to solve the equations are not suitable for varying flow rates [79].

Hilmer et al. [79] proposed an improved numerical method to solve the set

of first-order partial differential equations typical for dynamic disturber-character models of solar collectors. In contrast to most methods previously reported in the literature, the proposed approach is applicable for the assessment of the solar collector's performance for time-dependent fluid mass flux, spatial non-uniform solar irradiance and heat transfer coefficients. The $2n-$ model is chosen. One of the temperature nodes represents the fluid and the absorber capacities lumped together with the fluid temperature $T_f(x,t)$, whereas the another node represents the roof capacities lumped together with the temperature of the roof surface $T_r\,(x,t)$. For each node a heat balance is formulated. In order to calculate heat losses from the absorber surface, the absorber surface temperature $T_p\,(x,t)$ is introduced as an additional temperature node without heat capacity. T_p is calculated by assuming steady-state heat transfer between the absorber and fluid. The authors introduced heat balance equations as follows:

$$0 = S_f + \varepsilon_{eff}\sigma\left(T_{Sky}^4 - T_p^4\right) + h_e\left(T_{a,out} - T_p\right) + h_{sf}\left(T_f - T_p\right), \tag{4.2.10}$$

$$\left(C_{c,f} + C_{c,p}\right)\frac{\partial T_f}{\partial t} + C_{c,f}u\frac{\partial T_f}{\partial x} = h_{sf}\left(T_p - T_f\right) + h_{fr}\left(T_r - T_f\right), \tag{4.2.11}$$

$$C_{c,r}\frac{\partial T_r}{\partial t} = h_{fr}\left(T_f - T_r\right) + h_{ra}\left(T_{a,out} - T_r\right), \tag{4.2.12}$$

where ε_{eff} is the effective emittance of the absorber surface, σ is the Stefan-Boltzmann constant, T_{sky} is the equivalent sky temperature, T_p is the absorber surface temperature, T_r is the roof temperature, h_e is the convective heat transfer coefficient of external surface, h_{sf} is the surface-fluid heat transfer coefficient, h_{fr} is the fluid-roof heat transfer coefficient, h_{ra} is the roof-ambience heat transfer coefficient, $C_{c,p}$ is the absorber heat capacity per aperture unit area, $C_{c,r}$ is the roof heat capacity per aperture unit area.

In the proposed model the mean fluid velocity, u, at location x and time t is calculated from:

$$u = \frac{\dot{m}C_{p,f}l_{abs}}{C_{c,f}}, \tag{4.2.13}$$

where $\dot{m}\,(t)$ is the fluid mass flux, $C_{p,f}$ is the fluid specific heat capacity, l_{abs} is the length of the absorber tube.

The model assumes no heat transfer in a flow direction except by the forced convec-

tion in the fluid. The convective and radiative heat transfer coefficients are based on empirical formulas found in the literature, whereas the bond conductance between the absorber plate and tubes (one of the most important parameter affecting the thermal performance of flat plate collectors) was obtained numerically by the authors. The method enables the more accurate prediction of heat losses and outlet fluid temperatures during the operation time. The method was applied to simulate a large unglazed collector used for heating a public swimming pool in Germany. A validation with experiment results obtained for the collector showed a good short- and long-term accuracy of the model at constant and varying fluid mass flux.

Minn et al. [120] presented a non-linear distributed two-dimensional steady-state FV model that includes a temperature-dependence of fluid and material properties. The approach predicts the collector's efficiency and temperature distribution of fluid and absorber at various inlet fluid temperatures and meteorological conditions. The fluid flow is considered uniformly distributed among the equally pitched ten flow channels in a collector panel. The model considers a heat loss to ambient from the collector's cover and through the back of the absorber. However, numerical simulations were performed without assuming a prior value for the overall heat loss coefficient of the collector. The heat transfer coefficients and bond conductance are calculated with values from the literature. Based on a comparison between theoretical predictions and experimentally measured data, a satisfactory agreement within 4 % was found.

Most above-mentioned models are based on an extension of the electrical analogy by Duffie and Beckman [58]. These models are restricted to specific geometries and materials, and have a non-sufficient description of the radiative heat transfer in participating media. Continuous improvements of both the computers performance and computational algorithms led to models to describe the physical and geometrical complexity of the system more accurately.

Hassan and Beliveau [74, 75] formulated a three-dimensional unsteady FE model in order to evaluate the thermal performance of the integrated roof solar collector during 12 months. The heat losses to the ambient and into the building's interior, conduction in solid elements, forced convection in the flowing fluid and radiative heat exchange between surfaces forming the air gap and absorber tubes are taken into account. Two types of eight-node brick finite elements are used to describe solid and fluid layers. The air gap layer is, however, modeled with the same finite elements as solids. The temperature-independent thermo-physical properties of the fluid and materials are assumed. The presented model allows to fit any set of climate and operational conditions, time and location. A convection boundary condition and a

solar radiant flux are assumed to govern the heat exchange taking place between the environment and glass cover surface. At each time step of unsteady calculations the radiative flux passing through the glass cover is reduced with the help of subroutines that calculate absorption, reflection and transmittance according to glass properties. The convective heat transfer coefficient is based on the empirical formula found in the literature. The numerical method results are verified by analyzing the solar collector under steady-state conditions and comparing the results to the analytical method developed by Duffie and Beckman [58]. The error is less than 5 %. In the model, a detailed temperature distribution in the whole domain of the solar collector at any time of the simulation is achieved. The developed sub-model of the fluid, however, has a constant profile of the fluid flow velocity in tubes, whereas in the practice for relatively small magnitudes of fluid mass flux, there is a thin layer near the pipe surface where the fluid velocity decreases to zero [103].

Medved et al. [118] employed FVM to carry out a parametric analysis of the large-panel unglazed roof-integrated liquid-based solar collector's efficiency under steady-state conditions. The geometry of the numerical model was reduced to a segment containing one pipe with the flowing fluid. The Navier-Stokes equations with Newton's law of cooling and the Stefan-Boltzmann radiation law was used to establish the pressure, velocity and temperature fields. The water flow in the pipe was assumed as laminar with the same magnitude of fluid mass flux in each pipe in the panel. The airflow around the absorber due to natural convection was not considered. The short-wave and long-wave irradiance in the collector plane were assumed to be equal across the whole absorber area. The numerical model was verified with the outdoor experiments. The authors concluded that the numerical model, even with assumed simplifications could be used for determining the collector efficiency.

The thermal performance of liquid-based solar collectors is strongly affected by a fluid flow distribution through absorber tubes. Most solar collector models in the literature assume an uniform distribution of fluid flow through tubes, whereas in the practice there is always some degree of maldistribution [177]. Taking advantage of a continuous improvement of both computational algorithms and computers, later studies include the effect of a fluid flow pattern on the collector efficiency by means of computational fluid dynamics (CFD) computations.

Fan et al. [61] investigated experimentally and numerically fluid flow and temperature distribution in a solar collector panel with an absorber consisting of horizontally inclined strips. The fluid flow and heat transfer in the collector were studied with CFD. The three-dimensional numerical model included both combining and

dividing manifolds and 16 quadrangular absorber tubes. The existence of fins was represented by a heat flux into absorber tube walls, assuming the uniform energy generation in the tube wall. No other components of a solar collector were analysed. The model included heat transfer and buoyancy effects in the flowing fluid. A comparison between fluid temperatures from CFD simulations under steady-state conditions and thermal measurements showed a good agreement at high magnitudes of fluid mass flux. For low magnitudes of fluid mass flux, however, large differences between measured and calculated temperatures occurred due to an oversimplification of the collector model and a lack of the knowledge on airflow conditions inside the collector panel.

CFD was also employed by Martinopoulous et al. [116] in order to obtain a detailed flow field development and the temperature distribution in the novel honeycomb polycarbonate solar collector. The three-dimensional numerical model considered the solar irradiation, convection and heat transfer in the circulating fluid and between collector parts. A comparison between results obtained from steady-state simulations and experimental investigations showed that there is a good agreement regarding the collector efficiency. Similar flow patterns and temperature distributions were also observed. The authors concluded that a CFD model was a useful tool for investigations and optimizations of solar collectors.

Villar et al. [175] developed an unsteady three-dimensional model of FPC that included the effect of a fluid flow maldistribution in collector tubes. The model, based on mass and energy balances in finite volumes, took into account the forced convection inside tubes and between plates, and conduction in the absorber plate. The mass balance in a control volume was obtained by analyzing flow of the working fluid from one element to adjacent ones. The heat balance of the back insulation was established for control volumes defined in a normal direction to the collector plane. The temperature-dependent thermal properties of materials were considered. The cover was modeled as a single node. The heat transfer coefficients were calculated from formulas in the literature, whereas the heat transfer from an absorber to tubes was determined numerically by the heat balance of finite volumes adapted to the geometry. The model was positively validated under steady-state conditions with the experimental data obtained for a commercial parallel tube collector. The study, however, gives a poor guidance for the thermal modeling of a convective heat exchange in the air gap.

A more detailed thermal analysis of a convective heat exchange in the air gap of solar collectors was conducted by Dović and Andrassy [57]. The authors developed two-dimensional and three-dimensional CFD models to simulate a steady-state heat

exchange in plate collectors with and without tubes. The model of the free convection in the enclosure between the absorber, glass and casing, was based on the discretized standard set of equations comprising the equations for conservation of mass, momentum and energy. The FVM was employed to convert governing and radiation differential equations to algebraic equations suitable to be solved numerically. The reliability of the steady-state simulations was positively verified through a comparison with experimental measurements with a collector with tubes. The presented model, however, does not include a sub-model of the flowing fluid.

Selmi et al. [148] formulated a complete three-dimensional numerical model to predict the performance and temperature distribution within FPC. The CFD method was employed for modeling solar irradiation and modes of a mixed convection and radiation heat transfer between tube surface, glass cover, side wall, and insulating base of the collector, a mixed convective heat transfer in the circulating water inside the tube and conduction between the base and tube material. The results of numerical simulations under steady-state conditions indicated a good agreement with the experimental data. The authors, however, did not provide any details concerning the mathematical and numerical model.

A comprehensive thermal modeling of the heat transfer in conventional FPCs should comprise solar irradiation and modes of a mixed convection and radiation heat exchange between tube surfaces, glass cover, side walls, and insulating base of the collector, a mixed convective heat transfer in the fluid flowing through tubes and conduction between the base plate and tube material.

The concept of a solar collector presented in this study is based on the ventilated roof structure, hence a different heat transfer problem (Section 3.3.1) occurs as compared to conventional FPCs. The difference concerns mainly a convective heat exchange in the air-cavity. In general, the thermal modeling of ventilated roof structures is a very complex problem that requires a detailed knowledge on the airflow rate and its thermodynamic properties, thermo-physical properties of materials, coefficients, intensity of the solar radiation, outdoor air properties (temperature and humidity), velocity and direction of the wind [64]. While an extensive review of studies on inclined closed air-cavities relevant to FPC is available [77], only few numerical studies dealing with a convective heat exchange in solar collectors based on ventilated structures are reported in the literature.

A study by Anderson et al. [4] examining the performance of building integrated solar collectors characterized by a similar heat transfer problem as in this study, provides the best benchmark for comparison purposes. The authors, however, did not provide any details with respect to a numerical model of a solar collector.

An example of a solar system, in which the knowledge about the convective heat exchange performance in ventilated channels, is a building integrated photovoltaic-thermal (BIPV/T) collector. In such cases, the convective heat exchange reduces the temperature of the PV cells that are directly exposed to solar radiation hence increasing its efficiency. It is estimated that the efficiency of PV cells decreases linearly with the temperature increase at approximately 0.4–0.5 %/°C [167]. Several experimental studies on liquid cooled BIPV/T collector can be found in the literature [34, 90]. However, only few numerical studies exist from which modeling advices may be gleaned.

A study by Corbin and Zhai [48] examining the effect of the active heat recovery by a liquid cooled heat absorber on the performance of a BIPV/T collector provides an effective approach to solve the problem of interest. The authors employed CFD to solve the Reynolds Average Navier-Stokes governing partial differential equations for fluid flow and heat transfer with FVM. The developed three-dimensional CFD model, representing a section of the larger array showed a good agreement with experimental data collected from a full-scale collector. The study effectively deals with a steady-state buoyancy-driven natural convection and radiative heat exchange in the air-cavity. The heat transfer problem investigated by Corbin and Zhai differs, however, from that for the hidden solar collector. The CFD model did not include the wind effect on airflow in the ventilation channel.

Much more information on the thermal modeling of a convective heat exchange in the ventilated air-cavity is given by numerical results for double-skinned building envelope structures such as ventilated roofs.

Villi et al. [176] investigated the benefits of ventilated roofs for a reduction of summer cooling load in buildings. Two-dimensional CFD models were developed to solve a steady-state heat transfer problem in ventilated and non-ventilated roof structures by FVM. The ventilated structure, 8 m long and 30 ° inclined, consisted of two flat elements creating a cavity that enabled buoyancy-driven airflow. All materials were assumed to be homogenous and isotropic. Three widths of air-cavity (3, 5, and 10 cm) were investigated. A portion of the outside environment was included in the CFD model and discharge effects at intake and outlet vents were considered. The wind effect on airflow in the ventilation channel was, however, neglected. A constant relative pressure of 0 Pa was imposed across all surfaces surrounding the outside environment. The air was considered to be an incompressible gas. The obtained results were proved to be consistent with the literature available information. The CFD model did not consider the air-permeability of the exterior cladding surface and the influence of supporting elements (such as wooden rafters) on the flow

field within ventilated channels.

A similar approach for a solution of a steady-state heat transfer problem in ventilated roof structures was studied by Gagliano et al. [64]. In this study, the air was assumed as a compressible fluid. This assumption increased the accuracy of obtained results. Nevertheless, it made the analysis much more time-expensive.

Biwole et al. [20] numerically investigated the optimal width for a ventilation channel in double-skin roof structures created by adding a second sheet iron to the existing sheet metal roof. The FEM was employed to solve a steady-state two-dimensional heat transfer problem. The radiative heat exchange between the ceiling and building's interior was neglected in the model, since the impact of the long-wave radiation on the air temperature in the double-skin roof was concerned as negligible. Density variations of the air in the channel were considered as negligible when compared to the variation of air velocity hence the fluid was assumed as incompressible. The air velocity on both plates was equal to zero. The air velocity at the air-cavity entry was assumed as zero so as to simulate no-wind climate conditions. The total force on the exit boundary was set to zero in order to simulate the gap exit. The maximum air speed due to a natural convection noticed at the entry and the exit of the channel were 0.89 and 0.94 m/s, respectively. A comparison between predictions and measurements was performed. The authors indicated a remarkable difference between numerical and experimental results at the early and late hours, and likeness of results for the middle part of the day. It was resulted due to the thermal inertia of the sheet metal which was not taken into account by a numerical simulation under steady-state conditions. In real case, heat variations of the sheet metal are less rapid. The structure of solar collector to be investigated in this study comprises a sheet steel roofing. A reliable performance evaluation requires the thermal inertia of the roofing material to be considered in the model. Therefore, an unsteady conditions should be simulated.

In general, the literature dealing with simulations of the unsteady heat transfer in ventilated roof structures is limited. Most studies in this field are usually based on many simplifications, e.g. one-dimensional heat transfer, and refer to simulations of short time periods.

Hirunlabh et al. [80] conducted an unsteady numerical analysis of the air temperature variations in ventilated roof structures. A one-dimensional heat transfer model comprising a conductive, radiative and convective heat exchange in the ventilated roof structure was developed. The model assumed no effect of air-leakage and corrugation of monier tiles on convective heat transfer within the air-cavity and no participation of the air layer in the cavity radiation. Properties of the air were

assumed as a function of temperature, whereas properties of solid materials were assumed as temperature-independent. Based on the combination of three modes of heat transfer, a nodal formulation of a ventilated roof structure was provided by performing an energy balance at each node. The unsteady analysis for a one-day period, with the time step of 20 s was conducted with FDM. The validation of numerical model revealed few disagreements with the measured data mainly due to the wind effect which was not taken into account in the model.

In 2007, Cerne and Medved [29] indicated the lack of models which could be used for prediction of unsteady two-dimensional heat flow in ventilated building structures. The authors used CFD to conduct the unsteady multi-parametric analysis of a two-dimensional heat transfer problem in the low sloped roof with a forced ventilated air-cavity made from lightweight building components. The unsteady numerical analysis, referred to a 24 h period, was conducted with a commercial CFD software PHOENICS based on control volume method. The ambient temperature and solar radiation intensity for a standard clear-sky summer day were used to assess the thermal load of a building. The air-cavity in the 2D numerical model was 9 m length and 25 mm width. The effect of a corrugated thin metal sheet on convective heat transfer within the cavity was neglected. A constant airflow through the cavity and an uniform air velocity profile at the cavity inlet were assumed. Three values of airflow velocity, including 0.36, 0.72 and 1.08 m/s, were considered. The radiation attenuation in the air layer of the the air-cavity was neglected. The model was positively verified with experiments. Based on results of numerical simulations, performed with a 10 min time step, it was concluded that heat flow through the ventilated structures is markedly two-dimensional.

After reviewing the literature concerning thermal modeling of conventional solar collectors it was found that the multidimensional and unsteady character of the heat transfer problem is not considered in most of theoretical analyses. The thermal models are, in general, either simplified to much or limited to a specific design. There is an extensive research work based on unsteady one- or two-dimensional heat transfer models. Nevertheless, most of them provide a poor guidance for the thermal modeling of the convective heat transfer within the flowing fluid and the air-cavity. More detailed analyses of the convective heat transfer phenomena within the flowing fluid and air-cavities can be conducted with CFD models. The CFD analyses of the fluid flow and three-dimensional heat transfer in conventional solar collectors are, however, computationally time-consuming therefore a number of research works on this subject is quite low. If so exist, they are usually limited to simulations conducted under steady-state conditions.

The solar collector investigated in this study is based on a ventilated roof structure. More guidance for the thermal modeling of a convective heat exchange in the air-cavity may be offered by CFD analyses of ventilated roofs. Several studies investigating the effect of airflow in air-cavities of ventilated roofs can be found in the literature. Most CFD models are, however, based on a two-dimensional steady-state heat transfer and does not consider the influence of air-leakage and corrugation of a roofing material as well as other roof layers on airflow within ventilated channels. The wind effect on a convective heat exchange in ventilated channels is mostly neglected. The unsteady CFD models are referred to simulations of short time-periods only.

4.3 Summary

The concept of hidden solar collector is an excellent alternative to conventional solar collectors when used to power low-temperature applications, such as low-temperature space-heating systems dedicated for residential buildings characterized by a low heat demand or domestic hot water systems. The collector is based on a simple solar energy collection system that is made from typical polypropylene pipes located in an air-cavity of the ventilated roof. Thus, it is characterized by low manufacturing, mounting and maintaining cost. However, the main advantage that distinguishes the collector among all active energy systems is the lack of interference in the external architecture of the building.

Due to its structure, the investigated hidden solar collector is characterized by different heat transfer problems as compared to conventional solar collectors. Its thermal performance strongly depends on climate conditions. The ambient air temperature, solar radiation, wind speed and other meteorological data vary in time. As a consequence, the collector always operates under unsteady conditions which are non-linear in their nature. Thus, it is difficult to accurately analyze the efficiency of a hidden solar collector based on its response to average ambient climate conditions. A reliable evaluation of a hidden solar collector presented in this study requires the annual performance analysis based on experimental investigations. Such investigations are, however, impossible to be carried out at the recent stage of the research. Therefore, theoretical and numerical investigations are the only way to reach the general objective of this study. Due to the unsteady three-dimensional heat transfer comprising a conductive, radiative, natural and forced convective heat exchange, the performance analysis does need a numerical solution. Based on the literature review concerning the thermal modeling of the heat transfer in conventional solar collectors

and ventilated roof structures it can be concluded that CFD analysis is the best method for a solar collector presented in this study. The numerical solution for the formulated heat transfer problem is, however, very-time-expensive. Thus, a mathematical model for the considered case must be simplified to enable an unsteady simulation of the year-round collector operation.

Chapter 5

Model formulation

The heat transfer process in a hidden solar collector is complex (comprises all heat transfer phenomena) and multidimensional (Section 4.2.1). All physical phenomena taking part in the process are significantly influenced by time-varying weather conditions. Thus, it is difficult to accurately analyze the efficiency of HSC based on its thermal response to average climate conditions. What is more, a major application of HSC is to supply space-heating systems using seasonal heat storage systems. Since the maximum energy extraction from heat storage systems occurs when the availability of solar energy is minimum or none, it is of great importance to determine exact amount of energy collected particularly in a winter season. Hence, a reliable numerical performance analysis of the collector requires an unsteady simulation of the year-round operation under realistic climate conditions to be carried out. This study also aims at giving some recommendations to a design of HSC in order to maximize the amount of collected energy. For these purposes, the developed 3D numerical model of HSC should enable to conduct the simulation under both transient and steady-state conditions. As concluded in the previous chapter, the CFD analysis is the most accurate method for a numerical solution of a heat transfer problem in HSC. The application of this method for the simulation of unsteady heat transfer in a three-dimensional full-scale model of a one roof-field containing HSC may be, if possible, very-time-expensive. Hence, the main objective of the thermal modeling was to reach a compromise between the complexity of numerical model for simulation of both unsteady and steady-state heat transfer process in HSC, the accuracy of results and the computation run-time.

In the following, the thermal modeling approach assumed in order to investigate the performance of HSC together with the steps required in implementation of the numerical model are described in detail.

5.1 Thermal modeling - general assumptions

In this study, the Finite Element Method (FEM) was applied to solve the problem of three-dimensional heat transfer in HSC under both unsteady and steady-state conditions. The developed 3D FE model is capable to simulate the convective and radiative heat exchange between the external collector surface and outdoor environment, conductive heat transfer in solid layers, radiative heat exchange between the pipes and surfaces composing the air-cavity, and convective/radiative heat exchange between the internal collector surface and building interior. Proper modeling of fluid flow in HSC, including airflow in the air-cavity and water flow through the collector's pipes, is crucial, particularly, for reliable simulation of annual collector operation. Since the CFD-based model of fluids flow in HSC is expected to be very complex and computational-time consuming, a simplified approach was employed to model the convective heat transfer in both the air-cavity and water flowing through the collector's pipes. The air-cavity is modeled as an orthotropic solid body in which the heat is exchanged by conduction only. The assumption of time-varying orthotropic material thermal properties aims at including a various intensity of convective heat exchange within the air-cavity in perpendicular and parallel direction (along the main airflow direction) to the roofing surface. The magnitudes of thermal conductivity in both directions are assumed to be convective heat flux equivalent for equivalent heat transfer conditions and are to be based on CFD simulations results. In case of water in pipes, the Kirchhoff-Fourier approach is used to model the fluid flow through the collector's pipes. The heat exchange conditions in thin layers near the pipes' inner and outer surfaces are modified to include the influence of diffusion on heat exchange rate. All the parameters considered in the FE model considering the influence of convective heat transfer within the fluid domains (air and water), vary in dependence on climate conditions and operating parameters. To reach realistic results, a relationship for each parameter was determined on basis of additional series of CFD simulations of heat transfer process in the detailed 3D model of HSC under steady-state conditions. The set of boundary conditions, considered in CFD steady-state simulations, corresponds to characteristic climate conditions for the assumed location (Section 5.1.2) and the entire range of operating parameters (Section 5.5). The relationships, determined on basis of CFD simulations, were implemented in the FE model to modify thermal properties of the air layer as well as heat exchange conditions on both inner and outer pipes' surfaces in dependence on climate and operating conditions. Hence, indirectly including the influence of convective heat transfer within the air-cavity on heat exchange rate between pipes' and cavity-forming surfaces as well as improving assumed model of

water flowing through the collector's pipes.

One should notice that an employed approach is just a simplification and results obtained on basis of FE model are characterized by a discrepancy when compared to those obtained directly from the CFD method (Section 5.3.4). This approach allows, however, to simulate a year-round operation of HSC taking advantage of the accuracy gained from CFD simulations without computational costs. A similar approach for the solution of the heat transfer problem in the air-cavity of ventilated roof was proposed by Villi et al. [176].

There are, however, several constraints of the proposed approach for thermal modeling of HSC. Considering a number of numerical simulations required to reach the major objective of this thesis, the application of proposed approach is limited when the size of computational domain in numerical models corresponds to a full-scale roof-field of a typical single-family building. This refers especially to CFD simulations, which conducted even under steady-state conditions, require substantial computational power and run-time. In addition, since the geometry of air-cavity together with the gravity forces influence the buoyancy-driven convective heat exchange in the air domain, the relationships implemented in the FE model must be determined for a particular case of roof geometry and roof inclination whose magnitude should correspond to a maximum value of solar irradiance for a particular location. In other words, the results of unsteady simulation of the year-round collector operation are related to a one specified configuration of HSC and specific climate conditions. According to aforementioned constraints, the formulation of HSC model was preceded by making assumptions referred to the geometry of computational domain, material properties and angle of inclination with respect to ambient climate conditions for considered location.

5.1.1 Model geometry and material properties

The investigated type of solar collector is an integral indistinguishable part of the building (Fig. 4.1) whose size is limited only by the roof area. According to its structure, it can be assumed that HSC is composed of finite number of segments being parallel to the ridge of the building (Fig. 5.1). Each segment contains two flow-pipes of a solar energy collection system placed between battens. The inlets of flow-pipes in each segment are connected to a common supply system, whereas the outlets are connected to a common return system (Fig. 4.3). Due to the layout of pipes, being in accordance with the Tichelmann layout (Fig. 4.2b), the same hydraulic pressure conditions apply to every flow-pipe in all segments.

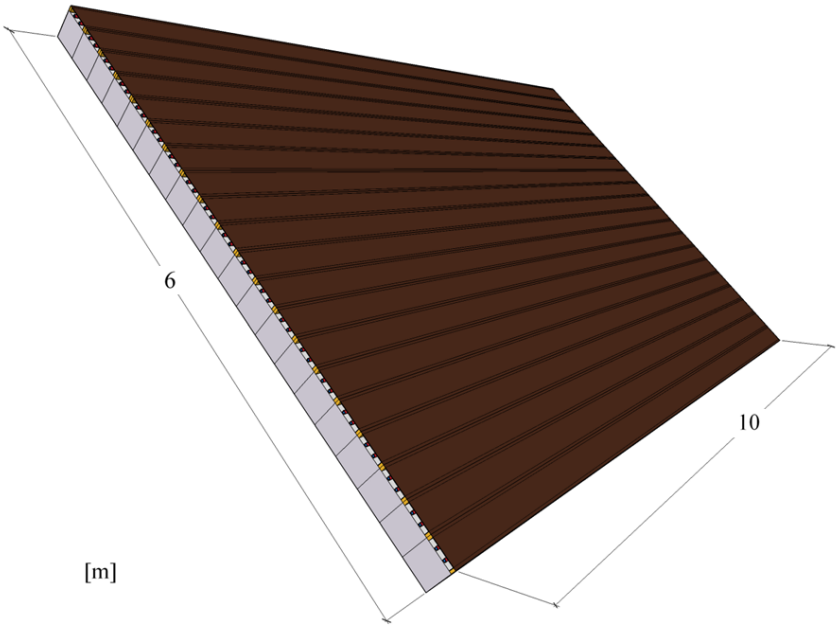

Figure 5.1: Distribution of HSC segments in roof-field

Therefore, it was reasonable to reduce a computational domain for both the FE- and CFD-based model to a one segment only. To simplify the airflow in the cavities, the test segment of HSC was chosen in the middle of HSC. It enabled to assume translational periodicity in air inlet and air outlet of the air cavity and corresponds to fully developed natural convection. A contribution of the header pipes to the amount of energy collected by the HSC is negligible when compared to flow-pipes running along the collector's segment, hence they are not considered in the developed models. Moreover, it also assumed that parts of supply and return pipes between the collector and HS system are perfectly insulated. Thus, the assumed magnitude of water temperature at inlets to the pipes is equal to considered temperature of heat storage medium (Section 5.5). The reduction of the computational domain was done by cutting the full-scale models with adiabatic surfaces. The reduction procedure defines no heat transfer through adiabatic surfaces (Eq 5.3.20 and Eq 5.3.31), whereas in real conditions some amount of heat is transferred through these surfaces. The reduction procedure was reasonable because the heat balance of a reduced model in a normal direction to adiabatic surfaces is close to zero. In a real implementation of HSC based on Tichelmann pipe layout, the segment length may be as long as the roof length. However, typical residential buildings often contain both windows and balconies in the roof structure. Thus, the pipes of solar energy collection system cannot be placed along the entire length of the roof and consequently short segments of the collector must be applied. According to assumed water flow control strategy

(Section 5.5), regardless of the segment length, the temperature of the fluid at the outlet from the collector is to be kept around the set magnitude. Thus, it can be stated that the amount of energy collected by HSC is proportional to its surface area. In other words, the total amount of energy collected by HSC installed on the whole roof-field of the building, may be determined on basis of numerical simulation results obtained for a segment model of representative dimension along the pipes. The segment of 3 m length was chosen to be representative for a challenging roof structure. The width of the segment is, in general case, dependent on the spacing of battens. It was assumed that the battens are at the distance of 0.3 m from each other. The height of the segment is dependent on the thickness of roof structure components. The segment with the height of 0.351 m was taken into account. The geometry of the 3D model of HSC for FEM simulations of unsteady and steady-state heat transfer is presented in Fig. 5.2. The absorber surface area, S_e, for the model of assumed geometry is 0.9 m^2.

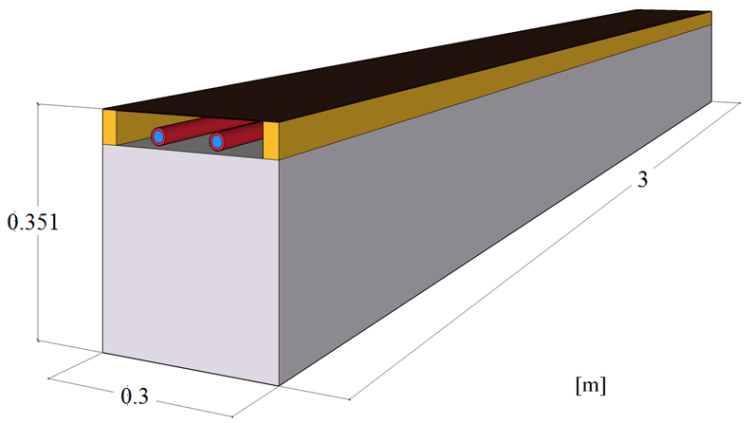

Figure 5.2: Geometry of 3D HSC model for FEM analysis

Fig. 5.3 illustrates the cross-section and dimensions of HSC model. The layers in the model of HSC include the steel roofing, battens, thermal insulation in the form of the polystyrene foam, air in the cavity and solar energy collection system created by 2 polypropylene pipes with an operating fluid. The following pipe dimensions were assumed: outside diameter $d_o = 25$ mm, inside diameter $d_i = 18$ mm, and length $l_p = 3000$ mm. The water was assumed as an operating fluid flowing through the pipes. However, in the real implementation, the water should be mixed with the antifreeze solution to protect a solar energy collection system during winter. For the purpose of FE model developing, the battens of a standard shape were chosen. In reality, however, the special type of battens possessing grooves along the length should be used (Section 4.1.1). Since, the grooves play an important role in

developing free convection in the air-cavity, they must have been included in the geometry of CFD model (Figs. 5.9 and 5.10). Both the rafters and underlay film layer which serves as the wind barrier, and the drainage plane to prevent rain water entry and working in the controlling interstitial condensation, were neglected. It was due to a negligible influence on the collector heat capacity and radiative heat exchange with pipe surfaces.

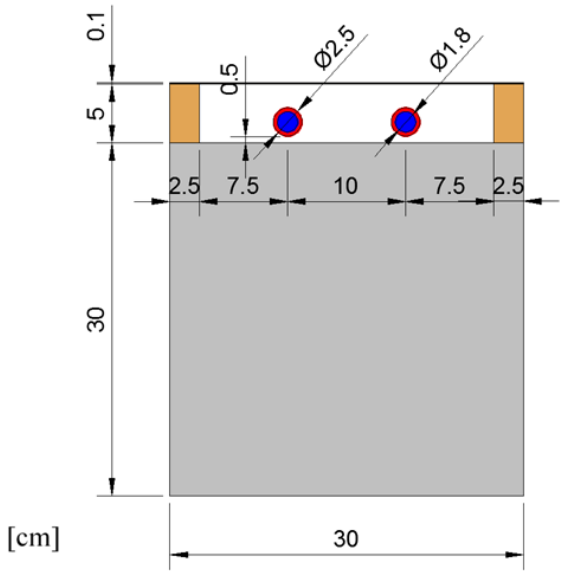

Figure 5.3: Cross-section of HSC model for FEM analysis

All materials of solid layers were assumed to be homogenous and isotropic. The thermo-physical properties of these materials (Table 5.1), used in both the FE- and CFD-based model, were assumed from the literature. The parameters of air layer and water in pipes assumed in particular models are discussed in Section 5.2.2 and Section 5.3.2.

Table 5.1: Thermo-physical parameters of solid layers assumed in numerical model of HSC

Material name	λ [W/ (m·K)]	ρ [kg/m^3]	C_p [J/(kg·K)]	ϵ [−]	α [−]
Steel roof	60.5 [6]	7854 [6]	434 [6]	0.9 [140]	0.85 [118]
Timber	0.16 [140]	720 [6]	1255 [6]	0.86 [140]	-
Polypropylene	0.40 [103]	910 [103]	2450 [103]	0.97 [87]	-
Polystyrene foam	0.035 [103]	35 [6]	1210 [6]	0.6 [87]	-

where λ, ρ, C_p, ϵ and α are the material thermal conductivity, density, specific heat, emissivity coefficient and solar absorptivity coefficient, respectively.

5.1.2 Ambient climate conditions

For the purpose of the annual operation simulation, it was assumed that HSC is a residential house component (the house meets the standard of passive houses – the building annual space-heating demand does not exceed 15 kWh/ (m^2year)[11]) located in Elblag, in the North-East region of Poland. In order to reach realistic results, the climate data of Typical Meteorological Year (TMY) for Elblag were chosen. The climate database [164] contains the hourly averaged data over a period of one year developed according to the ISO methodology [137]. The exemplary data of the hourly averaged ambient air temperature, hourly averaged wind speed and total horizontal solar irradiance, are shown in Figs. 5.4–5.6, respectively.

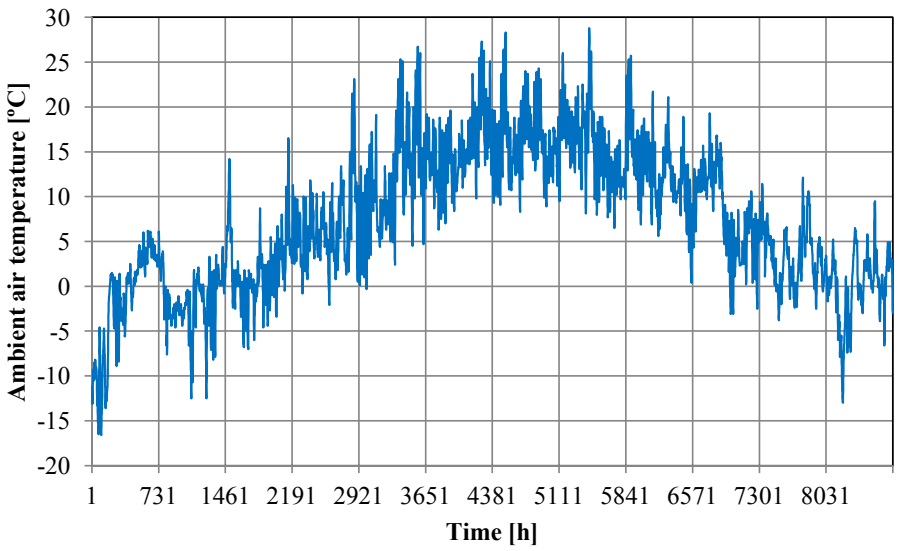

Figure 5.4: Hourly averaged ambient air temperature (one year time period) [164]

The term of ambient air temperature is related to the dry bulb temperature (DBT), which is measured by a thermometer exposed to the air, but shielded from the radiation and moisture. According to [164], the minimum and maximum ambient air temperature for specified location is -16.6 °C and 28.8 °C, respectively, whereas the annual average ambient air temperature is 7.3 °C. The maximum and annual average wind speed is 16 m/s and 3.16 m/s, respectively. The maximum and annual average total horizontal solar irradiance are 907.1 W/m^2 and 102.8 W/m^2, respectively. The annual solar irradiation on the horizontal plane is 900 kWh/m^2 per year, whereas the average daily solar irradiation is 8.88 MJ/m^2 per day. The total number of daytime hours (when $I > 0$ W/m^2) is 4063 hours. One should notice, that the amount of incident solar radiation on the specified surface is dependent on its orientation and tilt angle. Since every solar system should operate with the maxi-

mum performance, it is necessary to optimize both orientation and tilt angle of the collector's surface.

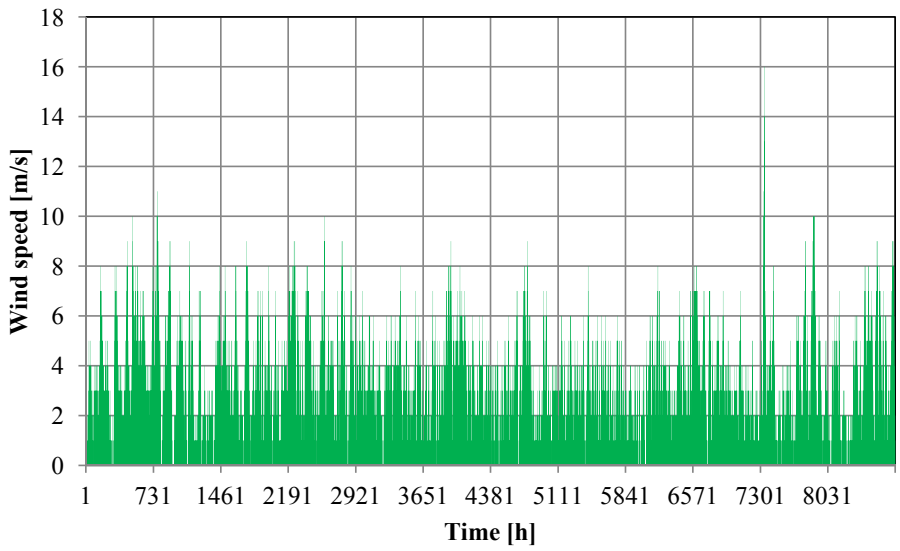

Figure 5.5: Hourly averaged wind speed (one year time period) [164]

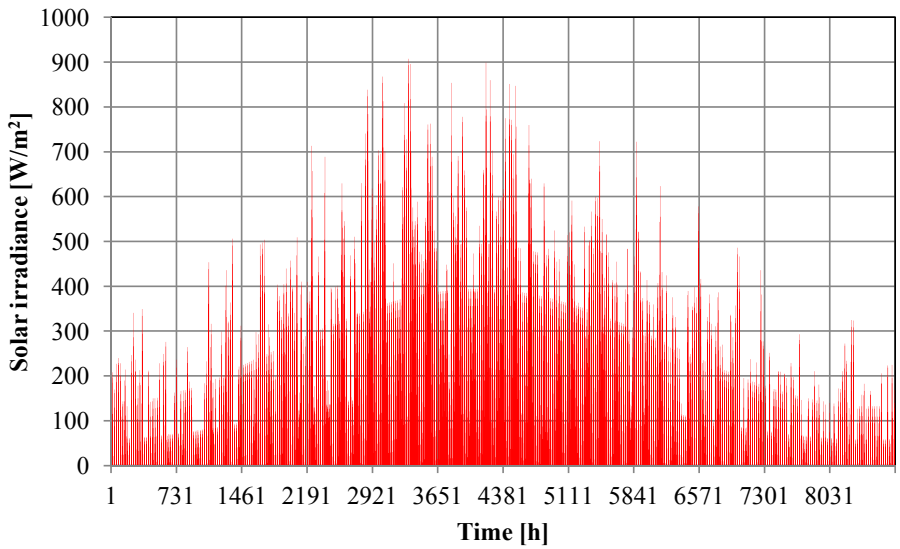

Figure 5.6: Total horizontal solar irradiance (one year time period) [164]

In general, solar systems in the northern hemisphere are south faced [72]. However, according to Felske [62] each orientation within 20° off-south is acceptable. More complicated is to determine the optimum tilt angle of a solar collector, β_{opt}, that can vary in dependence on the latitude of its location and the day of year [72]. There is a number of studies that were carried out by various researchers in order to determine the optimum tilt angle for solar systems. Hottel [83] estimated that

$\beta_{opt} = \phi_l + 20\,°$, Lof and Tybout [113] suggested that $\beta_{opt} = \phi_l + (10 \rightarrow 30\,°)$, Kern and Harris [97] concluded that $\beta_{opt} = \phi_l + 10\,°$, while Hyewood [86] pointed that $\beta_{opt} = \phi_l - 10\,°$, where ϕ_l is the latitude of the specified location. Some researchers suggested two values for the optimum tilt angle, one for summer and one for winter. According to Yellott [183] $\beta_{opt} = \phi_l \pm 20\,°$, while Lewis [111] suggested that $\beta_{opt} = \phi_l \pm 8\,°$, where plus and minus signs are used to indicate winter and summer, respectively. Several studies reported that the optimum tilt angle is very close to the latitude [69, 158].

The climate database [164] contains the pre-calculated values of the average incident solar radiation, I, for each hour of the day for surfaces of a different orientation and angle of inclination. Fig. 5.7 demonstrates the variation of the annual total solar irradiation versus the surface orientation and inclination angle. As can be seen from

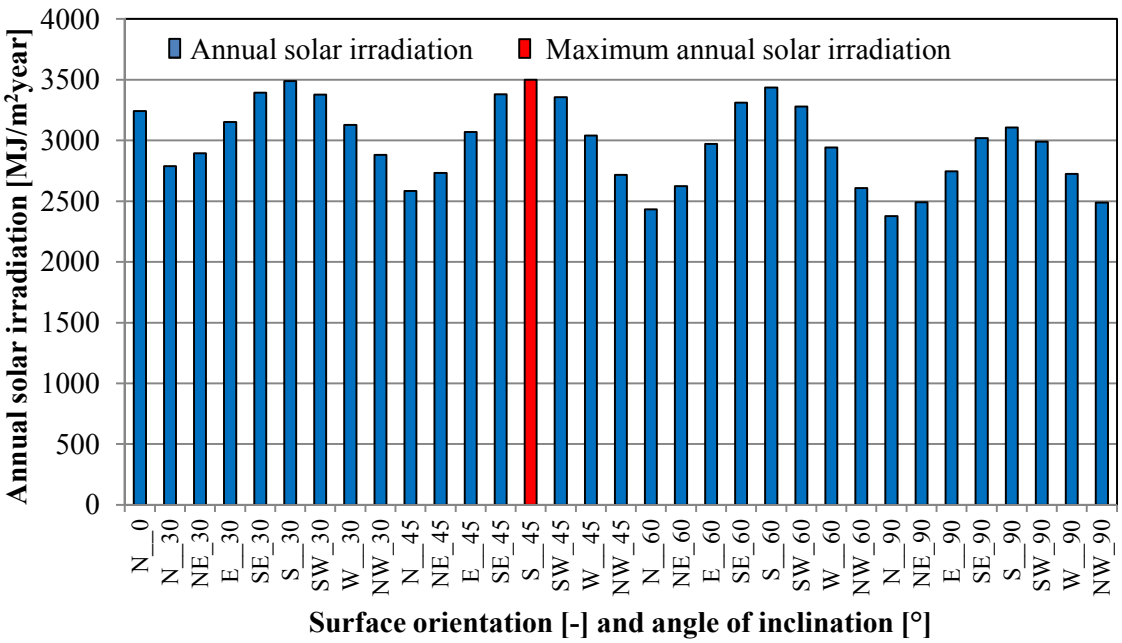

Figure 5.7: Annual solar irradiation versus surface orientation and inclination angle [164]

the graph, the maximum annual solar irradiation refers to the south-oriented surface inclined at angle of 45 °. Taking into account the latitude of Elbląg 54°167′N, the obtained directions for an optimum configuration do not agree with most of the aforementioned approaches [69, 83, 97, 113, 158, 183]. This analysis clearly indicates that in reality, both the orientation and inclination angle of the collector absorber should be estimated with respect to climate conditions of specified locations. In this study, it was assumed that HSC is south-facing and inclined at the angle of 45 °, that is the optimum configuration for meteorological conditions in Elblag [164]. The

variation of the daily solar irradiation on the south-oriented surface inclined at angle of 45 ° is shown in Fig. 5.8. The minimum and maximum daily solar irradiation on the considered surface is 0.93 MJ/m^2 per day and 28.09 MJ/m^2 per day, whereas the average daily solar irradiation is 8.88 MJ/m^2 per day.

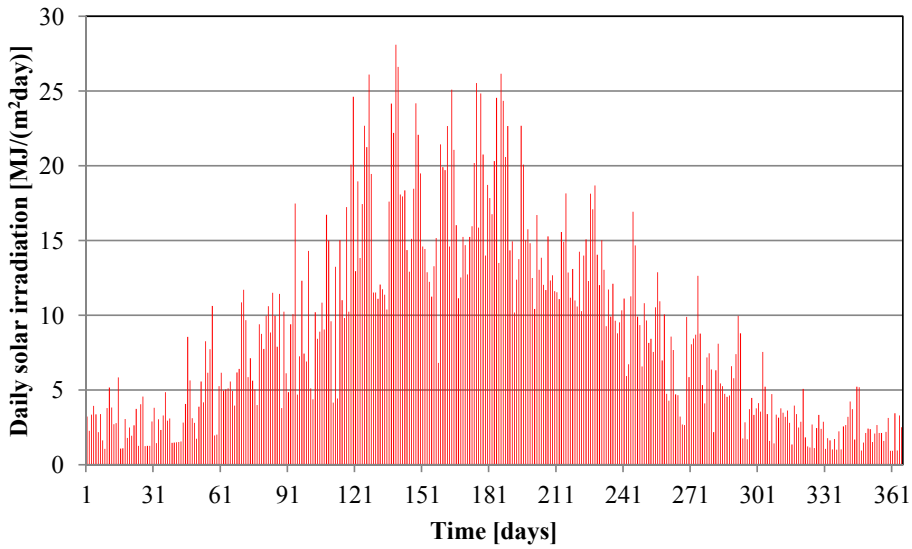

Figure 5.8: Variation of daily solar irradiation on south-oriented surface inclined at angle of 45 ° [164]

5.2 CFD model

5.2.1 Introduction

The Finite Volume Method (FVM) was applied to solve the problem of three-dimensional steady-state heat transfer in CFD model of HSC. The geometry of the model (Figs. 5.9 and 5.10) apply several modification when compared to the one for the FE model (Figs. 5.2 and 5.3). All the changes, discussed later on, are intended to better reflect the heat transfer process in HSC. The CFD model considers the following heat transfer mechanisms:

- convective and radiative heat exchange between the external surface of HSC and outdoor environment, wherein:
  - heat losses from an external surface of the absorber due to thermal emittance are neglected. It should be noticed, however, that in reality the thermal emittance from the roof surface, which determines the radiative heat exchange with the sky, is an important factor (particularly in low wind conditions) influencing the roof temperature [161],

- conductive heat transfer within the solid layers of HSC, wherein:
  - thermo-physical parameters of each solid layer are isotropic and temperature-independent (Table 5.1),
- convective heat exchange in the air-cavity of HSC, wherein:
  - in contrast to FE model (Figs. 5.2 and 5.3), the geometry of CFD model contains the grooves (5 mm height) under the battens (Figs. 5.9 and 5.10), thus an influence of the air movement within the ventilated roof structure on the heat exchange is considered,
  - convection is, however, limited to buoyancy-driven airflow caused by temperature gradients. The wind effect on the air movement in the air-cavity is neglected,
  - air is treated as a compressible, viscous and Newtonian fluid,
  - thermal conductivity and density of the air layer are temperature-dependent, whereas a specific heat is isotropic,
- convective heat transfer within the water flowing through the pipes, wherein:
  - forced, natural or mixed convective heat exchange is considered in dependence on prescribed boundary conditions,
  - laminar flow regime is assumed,
  - additionally, when compared to FE model (Section 5.1.1), segments of water domain at the inlets and outlets from the collector pipes are modeled to provide stable and reliable solution of the fluid flow by reducing an influence of transitional zone on the laminar water flow in the pipes. The outlet pipe region was prolonged in a distance of 15 pipe diameters in order to improve the convergence behavior of the CFD computations since a backflow may begin to appear in the outlet region, when a short outlet pipe is used [116]. The length of additional water segment at the inlet to collector equals to a number of 15 pipe diameters. Hence, the flow profile can be regarded as fully developed before the heated region (central segment of water sub-domain) for entire range of water velocity magnitudes considered in this study,
  - water is treated as a compressible, viscous and Newtonian fluid,
  - thermo-physical parameters of water are temperature-dependent,

- convective and radiative heat exchange between the internal collector surface and building indoor.

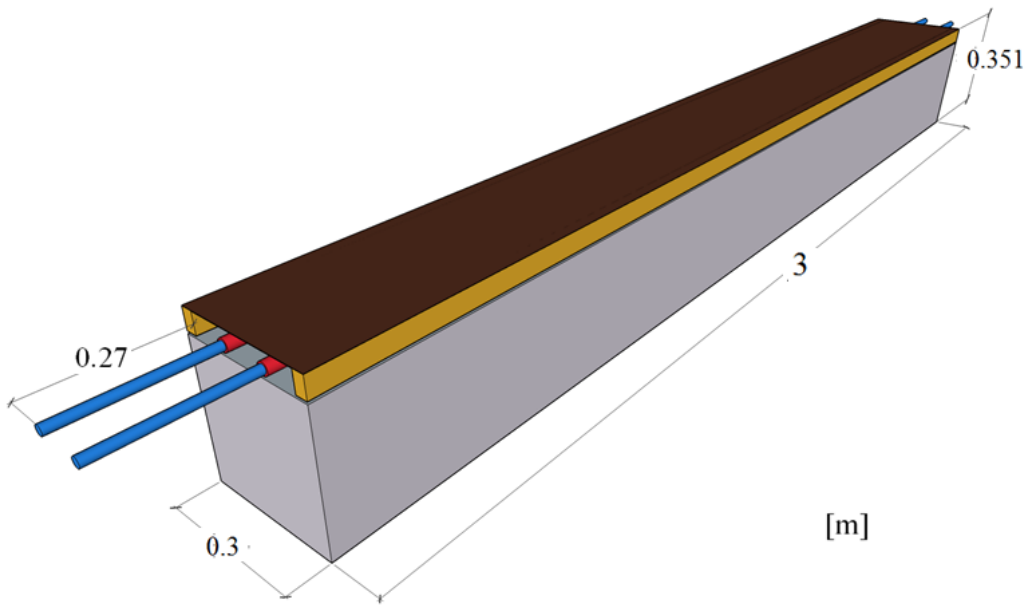

Figure 5.9: Geometry of 3D HSC model for CFD analysis

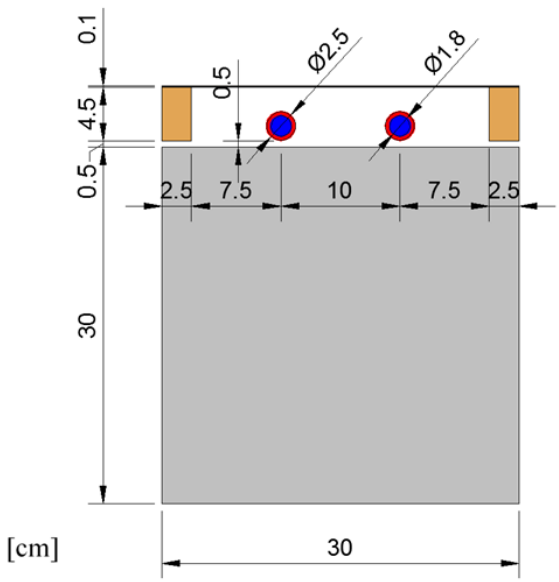

Figure 5.10: Cross-section of HSC model for CFD analysis

The radiative heat exchange between the pipes and surfaces composing the air-cavity is neglected in the CFD model. Its influence on the relationships to be determined is balanced by the boundary conditions assumed for the purpose of CFD

analyses (Section 5.2.5). Such an approach is reasonable since it reduces the time of each numerical simulation. With regard to above-mentioned physical assumptions, the following sub-sections presents the mathematical model of steady-state heat transfer process considered in the CFD model of HSC. The necessary steps for an implementation of the numerical model, from a discretization of the computational domain to a validation process, among the others considerations, are widely described.

5.2.2 Mathematical formulation

In general, the model of HSC can be divided into 3 computational sub-domains, including the sub-domains of water flowing through the pipes, air in the cavity and solid bodies (Fig. 5.11). In the developed CFD model, both sub-domain of air and water are treated as a compressible, viscous and Newtonian fluids. The air state variables obey the perfect gas law.

In the following, the equations of mass, momentum and energy conservation in a stationary frame are presented in the vector form. For turbulent flows, the instantaneous equations are averaged leading to additional terms. These terms, together with models for them, are discussed later on. The initial and boundary conditions used to complete the transport equations are described.

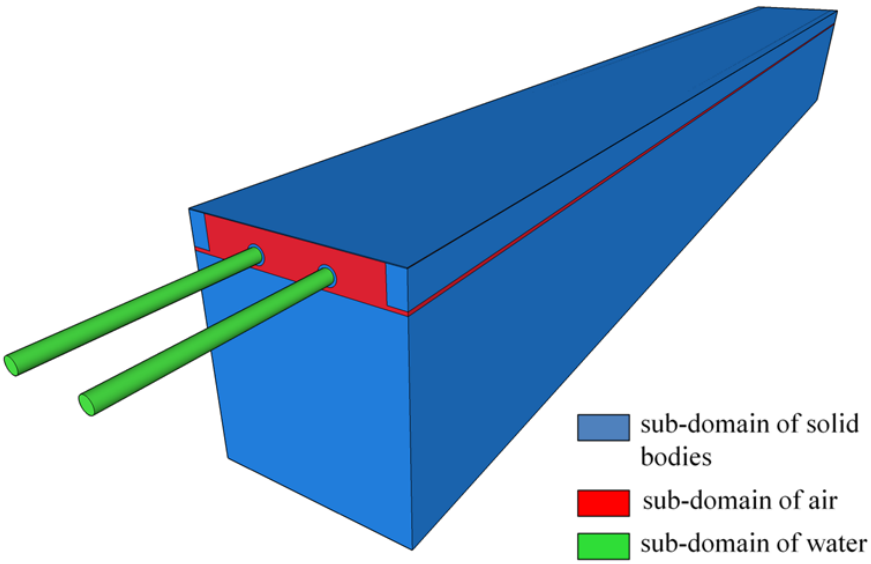

Figure 5.11: Division of computational domain with respect to heat transfer mechanisms considered in CFD analysis

5.2.2.1 Model of water flow through pipes of collector

The model of water flow through the collector's pipes is governed by the Navier-Stokes equations of momentum conservation together with the equations of mass and energy conservation. In the present model, the water is treated as a compressible, viscous and Newtonian fluid.

The Navier-Stokes equations are obtained by applying Newton's second law of motion to a fluid particle. Due to Newton's second law, the rate of fluid particle's momentum change equals the sum of surface forces and body forces acting on a particle. The surface forces include pressure and viscous forces, whereas body forces may exist e.g. according to the presence of a force field (e.g. gravitational, electromagnetic). The general form of momentum equations is [6]:

$$\frac{\partial\left(\rho\mathbf{U}\right)}{\partial t}+\nabla\cdot\left(\rho\mathbf{U}\otimes\mathbf{U}\right)=-\nabla p+\nabla\cdot\boldsymbol{\tau}+\mathbf{S_M}, \tag{5.2.1}$$

where ρ is the density, $\mathbf{U}$ is the vector of water velocity $\mathbf{U}\left(x,y,z\right)$, t is the time, $\nabla\cdot$ is the divergence operator, $\otimes$ is the dyadic operator, ∇ is the gradient operator, p is the thermodynamic pressure, $\boldsymbol{\tau}$ is the stress tensor and $\mathbf{S_M}$ is a body force vector acting on the fluid. The divergence operator of $\mathbf{U}$ is defined by:

$$\nabla\cdot\mathbf{U}=\frac{\partial u_x}{\partial x}+\frac{\partial u_y}{\partial y}+\frac{\partial u_z}{\partial z}. \tag{5.2.2}$$

The dyadic operator of two vectors, $\mathbf{U}$ and $\mathbf{U}$, is defined by:

$$\mathbf{U}\otimes\mathbf{U}=\begin{bmatrix} u_xu_x & u_xu_y & u_xu_z \\ u_yu_x & u_yu_y & u_yu_z \\ u_zu_x & u_zu_y & u_zu_z \end{bmatrix}. \tag{5.2.3}$$

The gradient of $p\left(x,y,z\right)$ is defined by:

$$\nabla p=\frac{\partial p}{\partial x}\mathbf{i}+\frac{\partial p}{\partial y}\mathbf{j}+\frac{\partial p}{\partial z}\mathbf{k}, \tag{5.2.4}$$

where $\mathbf{i}$, $\mathbf{j}$ and $\mathbf{k}$ are unit vectors in the Cartesian coordinate system.

For a Newtonian fluid, viscous stress is proportional to the rate of deformation [173]. Assuming that the fluid obeys the Newton's law of viscosity, the term $\boldsymbol{\tau}$ in Eq. 5.2.1 is related to the strain rate by [6]:

$$\boldsymbol{\tau} = \mu \left(\nabla \mathbf{U} + (\nabla \mathbf{U})^T - \frac{2}{3} \boldsymbol{\delta} \nabla \cdot \mathbf{U} \right), \tag{5.2.5}$$

where μ is the dynamic viscosity and $\boldsymbol{\delta}$ is the Kronecker Delta function:

$$\boldsymbol{\delta} = \begin{bmatrix} 1 & 0 & 0 \\ 0 & 1 & 0 \\ 0 & 0 & 1 \end{bmatrix}. \tag{5.2.6}$$

The present model of water flow obeys the conservation of mass equation. The equation ensures that the total mass of fluid is conserved, or, in other words, the total mass of a fluid system is completely accounted for. For a compressible single-phase fluid flow the conservation of mass equation is given as [6]:

$$\frac{\partial \rho}{\partial t} + \nabla \cdot (\rho \mathbf{U}) = 0. \tag{5.2.7}$$

The energy equation is derived from the first law of thermodynamics, which states that the rate of change of energy of a fluid particle is equal to the rate of heat added to the fluid particle together with the rate of work done on the particle.
The conservation of energy equation is defined as [6]:

$$\frac{\partial (\rho E)}{\partial t} + \nabla \cdot (\rho E \mathbf{U}) = -\nabla \cdot (\rho \mathbf{U}) + \nabla \cdot (\lambda \nabla T) + \nabla \cdot (\mathbf{U} \cdot \boldsymbol{\tau}) + \mathbf{S_E}, \tag{5.2.8}$$

where E is the specific energy of a fluid defined as the sum of internal (thermal) energy, e, and kinetic energy, $\frac{1}{2}\left(u_x^2 + u_y^2 + u_z^2\right)$, λ is the thermal conductivity, T is the temperature and $\mathbf{S_E}$ is the energy source.

In the present model of water flow, the energy conservation is ensured by the implementation of the conservation of enthalpy equation, which is equivalent to Eq. 5.2.8. Based on the relation:

$$h_{tot} = h + \frac{1}{2}\mathbf{U}^2, \tag{5.2.9}$$

where h_{tot} is the total enthalpy and $h\,(T, p)$ is the static enthalpy defined as:

$$h = e + \frac{p}{\rho}, \tag{5.2.10}$$

the total enthalpy equation is formulated as follows [6]:

$$\frac{\partial\left(\rho h_{tot}\right)}{\partial t}-\frac{\partial p}{\partial t}+\nabla\cdot\left(\rho\mathbf{U}h_{tot}\right)=\nabla\cdot\left(\lambda\nabla T\right)+\nabla\cdot\left(\mathbf{U}\cdot\boldsymbol{\tau}\right)+\mathbf{U}\cdot\mathbf{S_M}+\mathbf{S_E}, \quad (5.2.11)$$

where the term $\nabla\cdot(\mathbf{U}\cdot\boldsymbol{\tau})$ represents the work due to viscous stresses and is called the viscous work term. It models the internal heating by viscosity in the fluid. Since the considered velocities of water flow through the collector's pipes are low (not exceeding 0.02 m/s), it is reasonable to neglect it. The term $\mathbf{U}\cdot\mathbf{S_M}$ in Eq. 5.2.11 represents the work due to external momentum sources and is neglected as well. Consequently, the Eq. 5.2.11 takes the form:

$$\frac{\partial\left(\rho h_{tot}\right)}{\partial t}-\frac{\partial p}{\partial t}+\nabla\cdot\left(\rho\mathbf{U}h_{tot}\right)=\nabla\cdot\left(\lambda\nabla T\right)+\mathbf{S_E}. \quad (5.2.12)$$

In dependence on HSC application, the magnitude of water temperature is expected to vary within the range from 20 °C to 80 °C, where 20 °C is the technical minimum limit (Section 5.5). Hence, the water properties can vary in time and influence the flow characteristic. In the present model, the constitutive equations of state, required to form a closed system of equations describing flow and heat transfer in a compressible fluid, are assumed to be dependent on temperature only [116], where:

$$\rho\left(T\right)=-0.003284948\cdot T^2+1.687644\cdot T+785.6677, \quad (5.2.13)$$

$$C_p\left(T\right)=-8.54235\cdot 10^{-5}\cdot T^3+0.09488036\cdot T^2-34.2228\cdot T+8212.82, \quad (5.2.14)$$

and the equation of state for enthalpy is [6]:

$$dh=C_p dT+\left[v-T\left.\frac{\partial v}{\partial T}\right|_p\right]dp, \quad (5.2.15)$$

where C_p is the specific heat and $v=\frac{1}{\rho}$.

Eq. 5.2.13 and Eq. 5.2.14 are thermodynamically consistent what means that mathematical properties for exact differentials are satisfied. Applying this concept to Eq. 5.2.15, general equations of state obeys [6]:

$$\frac{\partial C_p}{\partial p}=\frac{\partial}{\partial T}\left(v-T\left.\frac{\partial v}{\partial T}\right|_p\right). \quad (5.2.16)$$

To avoid pressure-velocity decoupling in the discrete mass flow through a surface of the control volume, Rhie and Chow [141] method modified by Majumdar [115] is employed to remove the dependence of the steady-state solution on each iteration.

The water mass flux (rate of mass flow per unit area), $\dot{m}$, in the pipes of HSC is technically limited into the range from $0\,\mathrm{kg/(m^2{\cdot}s)}$ to $19.0\,\mathrm{kg/(m^2{\cdot}s)}$. The transition from laminar to turbulent flow is defined by a magnitude of Reynolds Number:

$$\mathrm{Re} = \frac{\bar{u}L}{\nu}, \tag{5.2.17}$$

where $\bar{u}$ is the average fluid velocity, L is the characteristic length scale (equal to inner pipe diameter d_i), and ν is the kinematic viscosity. For a pipe of inner diameter, equal to $d_i = 0.018\,\mathrm{m}$, the expected maximum water temperature in the collector's pipes equal to $80\,^\circ\mathrm{C}$, the corresponding parameters of water ($\nu = 0.000000365\,\mathrm{m^2/s}$ [181] and $\rho = 971.8\,\mathrm{kg/m^3}$ [181]) and the upper limit of water mass flux, equal to $\dot{m} = 19\,\mathrm{kg/(m^2{\cdot}s)}$, it is:

$$\bar{u} = \frac{\dot{m}}{\rho} = \frac{19}{971.8} = 0.0195\,\mathrm{m/s}. \tag{5.2.18}$$

Thus, the Reynolds Number is

$$\mathrm{Re} = \frac{0.0195 \cdot 0.018}{0.000000365} = 961.64\,[-].$$

The laminar flow regime in pipes occurs when $\mathrm{Re} < 2300$ [159]. Thus, the laminar flow regime is to be considered in the present model of water flow. In general, the water near the pipe wall, due to its higher temperature and lower density, circulates upward, whereas the water near the central region of the pipe, having a lower temperature and a higher density, circulates downward. Thus, it can be expected that in the laminar flow regime buoyancy effect cannot be ignored. The relative importance of buoyancy forces due to temperature variations in a laminar water flow through the collector's pipes can be estimated by using the ratio of Grashof and Reynolds number:

$$\frac{\mathrm{Gr}}{\mathrm{Re}^2} = \frac{g\beta L\Delta T}{\bar{u}^2}, \tag{5.2.19}$$

where g is the gravity acceleration, β is the thermal expansion coefficient [181], L is the characteristic length [m] (equal to inner pipe diameter d_i) and ΔT is the characteristic water temperature differences in cross-section plane. A value approaching

or exceeding unity indicates that buoyancy effects are significant in the flow, while small values indicate that buoyancy effects can be ignored. For the predicted maximum difference of water temperatures (in cross-section plane) equal to 1 °C, the ratio:

$$\frac{\mathrm{Gr}}{\mathrm{Re}^2} = \frac{9.81 \cdot 0.000632 \cdot 0.018 \cdot 1}{0.0195^2} = 0.29\,[-],$$

is less than the unity. The above formulation is, however, appropriate for a case when the water temperature reaches 80 °C. Such a condition is expected to occur only if the target of the collector application is to support domestic hot water system. The major aim of this study is to evaluate the ability of HSC to supply space-heating systems based on seasonal heat storage systems. For this application the maximum water temperature is expected to be less than 35 °C (Section 6.2.1). With regard to corresponding water parameters, the ratio of Grashof and Reynolds number is:

$$\frac{\mathrm{Gr}}{\mathrm{Re}^2} = \begin{cases} \geq & 1 \text{ for } \dot{m} \leq 8\,\mathrm{kg}/\left(\mathrm{m}^2 \cdot \mathrm{s}\right) \\ < & 1 \text{ for } \dot{m} > 8\,\mathrm{kg}/\left(\mathrm{m}^2 \cdot \mathrm{s}\right) \end{cases}. \tag{5.2.20}$$

Thus, the buoyancy effects must be taken into account in the model of water flow. Metais and Eckert [119] investigated experimentally fluid flows through horizontal pipes in different regimes. They presented the map of flow regimes for horizontal pipes (Fig. 5.12). For the characteristic numbers of water (appropriate for water temperature of 80 °C) and the pipes length in the collector section equal to $l_p = 3\,\mathrm{m}$, the expected parameters of the water flow in the pipes are:

$$\mathrm{Gr} = \frac{q\beta \mid \Delta T \mid d_i^3}{\nu^2} = \frac{9.81 \cdot 0.000632 \cdot 1 \cdot 0.018^3}{0.000000365^2} = 2.71 \cdot 10^5\,[-], \tag{5.2.21}$$

$$\mathrm{Pr} = \frac{\nu C_p \rho}{\lambda} = \frac{0.000000365 \cdot 4195 \cdot 971.8}{0.674} = 2.21\,[-], \tag{5.2.22}$$

$$\frac{\mathrm{Gr}\mathrm{Pr} d_i}{l_p} = \frac{2.71 \cdot 10^5 \cdot 2.21 \cdot 0.018}{3} = 3593.46\,[-], \tag{5.2.23}$$

and $\mathrm{Re} = 961.64\,[-]$. According to Fig. 5.12, the water flow in collector pipes is to be considered as forced convection and laminar flow. However, for the magnitude of water mass flux lower than $3\,\mathrm{kg}/(\mathrm{m}^2{\cdot}\mathrm{s})$, the mixed convection laminar flow occurs. Thus, the Full Buoyancy model is employed, and $\rho - \rho_{ref}$ in Eq. 5.2.24 is evaluated directly, where ρ_{ref} is a constant reference density assumed as $\rho_{ref} = 998.2\,\mathrm{kg}/\mathrm{m}^3$

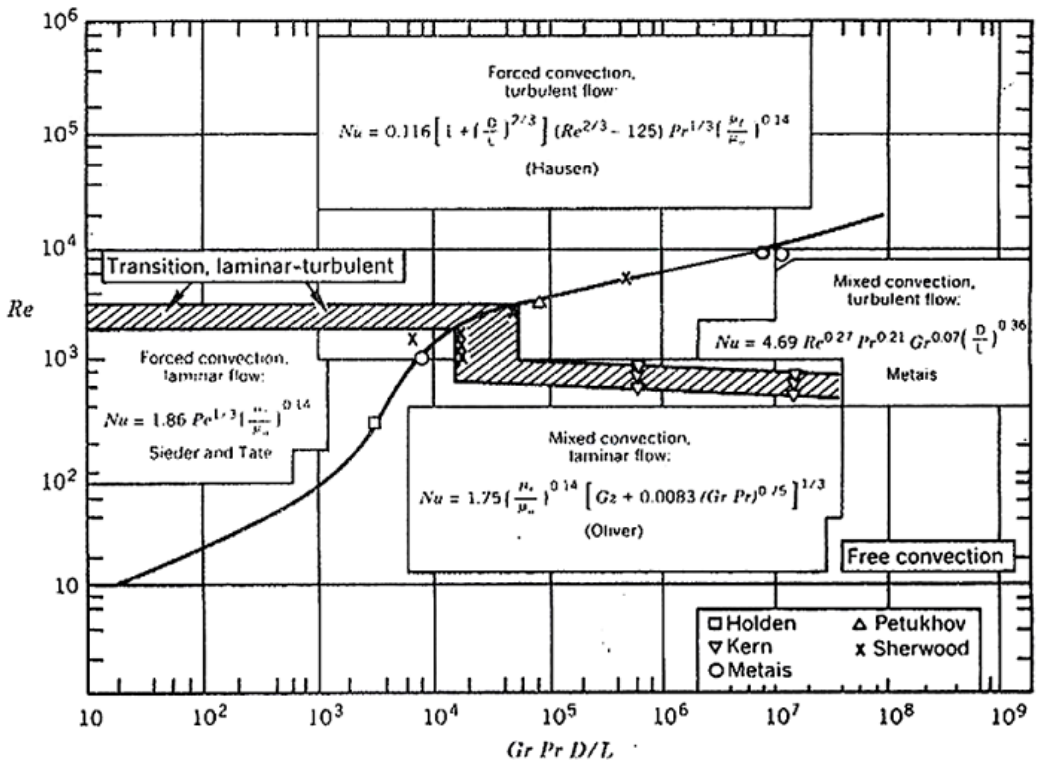

Figure 5.12: Flow regimes map for horizontal pipes by Metais and Eckert [119]

(magnitude appropriate for water temperature equal to 20 °C [181]). For buoyancy calculations, a source term added to the momentum equations (Eq. 5.2.1) is given as follows [6]:

$$\mathbf{S}_{\mathbf{M,buoy}} = (\rho - \rho_{ref})\,\mathbf{g}, \tag{5.2.24}$$

where $\mathbf{g}$ is a gravity vector. Consequently, the momentum equation for the model of water flow in the collector's pipes is:

$$\frac{\partial\,(\rho\mathbf{U})}{\partial t} + \nabla\cdot(\rho\mathbf{U}\otimes\mathbf{U}) = -\nabla p + \mathbf{S}_{\mathbf{M,buoy}}. \tag{5.2.25}$$

The pressure in the momentum equation (Eq. 5.2.25) excludes the hydrostatic gradient due to ρ_{ref}. This pressure is related to the absolute pressure as follows [6]:

$$p_{abs} = p + p_{ref} + \rho_{ref}\vec{g}\,(\vec{r} - \vec{r}_{ref})\,, \tag{5.2.26}$$

where $\vec{r}_{ref}$ is a reference location.

5.2.2.2 Model of airflow in roof cavity

In the developed CFD model, the air is treated as a compressible, viscous and Newtonian fluid. The airflow in the roof cavity obeys the conservation of mass equation given as Eq. 5.2.7. When compared to water flow, an alternative form of the energy equation, which is suitable for low-speed flows of compressible gases [6], is employed. It is called the thermal energy equation and is derived by subtracting the mechanical energy from the total energy equation. To do so, first, the mechanical energy equation is derived by taking the dot product of $\mathbf{U}$ with the momentum equation (Eq. 5.2.1) [6]:

$$\frac{\partial\left(\rho K\right)}{\partial t}+\nabla\cdot\left(\rho\mathbf{U}K\right)=-\mathbf{U}\cdot\nabla p+\mathbf{U}\cdot\left(\nabla\cdot\boldsymbol{\tau}\right)+\mathbf{U}\cdot\mathbf{S}_{\mathbf{M}}, \tag{5.2.27}$$

where K is kinetic energy given as:

$$K=\frac{1}{2}\mathbf{U}^2, \tag{5.2.28}$$

and next, subtracting Eq. 5.2.27 from the total energy equation (Eq. 5.2.11) yields the thermal energy equation [6]:

$$\frac{\partial\left(\rho h\right)}{\partial t}-\frac{\partial p}{\partial t}+\nabla\cdot\left(\rho\mathbf{U}h\right)=\nabla\cdot\left(\lambda\nabla T\right)+\mathbf{U}\cdot\nabla p+\boldsymbol{\tau}:\nabla\mathbf{U}+\mathbf{S}_{\mathbf{E}}. \tag{5.2.29}$$

The term $\boldsymbol{\tau}:\nabla\mathbf{U}$ is always positive and is called the viscous dissipation. It models the internal heating by viscosity in the fluid. In case of low-speed airflows, the viscous dissipation has an insignificant effect, thus it is reasonable to neglect it [7]. In consequence, the assumed energy equation is:

$$\frac{\partial\left(\rho h\right)}{\partial t}-\frac{\partial p}{\partial t}+\nabla\cdot\left(\rho\mathbf{U}h\right)=\nabla\cdot\left(\lambda\nabla T\right)+\mathbf{U}\cdot\nabla p+\mathbf{S}_{\mathbf{E}}. \tag{5.2.30}$$

Based on the literature data concerning the ventilated roof structures [64], it was found that the superficial temperature of the roof can reach values between 75 °C and 80 °C . Hence, it can be concluded that the air properties can vary significantly and influence the flow characteristic. However, in opposition to the water flow in pipes, the constitutive equations of state for an ideal gas are assumed. Density is calculated from the Ideal Gas law [6]:

$$\rho = \frac{w p_{abs}}{R_0 T}, \tag{5.2.31}$$

where w is molecular weight ($w = 28.96\,\mathrm{kg/kmol}$), p_{abs} is absolute pressure, and R_0 is universal gas constant ($R_0 = 8.314462\,\mathrm{J/(mol \cdot K)}$).
The specific heat C_p for air is assumed to be constant ($C_p = 1004.4\,\mathrm{J/(kg \cdot K)}$), thus [6]:

$$dh = C_p dT. \tag{5.2.32}$$

Now, the momentum equation for airflow in the roof cavity can be expressed:

$$\frac{\partial (\rho \mathbf{U})}{\partial t} + \nabla \cdot (\rho \mathbf{U} \otimes \mathbf{U}) = -\nabla p + \nabla \cdot \boldsymbol{\tau} + (\rho - \rho_{ref})\,\mathbf{g}, \tag{5.2.33}$$

where constant reference density of air is assumed as $\rho_{ref} = 1.168\,\mathrm{kg/m^3}$.

Even though air velocity in the air cavity of the solar collector is rather small, the air cavity is complex in shape and the flow is not free and uniform in its regime. The pipes located in the cavity additionally influence the flow characteristics. Considering a heat exchange process, the airflow in the cavity has to be analyzed in two aspects: the airflow around the pipes (characterized by $\mathrm{Re_{dp}}$) and the airflow in the dominant flow direction (characterized by Re). Thus, two Reynolds Numbers are considered [181]:

$$\mathrm{Re_{dp}} = \frac{u_{a,\infty} d_o}{\nu}, \tag{5.2.34}$$

$$\mathrm{Re} = \frac{u_{a,c} L}{\nu}, \tag{5.2.35}$$

where $u_{a,\infty}$ is the air velocity out of the pipe in the dominant flow direction, $u_{a,c}$ is the air velocity in the dominant flow direction, d_o is the outer diameter of a pipe and L is characteristic dimension equal to the cavity length in the flow direction, l_c. The initial simulations showed that maximum magnitudes are $u_{a,\infty} = 0.17\,\mathrm{m/s}$ and $u_{a,c} = 0.79\,\mathrm{m/s}$. Thus, for the pipes outer diameter $d_o = 0.025\,\mathrm{m}$ and the cavity length $l_c = 0.25\,\mathrm{m}$, the considered Reynolds Numbers are:

- $\mathrm{Re_{dp}} = 217.9\,[-]$,
- $\mathrm{Re} = 10015.6\,[-]$.

Turbulence occurs when the inertia forces in the fluid become significant compared to viscous forces, and is characterized by a high Reynolds number. According to

the magnitude of Reynolds Number and complicate geometry of the air-cavity in HSC, the flow regime is expected to be turbulent rather than laminar. Thus, turbulent airflow regime is assumed. In general, the turbulent flow is characterized by a chaotic motions of molecules along complex irregular paths. Turbulence fluctuations have a three-dimensional character [173]. In the turbulent flow, there is always plenty of rotational flows, called eddies. The eddies characterize with diverse dimensions. In other words, a wide range of length scales can be observed. The smallest turbulence length scales, observed in a standard engineering flow, can be hundredths of a millimeter. For these length scales, viscous forces are of the same order of magnitude as inertial forces (the Reynolds Number equals to 1). In these length scales, the kinetic energy of the flow is dissipated into the internal energy.

In principle, the Navier-Stokes equations model properly both laminar and turbulent flows without the need for additional information [163]. However, modeling of turbulent flows using the complete time-dependent Navier-Stokes equations is computationally-time-expensive. Both space and time discretizations are to be fine enough to resolve all rapid oscillations and chaotic motions at large range of scales. Such an approach to solve the Navier-Stokes equations is called Direct Numerical Simulation (DNS). At present, DNS is, however, computationally too demanding for routine engineering applications. Modeling turbulent flows at realistic Reynolds Numbers would generally involve length scales much smaller than the smallest finite volume mesh (grid), which can be practically used in a numerical analysis. To enable the effects of turbulence to be predicted with the usage of the realistic meshes, it is necessary to use some less demanding calculation methods. Usually, an averaged solution of a flow is satisfactory [7]. Two major modeling frameworks aimed at distinct levels of approximation are the Large Eddy Simulation (LES) approach and Reynolds-averaged Navier-Stokes (RANS) approach.

The LES approach is the first level of approximation, where the turbulent large eddies are resolved accurately, whereas the turbulent small-scale eddies are modeled with the usage of a turbulence model. Due to the subgrid-scale turbulence modeling, LES requires significantly less mesh points when compared to DNS approach. The computational power demand of LES varies between the one for DNS and the one for RANS.

The RANS approach introduces the next level of approximation to solve turbulent flows. It is probably the most widely used turbulence modeling approach since its application significantly reduces the computational effort when compared to other approaches. In the present work, CFD analyses include a number of simulations. Thus, the RANS approach is employed to model turbulent airflow in the

cavity of HSC. The approach is based on the concept of a flow variables (velocity and pressure) decomposition into time-averaged and fluctuating parts. For example, a velocity U_i may be divided into a time-average component, $\bar{U}_i$, and a time varying (fluctuating) component, u_i [6]:

$$U_i = \bar{U}_i + u_i, \tag{5.2.36}$$

where the averaged component is given by [6]:

$$\bar{U}_i = \frac{1}{\Delta t} \int_t^{t+\Delta t} U_i dt, \tag{5.2.37}$$

where Δt is the time scale that is large relative to the turbulent fluctuations, but small relative to the time scale to which the equations are solved.

In general, for compressible fluid flows the averaging is weighted by density (so called Favre-averaging). However, according to hypothesis of Morkovin [123, 23], if density fluctuations in turbulent flow are not significant, their influence on turbulent structures is negligible. This is usually true for flow characterized by Mach numbers below 5 [−] [7]. Since the maximum expected air velocities in the cavity of HSC does not exceed 1 m/s, it is assumed that density fluctuations due to turbulences are negligible in the present model. Thus, substituting the averaged quantities into the assumed transport equations (Eq. 5.2.7, 5.2.30, 5.2.33) and dropping the bars for averaged quantities (except for products of fluctuating quantities) result in the so-called Reynolds-averaged Navier-Stokes (RANS) equations (in tensor notation) [6]:

$$\frac{\partial p}{\partial t} + \frac{\partial}{\partial x_j} (\rho U_j) = 0, \tag{5.2.38}$$

$$\frac{\partial \rho U_i}{\partial t} + \frac{\partial}{\partial x_j} (\rho U_i U_j) = -\frac{\partial p}{\partial x_i} + \frac{\partial}{\partial x_j} (\tau_{ij} - \rho \overline{u_i u_j}) + (\rho - \rho_{ref}) \mathbf{g}, \tag{5.2.39}$$

where τ_{ij} is the molecular stress tensor (including both normal and shear components of the stress). Comparing to non-modified momentum equation (Eq. 5.2.33), the Reynolds-average momentum equation (Eq. 5.2.39) contains a new term, known as the Reynolds stresses, $\rho \overline{u_i u_j}$. The overbar denotes a time average. The additional term, also called turbulent stresses, is the correlation between the turbulent velocity fluctuations u_i and u_j, and it represents the transport of momentum in the mean flow due to turbulence.

The Reynolds-averaged energy equation is:

$$\frac{\partial \rho h_{tot}}{\partial t} - \frac{\partial p}{\partial t} + \frac{\partial}{\partial x_j}\left(\rho U_j h_{tot}\right) = \frac{\partial}{\partial x_j}\left(\lambda \frac{\partial T}{\partial x_j} - \rho \overline{u_j h}\right) + S_E, \tag{5.2.40}$$

where $\rho \overline{u_j h}$ is the additional fluctuation term and h_{tot} is the mean total enthalpy defined by:

$$h_{tot} = h + \frac{1}{2} U_i U_i + k. \tag{5.2.41}$$

The last term in Eq. 5.2.41 is the turbulent kinetic energy, given by:

$$k = \frac{1}{2} \bar{u_i}^2. \tag{5.2.42}$$

The additional unknown term in Eq. 5.2.39, introduced by the averaging procedure, is difficult to determine directly. In order to achieve "closed" system of equation, the Reynolds stresses are to be modeled by additional equations of known quantities. These equations define the type of turbulence model. The turbulence models have been specifically developed to account for the effects of turbulence without a resort to use a prohibitively fine mesh and direct numerical simulation. In consequence, the flow resulted with the use of RANS approach is the mean flow and only the effect of the turbulence on the mean flow is known, but not the turbulence itself.

In general, the turbulence models can be divided into two classes: eddy viscosity models and Reynolds stress models. At present, the widely employed approach in modeling of airflow in roof cavities is based on hypothesis that turbulence consists of small eddies which are continuously forming and dissipating, and in which the Reynolds stresses are assumed to be proportional to mean velocity gradients. This defines the so-called eddy viscosity models. The eddy viscosity hypothesis assumes that the Reynolds stresses can be related to the mean velocity gradients and eddy (turbulent) viscosity by the gradient diffusion hypothesis, in a manner analogous to the relationship between the stress and strain tensors in laminar Newtonian flow (in tensor notation) [6]:

$$-\rho \overline{u_i u_j} = \mu_t \left(\frac{\partial U_i}{\partial x_j} + \frac{\partial U_j}{\partial xi}\right) - \frac{2}{3}\delta_{ij}\left(\rho k + \mu_t \frac{\partial U_k}{\partial x_k}\right), \tag{5.2.43}$$

where μ_t is the eddy viscosity (turbulent viscosity). Analogous to the eddy viscosity hypothesis, it can be introduced the eddy diffusivity hypothesis, which states that the Reynolds fluxes of a scalar are linearly related to the mean scalar gradient [6]:

$$-\rho\overline{u_i\varphi} = \Gamma_t \frac{\partial \Phi}{\partial x_i}, \tag{5.2.44}$$

where φ is the general scalar variable, Φ is the additional variable, Γ_t is the eddy diffusivity written as:

$$\Gamma_t = \frac{\mu_t}{\mathrm{Pr_t}}, \tag{5.2.45}$$

where $\mathrm{Pr_t}$ is the turbulent Prandtl Number.

The Eq. 5.2.43 and Eq. 5.2.45 can express turbulent fluctuations in terms of functions of the mean variables only if the turbulent viscosity, μ_t, is known. Subject to these hypotheses, the Reynolds-averaged momentum equation become [6]:

$$\frac{\partial \rho U_i}{\partial t} + \frac{\partial}{\partial x_j}\left(\rho U_i U_j\right) = -\frac{\partial p'}{\partial x_i} + \frac{\partial}{\partial x_j}\left[\mu_{eff}\left(\frac{\partial U_i}{\partial x_j} + \frac{\partial U_j}{\partial x_i}\right)\right] + S_M, \tag{5.2.46}$$

where μ_{eff} is the effective viscosity defined by:

$$\mu_{eff} = \mu + \mu_t, \tag{5.2.47}$$

and p' is the modified pressure, defined by:

$$p' = p + \frac{2}{3}\rho k + \frac{2}{3}\mu_{eff}\frac{\partial U_k}{\partial x_k}. \tag{5.2.48}$$

The last term in the Eq. 5.2.48 involves the divergence of velocity and is neglected in the present model.
The Reynolds-averaged energy equation becomes:

$$\frac{\partial \rho h_{tot}}{\partial t} - \frac{\partial p}{\partial t} + \frac{\partial}{\partial x_j}\left(\rho U_j h_{tot}\right) = \frac{\partial}{\partial x_j}\left(\lambda_{eff}\frac{\partial T}{\partial x_j} + \frac{\mu_t}{\mathrm{Pr_t}}\frac{\partial h}{\partial x_j}\right) + S_E, \tag{5.2.49}$$

where λ_{eff} is the effective thermal conductivity coefficient related to turbulent Prandtl number. The turbulent Prandtl number for air is $0.7\,[-]$ [19]. It is assumed that turbulent Prandtl number is constant in the entire flow field.

Among the eddy viscosity models the two-equation turbulence models are widely used, as they offer a good compromise between numerical effort and computational accuracy [173, 176]. In this study, the two-equation Re-Normalization Group (RNG) $k-\varepsilon$ model [182] is applied since it is capable of accurately modeling the charac-

teristics of airflow and heat transfer within cavities formed by closely spaced heated horizontal plates [48, 170]. The model is identical to the well-known and widely used standard $k-\varepsilon$ model [109], except the values of the transport coefficients [65]. This modification enables to account for the effects of smaller scales of motion. The RNG $k-\varepsilon$ model assumes that the turbulence viscosity, μ_t, is related to the turbulence kinetic energy, k, and its dissipation rate, ε, via the relation [6]:

$$\mu_t = C_{\mu\mathrm{RNG}}\rho\frac{k^2}{\varepsilon}, \tag{5.2.50}$$

where $C_{\mu\mathrm{RNG}}$ is the constant equal to $0.085\,[-]$ [6]. The values of k and ε come directly from the differential transport equations for the turbulence kinetic energy and turbulence dissipation rate [6]:

$$\frac{\partial\left(\rho k\right)}{\partial t} + \frac{\partial}{\partial x_j}\left(\rho U_j k\right) = \frac{\partial}{\partial x_j}\left[\left(\mu + \frac{\mu_t}{\sigma_{k\mathrm{RNG}}}\right)\frac{\partial k}{\partial x_j}\right] + P_k - \rho\varepsilon + P_{kb}, \tag{5.2.51}$$

$$\frac{\partial\left(\rho\varepsilon\right)}{\partial t} + \frac{\partial}{\partial x_j}\left(\rho U_j \varepsilon\right) = \frac{\partial}{\partial x_j}\left[\left(\mu + \frac{\mu_t}{\sigma_{\varepsilon\mathrm{RNG}}}\right)\frac{\partial \varepsilon}{\partial x_j}\right] + \frac{\varepsilon}{k}\left(C_{\varepsilon 1\mathrm{RNG}}P_k - C_{\varepsilon 2\mathrm{RNG}}\rho\varepsilon + C_{\varepsilon 1\mathrm{RNG}}P_{\varepsilon b}\right), \tag{5.2.52}$$

where $\sigma_{k\mathrm{RNG}}$, $\sigma_{\varepsilon\mathrm{RNG}}$, $C_{\varepsilon 2\mathrm{RNG}}$ are constants equal to $0.7179\,[-]$, $0.7179\,[-]$ and $1.68\,[-]$, respectively [6]. The $C_{\varepsilon 1\mathrm{RNG}}$ is represented by the function:

$$C_{\varepsilon 1\mathrm{RNG}} = 1.42 - f_\eta, \tag{5.2.53}$$

where:

$$f_\eta = \frac{\eta\left(1 - \frac{\eta}{4.38}\right)}{\left(1 + \beta_{\mathrm{RNG}}\eta^3\right)}, \tag{5.2.54}$$

$$\eta = \sqrt{\frac{P_k}{\rho C_{\mu\mathrm{RNG}}\epsilon}}. \tag{5.2.55}$$

The term β_{RNG} in Eq. 5.2.54 is constant and equal to $0.012\,[-]$ [6]. Terms P_{kb} in Eq. 5.2.51 and $P_{\varepsilon b}$ in Eq. 5.2.52 represent the influence of the buoyancy forces. The buoyancy production term P_{kb} is given as [6]:

$$P_{kb} = -\frac{\mu_t}{\rho\sigma_p}g_i\frac{\partial\rho}{\partial x_i}, \tag{5.2.56}$$

where σ_p is the turbulence Schmidt number equal to 1 [−]. The term $P_{\varepsilon b}$ is assumed to be proportional to P_{kb} [6]:

$$P_{\varepsilon b} = \max(0,\ P_{kb}) \cdot \sin\gamma, \tag{5.2.57}$$

where γ is the angle between velocity and gravity vector.

The term P_k in Eq. 5.2.51 and Eq. 5.2.52 is the turbulence production due to viscous forces, which is modeled using [6]:

$$P_k = \mu_t \left(\frac{\partial U_i}{\partial x_j} + \frac{\partial U_j}{\partial x_i} \right) \frac{\partial U_i}{\partial x_j} - \frac{2}{3} \frac{\partial U_k}{\partial x_k} \left(3\mu_t \frac{\partial U_k}{\partial x_k} + \rho k \right). \tag{5.2.58}$$

For the compressible flow, $\frac{\partial U_k}{\partial x_k}$ is only large in regions with high velocity divergence, such as at shocks. The term $3\mu_t$ in the Eq. 5.2.58 is based on the "frozen stress" assumption [6]. This prevents the values of k and ε becoming too large through shocks, a situation that becomes progressively worse as the mesh is refined at shocks.

The separate problem to be solved is the airflow near to surfaces forming the air-cavity. The employed approach to model the airflow near to surfaces of solid bodies is discussed later on (Section 5.2.2.4.1).

5.2.2.3 Heat transfer in solid bodies

In solid parts (roofing material, tilling battens, polypropylene pipes and insulation layer), heat transfer is dominated by conduction. Due to the assumptions made for the CFD model of HSC, the energy equation is solved neglecting radiation effects. Thus, the following form of conservation of energy equation is used to account for the heat transfer in solid bodies:

$$\frac{\partial (\rho h)}{\partial t} = \nabla \cdot (\lambda \nabla T). \tag{5.2.59}$$

5.2.2.4 Boundary and initial conditions

The boundary and initial conditions are prescribed for the following variables: temperature $T(\mathbf{x})$, pressure $p(\mathbf{x})$ and velocity $\mathbf{U}(\mathbf{x})$. Each variable is a function of the position $\mathbf{x} = [x, y, z]^T$.

The CFD model of HSC can be divided into 3 computational sub-domains (Fig. 5.11). These are the sub-domains of water flowing through the pipes, air in the cavity and solid bodies. The boundary conditions are described for each sub-domain, separately.

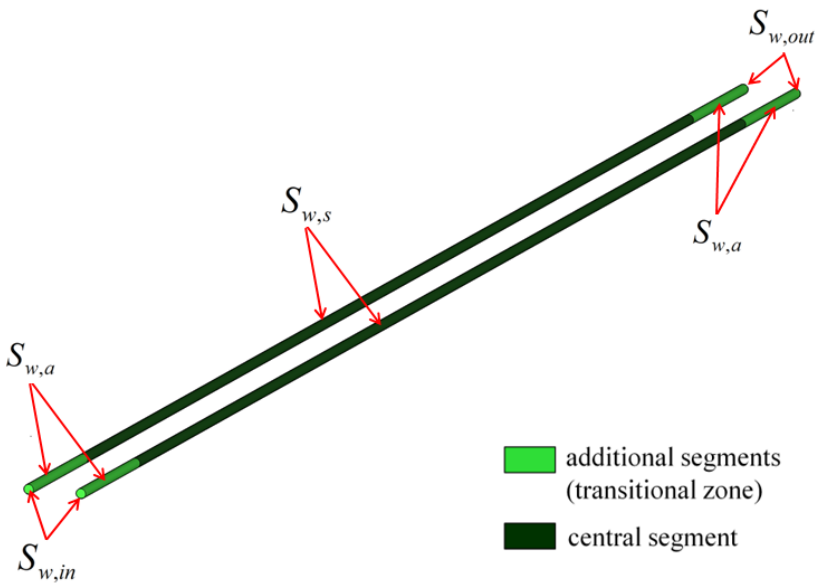

Figure 5.13: Boundary surfaces of water sub-domain in CFD model

The sub-domain of water refers to water-down and water-up models. Both the models are the same in terms of prescribed boundary condition, hence the following equations are referred to a model of water flow in the single pipe. The water flows into the domain across the inlet water surface, $S_{w,in}$, and flows out through the outlet water surface, $S_{w,out}$. At the inlet, a uniform velocity field and a constant pressure gradient equal to zero were imposed. Therefore, the transport equations were completed with the following Dirichlet and Neumann boundary conditions, respectively:

$$\mathbf{n} \cdot \mathbf{U}\left(\mathbf{x}\right)\big|_{S_{w,in}} = u_{w,in}, \tag{5.2.60}$$

$$\left.\frac{\partial p\left(\mathbf{x}\right)}{\partial \mathbf{n}}\right|_{S_{w,in}} = 0, \tag{5.2.61}$$

where $\mathbf{n}$ is the vector normal to inlet water surface $S_{w,in}$, $\mathbf{U}$ is the velocity vector and $u_{w,in}$ is the water flow velocity expressed by the ratio of the water mass flux to the density of the operating fluid (Eq. 5.2.18).

At the outlet, the average static pressure approach is employed and the velocity gradient is set to zero in order to impose the boundary conditions. In this case, the static pressure is allowed to locally vary on the outlet boundary such that the average pressure is constrained. It is applied by comparing the area weighted pressure average over the entire outlet surface to the value of 0 Pa. The pressure profile

at the outlet is shifted by this difference such that the new area weighted pressure average will be equal to 0 Pa. Consequently, the boundary conditions for pressure and velocity at the outlet water surface, $S_{w,out}$, are defined as:

$$\left.\frac{\partial \mathbf{U}(\mathbf{x})}{\partial \mathbf{n}}\right|_{S_{w,out}} = 0, \tag{5.2.62}$$

$$\frac{1}{S_{w,out}} \int_{S_{w,out}} p(\mathbf{x})\, dS_{w,out} = 0. \tag{5.2.63}$$

According to made assumptions (Section 5.5), the water temperature at the inlet water surface is uniform and equal to 20 °C. The Dirichlet boundary condition used to describe the temperature distribution at the inlet water surface, $S_{w,in}$, is given as:

$$T(\mathbf{x})|_{S_{w,in}} = T_{w,in} = 20°\mathrm{C}, \tag{5.2.64}$$

where $T_{w,in}$ is the inlet water temperature.

At the outlet water surface, $S_{w,out}$, the temperature gradient along the vector normal to the surface is set to zero. Therefore, the boundary condition is given as:

$$\left.\frac{\partial T(\mathbf{x})}{\partial \mathbf{n}}\right|_{S_{w,out}} = 0. \tag{5.2.65}$$

Considering the boundary conditions at a remaining surface forming the model of water, it must be noticed that it is divided into two regions: a water surface being adjacent to the solid domain of pipe, $S_{w,s}$, and water surfaces corresponding to additional segments of water sub-domain, $S_{w,a}$, related to transitional zone (Section 5.2.1). At the surfaces related to both regions, it is assumed that the velocity equals zero (no-slip), and the pressure gradient along the vector normal to the surface equals zero, as well:

$$\mathbf{U}(\mathbf{x})|_{S_{w,s}} = 0, \tag{5.2.66}$$

$$\left.\frac{\partial p(\mathbf{x})}{\partial \mathbf{n}}\right|_{S_{w,s}} = 0. \tag{5.2.67}$$

Additionaly, at the surfaces related to transitional zones, $S_{w,a}$, heat flux normal to the surface is assumed to be zero (adiabatic surface). The adiabatic boundary condition used to complete the governing equations is represented as:

$$-\lambda \nabla T\left(\mathbf{x}\right)|_{S_{w,a}} = q|_{S_{w,a}} = 0. \tag{5.2.68}$$

In the considered model of HSC, a heat exchange between the sub-domain of water (central segment) and pipe is based on flux continuity assumption. The equation describing the boundary condition for heat exchange between internal surface of pipe model, $S_{p,i}$ (Fig. 5.15), and surface of adjacent water model, $S_{w,s}$, is represented as:

$$q|_{S_{p,i}} = q|_{S_{w,s}}\,, \tag{5.2.69}$$

where q is the heat flux in a direction normal to the surface.

The boundary surfaces of the air-cavity model are presented in Fig. 5.14. According to made assumptions, the air flows in the cavity due to the natural convection. The temperature field creates a velocity field and in turn the velocity field effects the temperature field with the occurrence of free convective heat transfer. The physical geometry of HSC model, a flow pattern and a thermal solution are assumed to be of translational periodicity nature. Thus, the translational periodicity is applied at the inlet, $S_{a,in}$, and outlet, $S_{a,out}$, of air-cavity surfaces. In other words, it means that a periodic boundary at the inlet air-cavity surface, $S_{a,in}$, is transformed into the boundary condition at the outlet air-cavity surface, $S_{a,out}$, by pure coordinate translation. This assumption corresponds to fully developed natural convection.

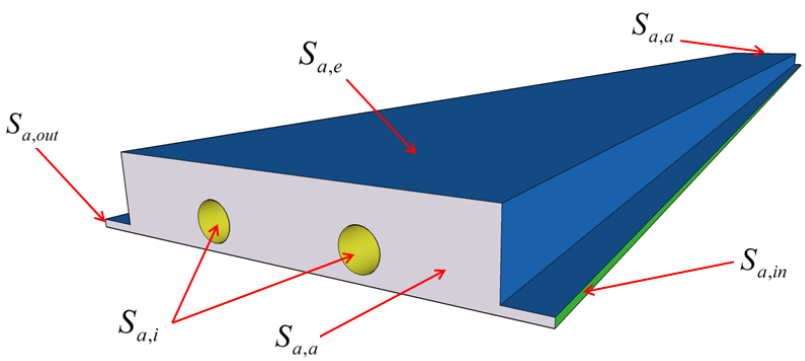

Figure 5.14: Boundary surfaces of air-cavity sub-domain in CFD model

At the remaining surfaces of the air model, the "no-slip" [6] condition is assumed. The boundary conditions for these surfaces are defined through the analogy to

Eq. 5.2.66 and Eq. 5.2.67. The flow variables in the near-wall regions of the air model are resolved using the scalable wall function approach [6]. The adopted approach is discussed separately in Section 5.2.2.4.1.

A heat exchange between the models of air and solid bodies is based on continuity equations. Hence, the boundary conditions for heat exchange between the surfaces of air model, $S_{a,i}$ and $S_{a,e}$, and corresponding surfaces of solid bodies, $S_{p,e}$ and $S_{c,i}$ (Fig. 5.15), are defined through the analogy to Eq. 5.2.69. On the other surfaces of the air model, $S_{a,a}$, the adiabatic boundary conditions are prescribed through the analogy to Eq. 5.2.68.

The boundary surfaces of solid bodies model are shown in Fig. 5.15. Assuming that HSC separates indoor zones at fixed temperature from outdoor environment, the boundary conditions at the internal, S_i, and external, S_e, surfaces of the collector are defined by the Newton's law. A heat exchange rate by convection and

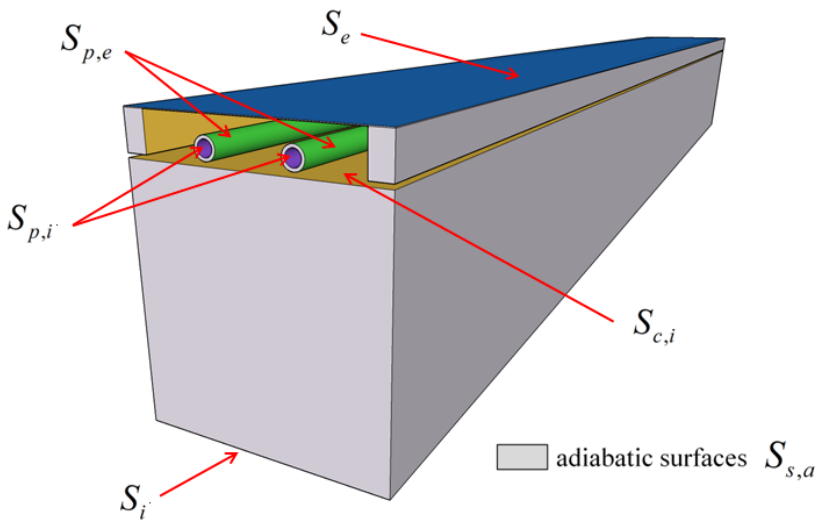

Figure 5.15: Boundary surfaces of solid bodies sub-domain in CFD model

radiation on the internal solar collector surface, S_i, is defined by convective/radiative heat transfer coefficient, h_i. Consequently, the boundary condition at the internal collector surface, S_i, used to complete the energy equation is:

$$\lambda \frac{\partial T(\mathbf{x})}{\partial \mathbf{n}}\bigg|_{S_i} = h_i \left[T_{S_i} - T_{a,in}\right], \tag{5.2.70}$$

where T_{S_i} is the average temperature of the internal collector surface and $T_{a,in}$ is the indoor air temperature. The convective/radiative heat transfer coefficient, h_i,

is constant and defined according to the ISO standard [136] as $h_i = 8.1\,\mathrm{W/(m^2{\cdot}K)}$. The indoor air temperature, $T_{a,in}$, is assumed to be constant ($T_{a,in} = 20\,^\circ\mathrm{C}$) and is related to the thermal comfort level.

A heat exchange between the external surface of the collector, S_e, and outdoor environment is considered by a convective and radiative heat exchange, separately. The convection is defined by the convective heat transfer coefficient, h_e, whereas the radiation is defined by the sol-air temperature, T_{sol}. Consequently, the boundary condition on the external collector surface, S_e, is given as:

$$\lambda \frac{\partial T\left(\mathbf{x}\right)}{\partial \mathbf{n}}\bigg|_{S_e} = h_e \left[T_{sol} - T_{S_e}\right], \tag{5.2.71}$$

where h_e is the convective heat transfer coefficient of external collector surface, T_{sol} is the sol-air temperature and T_{S_e} is the average temperature of the external collector surface.

According to brief description given by Gagliano et al. [64], the sol-air temperature, T_{sol}, is the fictitious temperature of the outdoor air, which in the absence of radiative heat exchange on the outer surface of the roof, would give the same rate of the heat flux through the roof as the actual combined heat transfer mechanism between the sun, roof surface, outdoor air and surroundings. In general, the sol-air temperature allows to take into account the effect of the solar radiation incident on the external roof surface [45, 132]. The sol-air temperature, T_{sol}, for the external surface of HSC is defined as follows [103, 161, 176]:

$$T_{sol} = T_{a,out} + \frac{\alpha I_e}{h_e}, \tag{5.2.72}$$

where $T_{a,out}$ is the outdoor air temperature, α is the absorptivity coefficient of external collector surface and I_e is the incident total solar radiation. The magnitude of sol-air temperature strongly depends on the absorptivity coefficient. In this study, the solar absorptivity coefficient of $0.85\,[-]$ equivalent to dark-brown painted steel roof was assumed to simulate realistic conditions since it is the most frequently used color for the roofing [118].

Besides the sol-air temperature, the wind driven changes of the convective heat transfer coefficient, h_e, influence the heat exchange rate on the external surface of the investigated solar collector. In the literature, various equations describing the correlation between the convective heat transfer coefficient, h_e, and wind speed,

w_s, can be found, e.g. the McAdams equation, $h_e = 5.7 + 3.8w_s$ [20]; the Karman equation,$h_e = 5.0w_s^{0.8}$ [118]; the Test equation, $h_e = 2.56w_s + 8.55$ [149]; the Soltau equation, $h_e = 9.3w_s^{0.8}$ [157]. A survey of convective heat transfer coefficients was given by Palyvos [131] and Kumar and Mullick [104]. According to Duffie and Beckman [58], a minimum value of approximately, 5 W/(m^2·K) occurs in solar collectors under no-wind conditions. Taking into account the results of Mitchell [121], the authors proposed an empirical formula to calculate the convective heat transfer coefficient that includes forced convection conditions:

$$h_e = \max\left[5, \frac{8.6 \cdot {w_n}^{0.6}}{{L_b}^{0.4}}\right], \tag{5.2.73}$$

where w_n is the wind speed vector component in direction normal to the external collector surface and L_b is the cube root of the building volume. The above formulation was employed in the considered model to include thermal losses to the ambient environment from the external collector surface. A value of 9.64 m was chosen as the cube root of the building. It corresponds to 896 m^3 of the building total volume. The convective heat transfer coefficient depends more on the wind speed rather than the building volume. The difference between convective heat transfer coefficients determined under constant wind conditions ($w_s = 3.16$ m/s, value corresponding to the annual average wind speed for the considered location [164]) for the building total volumes of 896 and 1792 m^3 does not exceed 9 %. Therefore, the assumption is realistic.

A heat exchange between surfaces of two adjacent solid layers is based on continuity equations. The equations describing the boundary conditions for the conductive heat transfer in solid layers (Eq. 5.2.59) between surfaces, $S_{s,1}$ and $S_{s,2}$, of two adjacent solid layers in HSC are represented by:

$$T(\mathbf{x})|_{S_{s,1}} = T(\mathbf{x})|_{S_{s,2}}, \tag{5.2.74}$$

$$q(\mathbf{x})|_{S_{s,1}} = q(\mathbf{x})|_{S_{s,2}}. \tag{5.2.75}$$

The adiabatic conditions are prescribed on the other surfaces of solid sub-domain, $S_{s,a}$, through the analogy to Eq. 5.2.68.

The following initial conditions are assumed: the air temperature in the cavity is uniform and equal to a magnitude that is lower than the considered sol-air temperature (Eq. 5.2.72) by 20 °C. The air is stagnant and the pressure value is

of atmospheric pressure order (101325 Pa). In case of water sub-domains, uniform magnitudes of temperature and static pressure equal to 20 °C and 0 Pa, respectively, are assumed for all the simulations. For the water flow initialization it is assumed that velocity component in the direction of fluid flow is non-zero and equal to magnitude calculated from the considered water mass flux. Remaining components are equal to 0 m/s. Initialization for the solid sub-domains refers to set an uniform temperature for each solid body. For the roofing material and battens the assumed temperature is the same as for air sub-domain. In case of pipes and insulation layer the temperature is analogous to that assumed for water sub-domains.

5.2.2.4.1 Near-wall treatment:scalable wall function

Turbulent flows are greatly influenced by wall boundaries [7], especially when dealing with flows through relatively narrow channels [33]. Numerous experiments show that the near-wall flow region can be divided into three sub-layers: viscous sub-layer, fully-turbulent sub-layer and buffer sub-layer between the two of aforementioned sub-layers. The closest to the wall is the viscous sub-layer, in which the flow is almost laminar-like, and viscosity plays a dominant role in momentum and heat transfer. In this layer, the mean dimensionless velocity u^+ shows a linear relationship with a dimensionless distance from the wall y^+ defined as [6]:

$$y^+ = \frac{\rho \Delta y u_\tau}{\mu}, \tag{5.2.76}$$

where Δy is the distance from near-wall point to the wall and u_τ is the shear (or friction) velocity. For the viscous sub-layer the dimensionless distance from the wall is $y^+ < 5\,[-]$ [33]. In the fully-turbulent sub-layer, for which $y^+ > 30\,[-]$, the turbulence dominates the flow. The relationship between U^+ and y^+ is approximated by logarithmic function. Thus, it is often called the log-law layer. In the buffer sub-layer the mean dimensionless velocity can be approximated by neither a linear relationship nor logarithmic function since the effects of molecular viscosity and turbulence are of equal importance.

In general, CFD modeling of the airflow near to walls assumes a no slip condition on walls. Such an assumption results in large gradients of solution variables, especially the tangential velocity. One of the main approach to simulate the near-wall flows is the "Low Re" approach. This method simulates the near-wall turbulence directly, hence very fine meshes and modified turbulence models are required. A magnitude of y^+ for a grid cell nearest to the wall (located in viscous sub-layer) is equal about $1\,[-]$. Such fine grids requires significant computational resources. An alternative is the wall-function approach. In this method, the viscosity affected sub-

layer region is bridged by employing semi-empirical formulas to give the near-wall boundary conditions for the mean flow and turbulence transport equations. These formulas connect the wall conditions (such as the wall-shear-stress) to the dependent variables at the near-wall mesh node which is presumed to lie in the fully-turbulent region of the boundary layer. In the log-law region, the near wall tangential velocity is related to the wall-shear stress, τ_ω, by means of a logarithmic relation defined as [6]:

$$u^+ = \frac{U_t}{u_\tau} = \frac{1}{\kappa} \ln\left(y^+\right) + C_l, \tag{5.2.77}$$

where the friction velocity u_τ is:

$$u_\tau = \left(\frac{\tau_\omega}{\rho}\right)^{0.5}, \tag{5.2.78}$$

and U_t is the known velocity tangent to the wall at a distance of Δy from the wall, τ_ω is the wall-shear-stress, κ is the Von Karman constant ($\kappa = 0.41\,[-]$) and C_l is a log-layer constant depending on wall roughness. Unlike the "Low Re" approach, the wall-function method enables to use relatively coarse meshes, since refining the grid leads to deterioration of results. Usually, the magnitudes of y^+ below $15\,[-]$ causes large errors in wall-shear-stress and wall heat transfer calculations [33]. The wall-function approach is widely used in industrial flows modeling. The use of wall-function approach to simulate near-wall flow in the HSC is, however, limited due to the geometry of considered computational domain. The magnitudes of y^+ corresponding to mesh developed in this study are less than $30\,[-]$, that is a lower bound of values desired for the log-law region. Thus, a new approach known as scalable wall-function [6] is adopted in the present study. It is based on standard wall-function, however, it prevents from deterioration of results when calculating on fine grids. The main idea is to replace the y^+ used in the logarithmic formulation (Eq. 5.2.77) with y^* and limit its value by a lower value of $\tilde{y^*} = \max\left(y^*, 11.06\right)$ where $11.06\,[-]$ is the value of y^* at the intersection between the logarithmic and the linear near-wall profile. The dimensionless distance from the wall, y^*, in the scalable wall-function is defined as [6]:

$$y^* = \mu / \left(\rho u^* \Delta y\right), \tag{5.2.79}$$

where u^* is the alternative velocity scale used instead of u_τ and is given by:

$$u^* = C_{\mu\mathrm{RNG}}^{0.25} k^{0.5}. \tag{5.2.80}$$

In contrast to u_τ, the alternative velocity scale u^* does not go to zero if U_t goes to zero. Due to the main assumption, the computed value of $\tilde{y^*}$ cannot be lower than 11.06 [−]. In consequence, all the grid points are outside the viscous sub-layer and all potential mesh inconsistencies are avoided. The boundary condition for the dissipation rate, ε, is defined by the following relation [6]:

$$\varepsilon = \frac{\rho u^*}{\tilde{y^*}\mu} \frac{C_{\mu\mathrm{RNG}}^{0.75}}{\kappa} k^{0.5}, \tag{5.2.81}$$

which is valid in the logarithmic region.

5.2.3 Numerical approach

The fluid flow problem was solved using a set of described RANS equations. In this study, the commercial software package ANSYS CFX 15.0 [6] was employed. The software uses an element-based Finite Volume Method which is thoroughly explained by Patankar [133], Versteeg and Malalasekera [173] and Blazek [23]. In FVM, the spatial computational domain is discretized into a set of finite volumes using a mesh. The constructed finite volumes are used to conserve relevant quantities such as mass, momentum, and energy. All equations are integrated over each control volume. The Gauss' Divergence Theorem is applied to convert volume integrals involving divergence and gradient operators to surface integrals. Subsequently, the volume and surface integrals are discretized. Up to this stage it is well known method of finite volume. Solution fields and other properties are stored at the mesh (grid) nodes.

To evaluate many of the terms, the solution field (control volume) or solution gradients must be approximated at integration points. However, in opposition to the most common approaches, e.g. implemented in ANSYS Fluent software [6], ANSYS CFX uses finite-element shape functions to perform these approximations. Finite-element shape functions describe the variation of a variable φ within an element as follows:

$$\varphi = \sum_{i=1}^{N_{node}} N_i \varphi_i, \tag{5.2.82}$$

where N_i is the shape function for node i and φ_i is the value of φ at node i and N_{node} is the number of nodes in element. The summation is made over all nodes of an element. Key properties of shape functions are:

$$\sum_{i=1}^{N_{node}} N_{i=1}, \tag{5.2.83}$$

and at node j,

$$N_i = \begin{cases} 1 & i = j \\ 0 & i \neq j \end{cases}. \tag{5.2.84}$$

The employed shape functions are linear in terms of parametric coordinates. They are used to calculate various geometric quantities as well, including integration points coordinates and surface area vectors. It is possible since the Eq. 5.2.82 also holds for the coordinates:

$$y = \sum_{i=1}^{N_{node}} N_i y_i. \tag{5.2.85}$$

This approach impacts mesh (grid) generation, particularly near walls and high gradient regions. It leads to finer meshes (grids).

In general, ANSYS CFX uses a co-located (non-staggered) grid layout such that the control volumes are identical for all transport equations. It can lead to a decoupled (checkerboard) pressure field [133]. Thus, an alternative discretization for the mass flows, proposed by Rhie and Chow [141] and modified by Majumdar [115], is used to avoid the decoupling and to remove the dependence of the steady-state solution on iteration. In this method, by applying a momentum-like equation to each integration point, the following expression for the advecting (mass-carrying) velocity at each integration point is obtained:

$$U_{i,ip} = \bar{U}_{i,ip} + f_{ip} \left(\left. \frac{\partial p}{\partial x_i} \right|_{ip} - \left. \overline{\frac{\partial p}{\partial x_i}} \right|_{ip} \right) - c_{ip} f_{ip} \left(U^0_{i,ip} - \bar{U}^0_{i,ip} \right), \tag{5.2.86}$$

where ip is the integration point and

$$f_{ip} = \frac{d_{ip}}{1 - c_{ip} d_{ip}}, \tag{5.2.87}$$

$$d_{ip} = -\frac{V}{A}, \tag{5.2.88}$$

and V is the volume of element and A is the approximation to the central coefficient of momentum equation, excluding the transient term

$$c_{ip} = \frac{\rho}{\Delta t}. \tag{5.2.89}$$

The ^{0} superscript denotes values at the previous time step, whereas the overbars indicate averaging of adjacent vertex values to the integration point. When substituted the following expression:

$$f_{ip}\left(\left.\frac{\partial p}{\partial x_i}\right|_{ip} - \left.\frac{\overline{\partial p}}{\partial x_i}\right|_{ip}\right) \tag{5.2.90}$$

into the continuity equation, it becomes a fourth derivative of pressure that scales with $(\Delta x)^3$. This expression represents a spatially third-order accurate term, also known as the pressure-redistribution term.

In all the CFD simulations, the spatially third-order Rhie and Chow discretization for the mass flow was employed.

5.2.3.1 Mesh generation

The solution of differential equations using FVM requires the subdivision of the calculation domain into a finite number of cells, hence forming the so-called computational mesh (grid). In this study, the mesh of CFD model was constructed using an ANSYS ICEM CFD software [6]. Two types of elements were used. The hexahedral elements were used to generate the mesh for sub-domains of roofing, battens and insulation layer. Whereas the computational grids for sub-domains of water, pipes and air layer were constructed from both the hexahedral and tetrahedral elements. According to geometry of CFD model, the mesh for each of sub-domains was generated using the sweep method control. The final domain discretization of the CFD model follows from 3 stages of mesh independence analysis based on series of the simulations under steady-state conditions. Two first stages examine the influence of mesh density in cross-sections of fluid sub-domains (air layer and water) on simulation results, whereas the last one concerns the mesh independence test of the whole computational domain in the length of the pipes direction. The parameters of horizontal and vertical convective-equivalent thermal conductivity coefficients of the air layer and convective heat transfer coefficients on inner and outer surfaces of both pipes were chosen as the criterion of the mesh density independence for particular stages. A preliminary mesh independence study of CFD model showed that an increase of mesh density of solid bodies' sub-domains only slightly improves the prediction accuracy of investigated parameters. Thus, a uniform grid design in a cross-sections of solid bodies' sub-domains was used for all of the numerical calculations. In all simulations, the solution was treated as convergent if the root mean square (RMS) value of residual for the governing equations were less than 1E-4.

A first stage of mesh independence study was conducted using 7 designs of mesh for the CFD model. Each model differed solely with respect to a grid density in a cross-section of the air layer sub-domain. The mesh density in the length of the pipes direction was identical for all models (120 sections on 3 m length and 27 sections

of each extra segment of water sub-domains). In consequence, the total number of cells for the considered models varied from 186840 to 1520160. The following values of variables were applied to determine the boundary conditions prescribed for all the tested grid densities:

- $T_{sol} = 63.9\,°\mathrm{C}$
- $h_e = 5.2\,\mathrm{W}/\left(\mathrm{m}^2 \cdot \mathrm{K}\right)$
- $h_i = 8.1\,\mathrm{W}/\left(\mathrm{m}^2 \cdot \mathrm{K}\right)$
- $\dot{m} = 9.5\,\mathrm{kg}/\left(\mathrm{m}^2 \cdot \mathrm{s}\right)$
- $T_{w,in} = 20\,°\mathrm{C}$

The magnitudes of sol-air temperature, T_{sol}, and convective heat transfer coefficient of external collector surface, h_e, correspond to average daytime (when $I > 0\,\mathrm{W/m^2}$) climate conditions of the summer season, whereas the magnitude of water mass flux, $\dot{m}$, corresponds the average value of the operating range (Section 5.5). The changes of mesh density in a cross-section of the air layer influences mainly the convective-equivalent thermal conductivity coefficients and convective heat transfer coefficients of outer pipes' surfaces. Thus, only these parameters were further chosen as the criterion for the first stage of analysis. The obtained results indicate a clear non-linear relationship between mesh density and predicted parameters (Figs. 5.16 and 5.17).

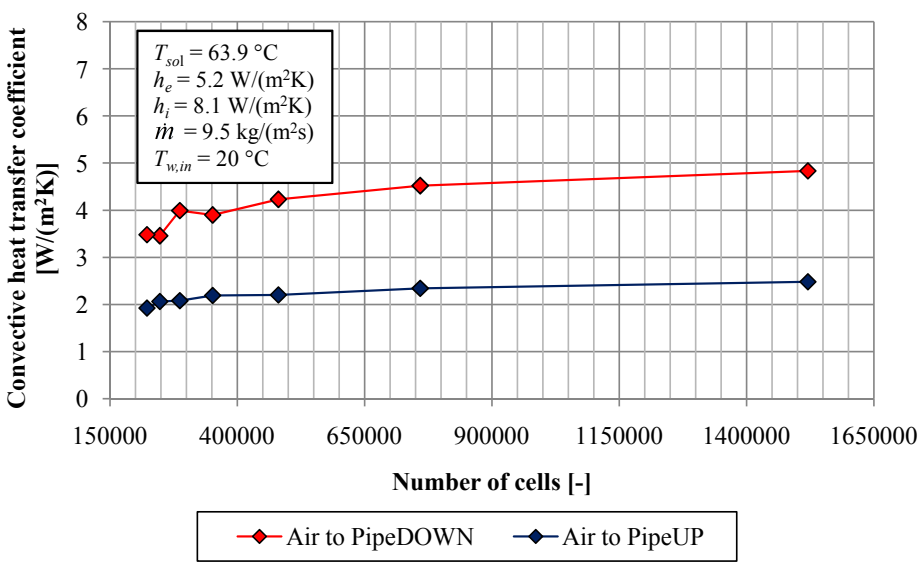

Figure 5.16: Relationship between mesh density in cross-section of air layer sub-domain in CFD model and convective heat transfer coefficient of outer pipes' surfaces

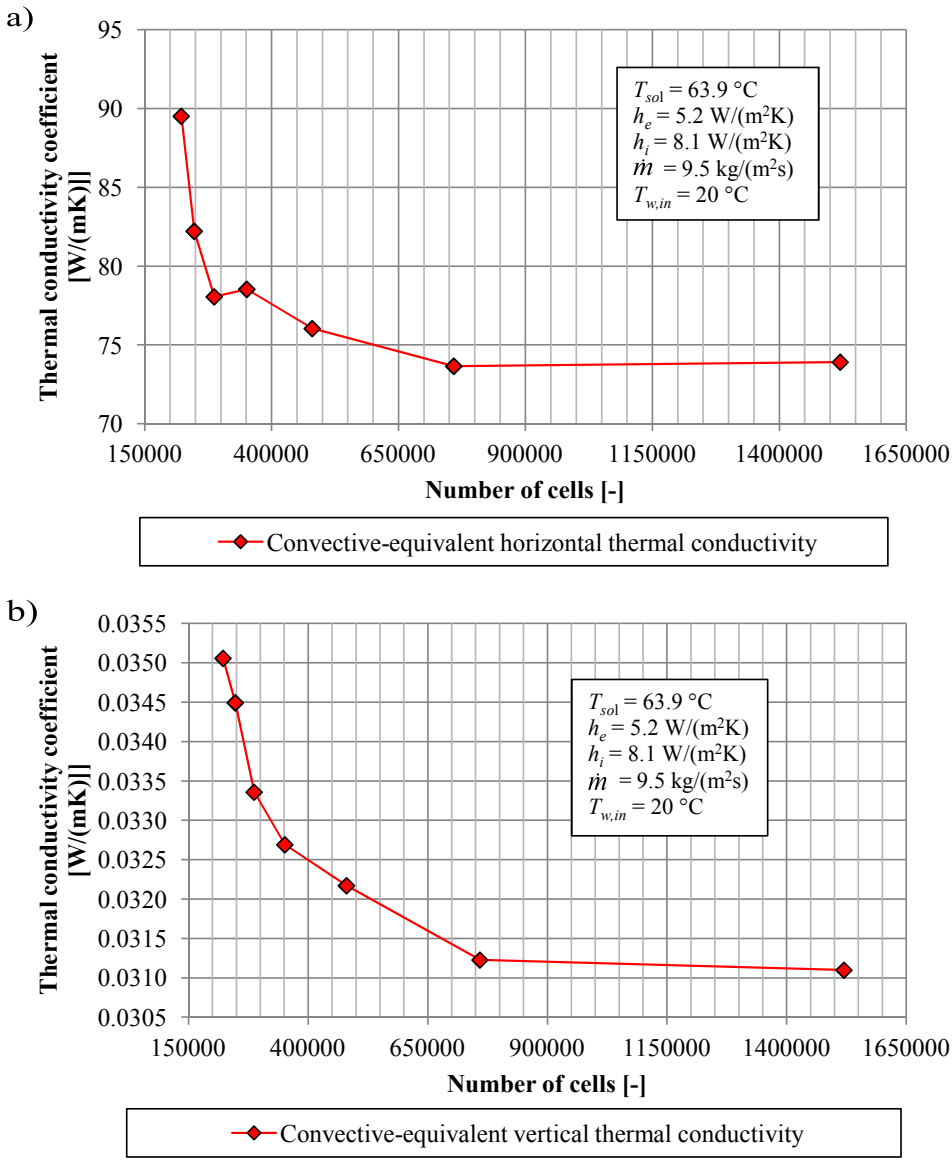

Figure 5.17: Relationship between mesh density in cross-section of air layer subdomain in CFD model and: a) horizontal convective-equivalent thermal conductivity of air layer, b) vertical convective-equivalent thermal conductivity of air layer

An increase of cells number in a cross-section of the air layer increases the values of convective heat transfer coefficients of outer pipes' surfaces. On the other hand an increase of the cells number decreases both horizontal and vertical convective-equivalent thermal conductivity coefficients. The difference in results between the test models, characterized by the lowest and highest mesh density does not exceed 2 % and 22.5 % for convective heat transfer coefficient of outer surface of lower and top pipe, respectively. In case of convective-equivalent thermal conductivity coefficients, the difference is about 21.1 % and 12.7 % for horizontal and vertical coefficient, respectively. The CFD model composed of 351360 cells was adopted for

the next stage analysis. When compared to CFD model characterized by the highest mesh density design, the differences for all of the considered parameters are 19.4 % and 11.7 %, 6.3 % and 5.1 %, respectively.

Further improvement of the mesh design in a cross-section of the CFD model, related to second stage of mesh independence test, was achieved by increasing mesh density of water sub-domains only. Considering results from the previous stage, 7 mesh designs for CFD model were developed. The total cells numbers investigated vary between 351360 and 474000. The test simulations were conducted with regard to analogous boundary conditions as in the first stage. At this stage, however, the criterions were the parameters of convective heat transfer of inner pipes' surfaces. The results of the simulations (Fig. 5.18) shows that an increase of the total cells number by increasing the number of nodes in the cross-section of the waters' sub-domains does not influence the criterions significantly. With an increase of the total cells number from 351360 to 474000, the differences in obtained values does not exceed 19.9 % and 19.6 % for the convective heat transfer coefficient of inner surface of lower and top pipe, respectively. The CFD model composed of 364392 cells was adopted for the next stage of analyses. When compared to CFD model characterized by the highest mesh density design, the differences for aforementioned criterion parameters are 9.4 % and 9.1 %, respectively.

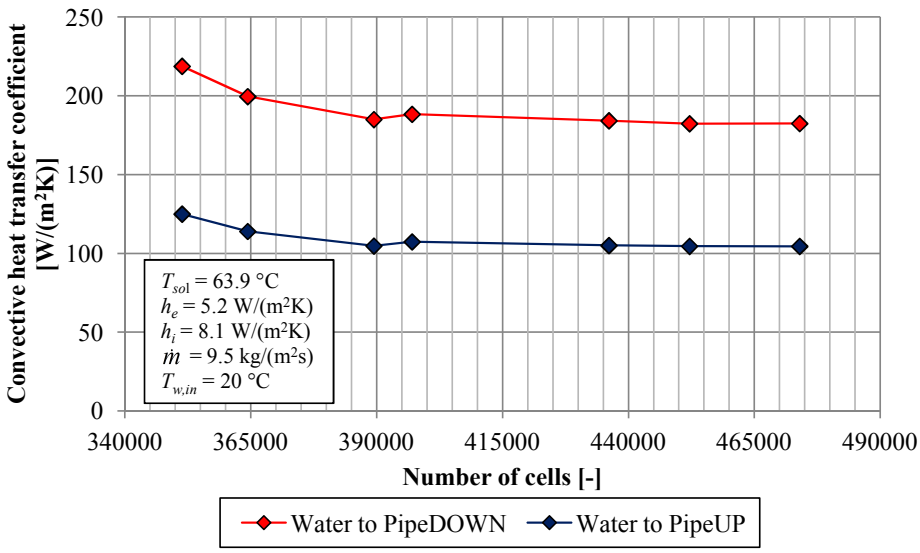

Figure 5.18: Relationship between mesh density in cross-section of water sub-domains in CFD model and convective heat transfer coefficient of inner pipes' surfaces

For the purpose of the last stage of analyses, concerning mesh independence test in the length of the pipes direction, 8 designs of grid for CFD model were developed. Each of the developed models was characterized by identical mesh density in a cross-section (adopted from results of previous stage). The total number of cells for the developed models vary from 269190 to 844380. As previously, the same boundary condition, corresponding to average daytime (when $I > 0\,\mathrm{W/m^2}$) climate conditions of summer season, were prescribed for each test model. In this stage, all the criterion parameters related to heat transfer in both the air layer and water sub-domains are considered. Simulation results are plotted in Figs. 5.19 and 5.20. It was found

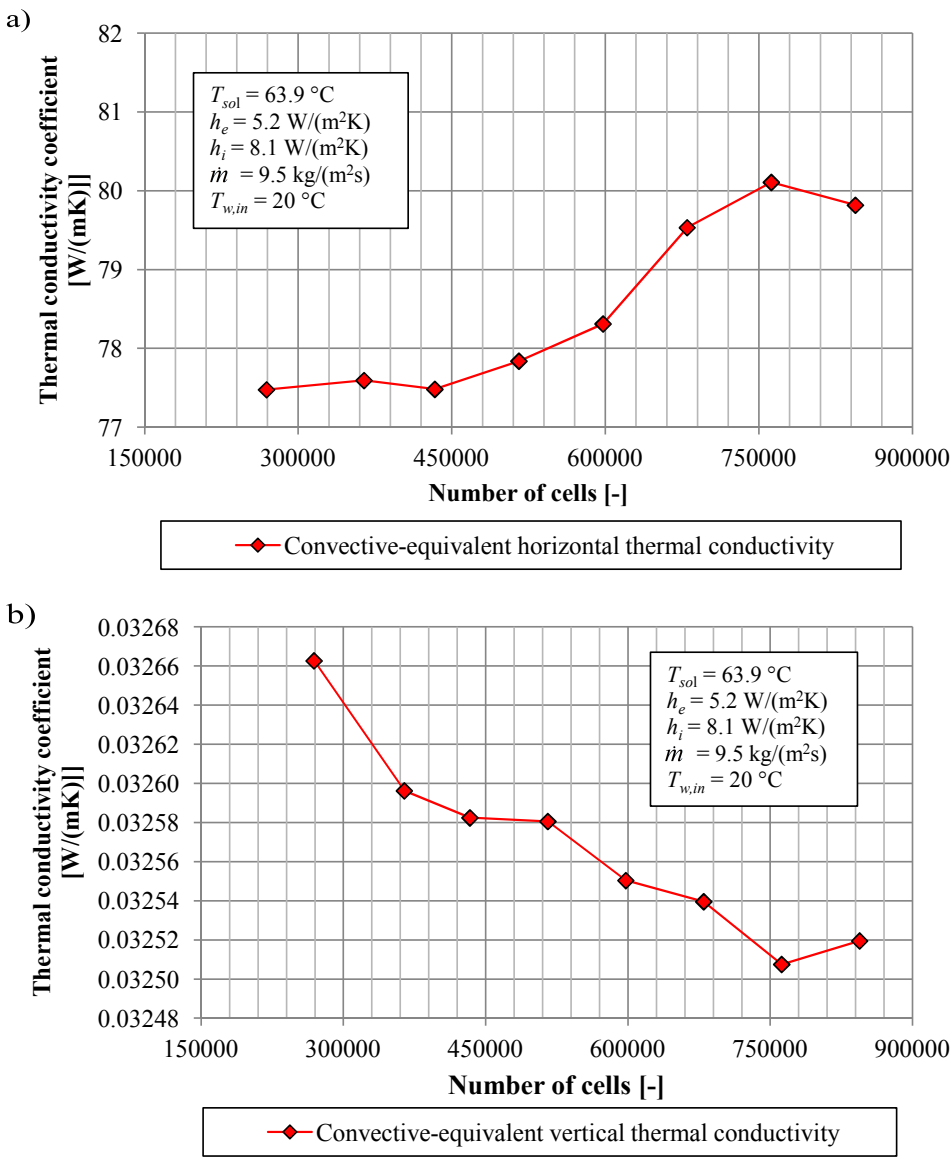

Figure 5.19: Relationship between mesh density in z-axis direction of CFD model and: a) horizontal convective-equivalent thermal conductivity of air layer, b) vertical convective-equivalent thermal conductivity of air layer

that the mesh with 364392 cells can provide reasonably good mesh-independent solutions and is thus selected for all the subsequent CFD simulations. When compared to a model characterized by the highest mesh density, the differences for criterion parameters are 2.8 % and 0.2 %, 0.03 % and 0.6 %, and 3.1 % and 3.7 % for horizontal and vertical convective-equivalent thermal conductivity coefficients, convective heat transfer coefficients of outer surface of lower and top pipe, and convective heat transfer coefficients of inner surface of lower and top pipe, respectively.

The final grid of cells, taken for further simulations, is presented in Fig. 5.21. The simulation time with the selected mesh design is, on average, 7 hours with 2500 iterations on a 3.6 GHz eight-core processor with 32GB of ram.

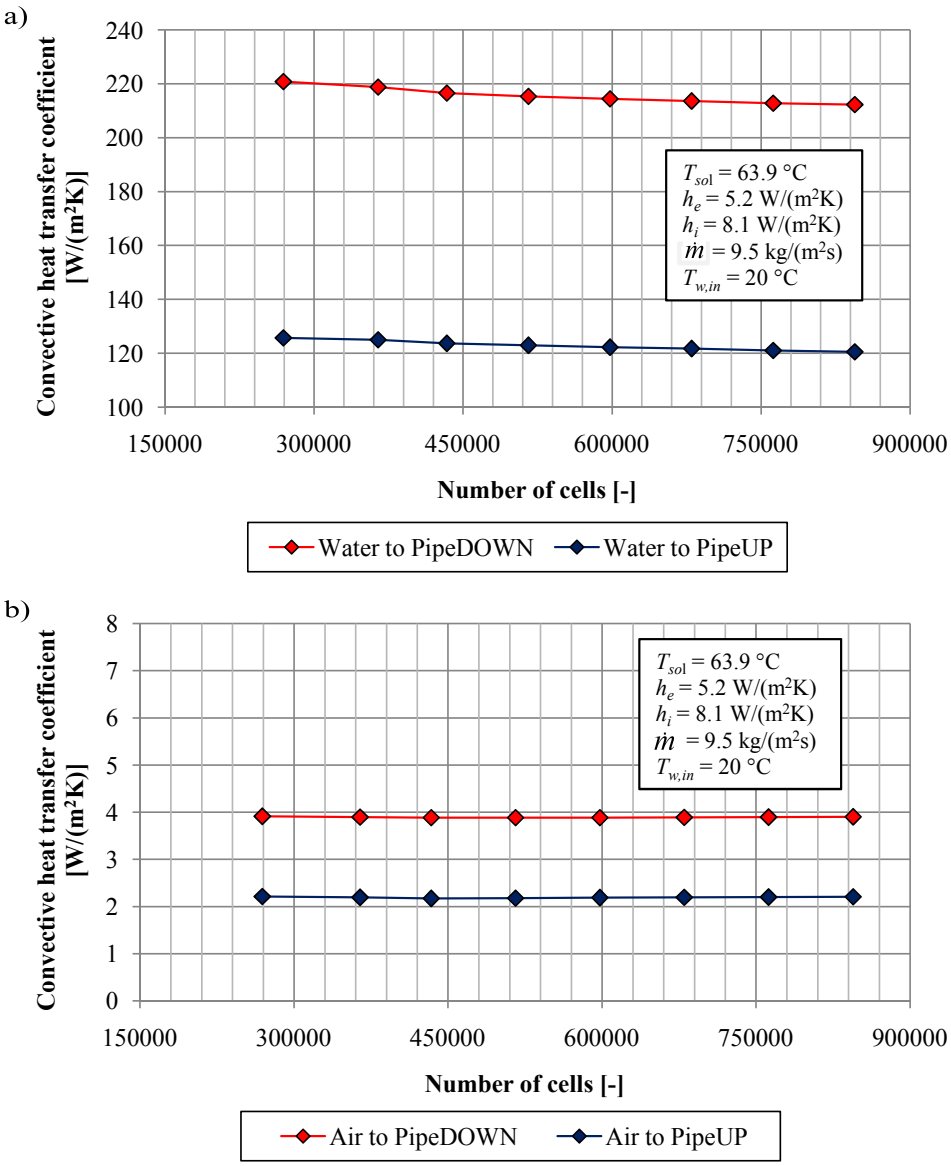

Figure 5.20: Relationship between mesh density in z-axis direction of CFD model and convective heat transfer coefficient on a) inner and b) outer pipes' surfaces

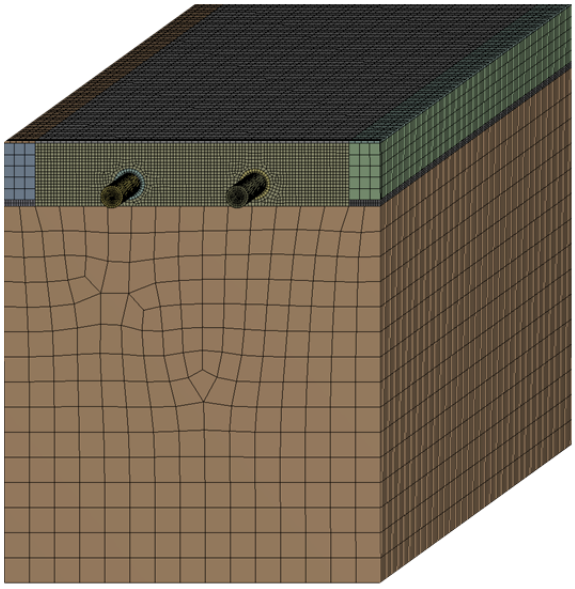

Figure 5.21: Complete CFD model of hidden solar collector

The temperature distribution in the cross-section of air and water sub-domains in the developed CFD model for the considered boundary conditions are presented in Fig. 5.22a and Fig. 5.22b, respectively, whereas the airflow streamlines are demonstrated in Fig. 5.23.

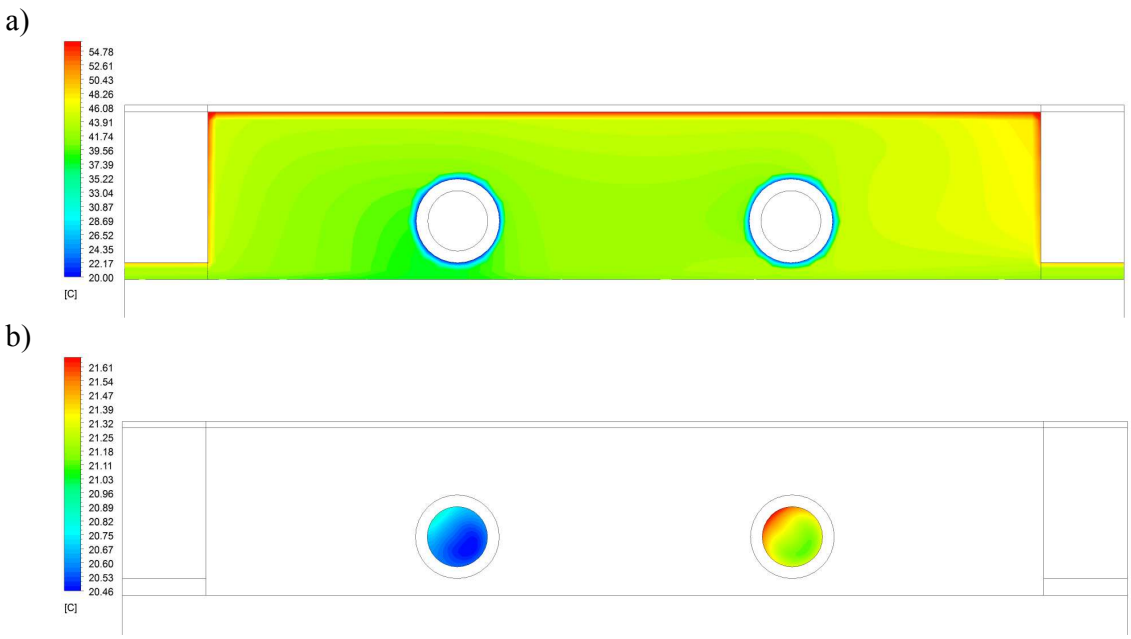

Figure 5.22: Temperature distribution in cross-section of a) air and b) water sub-domains in CFD model of HSC

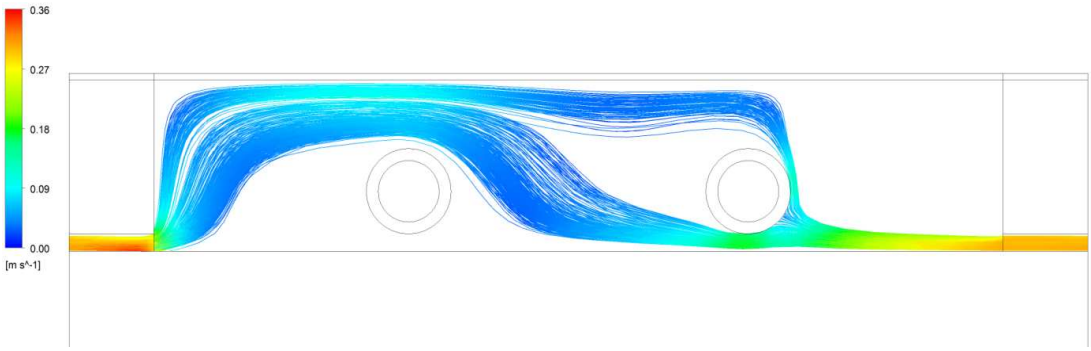

Figure 5.23: Airflow streamlines in cross-section of air sub-domain in CFD model of HSC

5.2.4 Validation of CFD model

The important parameters that determines the accuracy of CFD simulations are the mesh design and iterative convergence, the choice of turbulence models and near-wall treatment and so on. In order to evaluate if the developed CFD model of HSC is realistic and accurate, the results of numerical simulations must be validated in comparison with experimental data. There is, however, a lack of experimental results for the hidden solar collectors or any system alike. Thus, a validation was carried out indirectly, separately for the sub-model of water flow in the pipes and the sub-model of airflow in roof cavity round the pipes, by comparison with the analytical solutions available in literature.

5.2.4.1 Sub-model of water flow through pipes of collector

In the developed CFD model of HSC, the laminar flow regime in water sub-domains is considered (Section 5.2.2.1). Through the implementation of extra segments of water sub-domains (Fig. 5.9), the problem of the transitional zone is skipped (Section 5.2.1). According to operating conditions the forced convection is a dominant heat transfer mechanism in the flowing fluid rather than the natural. A validation of the developed sub-model was performed by comparing the convective heat transfer coefficient for water flow in a pipe obtained from results of steady CFD simulations, performed for constant wall heat flux conditions, to results of analytical solutions, which were verified with experiments.

The CFD simulation was carried out using an additionally-developed 3D model of water flowing through a pipe. However, only the domain of water is considered in the developed model. As in the complete CFD model (Fig 5.9, 5.10 and 5.13), the water domain is composed of 3 segments: inlet (transitional zone), central and

outlet (transitional zone) segment. The geometry, material properties, and spatial discretization of the computational domain correspond to those implemented in the single water sub-model of the complete CFD model. Hence, no mesh independence test was carried out. The boundary conditions for the numerical simulation were input as shown in Fig. 5.24. A constant magnitude of fluid flow velocity at the inlet surface, equal to 0.0095 m/s, corresponds to an average value of the operating range considered in this study. Thus, the flow profile is fully developed before the heated region. At the surface of heated region (central segment), a uniform heat flux equal to 10 W/m^2 is considered. Such a value is adopted in a similar case study reported in the literature [126]. Hence, it is assumed to be valid for the purpose of the model validation. The assumed magnitude of inlet water temperature equals to 20 °C. Other boundary conditions are prescribed by analogy to the water sub-model in the complete CFD model (Section 5.2.2.4). The flow field was initialized to the inlet conditions described in Fig. 5.24. The simulation was iterated until a residuals for all equations of 1E-04 was achieved.

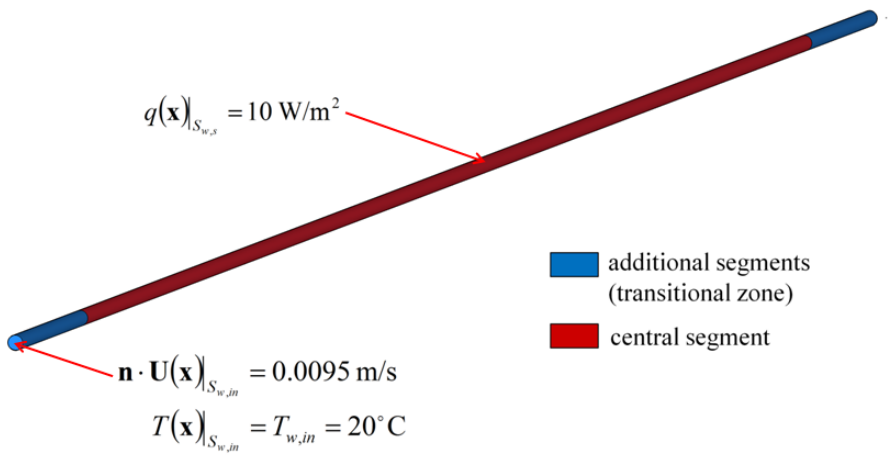

Figure 5.24: Boundary conditions for validation CFD model of water flow in pipes

Due to a complexity of heat transfer mechanism a variety of correlations to calculate the heat transfer coefficients on an interface between water and pipe can be found in the literature [181]. In general case of heat transfer in a flowing fluid characterized by a fully developed flow field, the choice of the correlation should be preceded by the analysis of thermal entrance region. The thermal entrance length for uniform heat flux cases, L_{eh}, can be estimated from [112]:

$$L_{eh} \approx 0.043 \mathrm{Re} \mathrm{Pr} d_i \tag{5.2.91}$$

For the considered heat transfer problem the length is 0.9 m. Since the total length of the heated region (central segment) equals to 3 m, the flow is to be treated as thermally developing. In consequence, the Nusselt number correlation for the thermally developing laminar flow in horizontal pipes proposed by Lienhard and Lienhard [112] was used to validate results from the CFD simulation. For a uniform wall heat flux conditions, the following formula estimates the exact result for local Nusselt number to within 1 % of error [112]:

$$\mathrm{Nu_w} = 4.364 + 0.263\mathrm{Gz}^{0.506}e^{-41/\mathrm{Gz}}. \tag{5.2.92}$$

The formula is applicable when $0 \leq \mathrm{Gz} \leq 667$ where Gz is the Graetz number given as:

$$\mathrm{Gz} = \frac{\mathrm{RePr}d_i}{lp}, \tag{5.2.93}$$

where d_i is the inner diameter of a pipe and l_p is the length of a pipe. In the considered case the Graetz number is 7.029 [−]. Hence, the empirical convective heat transfer coefficient, h_{we}, is given as:

$$h_{we} = \frac{\lambda \mathrm{Nu_w}}{d_i}, \tag{5.2.94}$$

where λ is the volume averaged thermal conductivity of water.

The average convective heat transfer coefficient, $\bar{h}_{wc}$, computed in numerical simulation is:

$$\bar{h}_{wc}\frac{q}{(T_S - T_w)}, \tag{5.2.95}$$

where q is the average wall heat flux, T_S is the average temperature of central segment surface and T_w is the average water temperature along the centerline.

Basing on the obtained results it was found that the theoretical correlation over predict the coefficient by 3.7 % when compared to the CFD results. The analogous analyses were conducted for the entire range of considered fluid flow velocities. The comparison between the two sets of data show that percentage differences are always less than 10.5 %. On the basis of these comparison it is possible to assert the validity of the proposed CFD model for the study of water flow in pipes of HSC.

5.2.4.2 Sub-model of airflow in roof cavity

In the developed CFD model of HSC, the turbulent flow regime in the air sub-domain was considered (Section 5.2.2.2). The airflow in the cavity is driven by the buoyancy forces caused by thermal gradients. A validation of the developed model was performed by comparing the convective heat transfer coefficient of external pipe surface obtained from results of stationary CFD simulations to analytical solutions, which were validated with experiments results.

For the purpose of this analysis a 3D model of airflow through the cavity of HSC was developed. As previously, the model is isolated what means that only the fluid domain is considered. The geometry, material properties, and spatial discretization of the computational domain correspond to those implemented in the air sub-model of the complete CFD model of HSC (Figs. 5.9, 5.10 and 5.14). Hence, no mesh independence test was carried out. The boundary conditions for the numerical simulation were input as shown in Fig. 5.25. The temperature difference between the upper, $S_{a,u}$, and bottom, $S_{a,b}$, surface of the model, equal to 60 °C, is adopted to induce moderate air movements in the collector cavity. The adiabatic boundary conditions are assumed for other surfaces besides the inlet air-cavity surface, $S_{a,in}$, and the outlet air-cavity surface, $S_{a,out}$ (Fig 5.14), for which translational periodicity is applied. The rest of boundary conditions and the initial conditions are prescribed by analogy to the air sub-model in the complete CFD model (Section 5.2.2.4). The simulation was iterated until a residuals for all equations of 1E-04 was achieved.

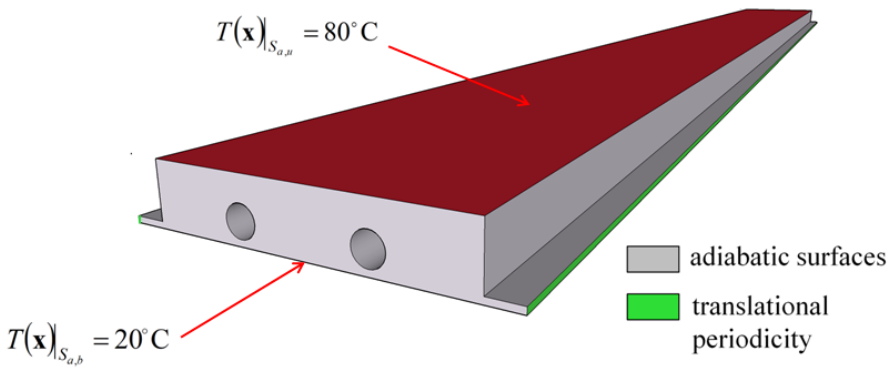

Figure 5.25: Boundary conditions for validation CFD model of airflow in cavity

In general, a variety of correlations to calculate the heat transfer into a single or a bundle of cylinders in a cross-flow configuration can be found in the literature [112]. There are, however, no correlation for the configuration investigated in this study. Thus, a simplified approach for the validation is employed. In the considered case, the validation was carried out for one (lower/first) pipe located in the panel's cavity. The average Nusselt number can be determined according to the empirical formula introduced by Żukaukas and referenced by Wiśniewski and Wisniewski [181], that is valid for $5 < \mathrm{Re_{dp}} < 10^3$:

$$\bar{\mathrm{Nu}}_{dp} = \left(0.43 + 0.5\mathrm{Re}_{\mathrm{dp}}^{0.5}\right)\mathrm{Pr}_{\mathrm{p}}^{0.38}\left(\frac{\mathrm{Pr_p}}{\mathrm{Pr_s}}\right)^{0.25}, \tag{5.2.96}$$

where $\mathrm{Re_{dp}}$ is the Reynolds number far enough from the pipe, and $\mathrm{Pr_p}$ and $\mathrm{Pr_s}$ are the Prandtl numbers evaluated at the mean bulk temperature and the mean wall temperature, respectively. For the considered boundary conditions the Reynlods number far enough from the pipe $\mathrm{Re_{dp}}$, given by Eq. 5.2.34, equals to 121.4 [−]. Consequently, the empirical convective heat transfer coefficient, h_{ae}, is:

$$h_{ae} = \frac{\lambda \bar{\mathrm{Nu}}_{dp}}{d_o}, \tag{5.2.97}$$

where λ is the volume averaged thermal conductivity of air and d_o is the outer diameter of a pipe.

The average convective heat transfer coefficient, h_{ac}, is computed as follows:

$$\bar{h}_{ac} = \frac{q}{(T_C - T_a)}, \tag{5.2.98}$$

where q is the average wall heat flux, T_C is the average surface temperature and T_a is the average air temperature out of the considered surface.

The analysis indicated that difference between the numerically and analytically determined convective heat transfer coefficients is about 10.8 %. Since the obtained numerical results are in good agreement with empirical correlation given by Zukauskas, the CFD model of airflow in the cavity of HSC was considered to be adequate to perform the further analysis.

5.2.5 Numerical analysis

Once validated, the CFD model of HSC was used to conduct the extensive parametric analysis. The major aim was to determine the relationships for convective-equivalent thermal conductivity coefficients in direction of the main airflow through the cavity (named later as convective-equivalent horizontal thermal conductivity coefficient and denoted as λ_{Heqv}) and direction perpendicular to the roofing surface (named later as convective-equivalent vertical thermal conductivity coefficient and denoted as λ_{Veqv}), and the relationships for convective heat transfer coefficients of both inner ($k_{w-p,down}$ and $k_{w-p,up}$) and outer ($k_{a-p,down}$ and $k_{a-p,up}$) pipes' surfaces. All the relationships for dependent parameters determined in function related to climate and operating conditions are then implemented in the FE model to include the influence of convective heat transfer in the air layer and improve the model of heat transfer in the fluids. In consequence, the simplified FEM model is as close to reality as it is possible.

The analysis is based on results of 80 stationary CFD simulation. Each simulation varies in regard to boundary conditions for heat transfer on external collector surface (Eq. 5.2.71) and water velocity at the inlet water surface (Eq. 5.2.60). For the first case, an independent parameter that is being modified is the sol-air temperature defined by Eq. 5.2.72. The considered values ranges from 5 °C to 200 °C. The assumed upper limit is higher, by approximately 10 °C, than the maximum magnitude of sol-air temperature corresponding to climate database of TMY [164]. Such an approach is reasonable since the CFD model does not include an influence of radiative heat exchange on temperature distribution on surfaces forming the air-cavity. It is assumed that freezing in water starts far enough below a minimum operating temperature. The convective heat transfer coefficient for external collector surface equals to 5.2 W/(m^2·K) and is constant for all the simulations. This order of magnitude corresponds the average daytime (when $I > 0\,\mathrm{W/m^2}$) climate conditions of the summer season for the location considered in this study (Section 5.1.2). Such an assumption does not influence the investigated parameters since the buoyancy-driven air movement in the cavity of the developed CFD model is resulted directly from the temperature difference between the forming surfaces. As the upper limit of considered sol-air temperature range exceeds by almost 8 °C the maximum value corresponding to assumed climate data base, the above assumptions are reasonable. For latter case, an independent parameter of water mass flux is being modified, hence modifying the water inlet velocity (Eq. 5.2.18). The considered range of values, from 0 to 19 kg/(m^2·s), corresponds directly to the technical limits assumed for the simulation of annual collector operation (Section 5.5). The set of points selected

from the ranges of independent parameters in order to modify boundary conditions in the CFD numerical analysis is presented in Fig. 5.26. All the simulations were iterated until a residual for equations of 1E-04 was achieved.

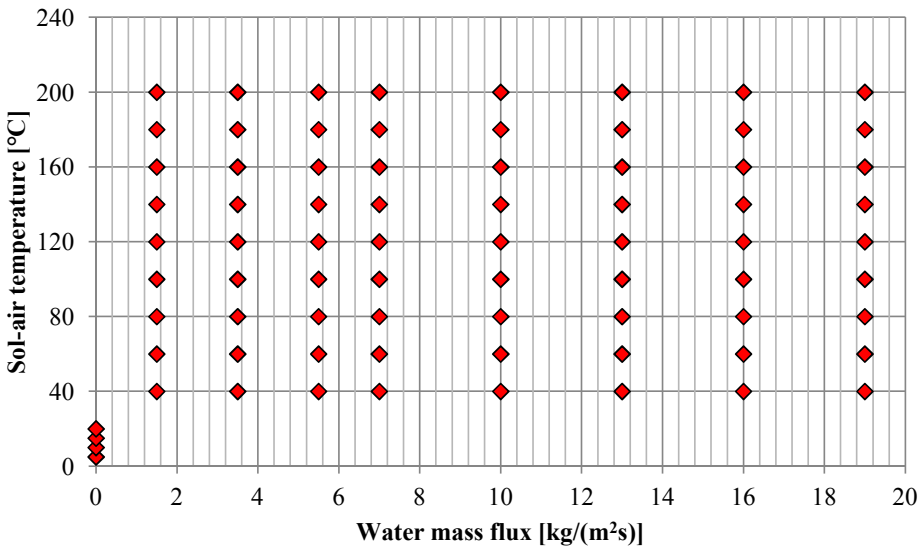

Figure 5.26: Characteristic points for boundary conditions in CFD analysis

The magnitudes of dependent parameters, for which the relationships are to be determined, are calculated on basis of simulation results as follows. The calculated temperatures of cavity surfaces and heat flux density for particular cavity planes (Fig. 5.27) were used to determine the convective-equivalent parameters for heat conduction (in the FE model) within the air layer. The convective-equivalent horizontal thermal conductivity of the air layer, λ_{Heqv}, was calculated using the following equation:

$$\lambda_{Heqv} = \frac{q_{Hflux} d_{ACH}}{\Delta T}, \tag{5.2.99}$$

where q_{Hflux} is the heat flux density at the outlet cavity plane $S_{a,po}$, d_{ACH} is the cavity dimension in the main airflow direction, equal to 0.25 m, and ΔT is the difference of temperatures at the inlet, $S_{a,pi}$, and outlet, $S_{a,po}$, cavity planes.
By analogy, the convective-equivalent vertical thermal conductivity of the air layer, λ_{Veqv}, was calculated using the following equation:

$$\lambda_{Veqv} = \frac{q_{Vflux} d_{ACV}}{\Delta T}, \tag{5.2.100}$$

where q_{Vflux} is the heat flux density at the bottom cavity plane $S_{a,pb}$, d_{ACV} is the height of cavity, equal to 0.05 m, and ΔT is the difference of temperatures at the bottom, $S_{a,pb}$, and upper, $S_{a,pu}$, cavity planes.

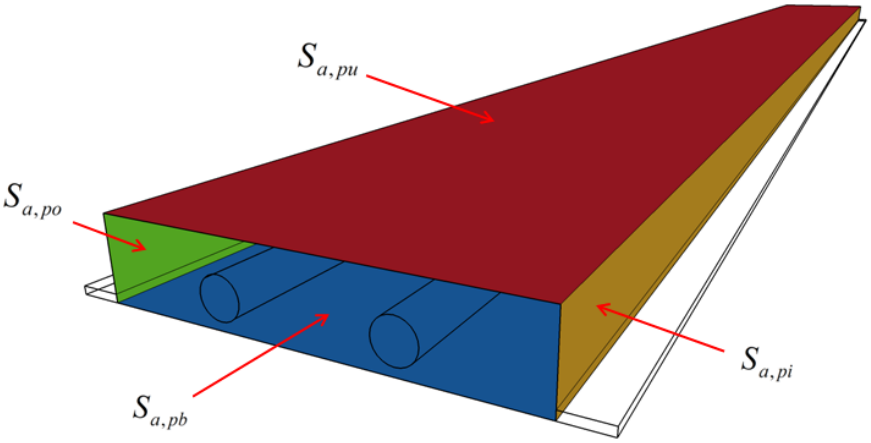

Figure 5.27: Air-cavity regions for CFD parametric analysis

The convective heat transfer coefficients of inner pipes surfaces, $k_{w-p,down}$ and $k_{w-p,up}$, are calculated using Eq. 5.2.95, whereas the convective heat transfer coefficients of outer pipes surfaces, $k_{a-p,down}$ and $k_{a-p,up}$, are calculated using Eq. 5.2.98. The particular regions of pipes taken into account to calculate the magnitudes of surface temperature and heat flux density are presented in Fig. 5.28.

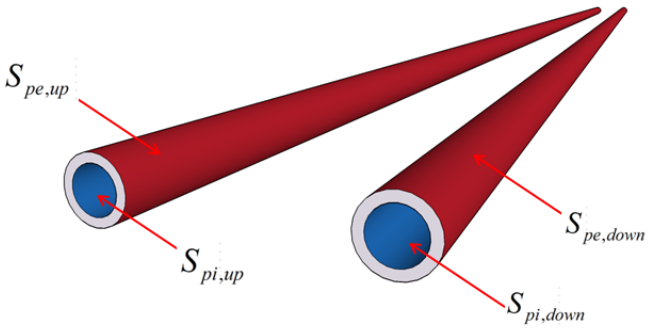

Figure 5.28: Pipes regions for CFD parametric analysis

The exemplary results of the analysis for convective-equivalent thermal conductivity coefficients determined under fixed water mass flux and variable sol-air temperature conditions and vice versa conditions are presented in Fig. 5.29 and Fig. 5.30, respectively. The obtained results clearly indicate that the change in values of investigated thermal parameters is driven by sol-air temperature rather than the water mass flux. In both cases, however, the changes are more significant for the

convective-equivalent horizontal thermal conductivity coefficient.With an increase of sol-air temperature from 40 °C to 200 °C the growth for horizontal magnitude overcomes the level of 841 %, whereas the growth for the vertical magnitude is only about 13 %. In case of water mass flux, a negative correlation was found. A percentage decrease for the horizontal and vertical magnitudes is close to 16 % and 8 %, respectively.

A similar character of correlation between the considered variables and dependent parameters was found for the convective heat transfer coefficients of both inner and outer pipes' surfaces. The obtained results (Figs. 5.31 and 5.32) point out a

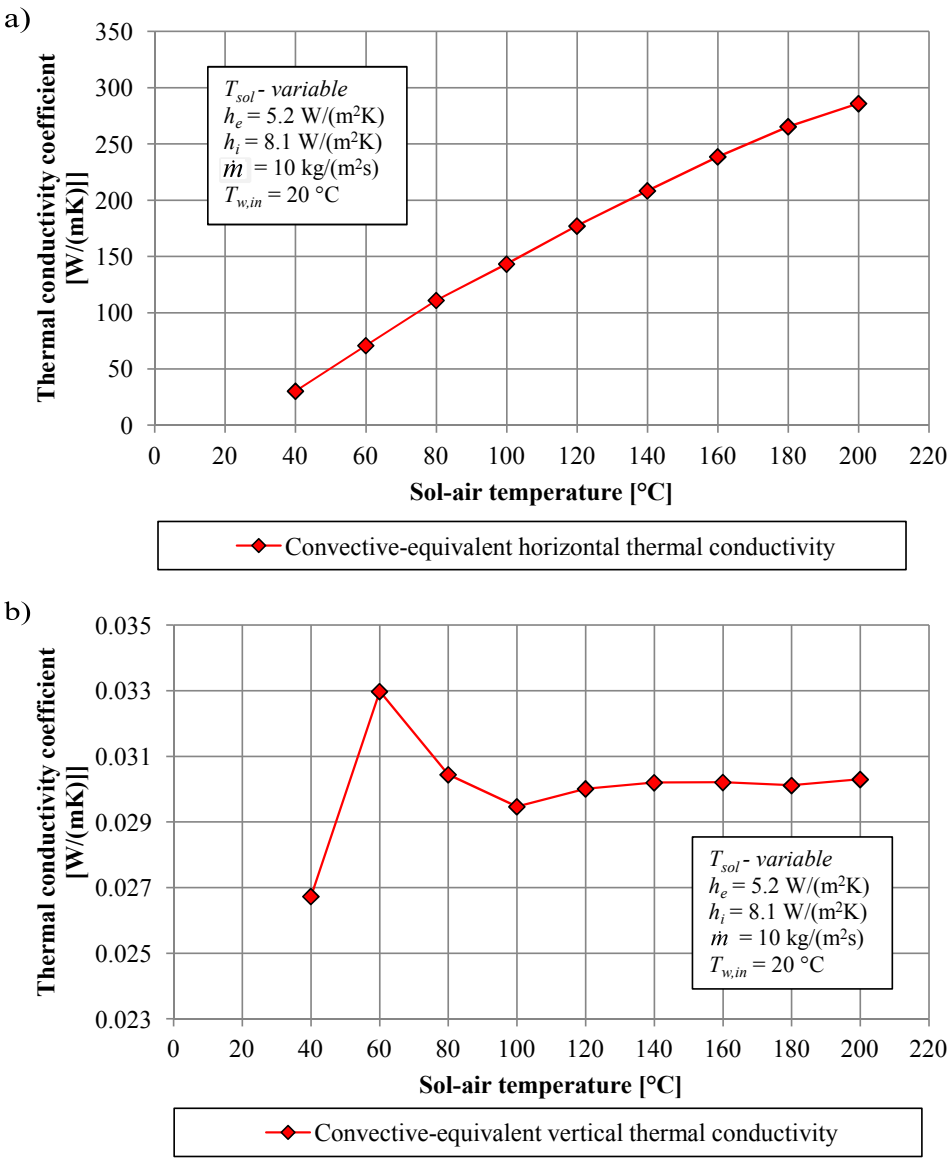

Figure 5.29: Convective-equivalent a) horizontal and b) vertical thermal conductivity coefficients determined for fixed water mass flux and variable sol-air temperature conditions

negligible impact of water mass flux on investigated parameters. It is a consequence of fluid flow profile that is fully developed in the central segment of water domain (heated region) for almost entire range of water mass flux assumed in this study (Section 5.5). A percentage decrease in values of investigated parameters with an increase of water mass flux from 1.5 to 19 kg/(m^2·s) is less than 11 % and 6 % for the convective heat transfer coefficients of inner and outer pipes' surfaces, respectively. On the other hand, the percentage growth in values with an increase of sol-air temperature does not exceed 261 % and 208 % for the coefficients on inner and outer pipe surface, respectively.

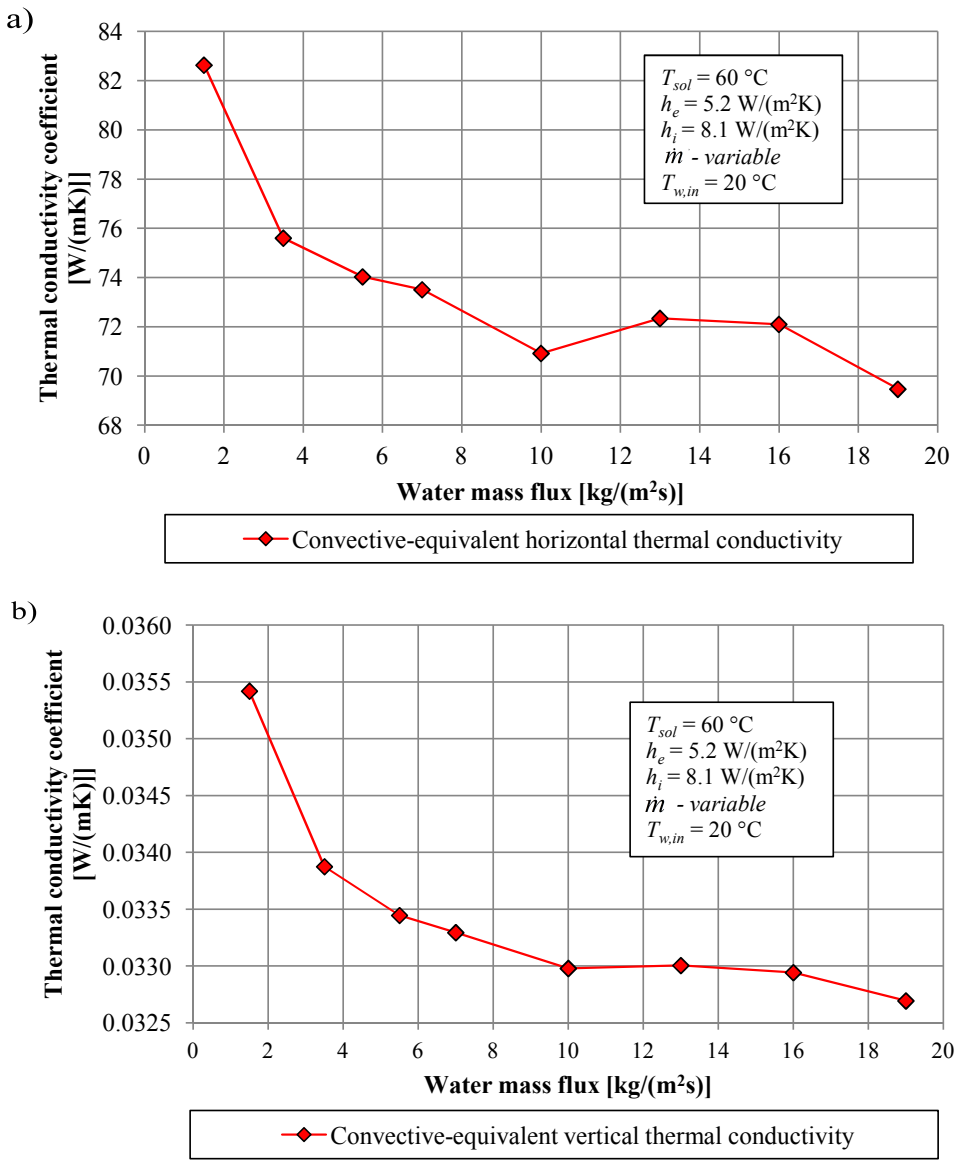

Figure 5.30: Convective-equivalent a) horizontal and b) vertical thermal conductivity coefficients determined for variable water mass flux and fixed sol-air temperature conditions

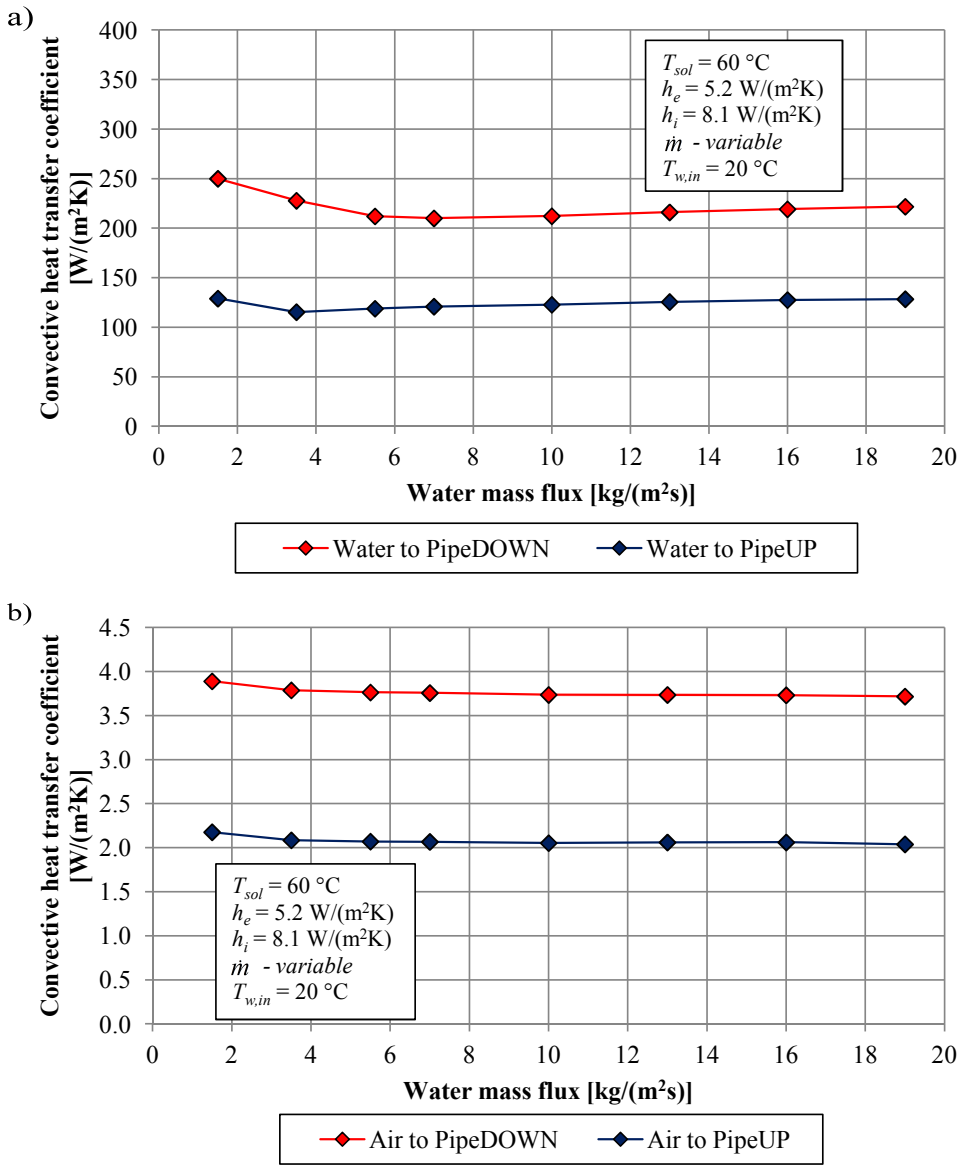

Figure 5.31: Convective heat transfer coefficients of a) inner and b) outer pipes' surfaces determined for variable water mass flux and fixed sol-air temperature conditions

The relationships for all the dependent parameters were approximated by the model of polynomial function estimated in the STATISTICA software package [160]. The nonlinear model of employed function is as follows:

$$f\left(T_{sol}, \dot{m}\right) = a_0 + b_1 T_{sol} + c_1 \dot{m} + b_2 T_{sol}^2 + c_2 \dot{m}^2 + b_3 T_{sol}^3 + c_3 \dot{m}^3 + b_4 T_{sol}^4 + c_4 \dot{m}^4 + b_5 T_{sol}^5 + c_5 \dot{m}^5 + b_6 T_{sol}^6 + c_6 \dot{m}^6. \quad (5.2.101)$$

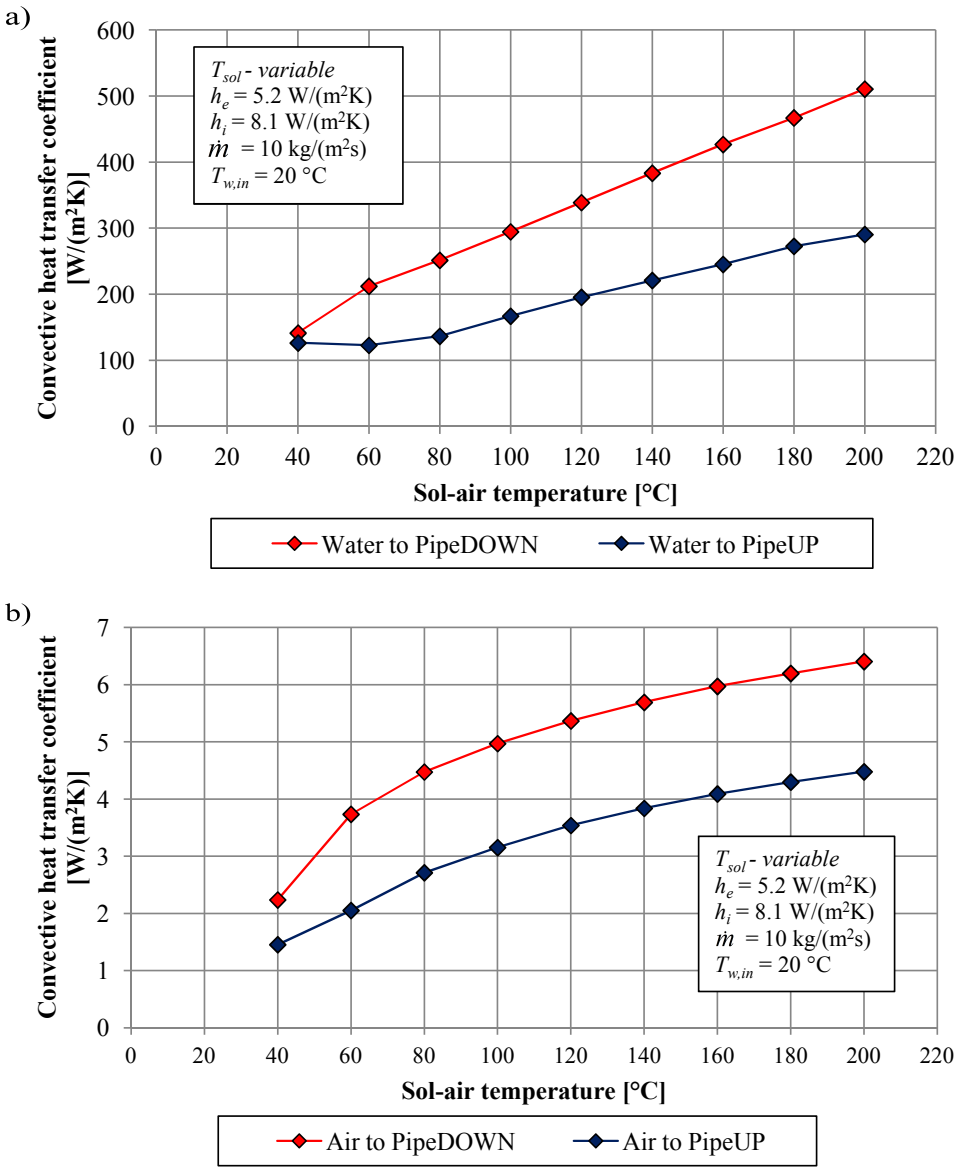

Figure 5.32: Convective heat transfer coefficients of a) inner and b) outer pipes' surfaces determined for fixed water mass flux and variable sol-air temperature conditions

The mean squared error, the minimum and maximum values of predicted parameter, and the maximum absolute value of residual for each relationship are presented in Table 5.2. All the estimated functions were implemented in the FORTRAN subroutine in order to modify heat transfer conditions at each step of the FEM transient simulation.

Table 5.2: Characteristics of functions estimated for dependent parameters

Dependent parameter	Mean squared error	Predicted magnitudes		Maximum absolute value of residual
		MIN	MAX	
$\lambda_{Heqv} = f\left(T_{sol}, \dot{m}\right)$ [W/(m · K)]	0.998 [-]	23.861	6050.547	22.139
$\lambda_{Veqv} = f\left(T_{sol}, \dot{m}\right)$ [W/(m · K)]	0.986 [-]	0.027	0.134	0.009
$k_{w-p,down} = f\left(T_{sol}, \dot{m}\right)$ [W/(m^2 · K)]	0.987 [-]	4.305	825.596	106.526
$k_{w-p,up} = f\left(T_{sol}, \dot{m}\right)$ [W/(m^2 · K)]	0.995 [-]	3.807	494.127	29.182
$k_{a-p,down} = f\left(T_{sol}, \dot{m}\right)$ [W/(m^2 · K)]	0.999 [-]	1.921	6.654	0.198
$k_{a-p,up} = f\left(T_{sol}, \dot{m}\right)$ [W/(m^2 · K)]	0.992 [-]	1.454	5.545	0.575

5.3 FE model

5.3.1 Introduction

The problem of three-dimensional unsteady and steady-state heat transfer in HSC was solved with the application of the Finite Element Method (FEM). The developed FE model, whose geometry is widely described in Section 5.1.1, considers the following heat transfer mechanisms:

- convective and radiative heat exchange between the external surface of HSC and outdoor environment, wherein:
  - shading of the outdoor roof surface is neglected. In practice, it is highly recommended for any solar systems to avoid shading of the absorber surface (external surface of roofing material). Since, the knowledge of maximum HSC performance is desirable, the assumption seems to be reasonable,
  - dust and dirt effect on the absorptivity coefficient of the roofing material is neglected. Uniform magnitude of the coefficient is assumed for an entire surface of the absorber throughout the transient simulation,

  - heat losses from an external surface of the absorber due to the thermal emittance are neglected. It should be noticed, however, that in reality the thermal emittance from the roof surface, which determines the radiative heat exchange with the sky, is an important factor (particularly in low wind conditions) influencing the roof temperature [161],

- conductive heat transfer within the solid layers of HSC, wherein:

  - o thermo-physical parameters of each solid layer are isotropic and temperature-independent (Table 5.1),

- radiative heat exchange between the pipes and surfaces composing the air-cavity, wherein:

  - radiation attenuation in the air layer is neglected,
  - each surface of a solid layer forming the air-cavity is isoemissive,
  - inlet and outlet openings (Fig. 5.2) do not take part in the heat transfer by radiation. Such an approach is commonly used in numerical analyses of the heat transfer in the ventilated roof structures [29],

- convective-equivalent conductive heat exchange in the air-cavity of HSC, wherein:

  - air layer is treated as an orthotropic solid body in which the heat is exchanged by conduction only. The influence of convective heat exchange in the air-cavity due to the buoyancy-driven airflow caused by thermal gradients is considered by means of sol-air temperature dependent convective-equivalent horizontal and vertical thermal conductivity coefficients. The assumption of orthotropic material was aimed to distinguish the intensity of heat exchange caused by the airflow in the dominant flow direction (parallel to roofing surface),
  - heat exchange conditions between air layer and pipes are modified in order to improve assumed model of heat transfer,
  - magnitudes of convective-equivalent thermal conductivity coefficients together with the coefficients applied to modify the heat exchange conditions vary in dependence on current magnitudes of sol-air temperature and water mass flux. The relationships for each coefficient are determined on basis of additional CFD simulations of steady-state heat transfer process in the detailed 3D model of HSC (Section 5.2.5). It must

be noticed, however, that the wind effect on the air movement in the air-cavity is neglected in the implemented relationships,

  - parameters of density and specific heat for the air layer are isotropic and temperature-independent,

- forced convective heat transfer within the water flowing through the pipes, wherein:

  - water is treated as a non-viscous and incompressible fluid. In consequence, the buoyancy-driven water flow is not considered in the model,
  - uniform velocity field is considered in the entire computational domain of water. Thus, the heat exchange conditions in the near-wall region of the flowing fluid are modified in order to improve the assumed model of heat transfer. The coefficient applied to modify heat exchange conditions vary in dependence on current magnitudes of sol-air temperature and water mass flux. The relationships for each coefficient was determined on basis of additional CFD simulations of steady-state heat transfer process in the detailed 3D model of HSC (Section 5.2.5),
  - thermal conductivity and specific heat of water are isotropic and temperature-independent,

- convective and radiative heat exchange between the internal collector surface and building indoor.

With regard to above-mentioned physical assumptions, the following sub-sections presents the mathematical model of steady-state and unsteady heat transfer process considered in the FE model of HSC. The necessary steps for an implementation of the numerical model, from a discretization of the computational domain to a comparison with CFD model, among the others considerations, are widely described.

It is important to emphasize that the developed FE model applies results of the CFD analyses (Section 5.2.5). Such an approach allows to simulate the year-round operation of HSC, taking advantage of the accuracy gained from CFD simulations without computational costs.

5.3.2 Mathematical formulation

The FE model of HSC, developed for simulation of both steady-state and unsteady heat transfer, is assumed to be a 3D thermal system. With respect to considered mechanisms of heat transfer, the computational domain of HSC can be divided into

three regions, including sub-domain of solid layers, water flowing through the pipes and air-cavity (Fig. 5.33). For all the sub-domains it is assumed that thermal and mechanical problems are uncoupled.

With respect to specified physical assumptions, the following sub-sections describe the governing equations for heat transfer process considered in particular sub-domains of HSC model in the unsteady and steady-state approach, respectively. The initial and boundary conditions used to complete the governing equations are described.

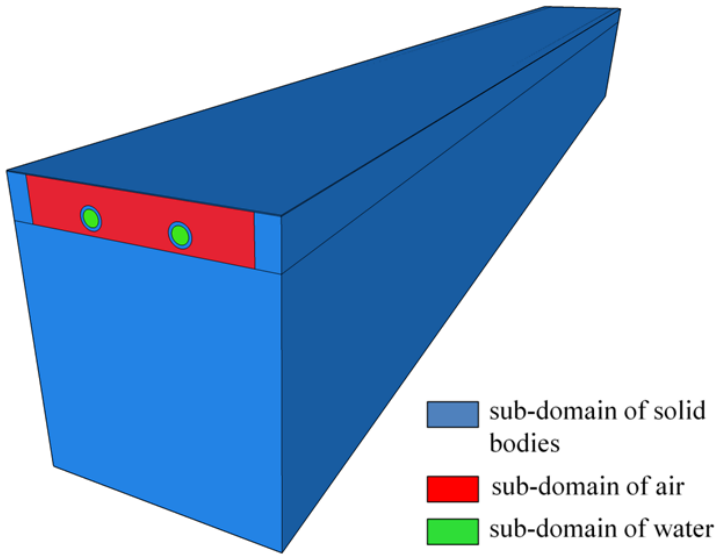

Figure 5.33: Division of computational domain with respect to heat transfer mechanisms considered in FE analysis

5.3.2.1 Unsteady approach

Heat transfer in solid layers

The process of heat transfer in a solid layers sub-domains is dominated by the conduction. The general form of governing differential equation describing the unsteady heat conduction in solid bodies (in vector notation) is [159]:

$$\frac{\partial \left(C_p \rho T\right)}{\partial t} = \nabla \cdot \left(\lambda \nabla T\right) + q_V, \tag{5.3.1}$$

where g_V is the internal heat source.

In the FE model, it was assumed that the thermo-physical properties of solid layers (listed in Table 5.1), including roofing, battens, polypropylene pipes and insulation layer, are isotropic and temperature-independent, and there are no internal heat

sources. Hence, the equation describing the unsteady heat conduction in the solid layers of HSC can be given as:

$$C_p \rho \frac{\partial T}{\partial t} = \lambda \nabla^2 T. \tag{5.3.2}$$

Heat transfer in water flowing through pipes

In the FE model of water flowing through the pipes, the heat exchange process is constrained to the conduction and forced convection. According to the control strategy assumed in order to investigate the capability of HSC to supply space-heating systems (Section 5.5), the average temperature of water flowing through the collector's pipes is kept between 20 °C and 25 °C. With regard to assumed range of water flow velocities, not exceeding 0.02 m/s, the laminar flow regime is to be considered throughout the time of collector operation (Section 5.2.2.1). In many practical problems, the flow of a conventional liquid, such as water, is incompressible to a high degree of accuracy [159]. Taking into account low magnitudes of flow velocities and low temperature variations in an operating fluid, it is reasonable to assume the water in HSC as an incompressible fluid. Assuming that the water density distribution remains uniform in space and constant in time, the continuity equation (Eq. 5.2.1) can be rewritten as:

$$\nabla \cdot \mathbf{U} = 0. \tag{5.3.3}$$

In the present model, it is also assumed that a viscosity of the water equals to zero. In general, the assumption of a non-viscous water is reasonable for low velocity fluid flows in a distance from surfaces of boundary walls [159] where the energy dissipation is negligible. With respect to the fluid flow problem under consideration, such an assumption results in a constant fluid flow velocity profile (Fig. 5.34a) in the entire computational domain. The velocity vector $\mathbf{U}$ is defined as:

$$\mathbf{U} = \begin{bmatrix} 0 \\ 0 \\ u_z \end{bmatrix}, \tag{5.3.4}$$

where u_z is the vector component along the main flow direction. This has, obviously, an impact on heat transfer process in the near-wall region. In case of the laminar flow of a viscous incompressible fluid, there is a thin layer near the pipe surface where the velocity decreases to zero (Fig. 5.34b). In this thin layer, the heat is transferred mostly by diffusion. Omitting of this phenomenon in the FE model might lead to

a significant errors in estimation of the heat exchange rate between the pipes and flowing water. In order to reach realistic results, it is reasonable to modify heat transfer conditions in the near-wall region of the flowing water. This was achieved through the usage of interface-type boundary condition for heat transfer between surfaces of polypropylene pipes and domains of water (Fig. 5.34c). The mathematical interpretation of applied approach is described later on.

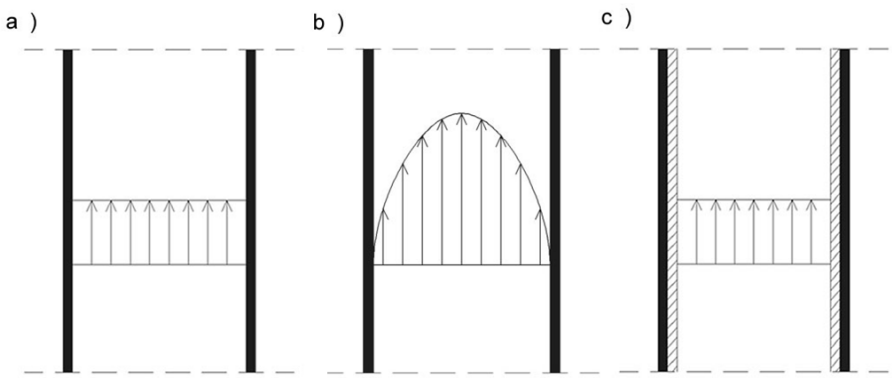

Figure 5.34: Velocity profiles for laminar flow of incompressible fluid according to a) non-viscous fluid model b) viscous fluid model c) applied approach

In the present model, the heat transfer is described by an extended form of the heat conduction equation (Eq. 5.3.2). Since the kinetic energy is negligible due to constant pressure flow field, the governing equation is derived from the internal energy balance equation [159]:

$$\rho \frac{\mathrm{D}e}{\mathrm{D}t} = \lambda \nabla^2 T - p \nabla \cdot \mathbf{U} + \phi + q_{V,} \tag{5.3.5}$$

where ϕ is the energy dissipation.

Substituting Eq. 5.3.3, neglecting the energy dissipation, ϕ, due to the assumption of a non-viscous fluid, and assuming no internal heat sources ($q_V = 0$), the internal energy balance equation (Eq. 5.3.5) becomes:

$$\rho \frac{\mathrm{D}e}{\mathrm{D}t} = \lambda \nabla^2 T. \tag{5.3.6}$$

Since the pressure effects are neglected, the following approximation may be introduced:

$$\mathrm{d}e = C_p \mathrm{d}T. \tag{5.3.7}$$

Substituting Eq. 5.3.7 into Eq. 5.3.6 results in a well-known Kirchhoff-Fourier energy equation:

$$C_p \rho \frac{\mathrm{D}T}{\mathrm{D}t} = \lambda \nabla^2 T. \tag{5.3.8}$$

Assuming that $u_x = u_y = 0$, the Kirchhoff-Fourier energy equation for the unsteady heat transfer problem considered in the FE model of water flowing through the pipes takes the form:

$$C_p \rho \left(\frac{\partial T}{\partial t} + u_z \frac{\partial T}{\partial z} \right) = \lambda \nabla^2 T. \tag{5.3.9}$$

The above equation is the same as the corresponding equation for heat transfer in solid layers (Eq. 5.3.2), except for the convection term. The assumed magnitudes of density, specific heat and thermal conductivity for the water sub-domain are $998.2\,\mathrm{kg/m^3}$, $4183\,\mathrm{J/(kg \cdot K)}$ and $0.599\,\mathrm{W/(m \cdot K)}$, respectively. The magnitudes are appropriate for water temperature of 20 °C [181]. In reality, variations of these parameters for the considered range of operating temperatures (between 20 °C and 35 °C) are negligible.

The above formulation of heat transfer process refers to the case when the maximum water temperature equal to 35 °C. Due to the control strategy (Section 5.5), such a condition occurs only if the target of the collector application is to supply a space-heating system based on seasonal heat storage systems. An additional aim of this study is to evaluate the ability of HSC to supply domestic hot water systems. According to the control strategy considered for this application, the water temperature can vary between 20 °C and 80 °C. For such conditions, the usage of the heat transfer model formulated for water flowing through the collector's pipes may result in the small errors, reduced by controlled convective heat transfer coefficient in the interface between water and pipe, determined on basis of CFD simulations (Section 5.2.5). However, the comparison of the FE model with CFD one should be conducted with regard to all the expected magnitudes of water temperature at outlets from the pipes.

Heat transfer in air-cavity

In opposition to the CFD model (Section 5.2), the FE model of HSC includes radiative heat exchange between surfaces composing the air-cavity and surfaces of collector's pipes. Since the air layer is considered as an orthotropic solid body

in terms of convective-equivalent thermal conductivity coefficients (Section 5.3), the analysis of an unsteady heat transfer process in the air-cavity required the governing equations of conduction and radiation to be included in the mathematical model.

The equation for the unsteady conductive heat transfer within the air layer is analogous to Eq. 5.3.2. The convective-equivalent horizontal, λ_{Heqv}, and vertical, λ_{Veqv}, thermal conductivity coefficients are dependent on current magnitudes of sol-air temperature, T_{sol}, and water mass flux, $\dot{m}$, whereas the other thermo-physical parameters are constant and temperature-independent. The adopted functions for convective-equivalent thermal conductivity coefficients are described in Section 5.2.5. The assumed magnitudes of density and specific heat for the air layer are $1.247\,\mathrm{kg/m^3}$ and $1006\,\mathrm{J/(kg \cdot K)}$, respectively. One should notice that in reality both the parameters vary in dependence on temperature change. It has, however, a negligible effect on the overall HSC performance. The assumed magnitudes of the parameters are in use for numerical simulation of solar collectors [75]. Up to this stage, the mathematical model includes indirectly an influence of the buoyancy-driven airflow on heat transfer process in the air-cavity. In general case, a reliable analysis of the heat exchange rate between surfaces forming the air-cavity and collector's pipes, due to the convective heat transfer, requires taking into account the thermal resistance of the near-wall region where the heat is transferred mostly by the diffusion. Similarly to the model of heat transfer in water flowing through the pipes, this was achieved by controlling convective heat transfer coefficient through the interface between surfaces of polypropylene pipes and the air-cavity sub-domain. An appropriate mathematical interpretation of the applied approach is described later on.

The radiative heat exchange between surfaces composing the air-cavity and surfaces of collector pipes is governed by the grey body radiation theory that means that the monochromatic emissivity of the body is independent of the wavelength of the radiation propagation. Accordingly, the radiative heat exchange between two differential surfaces in the air-cavity of HSC is defined by the following equation [139]:

$$Q_{1-2} = \epsilon_{1-2}\sigma F_1 \phi_{1-2}\left(T_1^4 - T_2^4\right), \tag{5.3.10}$$

where Q_{1-2} is the radiation heat flux between the bodies '1' and '2', ϵ_{1-2} is the emissivity between the bodies '1' and '2', σ is the Stefan-Boltzmann constant, F_1 is the surface area of body with temperature T_1, ϕ_{1-2} is the view factor (sometimes called a configuration factor or a shape factor), T_1 and T_2 are the absolute temperatures of bodies between which the heat exchange occurs.

For two finite areas F_1 and F_2, the view factor, ϕ_{1-2}, is given by [139]:

$$\phi_{1-2} = \frac{1}{F_1} \int_{F_1} \int_{F_2} \frac{\cos\beta_1 \cos\beta_2}{\pi R_{1-2}^2} \mathrm{d}F_1 \mathrm{d}F_2, \tag{5.3.11}$$

where β_1 and β_2 are the angles between the areas' normal, R_{1-2} is the distance between two differential areas. The view factor also satisfies the reciprocity relation:

$$F_1 \phi_{1-2} = F_2 \phi_{2-1}. \tag{5.3.12}$$

Boundary conditions

The boundary surfaces of solid layers, in which the heat is transferred by conduction, are shown in Fig. 5.35. Assuming that the collector separates indoor zones at fixed temperature from outdoor unsteady climate conditions, boundary conditions at the internal, S_i, and external, S_e, surfaces of HSC are defined by the Newton's law. A

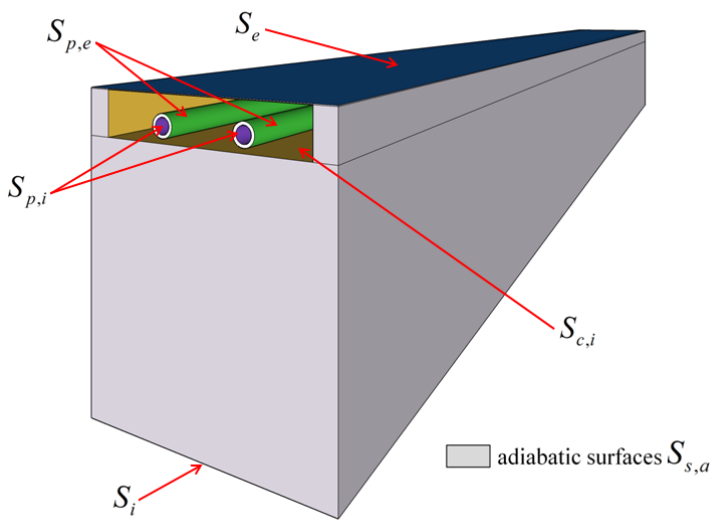

Figure 5.35: Boundary surfaces of solid bodies sub-domain in FE model

heat exchange rate by convection and radiation on the internal solar collector surface, S_i, is defined by the convective/radiative heat transfer coefficient, h_i. Consequently, the boundary condition at the internal collector surface, S_i, used to complete the energy equation is:

$$\lambda \frac{\partial T(\mathbf{x}, t)}{\partial \mathbf{n}} \bigg|_{S_i} = h_i \left[T_{S_i}(t) - T_{a,in} \right], \tag{5.3.13}$$

where T_{S_i} is the average temperature of the internal collector surface and $T_{a,in}$ is the indoor air temperature. The convective/radiative heat transfer coefficient, h_i, is con-

stant in time and defined according to the ISO standard [136] as $h_i = 8.1\,\mathrm{W/(m^2 \cdot K)}$. The indoor air temperature, $T_{a,in}$, is assumed to be constant in time throughout the unsteady simulation ($T_{a,in} = 20\,^\circ\mathrm{C}$).

A heat exchange between the external surface of the collector, S_e, and outdoor environment is considered by a convective and radiative heat exchange, separately. The convection is defined by the convective heat transfer coefficient for external collector surface, S_e, whereas the radiation is defined by the sol-air temperature, T_{sol}. Consequently, the boundary condition on external collector surface, S_e, is given as:

$$\lambda \frac{\partial T\left(\mathbf{x}, t\right)}{\partial \mathbf{n}}\bigg|_{S_e} = h_e\left(t\right)\left[T_{sol}\left(t\right) - T_{S_e}\left(t\right)\right], \tag{5.3.14}$$

where T_{sol} is the sol-air temperature and T_{S_e} is the average temperature of the external collector surface. According to the assumption of time-varying climate conditions, the so far presented formulations for the sol-air temperature (Eq. 5.2.72) and the convective heat transfer coefficient at external collector surface (Eq. 5.2.73) take the following form:

$$T_{sol}\left(t\right) = T_{a,out}\left(t\right) + \frac{\alpha I_e\left(t\right)}{h_e\left(t\right)}, \tag{5.3.15}$$

$$h_e\left(t\right) = \max\left[5, \frac{8.6 \cdot w_n\left(t\right)^{0.6}}{{L_b}^{0.4}}\right]. \tag{5.3.16}$$

Several FORTRAN subroutines were developed to read the data from the climate database [164] and modify current magnitudes of sol-air temperature and convective heat transfer coefficient at external collector surface for each time increment of the transient numerical simulation. To smooth out variations of the magnitudes, the time-dependent climate variables are approximated locally by a linear function.

A heat exchange between surfaces of two adjacent solid bodies, including roofing material, tilling battens, insulation is based on continuity assumptions. The equations describing the boundary conditions for the unsteady heat exchange between surfaces of two adjacent, among considered, solid bodies, $S_{s,1}$ and $S_{s,2}$, are represented as:

$$T\left(\mathbf{x}, t\right)|_{S_{s,1}} = T\left(\mathbf{x}, t\right)|_{S_{s,2}}, \tag{5.3.17}$$

$$q\left(\mathbf{x},t\right)|_{S_{s,1}} = q\left(\mathbf{x},t\right)|_{S_{s,2}}, \tag{5.3.18}$$

where q is the heat flux in a direction normal to the surface.

Through the analogy are formulated the equations describing the boundary conidtions for unsteady heat exchange between surfaces of air-cavity layer, $S_{a,e}$ (Fig. 5.36), being adjacent to the surfaces of solid bodies, $S_{c,i}$.

For the heat exchange between surfaces of the collector pipe and the air layer, being in proximity to one another, an interface is used. The mathematical form of the interface is that of a Cauchy type given below as:

$$-\lambda\frac{\partial T\left(\mathbf{x},t\right)}{\partial\mathbf{n}}\bigg|_{S_{a,i}} = -\lambda\frac{\partial T\left(\mathbf{x},t\right)}{\partial\mathbf{n}}\bigg|_{S_{p,e}} = k_{a-p}\left(T_{S_{a,i}}\left(t\right) - T_{S_{p,e}}\left(t\right)\right), \tag{5.3.19}$$

where $S_{a,i}$ is the air layer surface (Fig. 5.36) being adjacent to the external pipe surface $S_{p,e}$, k_{a-p} is the heat transfer coefficient describing the resistance to heat flow across the air-pipe interface, $T_{S_{a,i}}$ and $T_{S_{p,e}}$ are the local surface temperatures. The magnitude of k_{a-p} vary in time in dependence on sol-air temperature, T_{sol}, and water mass fllux, $\dot{m}$, hence, providing modified heat transfer conditions between the air layer and external pipe surfaces. In reality, the thermal resistance for down-pipe and up-pipe differs due to characteristics of airflow in the cavity. Thus, the two separate functions of $k_{a-p}\left(T_{sol},\dot{m}\right)$ for the lower and top pipe were estimated on basis of the CFD analyses (Section 5.2.5). The functions were implemented in the FORTRAN subroutine in order to modify the heat exchange rate at each time-increment of the FE transient simulation.

On other surfaces of solid bodies, $S_{s,a}$, and air-cavity, $S_{a,a}$, the adiabatic boundary conditions are prescribed. In other words, no heat transfer across these surfaces is allowed. The adiabatic boundary condition used to complete the equation governing the unsteady heat transfer for $S_{s,a}$ is represented as:

$$-\lambda\nabla T\left(\mathbf{x},t\right)|_{S_{s,a}} = q|_{S_{s,a}} = 0. \tag{5.3.20}$$

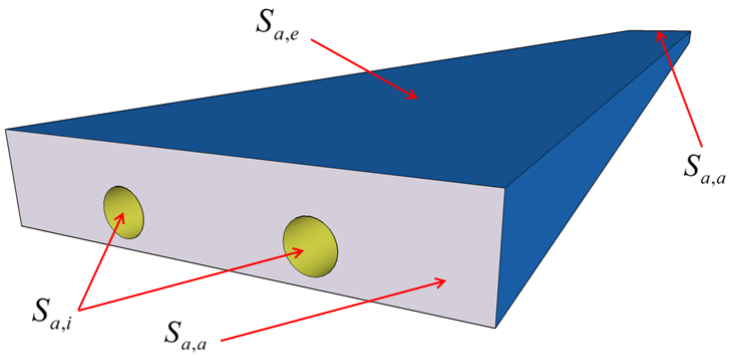

Figure 5.36: Boundary surfaces of air-cavity sub-domain in FE model

The sub-domain of water refers to water-down and water-up models (Fig. 5.37). Both the models are the same in terms of prescribed boundary condition, hence the following equations are referred to a single model of water. The water flows into the domain across the inlet water surface, $S_{w,in}$, and flows out through the outlet water surface, $S_{w,out}$. In the FE model, it is assumed that fluid flow velocity is uniform for

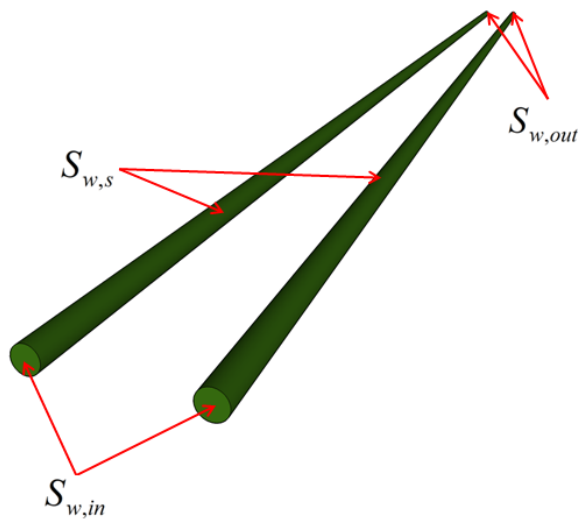

Figure 5.37: Boundary surfaces of water sub-domain in FE model

entire domain of water. Its magnitude varies throughout the transient simulation in dependence on outlet water temperature (Section 5.5). The Kirchhoff-Fourier energy equation (Eq. 5.3.9) requires to define explicit water velocities vector in each node of the FE mesh. The water flow velocity, $u_w(t)$, is computed from the water mass flux, $\dot{m}$, and the water density, ρ, according to Eq. 5.2.18. A FORTRAN subroutine was developed to control the water velocity at each time increment and in each mesh node during the unsteady heat transfer simulation in HSC.

According to made assumptions (Section 5.5), the water temperature at the inlet water surface, is uniform (equal to 20 °C) and constant in time. The Dirichlet boundary condition used to describe the temperature distribution at the inlet water surface, $S_{w,in}$, is given as:

$$T\left(\mathbf{x},t\right)\big|_{S_{w,in}} = T_{w,in} = 20\,^{\circ}\mathrm{C}, \tag{5.3.21}$$

where $T_{w,in}$ is the inlet water temperature.

At the outlet water surface, $S_{w,out}$, the temperature gradient along the vector normal to the surface is constant in time and equal to zero. Therefore, the boundary condition is given as:

$$\left.\frac{\partial T\left(\mathbf{x},t\right)}{\partial \mathbf{n}}\right|_{S_{w,out}} = 0. \tag{5.3.22}$$

For the heat exchange between surfaces of a collector pipe, $S_{p,i}$, and a domain of water, $S_{w,s}$, being in proximity to one another, an interface is prescribed through the analogy to Eq. 5.3.19 as follows:

$$-\lambda\left.\frac{\partial T\left(\mathbf{x},t\right)}{\partial \mathbf{n}}\right|_{S_{p,i}} = -\lambda\left.\frac{\partial T\left(\mathbf{x},t\right)}{\partial \mathbf{n}}\right|_{S_{w,s}} = k_{w-p}\left(T_{S_{p,i}}\left(t\right) - T_{S_{w,s}}\left(t\right)\right). \tag{5.3.23}$$

where $S_{w,s}$ is the water layer surface being adjacent to the internal pipe surface $S_{p,i}$, k_{w-p} is the heat transfer coefficient describing the resistance to heat flow across the water-pipe interface, $T_{S_{p,i}}$ and $T_{S_{w,s}}$ are the local surface temperatures. The magnitude of convective heat transfer coefficient describing the resistance to heat flow across the water-pipe interface, k_{w-p}, vary in time and in dependence on sol-air temperature, T_{sol}, and water mass flux, $\dot{m}$, hence, providing modified convective heat transfer conditions between flowing water and internal pipe surface. Two different functions of $k_{w-p}\left(T_{sol},\dot{m}\right)$ for the lower and top pipe were estimated on basis of CFD analyses (Section 5.2.5). The functions were implemented in the FORTRAN subroutine in order to modify the heat exchange rate at each time-increment of the FE transient simulation.

Initial conditions

The initial conditions ($t = 0$) for the unsteady heat transfer analysis were prescribed for the temperature distribution in the entire computational domain $T(\mathbf{x}, 0)$, water flow velocity, $u_w(0)$, convective heat transfer coefficient of external collector surface, $h_e(0)$, and sol-air temperature, $T_{sol}(0)$. Since the parameters of convective-equivalent horizontal, λ_{Heqv}, and vertical, λ_{Veqv}, thermal conductivity coefficients, heat transfer coefficients describing the resistance to heat flow across the water/pipe-down, $k_{w-p,down}$, and water/pipe-up interfaces, $k_{w-p,up}$, and heat transfer coefficients describing the resistance to heat flow across the air/pipe-down, $k_{a-p,down}$, and air/pipe-up interfaces, $k_{a-p,up}$, are dependent on sol-air temperature and water mass flux, it is necessary to apply appropriate magnitudes of these parameters in the model. The initial conditions, considered for the unsteady analysis, are as follows:

- temperature distribution, $T(\mathbf{x}, 0)$, in the computational domain is obtained from a simulation of the steady-state heat transfer in HSC. The equations governing the steady-state heat transfer (Eq. 5.3.24 and Eq. 5.3.25) are completed with appropriate boundary conditions (Eq. 5.3.26, 5.3.27, 5.3.28, 5.3.29, 5.3.30, 5.3.31, 5.3.32, 5.3.33, 5.3.34, 5.3.35). The magnitudes of convective heat transfer coefficient at external collector surface (h_e) and sol-air temperature (T_{sol}) are pre-calculated for data corresponding to the first hour of considered climate database. The magnitudes of convective-equivalent thermal conductivity coefficients for the air layer (λ_{Heqv} and λ_{Veqv}) and magnitudes of heat transfer coefficients describing the resistance to heat flow across the water/pipe interfaces ($k_{w-p,down}$ and $k_{w-p,up}$) and the air/pipe interfaces ($k_{a-p,down}$ and $k_{a-p,up}$) correspond to a pre-calculated magnitude of sol-air temperature and water mass flux equal to zero. The applied approach to determine the temperature distribution is reasonable, since the structure components of HSC are characterized by relatively low thermal inertia. The zero-magnitude of water mass flux comes directly from the following assumption for $u(0)$,

- for all the executed simulations of unsteady heat transfer in HSC, the considered climate database starts up from the beginning of 1st of January. Since, it is a time when $I = 0\,\mathrm{W/m^2}$, the water flow through the pipes is stopped. Hence, the initial condition for a water flow velocity is given as $u_w(0) = 0\,\mathrm{m/s}$,

- convective heat transfer coefficient of external collector surface and sol-air temperature at $t = 0$, as well as dependent parameters aimed at modifying thermal properties of the air layer (λ_{Heqv} and λ_{Veqv}) and heat exchange conditions on

inner ($k_{w-p,down}$ and $k_{w-p,up}$) and outer ($k_{a-p,down}$ and $k_{a-p,up}$) pipes' surfaces, are the same as in the steady-state simulation.

5.3.2.2 Steady-state approach

The mathematical model of the steady-state three-dimensional heat transfer problem in HSC is formulated through the analogy to the unsteady approach.

The conductive heat transfer in the solid bodies of FE model is governed by the following equation:

$$\nabla^2 T = 0. \tag{5.3.24}$$

The Kirchhoff-Fourier energy equation for the steady-state heat transfer problem considered in the FE model of water flowing through the pipes of HSC takes the form:

$$C_p \rho u_z \frac{\partial T}{\partial z} = \lambda \nabla^2 T. \tag{5.3.25}$$

The equation describing conductive heat transfer in the air layer is analogous to Eq. 5.3.24. The magnitudes of convective-equivalent thermal conductivity coefficients for air layer (λ_{Heqv} and λ_{Veqv}) correspond to the pre-calculated magnitude of sol-air temperature and the considered magnitude of water mass flux. The equation describing the radiative heat exchange between surfaces composing the air-cavity and surfaces of the collector's pipes is analogous to Eq. 5.3.10.

The boundary conditions used to complete equations governing the steady-state heat transfer process in HSC are defined as follows:

- at the internal collector surface, S_i:

$$\lambda \left. \frac{\partial T(\mathbf{x})}{\partial \mathbf{n}} \right|_{S_i} = h_i \left[T_{S_i} - T_{a,in} \right], \tag{5.3.26}$$

- at the external collector surface, S_e:

$$\lambda \left. \frac{\partial T(\mathbf{x})}{\partial \mathbf{n}} \right|_{S_e} = h_e \left[T_{sol} - T_{S_e} \right], \tag{5.3.27}$$

  where the sol-air temperature, T_{sol}, and convective heat transfer coefficient at external collector surface, h_e, are calculated according to Eq. 5.2.72 and Eq. 5.2.73, respectively, with respect to specified climate data,

- at the adjacent surfaces of solid bodies, $S_{s,i}$, and air-cavity layer, $S_{a,e}$, and surfaces of two adjacent solid layers: $S_{s,1}$ and $S_{s,2}$:

$$T\left(\mathbf{x}\right)|_{S_{s,1}} = T\left(\mathbf{x}\right)|_{S_{s,2}}\,, \tag{5.3.28}$$

$$q\left(\mathbf{x}\right)|_{S_{s,1}} = q\left(\mathbf{x}\right)|_{S_{s,2}}\,. \tag{5.3.29}$$

- for the heat exchange between surfaces of the collector pipe, $S_{p,e}$, and the air layer, $S_{a,i}$:

$$-\lambda\frac{\partial T\left(\mathbf{x}\right)}{\partial \mathbf{n}}\bigg|_{S_{p,e}} = -\lambda\frac{\partial T\left(\mathbf{x}\right)}{\partial \mathbf{n}}\bigg|_{S_{a,i}} = k_{a-p}\left(T_{S_{a,i}} - T_{S_{p,e}}\right), \tag{5.3.30}$$

  where the magnitudes of convective heat transfer coefficients describing the resistance to heat flow across the air/pipe interfaces ($k_{a-p,down}$ and $k_{a-p,up}$) correspond to the pre-calculated magnitude of sol-air temperature and the considered magnitude of water mass flux,

- at the adiabatic surfaces: $S_{s,a}$ and $S_{a,a}$:

$$-\lambda\nabla T\left(\mathbf{x}\right)|_{S_{s,a}} = q|_{S_{s,a}} = 0, \tag{5.3.31}$$

- for the water flow at the inlet water surface, $S_{w,in}$:

$$\mathbf{n}\cdot\mathbf{U}|_{S_{w,in}} = u_w, \tag{5.3.32}$$

- at the inlet water surface, $S_{w,in}$:

$$T\left(\mathbf{x}\right)|_{S_{w,in}} = T_{w,in} = 20\,^{\circ}\mathrm{C}, \tag{5.3.33}$$

- at the outlet water surface, $S_{w,out}$:

$$\frac{\partial T\left(\mathbf{x}\right)}{\partial \mathbf{n}}\bigg|_{S_{w,out}} = 0, \tag{5.3.34}$$

- for the heat exchange between surfaces of a collector pipe, $S_{p,i}$, and a domain of water, $S_{w,s}$:

$$-\lambda\frac{\partial T\left(\mathbf{x}\right)}{\partial \mathbf{n}}\bigg|_{S_{p,i}} = -\lambda\frac{\partial T\left(\mathbf{x}\right)}{\partial \mathbf{n}}\bigg|_{S_{w,s}} = k_{w-p}\left(T_{S_{p,i}} - T_{S_{w,s}}\right), \tag{5.3.35}$$

  where the magnitudes of convective heat transfer coefficients describing the resistance to heat flow across the water/pipe interfaces ($k_{w-p,down}$ and $k_{w-p,up}$) correspond to pre-calculated magnitude of sol-air temperature and considered magnitude of water mass flux.

5.3.3 Numerical approach

In this study, the commercial software package ABAQUS v 6.10 [49] is employed to solve the assumed mathematical model of unsteady and steady-state heat transfer in HSC. The software uses Finite Element Method which is thoroughly explained by Bathe [16] and Lewis et al. [110]. The computational domain of HSC is approximated geometrically with the first-order hexahedral heat transfer finite elements. The temperature approximation over each element is expressed in terms of the nodal temperatures and first-order polynomials in three dimensions as:

$$T = N^N(\mathbf{x})\,T^N, \quad N = 1, 2, ..., \tag{5.3.36}$$

where T^N are the nodal temperatures and N^N are the shape functions. The finite element equation for the three-dimensional heat conduction within solid bodies is derived by Galerkin method, whereas the Petrov-Galerkin discretization method [184] is applied for the heat transfer problem in the water flowing through collector's pipes. To approximate variations of the time-dependent variables, an implicit scheme with a backward difference algorithm is used. The linear system of algebraic equations that arises from the Newton procedure is solved directly with the Gaussian elimination algorithm.

The ABAQUS approach for unsteady heat transfer in a flowing fluid introduces a limit on the time increment, Δt. For a numerical stability, the local Courant number, defined by Eq. 5.3.37, must be less than or equal to 1.

$$C = u\frac{\Delta t}{b}, \tag{5.3.37}$$

where u is the water velocity over the element and b is the characteristic length measure. The water flow velocity at each time increment is computed from the water mass flux and fluid density (Eq. 5.2.18). Since the second parameter is assumed to be constant in time, the maximum time increment is related to the magnitude of water mass flux. According to the assumed control strategy (Section 5.5) the water mass flux can vary from 0 to 19 kg/(m^2·s) at each time increment of the unsteady analysis. Since the maximum time increment is a critical issue for the computational time, a set of preliminary simulations of unsteady heat transfer in HSC was carried out in order to determine a relationship between the water mass flux, $\dot{m}$, and the maximum time increment, Δt. A relationship between $\dot{m}$ and Δt is demonstrated in Fig. 5.38. The relationship can be approximated by the function $f(\dot{m})$:

$$f(\dot{m}) = 101.3\ \dot{m}^{-1.02}. \tag{5.3.38}$$

The function $f(\dot{m})$ is implemented in the FORTRAN subroutine to control the magnitude of current time increment. The maximum magnitude of the time increment is, however, limited to the value of 900 seconds.

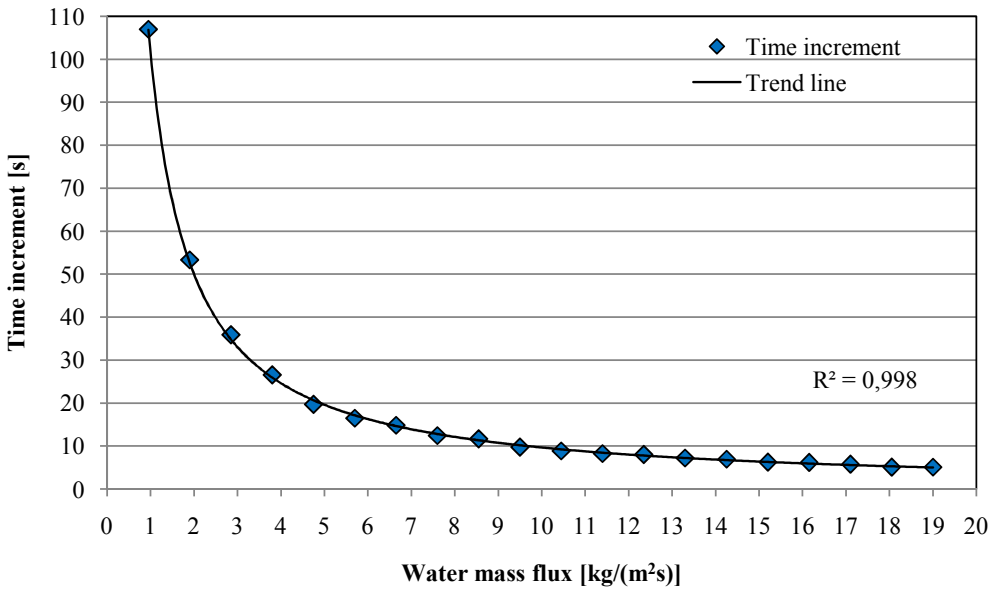

Figure 5.38: Relationship between water mass flux $\dot{m}$ and maximum time increment Δt

In the following, the process of finite element discretization together with the results comparison between the FE model and CFD model are described.

5.3.3.1 Mesh generation

The solution of differential equations using FEM requires the subdivision of the calculation domain into a finite number of elements, hence forming the so-called computational mesh. In this study, the first-order finite elements were used. The domain of FE model consists of 9 parts, such as: roofing material, two battens, air layer, two pipes, two parts of water flowing through collector pipes and insulation layer. With regard to the employed thermal modeling approach (Section 5.1), the air layer is considered as a solid body. In consequence, the computational domain of FE model can be divided into two regions (Fig. 5.39), which are discretized by different types of finite elements. The region of solid bodies is discretized with the diffusive heat transfer 8-node linear brick elements DC3D8 [49]. In turn, the region of the water flowing through collector pipes is discretized with convection/diffusion 8-node elements with a dispersion control DCC3D8D [49]. The use of elements with a dispersion control was reasonable since unsteady effects in the fluid are critical for the solution.

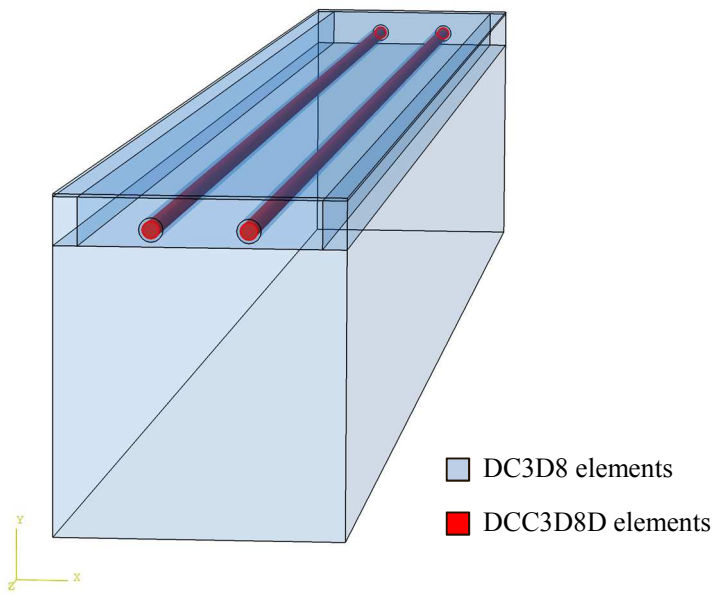

Figure 5.39: Division of FE model domain with respect to type of finite elements

A fine domain discretization into finite elements is a basic step in FEM analysis, since the quality of the mesh has a great influence on the results accuracy. In general, an increased number of finite elements yields a better representation of the model geometry. A rule of thumb is that more finite elements improve the accuracy of results in FEM analysis, but at the cost of longer computations run-time. Finding the point of intersection between an acceptable number of finite elements and time of calculation, is usually the main difficulty at the meshing stage. The following sub-sections are related to development of an appropriate mesh design for FE model of considered geometry.

In this study, the employed meshing approach is highly related to the model geometry and formulated heat transfer problem (Section 4.2.1). As the convective heat exchange within the air layer is considered indirectly by the equivalent solid body, the radiative heat exchange has a predominant contribution in the heat transmission from surfaces forming the air-cavity to pipes. This makes the number of facets composing surfaces of pipe parts to be a main criterion to develop an appropriate mesh design. Due to a complex geometry of the HSC model, the main problem of meshing was to keep the number of facets composing the surfaces of pipe parts in an acceptable range while providing a high quality mesh for the air layer part. In order to design the mesh more effectively, the part of the air layer was divided into 10 separated parts, two of which are referred to regions of complex geometry containing the channels for the pipe parts. As a consequence, the considered FE model is an assembly of 18 parts (Fig. 5.40), 16 of which are characterized by an uncomplicated

geometry. This approach enables to use structure brick elements in most regions of the FE model, hence reducing the time of calculations.

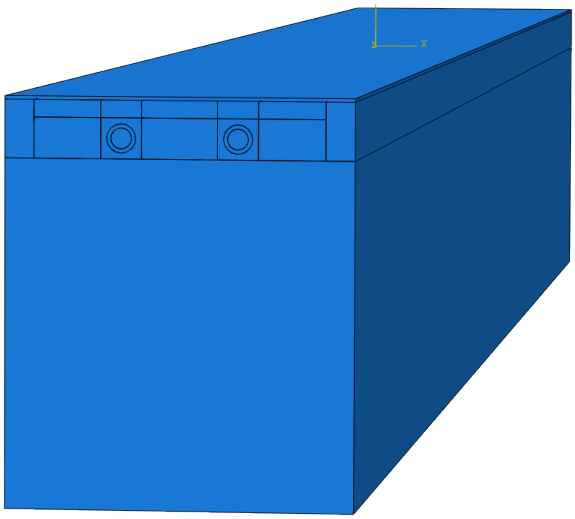

Figure 5.40: Assembly of parts forming FE model of HSC

Further improvements of a mesh design were achieved by making several partitions on faces of the parts that are adjacent to the air layer part. In general, a partitioning enables to divide it into more cells. More cells make the node seeding on edges of a particular part easier, hence a better control on a mesh design is obtained. The partitions in $xy-$ plane were made on faces of the roofing material, battens and insulation layer part. The partitions correspond to the layout of parts composing the air layer part. The final representation of the FE model assembly including the partitioning of each sub-model is presented in Fig. 5.41.

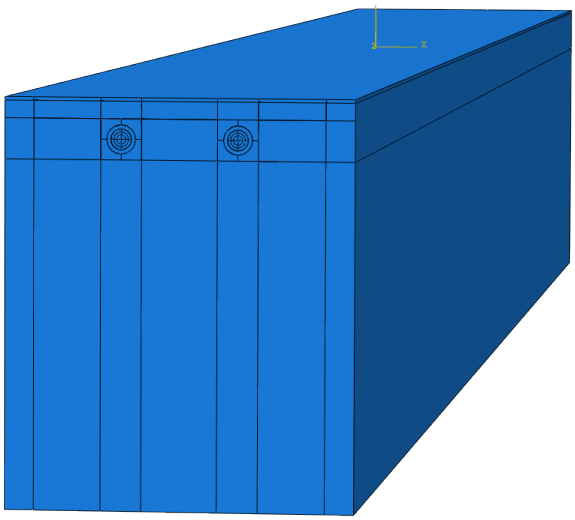

Figure 5.41: Final representation of FE model assembly including partitioning of each part

Fig. 5.42 shows an exemplary mesh design for the FE model of HSC based on the described meshing approach. The mesh is characterized by a continuity of nodes between consecutive parts of the model. Small elements of a similar shape are used to develop regions of a high influence on the heat exchange in HSC. In turn, larger elements are used to develop regions of a low influence. The presented exemplary FE model represents, however, only one of possible mesh discretizations. To give a final representation of the FE model, characterized by the high accuracy of the results at the low cost of the calculation time, it is necessary to conduct analysis of the mesh density effect on the results.

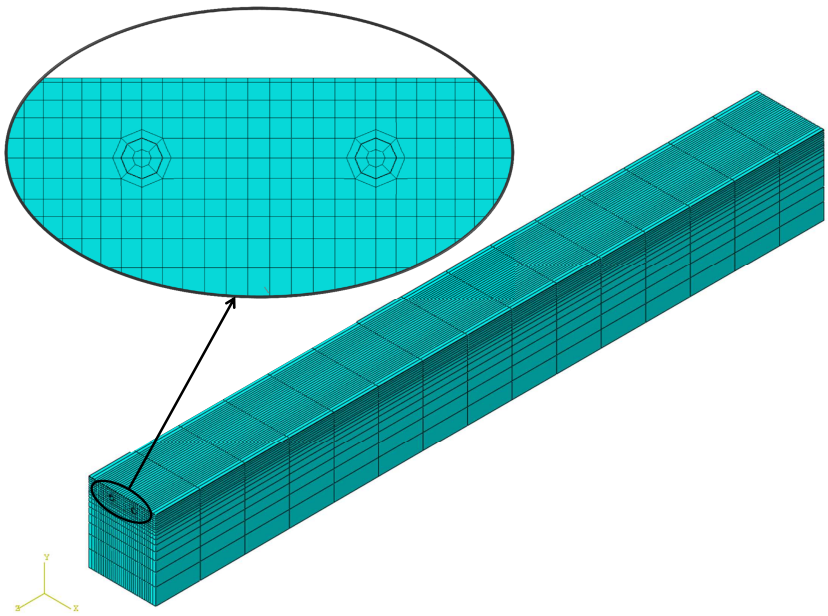

Figure 5.42: Example of domain discretization

5.3.3.1.1 Mesh independence test

The final domain discretization of the developed FE model follows from 3 stages of mesh independence test based on series of steady-state simulations. Two first stages concern the mesh design in the $xy-$plane where the second concerns the fluid parts only. The last stage concerns the mesh design in the $z-$axis direction. The outlet water temperature, $T_{w,out}$, defined as Eq. 5.4.1, was chosen as the criterion of the mesh density independence for all the stages. The approximated time required to conduct the unsteady simulation of the annual collector operation for each mesh design is also presented. The boundary conditions assumed for all the simulations are determined with regard to analogous magnitudes as in case of mesh independence test for CFD model (Section 5.2.3.1).

Mesh density in $xy-$plane

Each model differed solely with respect to the mesh density in the $xy-$plane. Each mesh is influenced by the number of facets composing the surfaces of pipe parts. For FE models in which the facets number in the $xy-$plane was 8, 16, 24, 32, 40, 48, the number of finite elements in the $xy-$plane was 284, 593, 1036, 1939, 2081, 2167, respectively. The mesh density in the $z-$axis direction was identical for all FE models (15 sections on 3m length). The same boundary conditions were prescribed for each model.

The obtained results indicate a strong non-linear relationship between the mesh density and predicted outlet fluid temperature (Fig. 5.43). An increase of the mesh density in the $xy-$plane decreases the outlet fluid temperature. The difference in results between FE models, characterized by the highest and the lowest mesh density, is over 14.2 %. The FE model composed of 1036 finite elements (corresponding to 24 facets at the pipe surfaces) in the $xy-$plane was adopted for the next stage of analyses. As compared to the FE model with the highest mesh density, the difference in the outlet water temperature does not exceed 1.5 %.

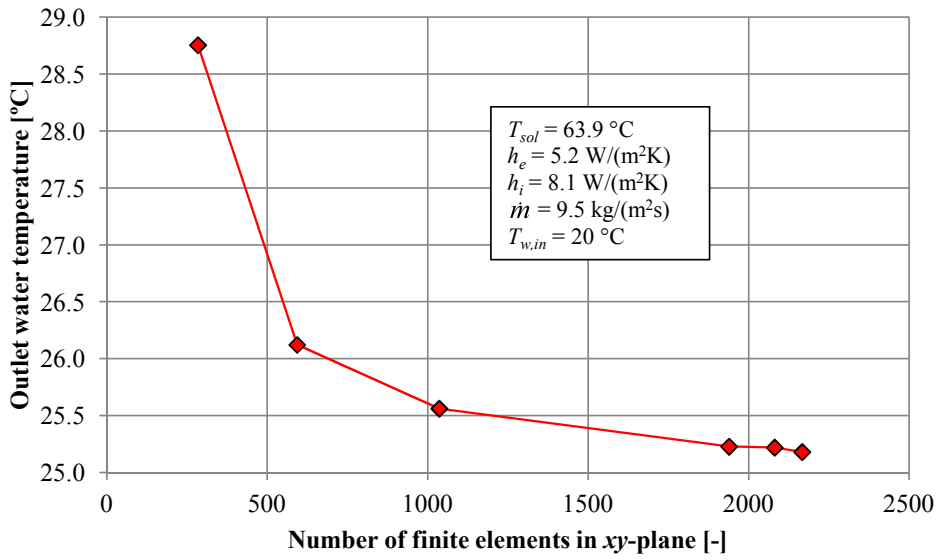

Figure 5.43: Mesh independence test in xy-plane

Mesh density in fluid parts

Considering results from the previous stage, additional steady-state simulations were conducted to estimate the effect of the fluid mesh density in the $xy-$plane on the performance of HSC. The models differed solely in the fluid mesh density in the $xy-$plane. The number of finite elements composing the cross-section of fluid parts for each FE model was 88, 112, 136, 160, 184, respectively. The same boundary

conditions were prescribed for each model.

The obtained results indicate a positive and almost linear relationship between the mesh density of fluid parts and predicted outlet water temperature (Fig. 5.44). The maximum difference in obtained results is negligibly small and equals to 0.25 %. Therefore, there is no need to increase the mesh density for fluid parts. The FE model in which the fluid parts in the $xy-$ plane are composed of 88 finite elements was adopted for the next stage of analyses.

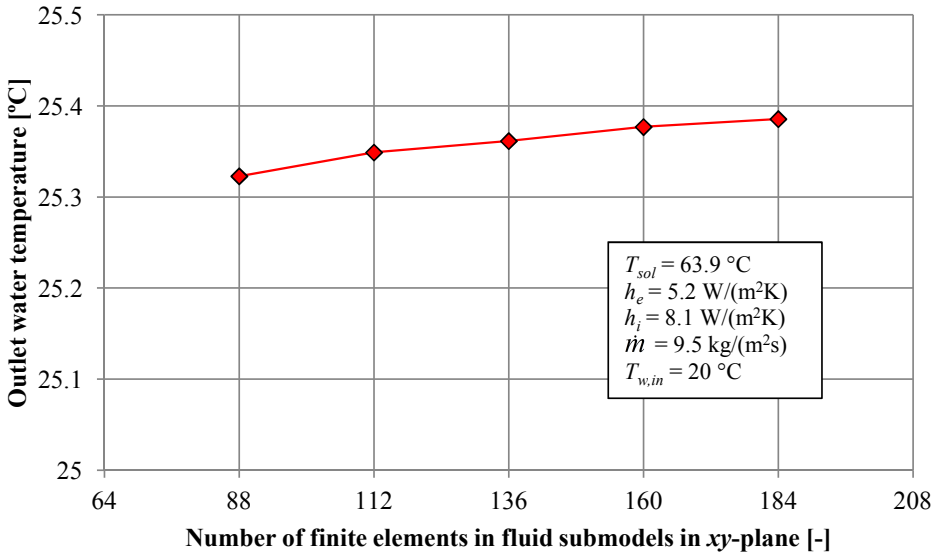

Figure 5.44: Mesh independence test for fluid parts in xy-plane

Mesh density in $z-$ axis direction

This stage employed the same method as previously. It was, however, very time-expensive due to a high increase of the total number of finite elements with a change of the mesh density in the $z-$axis direction. Therefore, it was reasonable to conduct this analysis as a last stage. In total, 9 FE models were developed. Each FE model was characterized by the identical mesh density in the $xy-$ plane (adopted from the previous stage). The number of mesh sections in the $z-$ axis direction for each FE model was 15, 18, 21, 24, 27, 30, 33, 36, 39, respectively. The same boundary conditions were prescribed for each model.

The obtained results of steady-state simulations indicate a strong non-linear relationship between the mesh density and predicted outlet water temperature (Fig. 5.45). An increase of the mesh density increases the outlet water temperature. This is due to an increase of facets taking part in a radiative heat exchange in the air-cavity. A maximum difference in the results between FE models is small and does not exceed 2.8 %. The FE model composed of 24 sections in the $z-$ axis direction was

recognized to be appropriate in order to conduct the thermal performance analysis of HSC. A further increase of the mesh density does not significantly influence the outlet water temperature. If the number of mesh sections at the length of pipes grows from 24 up to 39, the refined mesh will only slightly improve the accuracy of the predicted outlet water temperature, with the difference not exceeding 1.7 %.

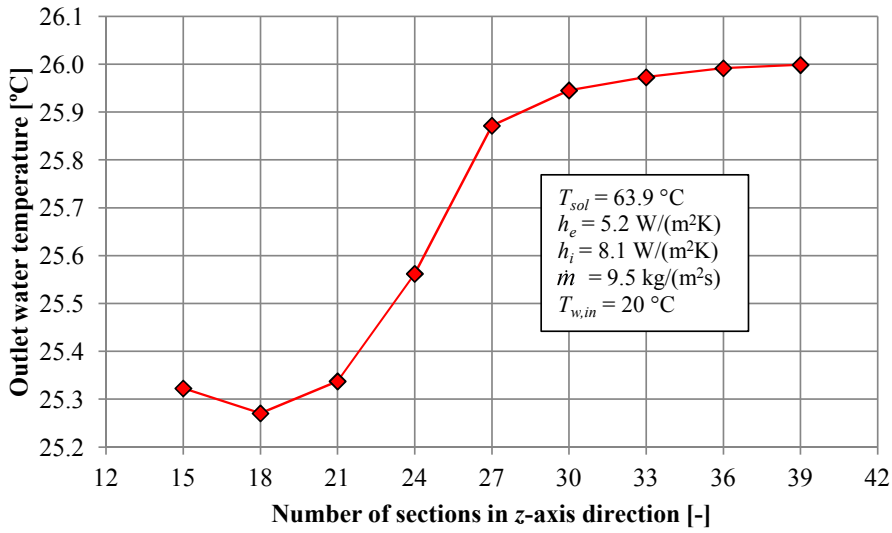

Figure 5.45: Mesh independence test in $z-$ axis direction

5.3.3.1.2 Final representation of FE model

The final FE model of HSC used for unsteady and steady-state simulations is composed of 24864 finite elements. The mesh for the complete model, solid bodies and fluid parts is demonstrated in Figs. 5.46–5.48.

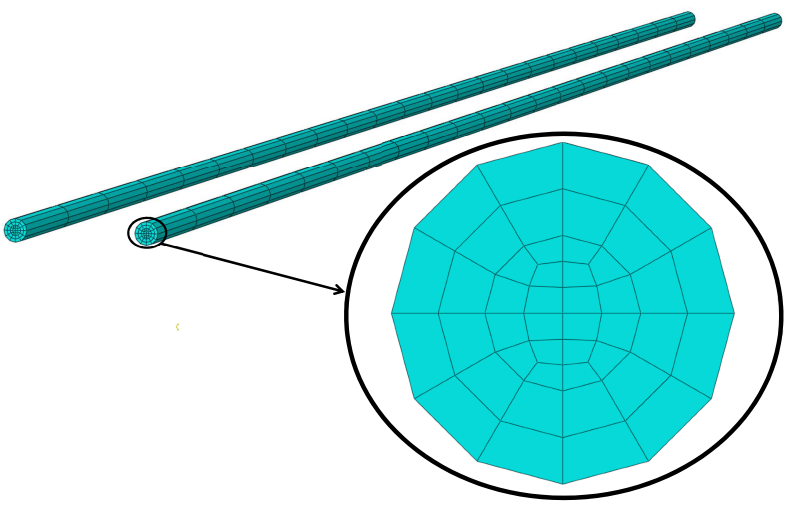

Figure 5.46: FE model of fluid parts discretized with convection/diffusion 8-node elements with dispersion control

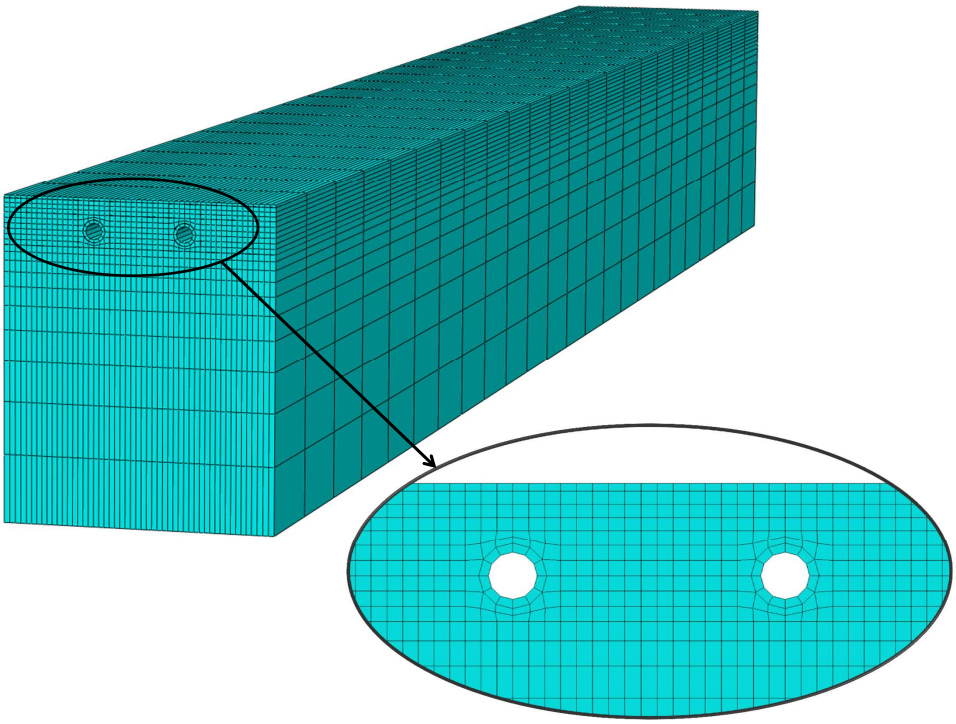

Figure 5.47: FE model of solid bodies discretized with diffusive heat transfer 8-node linear brick elements

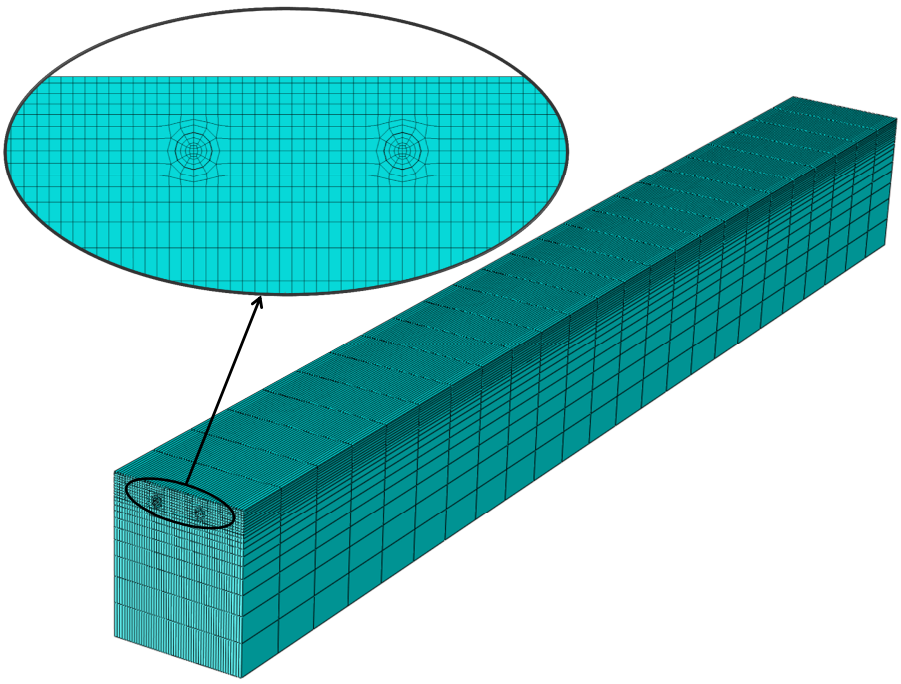

Figure 5.48: Complete FE model of hidden solar collector

5.3.4 Results comparison between FE model and CFD model

The FE model developed for the performance analysis of HSC during a year-round operation applies a simplified approach to simulate the convective heat transfer in both air-cavity and water flowing through the collector's pipes. Since the proper simulation of heat transfer in these domains is crucial to reach the main objective of this study, it was necessary to compare the results of FE model with the results of the equivalent CFD model. It was achieved by carrying out the FEM analyses of steady-state heat transfer process in HSC and comparing its results to the results obtained from the CFD analyses. As the CFD model used for the purpose of this analyses (Section 5.2.1) does not consider the radiative heat exchange between the pipes and surfaces composing the air-cavity, the so far developed FE model of steady-state heat transfer in HSC (Section 5.3.2.2) had to be appropriately modified (neglecting Eq. 5.3.10 in the mathematical model). Such an approach is reasonable since the CFD model was positively validated against the analytical solution (Section 5.2.4). The magnitude of water temperature at the outlets from the pipes (Eq. 5.4.1) is an efficiency index used for the comparison purpose. Predictions were executed for 15 computational cases. All the cases differ with boundary conditions for the heat transfer on the external collector surface and the water flow velocity in pipes. Variations of these boundary conditions are based on considered magnitudes of the sol-air temperature (60, 120 and 180 °C) and the water mass flux (0.95, 5.5, 10, 14.5 and 19 kg/(m^2·s)). For the purpose of FEM analysis, the sol-air temperature and water mass flux dependent parameters are appropriately modified in the model. In both the CFD and FE model, the magnitude of convective heat transfer coefficient on external collector surface, h_e, corresponds to the average daytime (when $I > 0\,\mathrm{W/m^2}$) climate conditions of the summer season and equals to $5.2\,\mathrm{W/(m^2 \cdot K)}$. The selected cases are in a scope of boundary conditions simulated in the unsteady heat transfer process.

Fig. 5.49 illustrates a comparison between results obtained for both models. The obtained magnitudes of water outlet temperature ranges from 21 °C to 65 °C for the CFD approach, and 21 °C to 90 °C for the FEM approach. Hence, the conclusions from this analysis refer to both the applications of HSC investigated in this study. The analysis demonstrates that the FE model tends to overestimate the outlet water temperature for the entire ranges of considered water mass flux and sol-air temperatures. The calculated error between results obtained from the CFD and FEM simulations varies from 4 % to 41 %. The level of discrepancy between the results depends on the water mass flux magnitudes rather than the magnitude of sol-air temperature. For the computational cases in which the water mass flux is

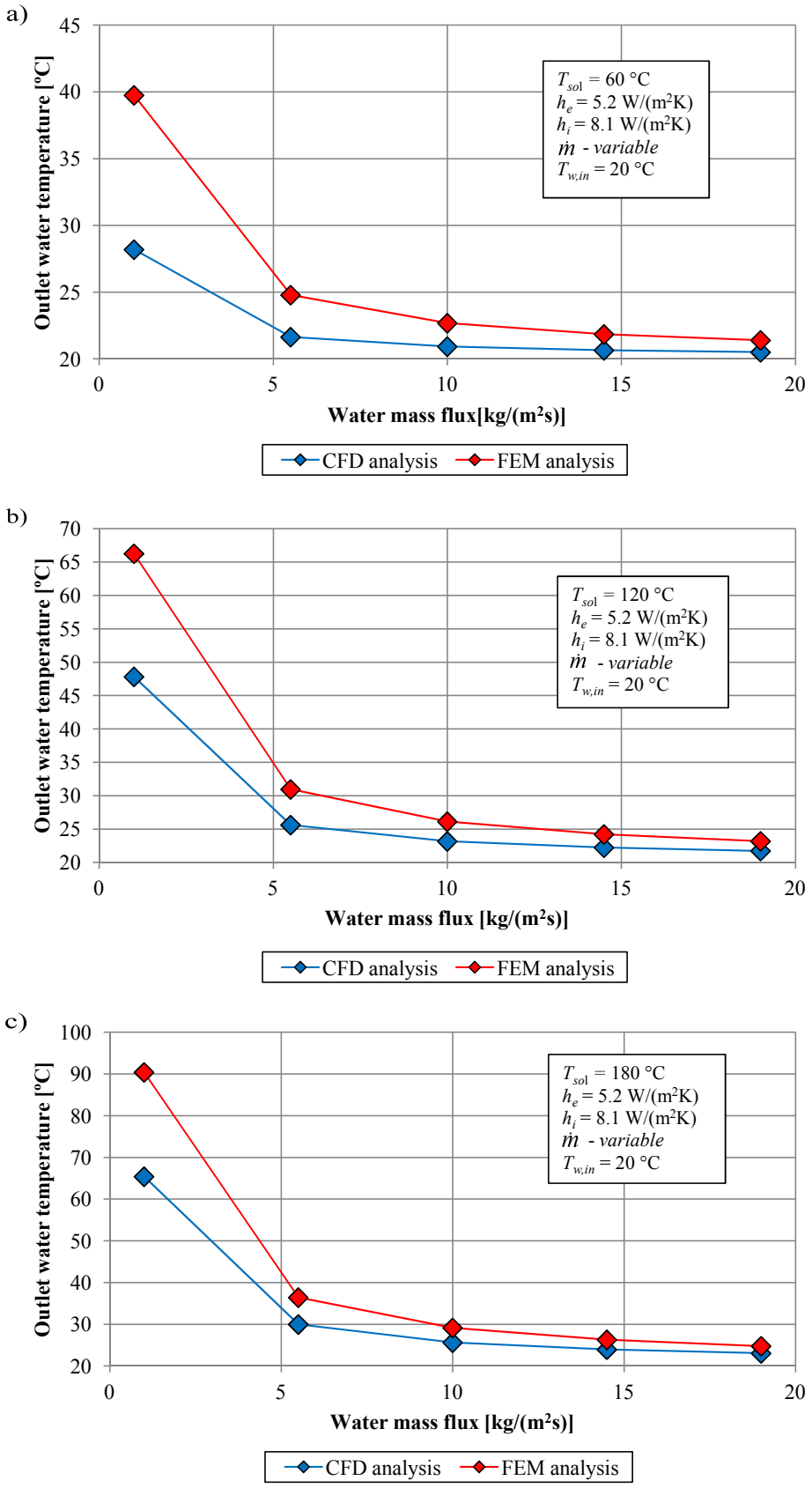

Figure 5.49: Comparison of CFD and FEM simulation results obtained for variable water mass flux and sol-air temperature equal to: a) 60 °C, b) 120 °C and c) 180 °C

0.95 kg/(m^2·s), 5.5 kg/(m^2·s), 10 kg/(m^2·s), 14.5 kg/(m^2·s) and 19 kg/(m^2·s), the range of error is 38-41 %, 15-21 %, 8-14 %, 6-10 % and 4-7 %. This analysis indicates that the assumed approach to simulate the convective heat transfer in both air-cavity and water flowing through the collector's pipes in the FE model of HSC is valid for particular magnitudes of water mass flux, especially in range from 10 kg/(m^2·s) to 19 kg/(m^2·s). Thus, it can be concluded that the quality of transient simulation results obtained by FE model, for both the application cases, are dependent on the operating fluid flow characteristics.

5.4 Efficiency indices

Various indices may be used to describe the thermal performance of solar energy collection systems. In this study, the indices expressed in terms of the outlet water temperature, $T_{w,out}$, the hourly averaged outlet water temperature, $\bar{T}_{w,out}$, the useful heat per time unit provided by the collector, Q, the heat collected during the one-day operation (heat gain), Q_d, the solar collector efficiency index, η, and the daily averaged solar collector efficiency, $\bar{\eta}_d$, were used.

According to the assumed control strategy (Section 5.5), the operating fluid enters the collector's pipes at the constant temperature, $T_{w,in}$. The energy transferred to the water increases its temperature, up to the magnitude measured at the outlet water surface, $S_{w,out}$. The outlet water temperature, $T_{w,out}$, is calculated at each time increment, Δt, of the unsteady simulation. Since the water temperature field at the outlet surface, $S_{w,out}$, is not uniform $T_{w,out}$ is defined as:

$$T\left(\mathbf{x},t\right)|_{S_{w,out}} = T_{w,out}\left(t\right) = \frac{1}{S_{w,out}} \int_{S_{w,out}} T\left(\mathbf{x},t\right) dS_{w,out}, \tag{5.4.1}$$

where $S_{w,out}$ is the area of the outlet water surface.

The hourly averaged outlet water temperature, $\bar{T}_{w,out}$, is given as:

$$\bar{T}_{w,out} = \frac{1}{\Delta t} \int_{t_1}^{t_2} T_{w,out}\left(t\right) dt, \tag{5.4.2}$$

where Δt denotes the time step of 1 hour.

The resulting temperature increase in the water flowing through the collector pipes, ΔT, can be converted into the useful heat provided by the collector to water, Q [10]:

$$Q = \dot{m} C_p \left(T_{w,out} - T_{w,in} \right), \tag{5.4.3}$$

where $\dot{m}$ is the water mass flux, C_p is the specific heat of water and $T_{w,in}$ is the inlet water temperature. The useful heat, Q, can be used to analyze the thermal response of the investigated collector under the averaged climate conditions.

The useful heat defined at the daily level, Q_d, provides the information on the global performance of HSC. The heat collected during the one-day operation (daily heat gain), Q_d, is defined as:

$$Q_d = \int_{t_1}^{t_2} Q\left(t\right) \mathrm{d}t, \tag{5.4.4}$$

where t_1 and t_2 denote the start time the end time of the collector operation (Section 5.5), respectively. The heat gain, Q_d, is useful to evaluate the potential of HSC to supply space-heating systems based on low-temperature heat sources.

Basing on the known magnitudes of the water mass flux, $\dot{m}$, inlet water temperature, $T_{w,in}$, outlet water temperature, $T_{w,out}$, and incident solar radiation I_e, it is possible to determine the solar collector efficiency, η, using a calorimetric method [118]:

$$\eta = \frac{\dot{m} C_p \left(T_{w,out} - T_{w,in} \right)}{I_e S_e} = \frac{Q}{I_e S_e}, \tag{5.4.5}$$

where I_e is the net solar irradiance on the external collector surface and S_e is the area of the external collector surface.

An important index of the HSC performance may be obtained as the solar collector efficiency defined at the daily level, $\bar{\eta_d}$ [10]:

$$\bar{\eta_d} \equiv \frac{1}{t_2 - t_1} \int_{t_1}^{t_2} \eta\left(t\right) dt, \tag{5.4.6}$$

where t_1 and t_2 denote the time of the sunrise and sunset, respectively. The daily averaged solar collector efficiency, $\bar{\eta_d}$, can be used to compare HSC with other solar collectors.

5.5 Control strategy

The control strategy in solar energy collection systems can be diversified in respect to objective, complexity and way of operation. The maximization of the energy gain through the control of the fluid mass flux is, however, one of the most common method to increase the performance of solar systems [17, 84, 102]. More recently, Hollands and Brunger [82], and Badescu [10] dealt with the optimization of the fluid mass flux in a closed-loop system.

The concept of solar collector investigated in this study is considered to form a typical closed-loop system with HS system, in which the water mass flux is the control parameter. A typical control system for a closed-loop solar thermal system contains two temperature sensors, one is mounted on the collector absorber plate near the fluid outlet, whereas another one is mounted at the bottom of the storage tank. When no fluid flow through the collector occurs, the sensor measures the mean plate temperature. When fluid flow occurs, the sensor measures the fluid temperature at the outlet. In such systems, the controller turns on a pump when the amount of solar energy that is delivered to the load just exceeds the amount of energy needed to operate the pump [9]. Among the others, there are two types of controllers that are often used in closed-loop applications. One is an 'ON/OFF' controller that is based on two allowable values of the fluid mass flux: maximum and zero, whereas the other one is a proportional controller that defines the current quantity of fluid mass flux as a linear function of the difference between the outlet fluid temperature and the temperature inside the storage tank [10].

In this study, the main objective of the control strategy is to maximize the useful heat gain through the optimization of water mass flux at each time increment of the transient numerical simulation. In general, the heat gain is considered as useful heat when the average temperature of energy carrying medium at outlet from the collector is sufficient to provide a heat exchange with the energy storage medium. For a purpose of the annual performance analysis of HSC, it is assumed that the outlet water temperature, $T_{w,out}$ (Eq. 5.4.1), higher by approximately 5 °C than the average temperature of the storage medium is appropriate. The considered temperature of the storage medium is uniform, constant in time and equal to 20 °C. Since the heat losses from the header pipes are assumed to be negligible (Section 5.1.1), the temperature of water at inlets to the pipes is constant throughout the transient simulation ($T_{w,in}$= 20 °C). One should notice that in reality the temperature in HS systems vary in time. In case of the seasonal HS systems, the maximum operational temperature occurs in the second part of summer season (August–September). In general, an increase of the fluid temperature at the inlet to the collector decreases the

amount of collected energy. Since the water temperature at inlets to HSC is assumed to be constant during a year-round operation, the developed FE model of HSC tends to slightly underestimates the amount of collected energy. Nevertheless, the assumed magnitude of water temperature at the inlet is in range of temperature typical for GHS systems. According to Chwieduk [39], the operational temperature range of 10–30 °C is typical for ground heat storage systems used in combination with solar collectors and space heating systems in single detached houses as well as terraced housing. The general schema of assumed control strategy for water mass flux in HSC is presented in Fig. 5.50. When the application of HSC aims at supplying a space-heating system, the water flow through the pipes is turned on when the outlet water temperature, $T_{w,out}$, for both the pipes is equal or just exceeds the value of 25 °C. On the other hand, the water flow is turned off when the outlet water temperature is lower than 20 °C. This study also aims at verifying the ability of HSC to support domestic hot water system, as an additional part of the active solar system applied, mainly, to meet space-heating loads. For a purpose of this analysis, it assumed that the water starts to flow through the pipes when the magnitude of the outlet water temperature for both the pipes is equal or just exceeds the magnitude of 55 °C. The flow is stopped when the outlet water temperature of the fluid flowing with the lowest allowable velocity cannot reach the level of 55 °C. Such an approach is reasonable to maintain the temperature of 50 °C in a typical water storage tank. After releasing the excess of energy in the water storage tank, the water is then transferred to the seasonal HS system before being returned to the solar collector. Hence, a considered magnitude of the inlet water temperature equal to 20 °C. For both the investigated applications, the upper limit of considered range for water mass flux is 19 kg/(m^2·s) (corresponding magnitude of water velocity is 0.019 m/s) The control strategy is based on the product magnitude of water mass flux and difference of average water temperature at inlet and outlet from pipes, $\dot{m}\,(T_{w,out} - T_{w,in})$. The magnitude of water mass flux is modified so that the product is higher for the every following time increment. Based on several preliminary transient simulations, a constant magnitude of water mass flux change, $\Delta\dot{m}$, was set to 0.95 kg/(m^2·s). The water flow is stopped when the application of minimum magnitude of water mass flux (0.95 kg/(m^2·s)) does not increase the outlet water temperature over the required temperature level.

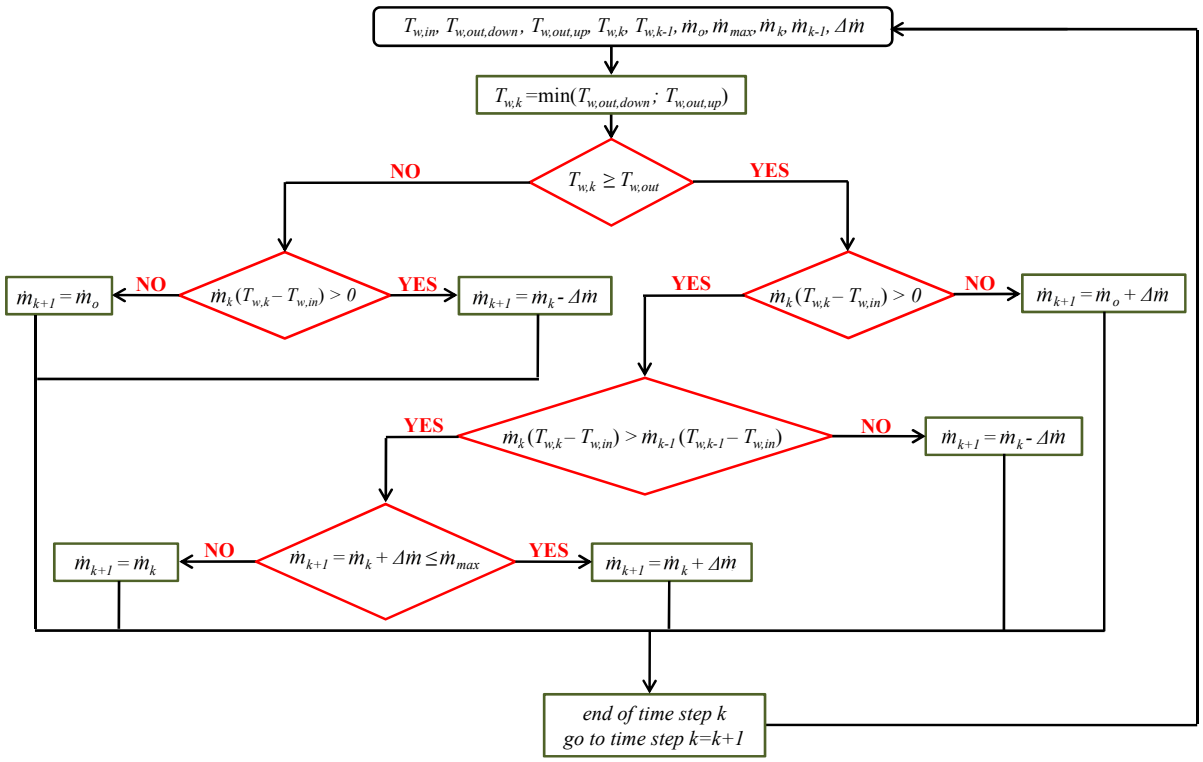

Figure 5.50: Schema of assumed water mass flux control strategy

5.6 Summary

FEM was applied to solve the problem of three-dimensional heat transfer in HSC under both unsteady and steady-state conditions. The developed FE model is based on several geometrical and physical assumptions as well as takes advantage of results obtained from additional series of CFD analyses in order to reliably simulate the thermal behavior of the 3D system. Besides the convective and radiative heat exchange between the external collector surface and outdoor environment, conductive heat transfer in solid layers, radiative heat exchange between the pipes and surfaces composing the air-cavity, and convective/radiative heat exchange between the internal collector surface and building interior, the model is capable to simulate the forced convective heat transfer in the water flowing through the collector's pipes and to include the influence of convective heat transfer in the air layer on heat exchange rate within the air-cavity without the use of computational-time-expensive CFD method. This is a great advantage which makes the model to be useful for the purpose of HSC performance analysis during a year-round operation. A compromise between the accuracy of results and time of calculation was achieved through the mesh design optimization. The developed FE model was positively compared against

the CFD model. However, the conducted analysis was mainly aimed at validation of the approach applied in order to simulate convective heat transfer mechanism in the FE model. A complete and reliable validation of the FE model requires to compare the results of the numerical simulation with measured data from the experimental investigation of HSC. Such an investigation is, however, impossible to be carried out at the present stage of the research and stays as a target for the future work.

The commercial software package ABAQUS v 6.10 [49] was employed to develop the FE model and conduct numerical simulations of heat transfer in HSC under steady-state and unsteady conditions. Several existing user subroutines were modified and several new subroutines (Fig. 5.51) were implemented in the FORTRAN language in order to:

- managing the entire process of FE simulation,
- processing of temporary results at each step and time increment of the unsteady simulation,
- generating final results of the simulation at each step and time increment of the unsteady simulation,
- modifying boundary conditions for heat exchange on inner (Eq. 5.3.23) and outer (Eq. 5.3.19) pipes' surfaces at each step and time increment of the unsteady simulation in order to reach realistic results,
- modifying thermal conductivity coefficients for the air layer at each step and time increment of the unsteady simulation in order to indirectly simulate convective heat transfer in the air-cavity,
- modifying the magnitude water velocity u_w, according to assumed control strategy for water mass flux (Section 5.5), at each step and time increment of the unsteady simulation in order to maximize the performance of HSC,
- processing the climate data of the Typical Meteorological Year for the North-East region of Poland (Elbląg) [164] in order to compute the sol-air temperature, T_{sol} (Eq. 5.3.15), and convective heat transfer coefficient at external collector surface, h_e (Eq. 5.3.16), and modify a boundary condition for heat transfer on external collector surface (Eq. 5.3.14) at each step and time increment of the unsteady simulation in order to reach realistic results,
- controlling the current time increment, Δt, in order to decrease the calculation time.

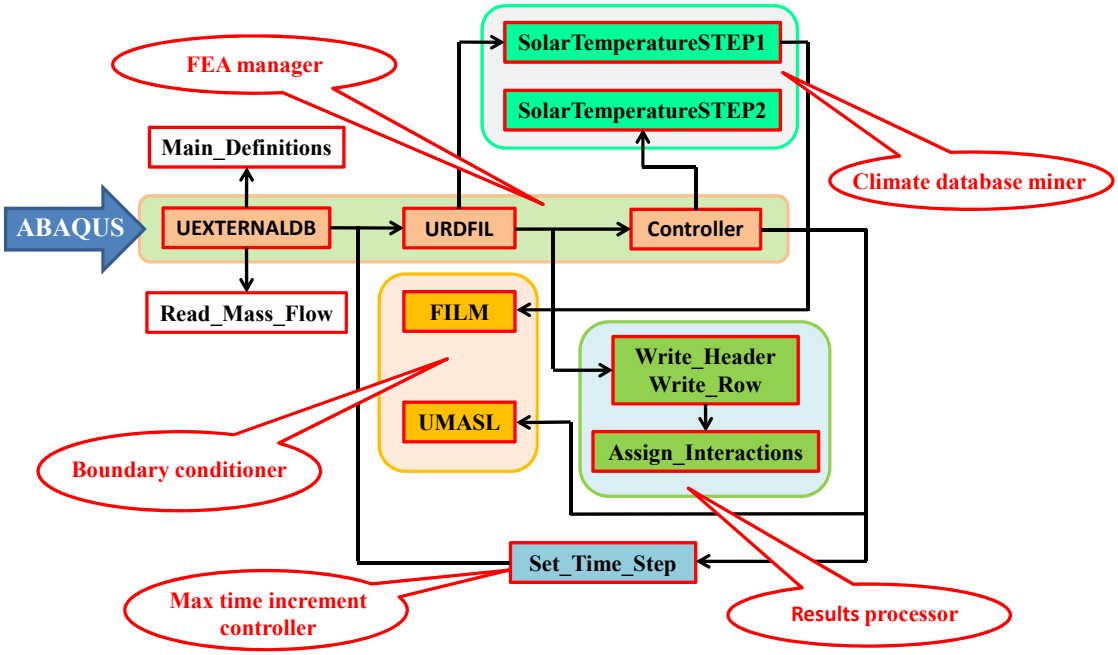

Figure 5.51: FORTRAN program controlling simulation of unsteady heat transfer in FE model of HSC developed in ABAQUS [49]

Chapter 6

Results and discussion

The general objective is to evaluate the potential of HSC to supply space-heating systems based on very-low-temperature heat sources dedicated for residential detached houses characterized by a low heat demand and to support DHW systems. The thermal response of the collector to variations of environmental, material and operational parameters is also the object of interest. The identified relationships enabled to check the adequacy of the FE model in its response to change in particular parameter and to provide guidelines for increasing the collector performance. The FE models developed for these purposes (Section 5.3) enable to carry out the unsteady simulation of the year-round operation and steady-state simulations of a 3D system. The total number of conducted transient and steady-state numerical simulations (without preliminary and mesh independence tests) is 4 and 70, respectively.

6.1 Parametric analysis

The effect of three categories of parameters including environmental (solar radiation, wind speed, ambient air temperature), material (solar absorptivity), and operational parameters (water mass flux) on the performance of HSC was investigated. It was done through the identification of a relationship between the particular parameter and the efficiency indices including the outlet water temperature (Eq. 5.4.1) and the useful heat provided by the collector (Eq. 5.4.3). All the parameterized simulations were carried out under steady-state conditions. One particular parameter was varying while other parameters were kept constant. The base values of environmental parameters correspond correspond to the average data for the daytime (when $I > 0\,\mathrm{W/m^2}$) of the hottest day (15th of August) of the year [164]:

$I = 366.379\,\mathrm{W/m^2}$ – the solar irradiance,

$T_{a,out} = 23.06\,^{\circ}\mathrm{C}$ – the ambient air temperature,

$w = 5.4\,\mathrm{m/s}$ – the wind speed.

In turn, the base values of the material and operational parameters are:

$\alpha = 0.85\,[-]$ – the absorptivity coefficient of external collector surface,

$T_{w,in} = 20\,^{\circ}\mathrm{C}$ – the inlet fluid temperature,

$\dot{m} = 9.5\,\mathrm{kg/(m^2{\cdot}s)}$ – the water mass flux.

The base magnitude of water mass flux corresponds to the mean value of the range considered in this study (Section 5.5). The above assumptions were used to modify boundary conditions (Section 5.3.2.2) for a steady-state heat transfer in the FE model of HSC. In reality, HSC does not experience a steady state since temperatures and radiation change due to the thermal mass which causes a time lag in the temperature response. However, the knowledge of the steady-state heat transfer rate is useful in analyzing the heat gain of roof structures under averaged climate conditions [161].

6.1.1 Environmental parameters

The effect of environmental parameters on the performance of conventional solar collectors is predictable. In general, an increase of the solar irradiance and ambient air temperature increases the collector performance. On the other hand, an increase of the wind speed affects the convective heat losses from the collector, hence decreasing its performance. In the case of HSC, due to its structure, a thermal response sensitivity on the variation of aforementioned parameters is expected to differ as compared to conventional solar collectors. Thus, relationships between the performance of HSC and environmental parameters, including the solar radiation, wind speed, and ambient air temperature, were investigated. This stage of analyses indicates only trends between dependent (efficiency indices) and independent variables (environmental parameters). The specific use of the equations presented in Figs. 6.1–6.3 is not valid since it is of no interest in predicting the dependent variable from a single independent variable.

Solar irradiance

The incident solar radiation is the most important environmental parameter influencing the performance of any solar system. For the purpose of this analysis, the considered solar irradiance varies from 0 up to 1053.8 W/m^2 . These magnitudes correspond to minimum and maximum available magnitudes according to [164]. In order to determine a relationship between the solar irradiance and efficiency indices, 12 numerical simulations were carried out. Each steady-state simulation was different with respect to a boundary condition prescribed for the external collector surface (Eq. 5.3.27), which was modified with regard to the assumed range of the solar irradiance.

As expected, the obtained results (Fig. 6.1) indicate a strong relationship between the solar irradiance and both outlet water temperature and useful heat provided by the collector. The character of the observed trend line is, however, almost linear for both the efficiency indices. To compare, Hassan [76] indicated a positive clear exponential relationship between the outlet fluid temperature and solar irradiance for FPC systems. This dissimilarity is a consequence of various mechanisms dominating the heat transfer process in each type of collectors. In the concept of HSC, due to a non-transparent roofing material, the solar heat is transmitted to a solar energy collection pipe system by convection rather than radiation (Section 4.2.1). Since the influence of the convective heat transfer in the air-cavity is included in the developed FE model (Section 5.3.1), the identified relationship suggests a good adequacy of the FE model in its response to a change of the solar irradiance.

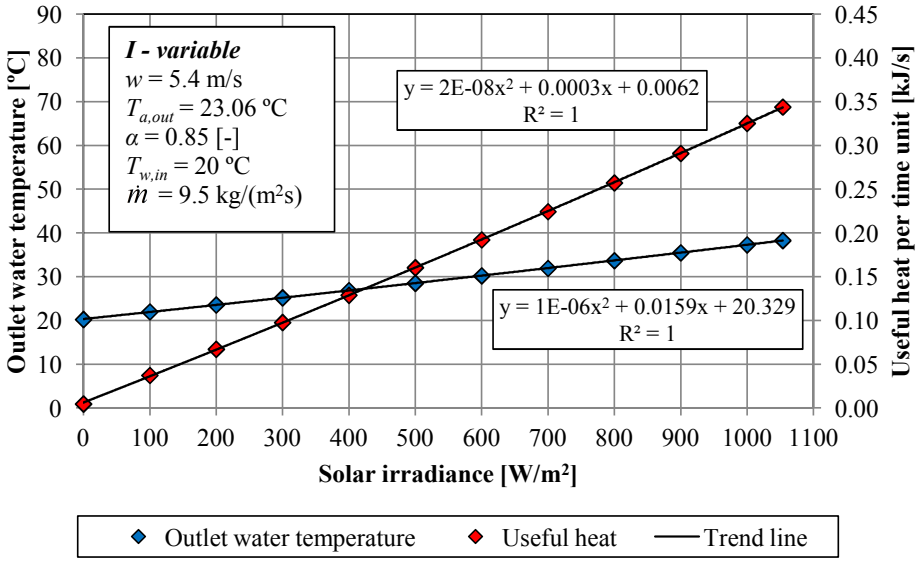

Figure 6.1: Variation of HSC performance versus solar irradiance

Wind speed

In general, the wind is an environmental factor that strongly increases the heat losses in solar collectors. In the assumed FE model of HSC, the effect of the wind speed on the heat transfer process is considered by the convective heat transfer coefficient, h_e (Eq. 5.2.73). Therefore, the relationship to be determined was based on the wind speed expressed in terms of the convection heat transfer coefficient. According to [164], the wind speed for a considered location ranges from 0 m/s up to 16 m/s. With respect to Eq. 5.2.73, the corresponding convective heat transfer coefficient ranges from 5 up to 18.337 W/(m^2·K). In order to determine a relationship between the wind speed and efficiency indices, 17 numerical simulations were conducted. Each steady-state simulation was different with respect to a boundary condition prescribed for the external collector surface (Eq. 5.3.27), which was modified by the assumed range of convective heat transfer coefficients.

As expected, the obtained results (Fig. 6.2) indicate a negative relationship between the convective heat transfer coefficient (expressing the wind speed) and both outlet water temperature and useful heat provided by the collector. The power law model is suitable to describe the character of trend lines for both the efficiency indices. The trend line observed for the outlet water temperature is in a good accordance with the one reported by Hassan [76] who investigated numerically the performance of FPC. The identified relationship indicates a good adequacy of the FE model in its response to a change of the wind speed.

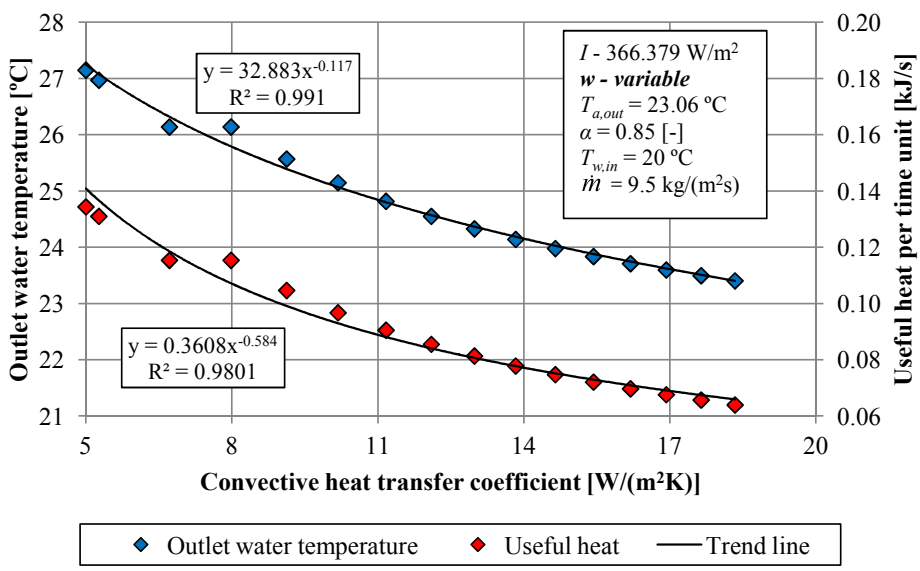

Figure 6.2: Relationship between HSC performance and convective heat transfer coefficient

Ambient air temperature

The ambient air temperature is another environmental factor influencing the performance of solar collectors. Its effect is, however, dependent on a structure of the particular collector, e.g. evacuated-tube solar collectors (Section 3.3.1) are able to operate efficiently even during the winter season when the ambient temperature is frequently below the zero Celsius degree. The concept of HSC is based on a ventilated roof structure, hence in real conditions the performance of HSC is expected to be influenced by a temperature of the air flowing into the roof structure. The assumed FE model, however, neglects the wind-driven airflow in ventilated roof channels (Section 5.3.1). As a consequence, a parameter of the ambient air temperature is assumed to contribute only to a heat exchange on the collector's external surface, as for typical FPCs. The considered ambient air temperature varies from -16.6 °C up to 28.8 °C. These magnitudes correspond to minimum and maximum available values according to [164]. In order to determine a relationship between the ambient air temperature and efficiency indices, 10 numerical simulations were carried out. Each steady-state simulation was different with respect to a boundary condition prescribed for the external collector surface (Eq. 5.3.27), which was modified in the assumed range of ambient air temperatures.

The obtained results (Fig. 6.3) obviously indicate a strong relationship between the ambient air temperature and both outlet water temperature and useful heat provided by the collector. Nevertheless, a linear character of the observed trend lines suggests that the effect of the ambient air temperature on radiative heat exchange in the air-cavity is negligibly small as compared to the solar radiation (Fig. 6.1).

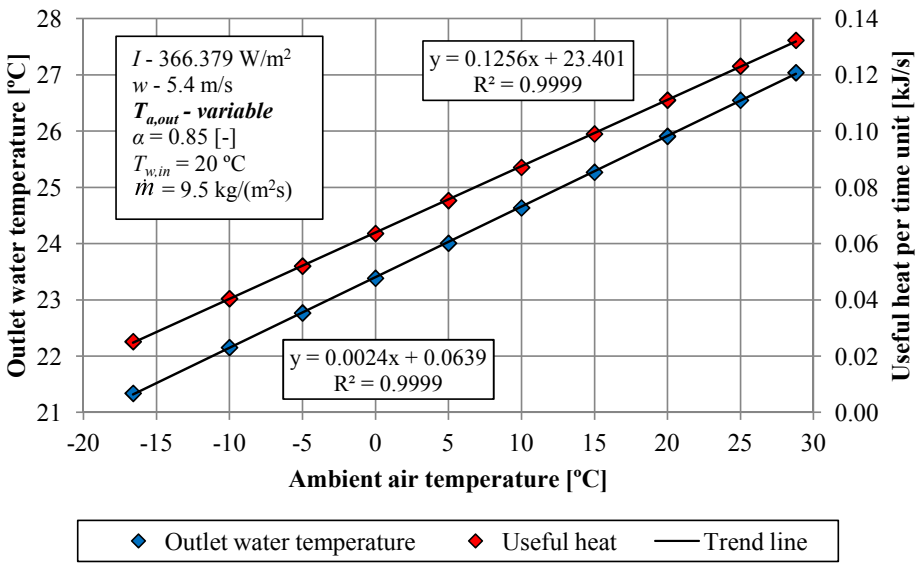

Figure 6.3: Variation of HSC performance against ambient air temperature

6.1.2 Optical parameters of roofing material

Basing on the results of previous parametric analyses, it is expected that optical properties of the roofing's external surface (including solar absorptivity and thermal emissivity coefficients) have a significant impact on the performance of HSC. This especially concerns the solar absorptivity coefficient, since the absorption of the solar radiation together with the temperature differences between ambient air and interior temperatures, are the main factors driving the roof heat transfer. Suehrcke et al. [161] investigated the effect of the roof solar absorptivity on the building thermal performance in a hot climate. The authors reported that roofs with the high solar absorptivity coefficient have by about 30 % higher total heat gain than roofs with the low coefficient. The solar absorptivity coefficient for a specified roofing material is correlated with the color of its surface that is apparent from the reflected visible part of the solar radiation. In general, a black roofing surface with the low visible reflectance suggests a high solar absorptivity close to 1 [−], whereas the very light roofing surface suggests a low solar absorptivity close to 0 [−].

Since the developed FE model neglects the effect of the thermal emittance from the external collector surface, only the effect of the solar absorptivity coefficient on the performance of HSC was investigated. The effect of the solar absorptivity coefficient on heat transfer process is considered by the sol-air temperature, T_{sol} (Eq. 5.2.72). For a full range of the solar absorptivity coefficients (from 0 [−] to 1 [−]), the corresponding sol-air temperature for the considered solar irradiance, ambient air temperature and wind speed varies from 23.06 °C up to 76.861 °C. In order to determine a relationship between the solar absorptivity coefficient of the roofing surface and efficiency indices, 11 numerical simulations were carried out. Each steady-state simulation was different with respect to a boundary condition prescribed for the external collector surface (Eq. 5.3.27), which was modified by the assumed range of sol-air temperatures.

In conformity with expectations, the obtained results (Fig. 6.4) indicate a positive almost linear relationship between the solar absorptivity coefficient and both outlet water temperature and useful heat provided by the collector. A 34 % increase in the outlet water temperature and over twenty eight-fold increase in the useful heat is observed for the surface with the solar absorptivity coefficient of 1 [−] in comparison with the solar absorptivity coefficient of 0 [−]. However, these limit coefficients do not exist in reality. In the literature [161], the values of 0.39 [−], 0.7 [−] and 0.9 [−] are reported for a standard white, red and black oil painted steel roofing, respectively. The solar absorptivity coefficient of 0.85 [−] equivalent to the dark brown painted steel roof is assumed. The obtained results indicate the possibility

to increase the outlet water temperature by 13 % and 4 % with the use of the dark brown painted steel roofing in comparison with the standard white and conventional red painted steel roofing, respectively. For the useful heat, it is 105 % and 20 %, respectively. With an increase of the absorptivity of the roofing material from 0.85 [−] to 0.9 [−], which is typical for the black oil painted steel roofing, the outlet water temperature increases by only 1.3 %, whereas the increase of the useful heat slightly exceeds 5 %. With regard to considered applications of HSC, the analysis points that the solar absorptivity coefficient is a factor that may limit the use of the investigated solar collector. For the assumed climate conditions, the magnitude of water outlet temperature does not exceed the level of 25 °C for the coefficient lower than 0.7 [−], hence the collected energy is not useful to supply space-heating systems. For the solar absorptivity coefficient corresponding to brown painted steel roof (α = 0.85 [−]), the obtained magnitude of outlet water temperature is 26.08 °C. Thus, it can be concluded that the assumed parameters of roofing material are reasonable to analyze the performance of HSC applied to supply space-heating systems. It should be noticed that for the entire range of solar absorptivity coefficients considered for the purpose of this analysis, the outlet water temperature does not exceed the level of 55 °C. This clearly indicates that for the assumed magnitude of water mass flux, equal to 9.5 kg/(m^2·s), the collector is not capable to support DHW systems under considered climate conditions.

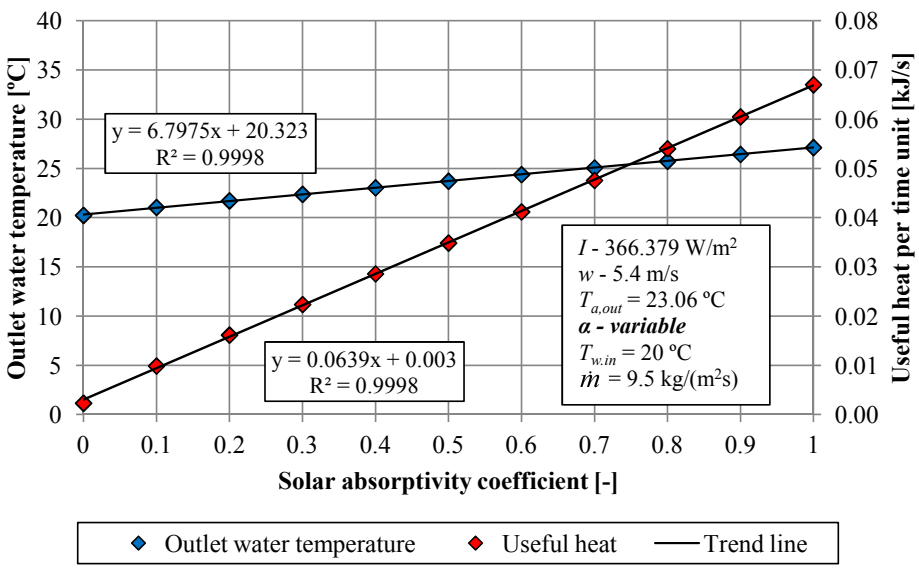

Figure 6.4: Influence of solar absorptivity coefficient on HSC performance

6.1.3 Operational parameter

The water mass flux is a crucial parameter influencing the performance of solar collectors. In general, this operational parameter should vary in time in dependence on outlet water temperature to maximize the amount of collected energy. The operational range of the water mass flux is to be related to the operational strategy, type of piping materials (many piping materials have a recommended maximum velocity requirement, e.g. a maximum recommended velocity in the case of copper pipe for cold and hot water lines is 2.45 m/s and 1.22 m/s [76], respectively) and intensity of the heat transfer process within the collector. According to the structure of HSC, the intensity of the heat transfer process within the collector is expected to be lower as compared to conventional solar collectors, e.g. FPCs. Therefore, the range of the water flow velocity in the investigated solar energy collection system should be kept at the relatively low level to collect the maximum energy. According to assumed control strategy (Section 5.5), the magnitude of water mass flux varies from 0.95 kg/(m^2·s) up to 19 kg/(m^2·s). In order to determine a relationship between the water mass flux and efficiency indices, 20 numerical simulations were carried out. Each steady-state simulation was different with respect to a boundary condition prescribed for the operating fluid (Eq. 5.3.32) which was modified with regard to the assumed range of the water mass flux.

The obtained results (Fig. 6.5) indicate a negative non-linear relationship between the water mass flux and outlet water temperature. On the other hand, a positive non-linear relationship is found for the useful heat provided by the collector. The useful heat increases with the increase of the water mass flux. However, no significant increase in the performance, in term of the useful heat, can be achieved with the water mass flux higher than 14.25 kg/(m$^2 \cdot$ s). The maximum performance in term of outlet water temperature is obtained, obviously, for the lowest magnitude of water mass flux. These results clearly show that the performance of HSC is strongly correlated with the water mass flux. With regard to considered applications of HSC, this analysis points that the magnitude of water mass flux should be kept at possibly low level so as the collector could provide the energy useful to meet DHW requirements ($T_{w,out} > 55\,°$C). In case of HSC applied to supply space-heating systems, it should be sufficiently high so as the collector could provide the maximum amount of energy useful to supply space-heating systems ($T_{w,out} > 25\,°$C). For the considered climate conditions, the magnitude of water mass flux should not exceed the limits of 0.95 kg/(m$^2 \cdot$ s) and 11.4 kg/(m$^2 \cdot$ s), to effectively supply DHW and space-heating systems, respectively. Basing on found relationships, it can be also concluded that the assumed range of the water mass flux is reasonable to analyze

the performance of HSC in case of both the applications.

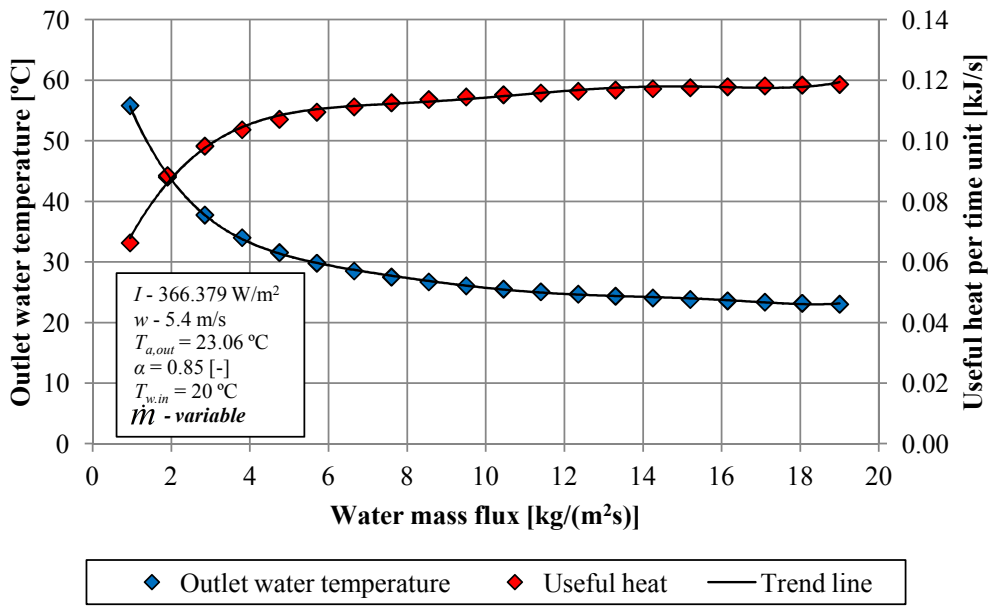

Figure 6.5: Variation of HSC performance in dependence on water mass flux

6.1.4 Summary

The obtained results point a diverse effect of particular parameters on the performance of HSC. An increase solar irradiance, ambient air temperature and solar absorptivity, always increase both the outlet water temperature and useful heat provided by the collector. An increase of wind velocity always decrease both the efficiency indices. In turn, a decrease of water mass flux always results in an increase of the outlet water temperature at a cost of reduced useful heat and vice versa. The identified relationships are in good agreement with the literature findings. Hence, the FE model could be used for the annual performance analysis. The obtained results also provide the guidelines for increasing the collector performance. It was found that the collector with the roofing surface characterized by solar absorptivity coefficient lower than 0.7 [−] may be not capable to provide the energy useful to supply both space-heating and domestic hot water systems. Thus, the steel roofing materials of dark-brown- or black-painted surfaces are recommended for the efficient operation of HSC.

6.2 Simulation of year-round HSC operation

The capability of HSC to supply space-heating systems based on very-low-temperature heat sources dedicated for residential detached houses characterized by a low heat demand and to support DHW systems is evaluated for a year period on the hourly and daily basis. The major output of both the unsteady analyses is the hourly averaged outlet water temperature (Eq. 5.4.2) and the daily amount of collected energy (heat gain) (Eq. 5.4.4). The analysis of the daily averaged solar collector efficiency (Eq. 5.4.6) is also conducted. The temperature distribution in the operating fluid and entire collector during the hottest day in August [164] are depicted in Fig. 6.6a and Fig. 6.6b.

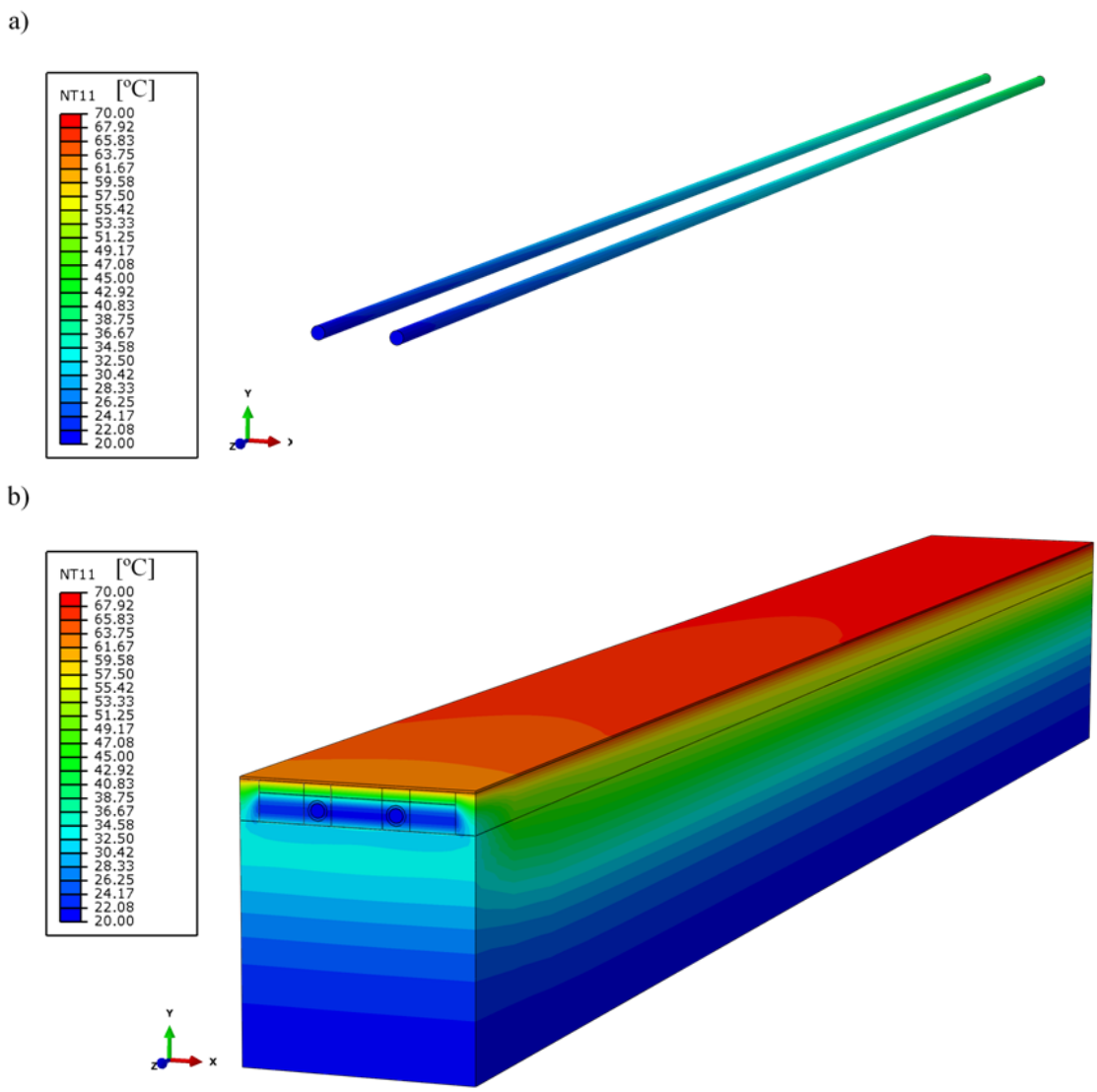

Figure 6.6: Temperature distribution in a) operating fluid and b) entire collector during daytime in August

In case of the analysis of HSC applied to space-heating systems, the additional two unsteady simulations referred to the collector operation during a one month period were conducted.

In the following, the analyses results for both the HSC applications are presented and discussed.

6.2.1 Supplying space-heating systems

6.2.1.1 Outlet water temperature

The simulation results of the year-round HSC operation applied to supply space-heating systems, in the form of hourly averaged water temperature at the outlets from the collector's pipes, are demonstrated in Fig. 6.7. Since it is of great interest to compare the performance of HSC during winter (heating season) and summer season, the length of the heating season (from September 26 to May 5) is determined according to Polish standard PN-B-02025 [138]. The results clearly points out that the calculated hourly averaged magnitudes of outlet water temperature are less than the inlet water temperature, assumed as 20 °C, for the most time of the winter season. According to the assumed control strategy (Section 5.5), in such cases, the water flow through the pipes is stopped. One should notice, that the minimum temperature of the operating fluid during the heating season is almost 15 °C below the zero Celsius degree. This clearly indicates the need for a use of water with the antifreeze solution as an operating fluid in the real application of HSC under

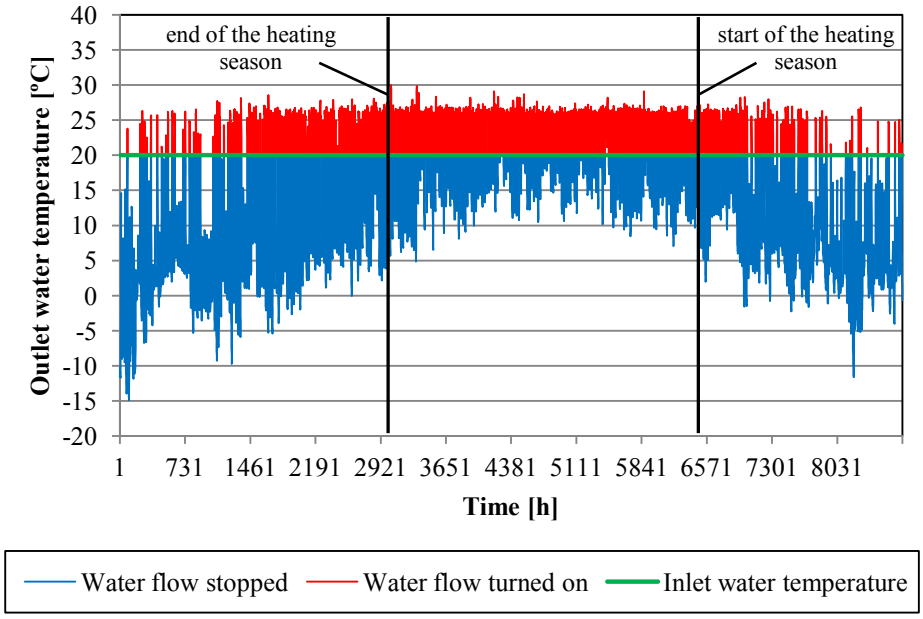

Figure 6.7: Annual variation of hourly averaged outlet water temperature

Polish climate conditions. In turn, for the summer season, the computed magnitudes of outlet water temperature exceeds the level of 20 °C for most of the daytime (when $I > 0\,\mathrm{W/m^2}$), thus the water flow through the collector's pipes is turned on. While operating, the magnitudes of outlet water temperature oscillate around the set point, assumed as 25 °C. The maximum magnitude of hourly averaged outlet water temperature is 29.9 °C, whereas the maximum instantaneous water temperature does not exceed 32.5 °C. These magniutudes indicates that an upper limit of the assumed water mass flux range is not sufficient enough to keep the required temperature level of the energy carrying medium.

The analysis of the operating-time (Fig. 6.8) shows that the water flow through the collector's pipes is turned on from 0.5 to 15 hours per day during the summer season. One should notice that, according to the assumed climate database [164], the maximum number of daytime hours per day (when $I > 0\,\mathrm{W/m^2}$) is 15. The cases when the operating-time reaches the number of 15 hours correspond to days for which the ambient air temperature after the sunset is still over 20 °C. The total operating-time of HSC during the summer season is 1579 hours, what corresponds to 78 % of the total daytime available in this season. To compare, during the winter season the water flow is turned on for only 716 hours, what corresponds to 35 % of the available daytime. Taking into account that the heat collected by HSC is considered as useful to supply space-heating systems when the temperature of operating fluid surpasses the level of 25 °C, it must be pointed that the effective operating-time of the collector is 910 hours and 353 hours for the summer and winter season, respectively. These

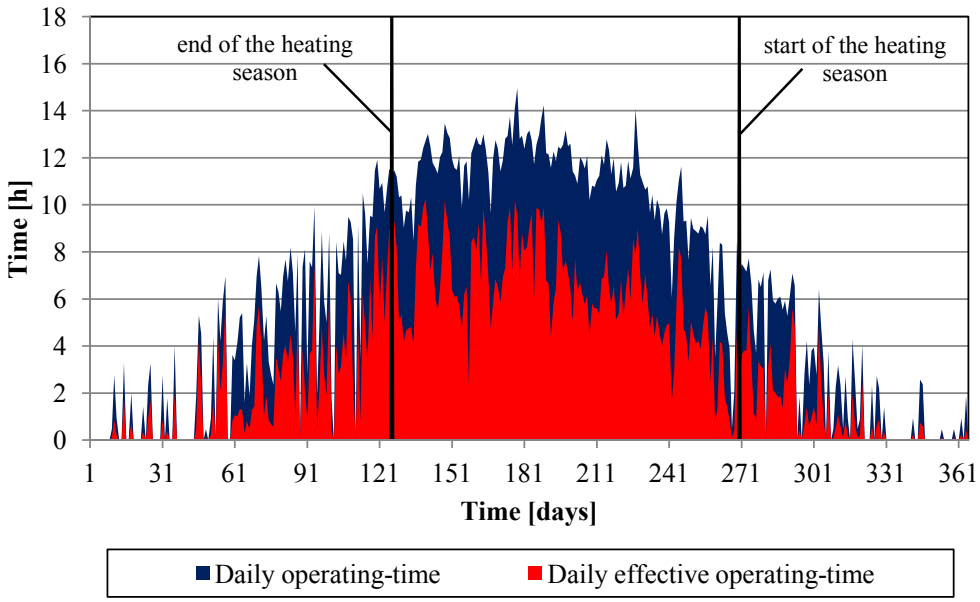

Figure 6.8: Annual variation of operating-time of HSC applied to supply space-heating systems

magnitudes correspond to 45 % and 17 % of the total daytime available during the summer and winter season, respectively.

As the water in the collector's pipes starts to flow when the temperature of energy carrying medium at the outlets exceeds the level of 25 °C, the observed differences between the total operating time and its part wherein the collector supplies the useful heat gain indicate the presence of disturbances while operating. The analysis of HSC performance related to a single daytime period provides useful information to evaluate the operation of the collector. Fig. 6.9 and Fig. 6.10 present the characteristics of the collector operation, with respect to variations of the outlet water temperature and the water mass flux, during the most sunny day of July (5th of July) and January (26th of January), respectively.

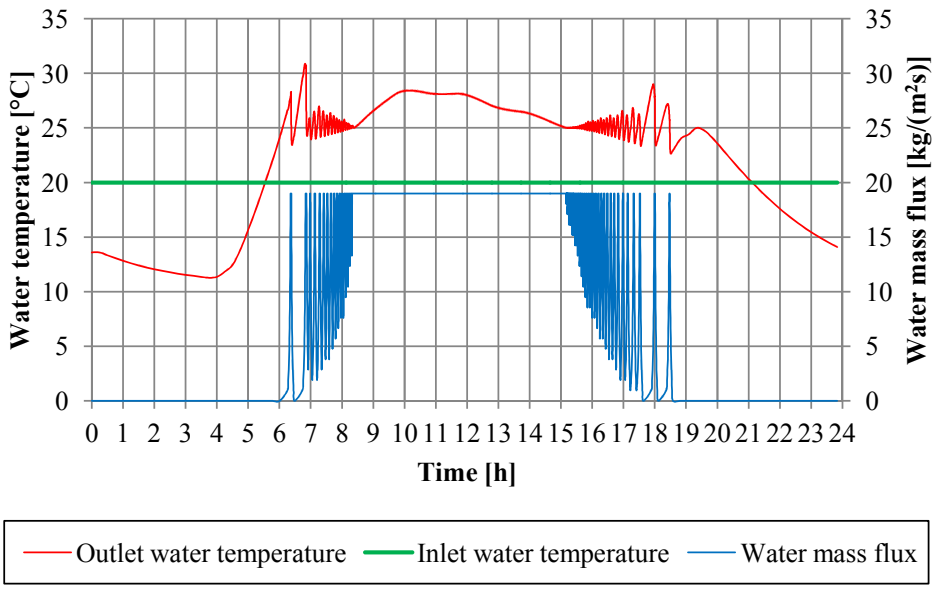

Figure 6.9: Operation characteristics of HSC applied to supply space-heating systems during the most sunny day of July (5th of July)

During the summer day (Fig. 6.9), the operating-time period can be divided into three parts with respect to character of water mass flux variations. For the first 2.5 hours of the collector operation, there are strong fluctuations of the water mass flux resulting in frequent but short in time decreases of the outlet water temperature below the level of 25 °C. During this time period, the collector operates effectively for 1.1 hours and collects 0.48 MJ of the heat. After the first part of the operating-time, the collector operates effectively for 6.8 hours. Throughout this time, despite applying the maximum magnitude of water mass flux, equal to 19 kg/(m^2·s), the temperature of the operating fluid at the collector's outlets is higher than 25 °C, on average, by 2.1 °C. The total amount of collected heat is 6.79 MJ. However, it is

expected that applying a higher magnitude of water mass flux would increase the performance of HSC during this time period. At the third part of the operating-time, which lasts for 3.5 hours, the fluctuations of water mass flux begin and become stronger with a decrease of available solar radiation. During this time period, the collector operates effectively for 1.7 hours and collects, in total, 0.74 MJ of useful energy. During the considered summer day, the number of operating-time hours is 12.3. Through over 78 % of this time the temperature of water at the collector's outlets exceeds 25 °C hence providing the useful heat gain (in total 8.01 MJ).

To compare, during the winter day (Fig. 6.10) the strong fluctuations of the water mass flux occurs throughout the operating-time that equals to 3 hours. Only through 51 % of this time period the collector operates effectively providing in total 0.56 MJ of the useful energy.

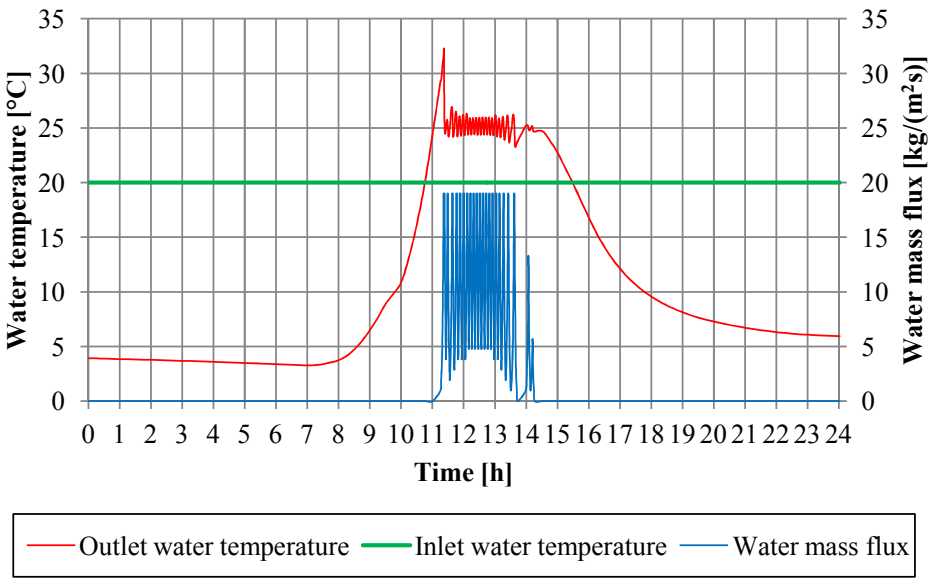

Figure 6.10: Operation characteristics of HSC applied to supply space-heating systems during the most sunny day of January (26th of January)

Summarizing, the analysis of the HSC performance for the most sunny day of July and January, indicates that in both the cases the disturbances during the collector operating-time are a consequence of applied water mass flux control strategy (Section 5.5). Due to the assumption of a constant magnitude of water mass flux change at each time increment of the transient simulation ($\Delta\dot{m} = 0.95\,\mathrm{kg/(m^2{\cdot}s)}$), the controller is not capable to effectively keep the outlet water temperature above the required level during the entire time of the collector operation. Since the problem relates to 42 % and 51 % of the total HSC operating-time during the summer and winter season, respectively, it can be stated that the obtained results of year-round

operation simulation are underestimated. The analysis conducted for the summer day also revealed that the problem of outlet water temperature exceeding the assumed set point due to the application of the too low magnitude of the water mass flux refers to a significant part of the operating-time when the collector is capable to supply the useful heat energy. This could have an additional influence on decreasing the performance of HSC during a year-round operation. The noticeable magnitudes of the outlet water temperature, reaching the level of 32 °C, observed at the beginning of the collector operation, both during the summer and winter day as well as at the end of the summer day, are a consequence of the applied time increment control function (Section 5.3.3). For the purpose of the transient simulation, it was assumed that the magnitude of the time increment corresponding to time periods when the water flow through the pipes is stopped equals to 900 seconds. In general, such an approach may cause a significant but temporary temperature increase of the energy carrying medium when $I > 0\,\mathrm{W/m^2}$. The observed cases refer, however, to the time periods when the solar radiation is relatively low, and hence are of negligible impact on the total performance of HSC applied to supply space-heating systems.

6.2.1.2 Heat gain

The unsteady simulation results of the year-round operation in the form of the daily collected energy (heat gain) are demonstrated in Fig. 6.11. The obtained results clearly indicate a difference in the heat collection during the winter (heating season) and summer seasons. The amount of energy collected during the summer season

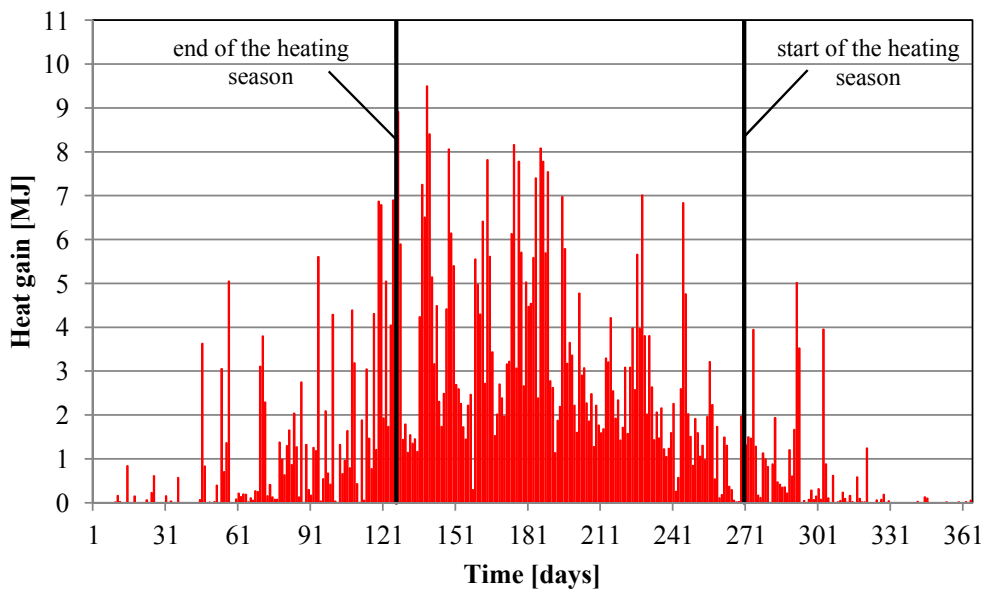

Figure 6.11: Annual variation of daily amount of collected energy

is 459 MJ, what corresponds to 74.3 % of the annual amount of energy collected by HSC. During the winter season, with a decrease of the environmental parameters and operating-time (Fig. 6.8), a significant decrease of heat gain is observed. In this time period, the amount of collected energy is only 158.8 MJ. However, over 75 % of this amount is collected in the second part of the heating season (from January to May). It is a good result from the practical point of view, especially when the collected energy is provided to GHS systems [39, 135]. In general, the second part of the heating season could be a discharge period for the seasonal storage systems hence each portion of the supplied energy is desirable.

Fig. 6.12 presents the analysis results of the heat gain magnitudes and the corresponding magnitudes of the water mass flux. Such an analysis is of great importance to evaluate the quality of the FE simulation results. The comparison between stationary simulation results obtained by the CFD and FE models (Section 5.3.4) shows that the discrepancy between results of CFD and FE models exceeds the level of 4 % and 38 % when the applied water mass flux is lower than 19 kg/(m^2·s) and 1 kg/(m^2·s), respectively. As shown in Fig. 6.12, over 67 % of the annual amount of energy is collected by the water flowing with the maximum allowable velocity, corresponding to 19 kg/(m^2·s), whereas only 1.8 % of the total heat gain correspond to water mass flux equal to 0.95 kg/(m^2·s). With regard to the summer seasons, the percentage part of total heat gain corresponding to boundary magnitudes of considered water mass flux range, is 67.4 % and 1.6 %, respectively. For the winter season

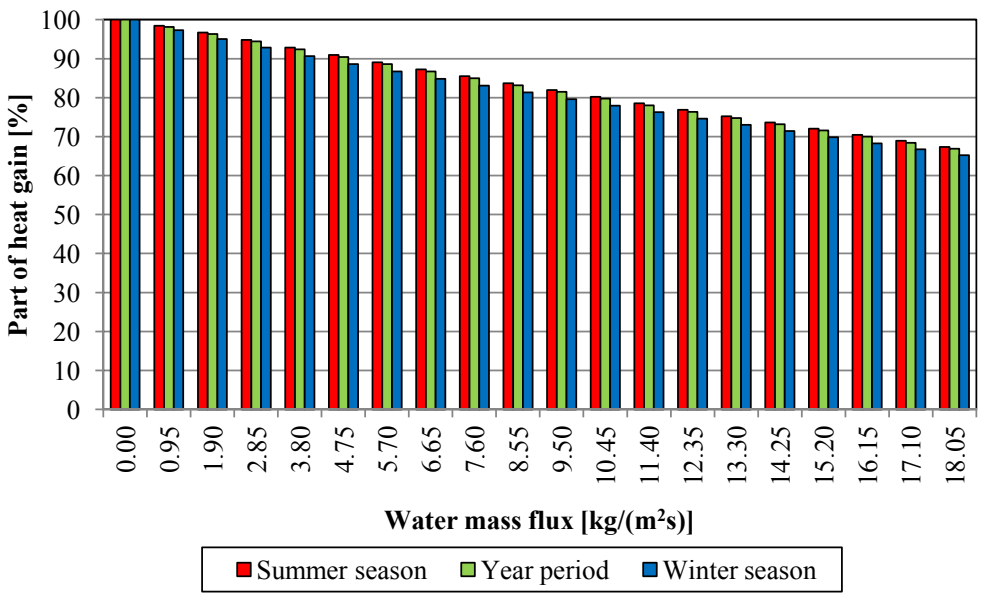

Figure 6.12: Relationship between water mass flux and amount of energy collected by HSC applied to supply space-heating systems

it is 65.2 % and 2.7 %, respectively. Hence, it can be stated that the obtained results are characterized by a reasonable level of quality and thus are useful for the purpose of approximate estimation of the HSC performance applied to supply space-heating systems.

The monthly amounts of the energy collected by HSC with the 0.9 m^2 absorber area are compared in Fig. 6.13. The biggest amount of heat, equal to 132.4 MJ, is collected in May, whereas the smallest amount, equal to 0.3 MJ, is collected in December. These magnitudes, respectively, correspond to 21.4 % and 0.1 % of the annual amount of collected energy, equal to 617.7 MJ. Calculated per square meter of the absorber surface area, the total heat gain is 686.4 MJ/m^2 (equivalent to 190.7 kWh/m^2, approximately 0.52 kWh/ (m^2day)). The obtained results are in accordance with results reported by Colon and Merrigan [47]. On basis of the year-long measurements, the authors reported that the roof integrated solar collector, based on the similar structure concept as HSC, was capable to provide approximately 0.9 kWh/m^2 per day. The difference, may be a consequence of applied control strategies and considered climate conditions. The measurements were conducted in Florida, USA. Latała [108] examined experimentally the performance of vacuum tube and flat plate collectors under Polish climate conditions. The results of measurements conducted in Kraków from June to December indicate that the ETC and FPC were capable to provide on average 2.43 kWh/m^2 and 1.75 kWh/m^2 of useful heat per day. To compare, during the analogous time period the daily averaged amount of useful heat provided by HSC is only 0.56 kWh/m^2. Thus, it

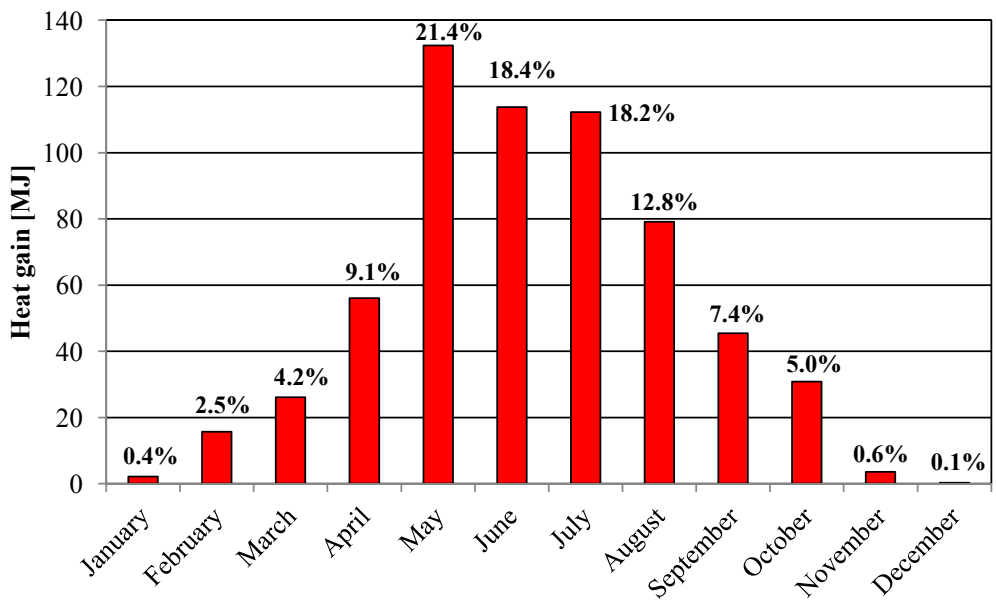

Figure 6.13: Monthly amount of energy collected by HSC of 0.9 m^2 surface area

can be stated that the performance of HSC is over 3 times lower in comparison to typical solar collectors.

With the assumption that HSC is a building component of a residential detached house that covers a roof of 60 m^2, the total annual amount of collected energy is 41182.4 MJ (equivalent to 11439.5 kWh). Assuming that the considered building meets standards of passive houses (the building annual space heating demand does not exceed 15 kWh/(m^2year) [11]) and the heated floor area is 250 m^2, the required energy to satisfy annual space-heating loads is 3750 kWh (equivalent to 13.5 GJ). For these assumptions, it can be found that the required energy to satisfy annual space-heating loads is over 3 times lower than the energy collected by HSC during a year-round operation. The obtained results clearly indicates a great potential of HSC to supply the very-low-temperature space-heating systems in a building characterized by a low heat demand. One should notice, that the performance of the investigated solar collector is significantly limited due to the climate conditions and assumption of the constant water temperature at inlets to collector's pipes ($T_{w,in}$ = 20 °C) throughout the operating-time. In reality, the magnitude of inlet water temperature vary in time in dependence on operating temperature in the seasonal heat storage system. Thus, it can be concluded that the final evaluation of the HSC potential to supply the space-heating systems requires the effectiveness of the heat storage system to be taken into account by the FE model of HSC.

In general, the evaluation of a use of any solar collector to supply the space-heating systems in the buildings, should take into account the cost associated with its operation, including the cost of the pump and control system operation. For HSC of 60 m^2 absorber surface area and the considered range of water mass flux, the power input of the exemplary pump is 3–42.5 W, whereas the power input for the control system is constant and equal to 12 W. Fig. 6.14 presents the daily amount of energy collected and energy required to power HSC of 60 m^2 surface area during a year-round operation. The analysis demonstrates that the daily energy required to power the collector does not exceed the level of 0.84 kWh. During the summer and winter season the collector consumes 96.2 kWh and 107.5 kWh of electricity, respectively. These magnitudes, respectively, correspond to 47 % and 53 % of the annual energy consumption, equal to 203.7 kWh. Taking into account the current total price of the electric energy (0.61 pln/kWh corresponding to the national average) the total cost of the year-round HSC operation applied to supply space-heating system is 124.3 pln. To compare, with the assumption that the heat is supplied to the considered building (annual space-heating loads of 13.5 GJ) from the district heating network, for which the total price is 50 pln/GJ (corresponding to the national average), the total cost

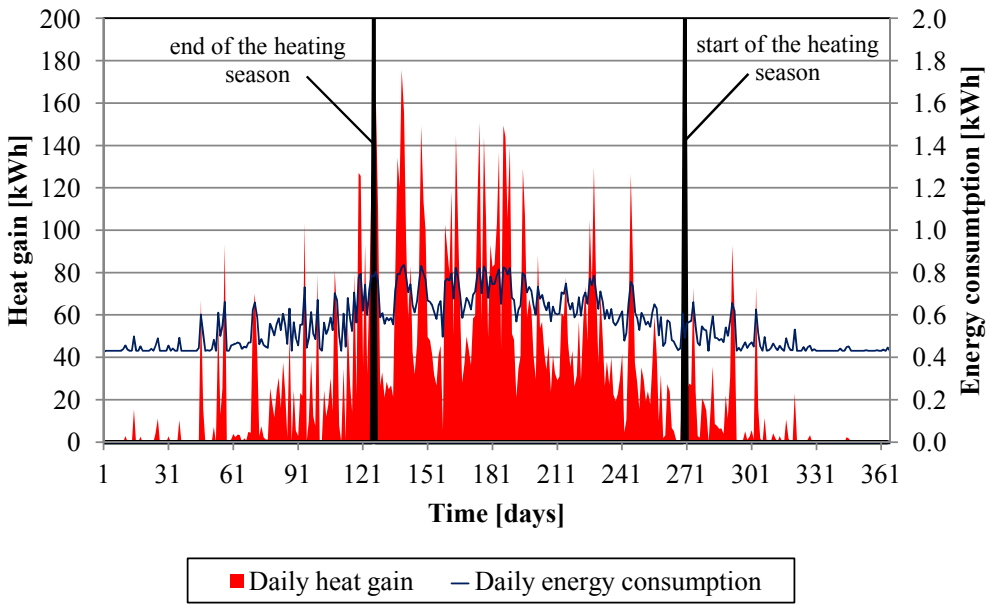

Figure 6.14: Annual variation of daily amount of collected energy and energy required to power HSC of 60 m^2 surface area

of space-heating is 675 pln. This clearly points that applying of HSC to supply space-heating systems may significantly reduce the cost of building operation.

The additional simulations of the HSC operation were conducted to verify an influence of the collector orientation on its performance. Since the CFD functions implemented in the FE model (Section 5.2.5) are determined for a specified roof inclination, the additional analyses refer to the climate data for the south-east- and south-west-oriented surface inclined at angle of 45° [164] (later named as SE45 and SW45, respectively). According to significant computational cost, the simulations were conducted only for May, the month in which the south-oriented (S45) collector gains the biggest amount of energy during a year-round operation (Fig. 6.13). The comparison of results (Fig. 6.15) (due to technical reason the considered time of operation is reduced to 29 days of May), demonstrates differences in the amount of energy collected by HSC (0.9 m^2 absorber surface area) in particular configurations. The smallest heat gain, equal to 117.2 MJ, refers to SE45, what corresponds to 94.3 % of the energy collected in case of S45, that is characterized by the best performance. In case of SW45, it is 121.3 MJ and 97.6 %, respectively. The observed differences in the performance of HSC in May are relatively small. Nevertheless, the maximum difference, equal to 7.1 MJ, overcomes the amount of energy collected by S45 in the winter time period from November to January (Fig. 6.13). This clearly points the importance of the orientation for the HSC performance. The analysis also shows that besides the solar radiation, the other environmental parameters

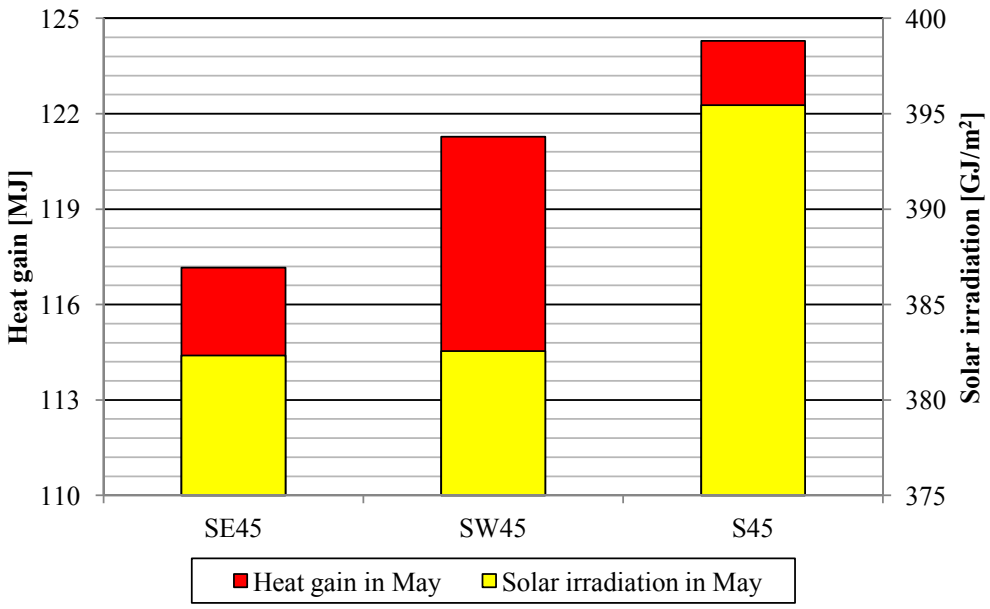

Figure 6.15: Variation of collected energy and solar irradiation in May in dependence on HSC orientation

have a significant effect on the HSC performance. It is noticeable, especially, when comparing the amount of heat gain and solar irradiation for SE45 and SW45. During the considered time period the available solar irradiation for both the configurations is almost the same, differing by only 0.2 GJ/m^2 (equivalent to 0.06 % of the solar irradiation for SW45), whereas the difference in the amount of heat gain equals to 4.1 MJ (equivalent to 3.4 % of the heat gain for SW45). Since, the magnitudes of ambient air temperature are analogous for both the cases, the observed differences are a consequence of wind-driven thermal losses on the external collector surface.

6.2.1.3 Efficiency index

The unsteady simulation results of the year-round operation, in the form of the daily averaged solar collector efficiency, are shown in Fig. 6.16. As expected, the relatively low daily averaged efficiency occurs during the year-round operation. The maximum value is 0.30 [−], whereas the annual averaged is just 0.09 [−]. The obtained results are, obviously, highly correlated with environmental parameters, especially the solar irradiation (Fig. 5.8). The average daily efficiency during the winter season does not exceed 0.04 [−]. During the summer season it is slightly above 0.17 [−]. To compare, the efficiency index in range 0.4-0.5 [−] is typical for conventional flat plate collectors under Polish climate conditions [66]. To prove the consistency of the developed FE model, the obtained results can be compared with the results by Anderson et al. [4], who investigated experimentally a large area building integrated

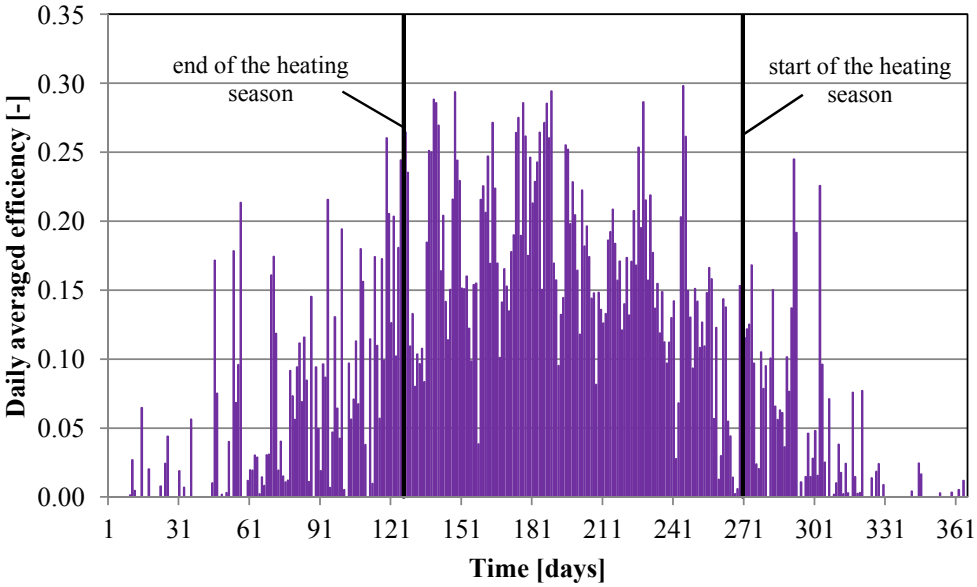

Figure 6.16: Annual variation of daily averaged solar collector efficiency

solar collector dedicated for pool heating in New Zealand. The authors reported that the average solar collector efficiency over the summer season was 0.22 [−].

Fig. 6.17 depicts the variation of the hourly averaged solar collector efficiency for the most sunny day of January and July. The hourly averaged efficiency is much higher than the daily averaged one. For the considered winter and summer days, the daily averaged efficiency is 0.04 [−] and 0.24 [−], respectively. Whereas, the maximum hourly averaged efficiency is 0.14 [−] and 0.45 [−] for the winter and summer day, respectively. This is due to the fact that daily averaged values (Eq. 5.4.6), include those periods of the daytime ($I > 0\,\mathrm{W/m^2}$) when the collector does not operate (just after the sunrise). One should notice that in both cases, the maximum values do not correspond to time periods when the incident solar radiation is the most abundant. The efficiency values during the time when the peak solar irradiation occurs are 0.10 [−] and 0.38 [−] for the winter and summer day, respectively. The observed time lag, is a consequence of the collector's thermal inertia. The heat storage in collector's structure components delays the heat transfer into pipes. When the solar intensity decreases, the heat stored in structure components is transferred into pipes, hence increasing the hourly averaged efficiency. The low values obtained for morning hours are (besides being caused by thermal inertia) a consequence of assumed control strategy (Section 5.5). Both during the winter and summer day, it takes some time for the collector to start operating after the sunrise. Thus, the efficiency is limited at the beginning of the day.

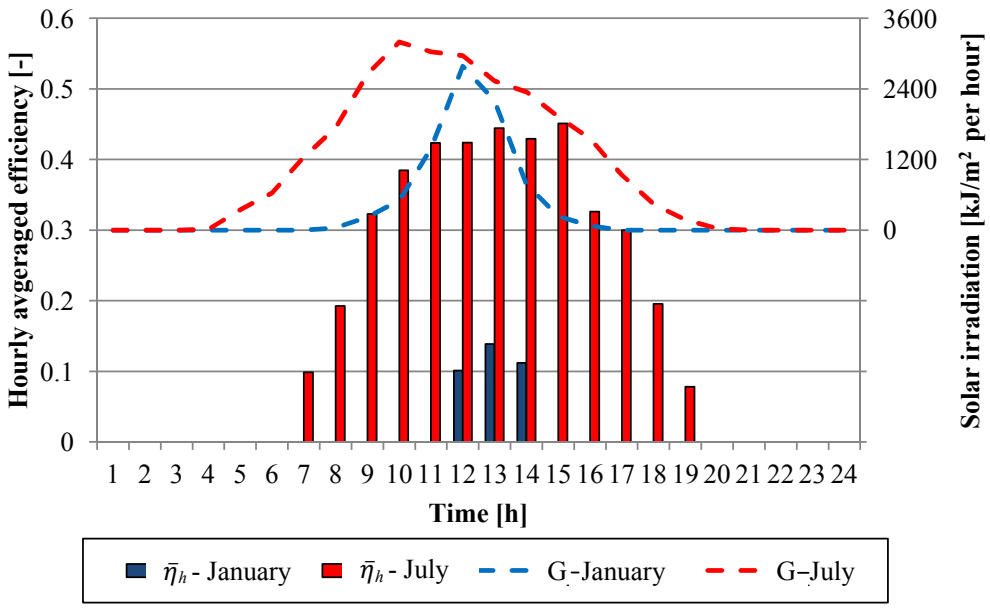

Figure 6.17: Hourly averaged solar collector efficiency for the most sunny day of January (26th of January) and July (5th of July)

6.2.2 Supporting domestic hot water systems

The capability of HSC to support domestic hot water (DHW) systems under Polish climate conditions was evaluated on basis of the year-round collector operation simulation. The general requirement for DHW system is to provide the water of temperature equal to 50 °C [169]. For the purpose of this analysis it is assumed that energy collected by the collector is useful to support DHW systems when the outlet water temperature is higher than 55 °C. Such an approach is reasonable to maintain the required temperature level in the water storage tank.

With regard to the assumed criterion of hot water temperature, the obtained results, in the form of the effective operating-time analysis (Fig. 6.18), indicate that HSC is capable to collect the useful energy for 198 hours during the entire year period what corresponds to only 5 % of the total time when $I > 0\,\mathrm{W/m^2}$. Over 78 % of the effective operating-time refers to the summer season. During this time, the collector operates effectively, on average, 1.2 hours per day, whereas the maximum magnitude of the effective operating-time per day is 2.3 hours. The number of days when the collector could not meet any part of DHW requirements during the summer season is 12. To compare, during the winter season the collector operates effectively, on average, 0.7 hours per day, whereas the number of void days is 159. One should notice, that through over 78 % of the total annual operating-time, the outlet water temperature is below the required 55 °C, hence decreasing the overall performance of the collector. Thus, the presented results for DHW are significantly underestimated.

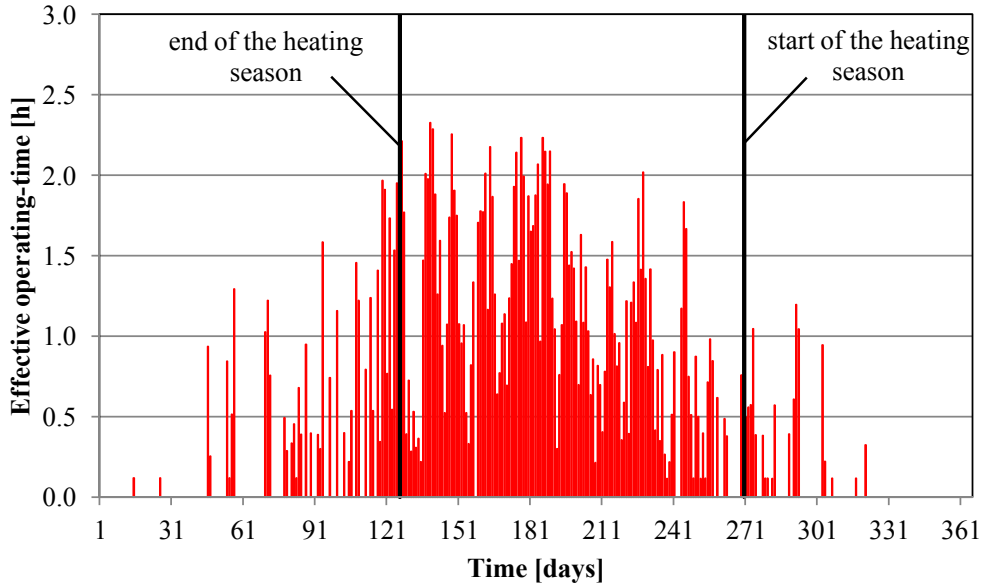

Figure 6.18: Annual variation of effective operating-time of HSC applied to supply domestic hot water system

The analysis of HSC performance during the summer day (Fig. 6.19) indicates that the observed difference is resulted from the applied control system (Section 5.5). The control strategy for the purpose of this analysis is analogous to the one that is used for the transient simulation of the HSC operation applied to supply space-heating system. Hence, the oscillations of the outlet water temperature around the set point, due to strong fluctuations of water mass flux, limits the effective operating-

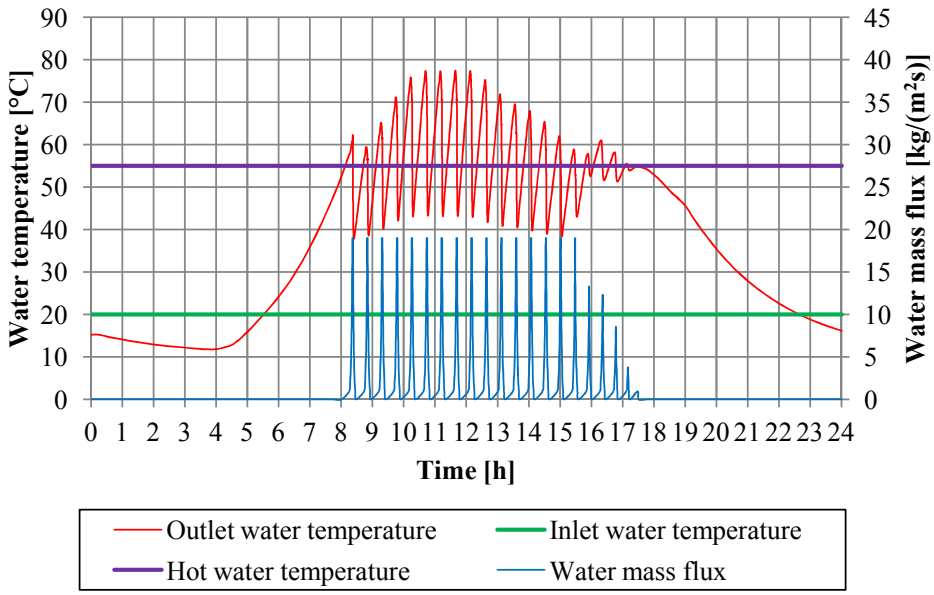

Figure 6.19: Operation characteristics of HSC applied to support domestic hot water system during the most sunny day of July (5th of July)

time of the collector. For the considered summer day, it is 2.3 hours corresponding to only 25 % of the total time when the control system operates to keep the outlet water temperature above the required temperature level. One should notice that during the operating-time the water flow through the collector's pipes is stopped for several times. According to the assumed time increment control function (Section 5.3.3), the magnitude of time increment corresponding to the water mass flux of 0 kg/(m^2·s) equals to 900 seconds. Hence, for the considered summer day, the water flow is stopped through over 48 % of the total operating-time. This clearly indicates a great potential to increase the performance of HSC by applying an improved control strategy for the water flow and time increment.

Assuming that the total hot water consumption in the residential detached house occupied by 4 persons (hot water consumption per person per day is 35 l [142]) is 140 l/day, the daily energy required to heat the water (assuming that the temperature of cold water from the water supply system is 5 °C) is 26378 kJ. For the considered summer day, the total amount energy collected by HSC (of 0.9 m^2 absorber surface area), that is useful to heat the water from the supply system ($T_{w,out} > 55$ °C), is 1941 kJ. The obtained results correspond to 7.4 % of the daily energy demand. The size of the collector can be, however, adjusted to the water-heating demand. With the assumption that HSC is a building component of a residential detached house that covers a roof of 60 m^2, the total amount of the useful energy collected during the considered summer day is almost 5 times higher than the DHW system demands.

The analysis of daily amount of useful energy collected by HSC of 60 m^2 absorber surface area (Fig. 6.20) demonstrates that the use of HSC under Polish climate conditions to support DHW systems is effective only during spring and summer months, especially from May to August. During this time period the daily DHW requirements can be meet, on average, by 81 %, whereas during the winter season it is only 28 %. Taking into account the obtained results together with the number of void days for particular season, it can be stated that the use of HSC to support DHW systems during the winter is inefficient. The obtained results are, however, in good agreement with literature findings related to solar collector use under Polish climate conditions. According to the study of Chwieduk [41], the total water requirements can be provided on average of 80-100 % during the time period from May to August with the use of FPCs. On the other hand, Zawadzki [185] reported that the use of solar collectors is completely inefficient during the winter season. Wisniewski et al. [179] indicated that the properly designed active solar system could meet 60–70 % of the anuual DHW requirements. One should notice, that the performance of the

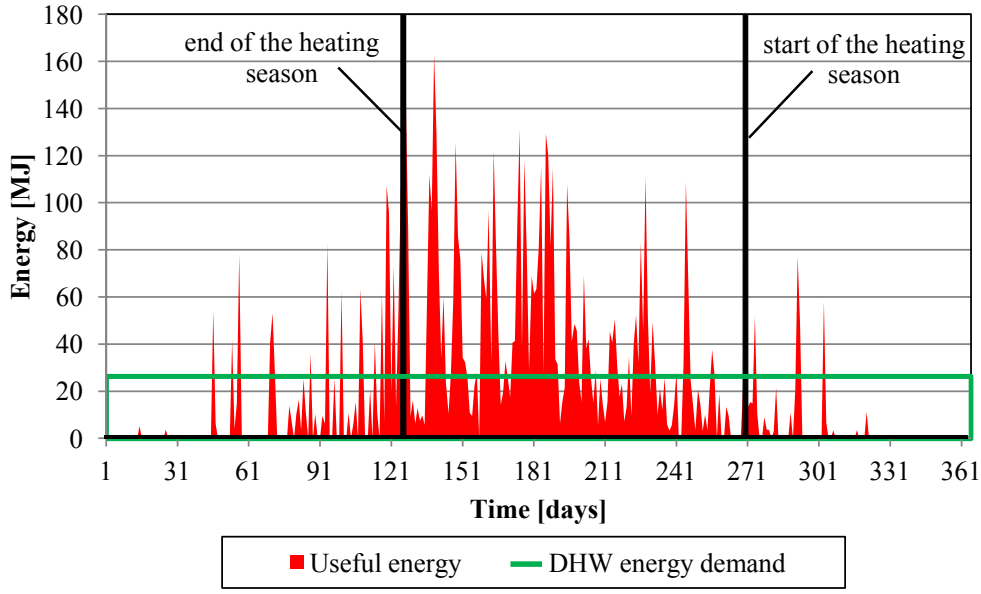

Figure 6.20: Annual variation of daily amount of energy useful to support DHW systems collected by HSC of 60 m^2 surface area

investigated solar collector is significantly limited due to the assumption of constant water temperature at inlets to the collector's pipes ($T_{w,in}$ = 20 °C) throughout the operating-time. It is expected that, in reality, the operational temperature in the seasonal HS system that is supplied with the excess of energy from the water storage tank, overcomes the level of 20 °C.

The analysis of heat gain magnitudes and the corresponding magnitudes of water mass flux (Fig. 6.21) demonstrates that over 59 % of the annual amount of energy useful to support domestic hot water systems is collected by the water flowing with the velocity corresponding to magnitudes of water mass flux lower than 10.45 kg/($m^2 \cdot s$). According to the comparison analysis (Section 5.3.4), for the magnitudes lower than 10 kg/(m^2·s), the discrepancy between results of the CFD and FE models exceeds 8 %. The amount of energy corresponding to the maximum allowable magnitude of water mass flux (19 kg/(m^2·s)), for which the minimum discrepancy is 4 %, equals to only 22.7 %. Whereas, over 13 % of the heat gain corresponds to the magnitude of 0.95 kg/(m^2·s), for which the discrepancy could reach the level of 41 %. The obtained relationship also shows that during the winter season the collector operates effectively with relatively higher magnitudes of water mass flux when compared to the summer season. Based on this analysis, it was found that the obtained results are characterized by a limited level of quality. Thus, the validation of FE model against the experimental measurements carried out on a collector with identical design parameters is crucial for the reliable use of the developed FE model.

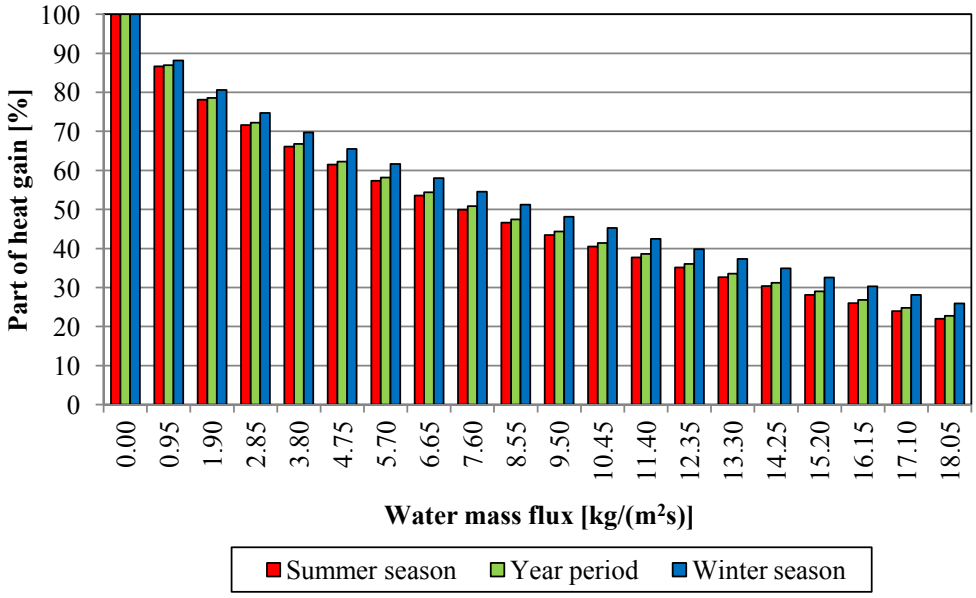

Figure 6.21: Relationship between water mass flux and amount of energy collected by HSC applied to support domestic hot water systems

Chapter 7

Conclusions and future work

The developed FE model of innovative solar collector is capable to simulate three-dimensional unsteady heat transfer process. The model applies a simplified approach to simulate convective heat transfer in the water flowing through the collector's pipes and the air in the roof cavity. The results of comparison between the FE model and the equivalent CFD model indicate that a validity of the assumed approach vary in dependence on boundary conditions, among which the water flow velocity is of crucial influence. The lowest discrepancy between the results, not exceeding the range of 4–7 %, was found for the computational cases when the water flows through the collector's pipes with the maximum allowable velocity (corresponding to 19 kg/(m^2·s)), whereas the biggest discrepancy, varying from 38 % to 41 %, corresponds to the cases when the water flows through the collector's pipes with the minimum allowable velocity (corresponding to 0.95 kg/(m$^2 \cdot s$)). Thus, it can be concluded that the quality of simulation results obtained by FE model are dependent on the operating fluid flow characteristics. The CFD model of HSC developed for the purpose of the comparison analysis, was positively validated against the results of analytical and experimental solutions. Due to the lack of experimental results for hidden solar collector, the validation was carried out indirectly, separately for the sub-model of water flow in the pipes and the sub-model of airflow in a roof cavity round the pipes. In both the cases, the analysis was conducted on basis of steady-state simulations with regard to various boundary conditions. For all the simulations, the calculated error does not exceed 10.5 % and 10.8 % for the sub-model of water in the collector's pipes and the sub-model of air in the roof cavity, respectively. Thus, it can be concluded that the developed FE model of HSC is close enough to reality.

The FE model was used to carry out simulations of HSC operation under both steady-state and transient conditions. The following conclusions can be derived from the results of steady-state simulations presented in this study:

- based on the analysis of the HSC thermal response to varying environmental parameters, the FE model was positively verified against literature findings,

- solar absorptivity coefficient of the roofing material has a significant influence on the performance of HSC. The magnitude of outlet water temperature obtained by HSC of black oil painted roofing surface ($\alpha = 0.90\,[-]$) is by approximately 15 % higher as compared to the collector with a standard white painted roofing surface ($\alpha = 0.39\,[-]$), whereas in case of the useful heat provided by the collector, the increase is 216.5 %. There is, however, a moderate difference in the performance of collectors with the roofing surfaces of commonly used colors. An increase of the outlet water temperature of 4.1 % and 5.4 % is obtained when the steel roofing is dark-brown painted ($\alpha = 0.85\,[-]$) and black oil painted ($\alpha = 0.9\,[-]$), respectively, instead of the conventional red painting ($\alpha = 0.7\,[-]$). In case of the useful heat, the increase is 20.1 % and 26.8 %, respectively. Based on the analysis of outlet water temperature magnitudes obtained by various configurations of HSC, it was found that the collector with the roofing surface characterized by solar absorptivity coefficient lower than 0.7 [−], may be not capable to provide the energy useful to supply both space-heating and domestic hot water systems. Thus, it can be concluded that the steel roofing materials of dark-brown- or black-painted surfaces are recommended for the efficient operation of HSC.

The transient simulations were carried out to evaluate the performance of HSC applied to supply space-heating systems based on very-low-temperature heat sources dedicated for residential detached houses characterized by a low heat demand and to support DHW systems for a year period under Polish climate conditions. With regard to the simulation results for the first of considered collector applications, the following conclusions can be derived:

- temperature of the operating fluid during the winter season drops to 15 °C below the zero Celsius degree. Thus, the application of HSC under Polish climate conditions requires the use of water with the antifreeze solution as an operating fluid,

- total operating-time of HSC during a one year period is 2295 hours, what corresponds to 56 % of the total available daytime (when $I > 0\,\mathrm{W/m^2}$). However, only through 55 % of the total operating-time, the temperature of water at the collector's outlets exceeds the level of 25 °C, hence providing the energy useful to supply the space-heating systems. The observed differences are a consequence of the strategy applied to control the magnitude of water mass

flux at each time increment of the transient simulation. The problem of disturbances in the efficient operation of HSC relates to 42 % and 51 % of the total operating-time during the summer (from May 6 to September 25) and winter season, respectively. Thus, it can be stated that the assumed control strategy leads to decreasing the performance of HSC,

- upper limit of the assumed water mass flux range is not sufficient to decrease the temperature of the energy carrying medium to the required level during the entire time of effective collector operation. The magnitude of outlet water temperature could be higher by, on average, 2 °C than the assumed set point for more than 6 hours of the continuous collector operation. This contributes to the additional decrease of the HSC performance,

- variation of the useful energy collected during a year-round operation is highly correlated with the climate conditions. The total energy collected by HSC of 0.9 m^2 absorber surface area during a year-round operation is 617.7 MJ (equivalent to 190.7 kWh/m^2). Over 74.3 % of this amount refers to the summer season. The maximum heat corresponding to 132.4 MJ is collected in May, whereas the minimum, equal to 0.3 MJ, is collected in December. The amount of thermal energy collected by HSC from June to December is over 3 times lower as compared to the energy collected by conventional solar collectors during the same time period under Polish climate conditions,

- during a year-round operation HSC of 60 m^2 absorber surface area is capable to collect approximately 3 times more energy than it is required to satisfy annual space-heating loads in a residential detached house with the 250 m^2 heated area, which meets standards of passive houses. Therefore, it can be concluded that there is a great potential of HSC to supply space-heating systems based on very-low-temperature heat sources dedicated for residential buildings characterized by a low heat demand. One should notice that the magnitude of inlet water temperature is constant, equal to 20 °C, throughout the operating-time. In reality, this magnitude varies in time and in dependence on operating temperature in the seasonal heat storage system. Thus, it can be concluded that the final evaluation of the HSC potential to supply the space-heating systems requires the effectiveness of the heat storage system to be taken into account by the FE model of HSC,

- daily energy required to power HSC of 60 m^2 absorber surface area does not exceed the level of 0.84 kWh. Total cost of the year-round collector operation is

124.3 pln, what approximately corresponds to 18.5 % of the total cost of space-heating in the considered building (annual space-heating loads of 13.5 GJ) with the assumption that the heat is provided from the district heat network,

- annual averaged solar collector efficiency is hardly over the level of 0.09 [−]. For the winter and summer season it is 0.04 [−] and 0.17 [−], respectively. The maximum hourly averaged efficiency is 0.51 [−]. Since, the value of 0.5 [−] is a typical magnitude for conventional flat plate collectors, it can be stated that HSC is characterized by low efficiency to convert solar energy into the useable heat,

- over 67 % of the annual amount of useful energy is collected by the water flowing with the maximum allowable velocity, whereas only 1.8 % of the total heat gain corresponds to the minimum water flow velocity. With regard to conclusions from the comparison analysis between the CFD and FE model, it can be stated that the obtained results are characterized by a reasonable level of quality and thus are useful for the purpose of approximate estimation of the HSC performance applied to supply space-heating systems. Nevertheless, the FE model of HSC should be validated against experimental measurements carried out on a collector with identical design parameters.

The following conclusions can be derived from the results of the unsteady performance analysis of HSC applied to support DHW systems:

- total time when the collector is able to collect the energy useful to support DHW systems ($T_{w,out} > 55\,°\mathrm{C}$) is 198 hours what corresponds to only 22 % of the total operating-time. Over 78 % of the effective operating-time refers to the summer season. The observed difference between the time of effective and ineffective collector operation is resulted from the applied water flow control strategy and, additionally, from the time increment control function. Thus, it can be concluded that the obtained results are significantly underestimated,

- application of HSC to support DHW systems is effective during the spring and summer months, especially from May to August. During this time period the collector of 60 m^2 absorber surface area is capable to meet, on average, 81 % of the daily DHW requirements (assuming that house is occupied by 4 persons). During the winter season it is only 28 %. The number of days when the collector cannot meet any part of DHW requirements is 159 and 12 for winter and summer season, respectively. The obtained results are in agreement

with literature finding. One should notice that, through the analogy to space-heating application, the temperature of water at inlets to the collector's pipes is constant, equal to 20 °C, throughout the operating-time. This, additionally, contributes to underestimation of the useful energy amount that is possible to collect by HSC,

- over 59 % of the annual amount of useful energy is collected by the water flowing with the velocity corresponding to magnitudes of mass flux lower than 10.45 kg/(m^2·s). The amount of energy corresponding to maximum and minimum allowable water flow velocity is 22.7 % and 13 %, respectively. With regard to conclusions from the comparison analysis between CFD and FE models, it can be stated that the obtained results are characterized by limited level of quality. Thus, the validation of FE model against the experimental measurements carried out on a collector with identical design parameters is crucial for the reliable use of the developed FE model.

The following suggestions are derived for the future work on hidden solar collectors:

- control strategy of water mass flux magnitude at each time increment of the transient simulation must be improved. The performance of HSC using the Proportional-Integral (PI) controller need to be investigated,
- magnitude of water temperature at inlets to the collector's pipes is to be controlled at each time increment of the transient simulation. The additional control function in order to simulate the effectiveness of seasonal heat storage system must be implemented in the FE model of HSC so as to reach more reliable results,
- control function of time increment magnitude for the unsteady simulations need to be modified. The unsteady performance analysis of HSC, for which the maximum time increment is 60 seconds, is to be carried out,
- it is necessary to estimate the performance of HSC in dependence on structure configurations, including the height and wide of the air-cavity, and the number of pipes in the segment of the collector. An influence of the roof inclination on total amount of collected energy is also a target,
- influence of radiant barrier in the air-cavity on the amount of collected energy should be investigated,
- performance of HSC using the water with antifreeze solution as the energy carrying medium instead of the pure water must be determined,

- application of HSC to supply, only, a typical DHW system is to be conducted. An appropriate control function for inlet water temperature, in correspondence to current operating temperature in the water storage tank, should be implemented in the FE model of HSC so as to provide reliable results,
- geographical dependence of the performance in order to define preferred regions for particular applications of HSC should be determined.

The results of this thesis provide a valuable contribution to the realization of the ongoing research project "Innovative comprehensive and solution system for the energy-efficient, characterized by a high-class comfort, house building in a unique prefabrication technology, and installation of composite panels" financed by the National Centre for Research and Development (in Poland). The project inter alia aims at implementation of the Thermal Barrier heating/cooling technology (Section 3.3.2.4) in the house building sector, which is supplied by the solar energy collected by the hidden solar collector. Within the project, the author of this thesis is responsible for the implementation of the active solar energy system for supplying the TB technology. The main stage of the project concerns an experimental investigation basing on a full-scale test building. The in-situ measurements of the solar collector performance during a year-round operation will enable the validation of the FE model of HSC used in this study.

Bibliography

[1] Akpinar, A., Komurcu, M.I., Onsoy, H., Kaygusuz, K. Status of geothermal energy amongst Turkey's energy sources. *Renewable and Sustainable Energy Reviews* 12 (2008), pp. 1148–1161.

[2] Alzoubi, H.H., Alshboul, A.A. Low energy architecture and solar rights: Restructuring urban regulations, view from Jordan. *Renewable Energy* 35 (2010), pp. 333–342.

[3] Amer, E.H., Nayak, J.K. Evaluation of a transient test procedure for solar flat-plate collectors. *Energy* 24 (1999), pp. 979–995.

[4] Anderson, T.N, Duke, M., Carson, J.K., Künnemeyer, R., Smith, B. The development of a novel large area building integrated solar collector for pool heating. *Proceedings: AuSES Annual Conference*, Canberra, 2010.

[5] Anderson, T.N., Duke, M., Carson, J.K. The effect of colour on the thermal performance of building integrated solar collectors. *Solar Energy Materials and Solar Cells* 94 (2010), pp. 350–354.

[6] ANSYS CFX-Solver Theory Guide, Release 15.0, ANSYS Inc., Canonsburg, USA, November 2013.

[7] Arendt, K. Influence of extenral walls' thermal capacitance on indoor thermal comfort. *Ph.D. thesis* (2012), Gdansk University of Technology.

[8] Badescu, V. *Modeling solar radiation at the earth's surface: recent advances.* Springer-Verlag Berlin Heidelberg, Germany, 2008.

[9] Badescu, V. Optimal control of flow in solar collectors for maximum exergy extraction. *International Journal of Heat and Mass Transfer* 50 (2007), pp. 4311–4322.

[10] Badescu, V. Optimal control of flow in solar collector systems with fully mixed water storage tanks. *Energy Conversion and Management* 49 (2008), pp. 169–184.

[11] Badescu, V. Simulation analysis for the active solar heating system of a passive house. *Applied Thermal Engineering* 25 (2005), pp. 2754–2763.

[12] Badescu, V., Staicovici, M.D. Renewable energy for house heating Model of the active solar heating system. *Energy and Buildings* 38 (2006), pp. 129–141.

[13] Bainbridge, D.A. *A Water Wall Solar Design Manual for environmentally responsive buildings that increase comfort, save money, and protect the environment.* San Diego, 2005.

[14] Bakis, R. Electricity production opportunities from multipurpose dams (case study). *Renewable Energy* 32 (2007), pp. 1723–1738.

[15] Balaras, C.A, Droutsa, K., Dascalaki, E., Kontoyiannidis, S. Heating energy consumption and resulting environmental impact of European apartment buildings. *Energy and Buildings* 37 (2005), pp. 429–442.

[16] Bathe, K.J. *Finite Element Procedures in Engineering Analysis.* Prentice-Hall, Englewood, New Jersey, USA, 1982.

[17] Bejan, A., Schultz, W. Optimum flow-rate history for cooldown and energy storage processes. *International Journal of Heat and Mass Transfer* 25 (1982), pp. 1087–1092.

[18] Benli, H., Durmus, A. Performance analysis of a latent heat storage system with phase change material for new designed solar collectors in greenhouse heating. *Solar Energy* 83 (2009), pp. 2109–2119.

[19] Ben-Nakhi, A., Mahmoud, M.A. Conjugate turbulent natural convection in the roof enclosure of a heavy construction building during winter. *Applied Thermal Engineering* 28 (2008), pp. 1522–1535.

[20] Biwole, P.H., Woloszyn, M., Pompeo, C. Heat transfers in a double-skin roof ventilated by natural convection in summer time. *Energy and Buildings* 40 (2008), pp. 1487–1497.

[21] Bogdanienko, J., Chochowski, A., Chwieduk, D., Domański, R., Gogół, W., Krzyżanowski, J., Laskowski, L., Mikielewicz, J.,

Pabis, J., Pluta, Z., Podogrodzki, J., Pomierny, W., Wnuk, R. *Solar energy thermal conversion in Polish conditions.* W. Gogół (Ed). Polish Academy of Sciences, IV Division of Technical Sciences, Thermodynamics and Combustion Committee. Warsaw, 1993 (in Polish).

[22] Blanco, J., Malato, S., Fernandez-Ibanez, P., Alarcon, D., Gernjak, W., Maldonado, M.I. Review of feasible solar energy applications to water processes. *Renewable and Sustainable Energy Reviews* 13 (2009), pp. 1437–1445.

[23] Blazec, J. *Computational Fluid Dynamics: Principles and Applications*, Elsevier Science Ltd., Kidlington, 2001.

[24] BP Statistical Review of World Energy, BP p.l.c. June 2006.

[25] Burch, J., Christensen, C., Salasovich, J., Thornton, J. Simulation of an unglazed collector system for domestic hot water and space heating and cooling. *Solar Energy* 77 (2004), pp. 399–406.

[26] Butti, K., Perlin, J. *A Golden Thread: 2500 Years of Solar Architecture and Technology.* Cheshire Books, distributed by Van Nostrand Reinhold Company, New York and London, 1980.

[27] Carslaw, H.S., Jaeger, J.C. *Conduction of Heat in Solids, Second Edition.* Oxford University Press, Fairlawn, NJ, 1959.

[28] Causon, D.M., Mingham, C.G., Qian, L. *Introductory Finite Volume Methods for PDEs.* Ventus Publishing ApS, Bookboon.com, 2011.

[29] Cerne, B., Medved, S. Determination of transient two-dimensional heat transfer in ventilated lightweight low sloped roof using Fourier series. *Building and Environment* 42 (2007), pp. 2279–2288.

[30] Chami, N., Zoughaib, A. Modeling natural convection in a pitched thermosyphon system in building roofs and experimental validation using particle image velocimetry. *Energy and Buildings* 42 (2010), pp. 1267–1274.

[31] Chan, Hoy-Jen, Riffat, S.B., Zhu, J. Review of solar heating and cooling technologies. *Renewable and Sustainable Energy Reviews* 14 (2010), pp. 781–789.

[32] Chen, C.J. *Physics of Solar Energy.* John Wiley & Sons, Inc., Hoboken, New Jersey, 2011.

[33] Chmielewski, M., Gieras, M. Three-zonal Wall Function for $k - \varepsilon$ Turbulence Models. *Computational Methods in Science and Technology* 4 (2013), pp. 107–114.

[34] Chow, T.T., He, W., Ji, J. An experimental study of facade-integrated photovoltaic/water-heating system. *Applied Thermal Engineering* 27 (2007), pp. 37–45.

[35] Chwieduk, D., Bogdanska, B. Technical note Some recommendations for inclinations and orientations of building elements under solar radiation in Polish conditions. *Renewable Energy* 29 (2004), pp. 1569–1581.

[36] Chwieduk, D. *Development of support mechanisms to promote heat and cool production based on renewable energy sources with focus on solar collectors.* Expertise for Ministry of Economy, 2009 (in Polish).

[37] Chwieduk, D. *Energetyka słoneczna w budynku (Solar energy in building).* ARKADY, Warsaw, 2011 (in Polish).

[38] Chwieduk, D. Prospects for Low Energy Buildings in Poland. *Renewable Energy* 16 (1999), pp. 1196–1199.

[39] Chwieduk, D. Seasonal Ground Heat Storage. *Proceedings of 6th International Symposium of Heat Transfer and Renewable Ener*gy, Swinoujscie, Poland, 1996 (in Polish).

[40] Chwieduk, D. *Słoneczne i gruntowe systemy grzewcze. Zagadnienia symulacji funkcjonowania i wydajności cieplnej.* IKE, 1994 (in Polish).

[41] Chwieduk, D. Solar Energy Use for Thermal Application in Poland. *Polish Journal of Environmental Studies* 3 (2010), pp. 473–477.

[42] Chwieduk, D. Towards sustainable-energy buildings. *Applied Energy* 76 (2003), pp. 211–217.

[43] Chwieduk, D. Underground Thermal Energy Storage in Poland. *Proceedings of The Second Stockton International Geothermal Conference*, New Jersey, 1998.

[44] Ciampi, M., Leccese, F., Tuoni, G. Energy analysis of ventilated and microventilated roofs. *Solar Energy* 79 (2005), pp. 183–192.

[45] Ciampi, M., Leccese, F., Tuoni, G. Ventilated facades energy performance in summer cooling of buildings. *Solar Energy* 75 (2003), pp. 491–502.

[46] Close, D.J. A design approach for solar processes. *Solar Energy* 11 (1967), pp. 112.

[47] Colon, C., Merrigan, T. Roof integrated solar absorber: the measured performance of "invisible" solar collectors. *Proceedings of ASES National Solar Energy Conference*, Washington, 2001.

[48] Corbin, C.D., Zhai, Z.J. Experimental and numerical investigation on thermal and electrical performance of a building integrated photovoltaic–thermal collector system. *Energy and Buildings* 42 (2010), pp. 76–82.

[49] Dassault Systèmes Simulia Corp., ABAQUS Version 6.10 Documentation, Providence, RI, USA, 2010.

[50] de Ron, A.J. Dynamic modeling and verification of a flat-plate solar collector. *Solar Energy* 24 (1980), pp. 117–128.

[51] Dincer, I., Rosen, M.A. A worldwide perspective on energy, environment and sustainable development. *International Journal of Energy Research* 22 (1998), pp. 1305–1321.

[52] Dincer, I. Energy and environmental impacts: present and future perspectives. *Energy Sources* 20 (1998), pp. 427–453.

[53] Dincer, I. Environmental impacts of energy. *Energy Policy* 27 (1999), pp. 845–854.

[54] Directive of the European Parliament and of the Council on the energy performance of buildings, COM(2001) 226 final, 2001/0098 (COD), 2001.

[55] Domański, R. *Thermal Energy Storage*. PWN, Warsaw, 1990.

[56] Dong, L., Liu, H., Riffat, S. Development of small-scale and micro-scale biomass-fuelled CHP systems - A literature review. *Applied Thermal Engineering* 29 (2009), pp. 2119–2126.

[57] Dović, D., Andrassy, M. Numerically assisted analysis of flat and corrugated plate solar collectors thermal performances. *Solar Energy* (2012); article in press.

[58] Duffie, J.A., Beckman, W.A. *Solar Engineering of Thermal Processes.* John Wiley & Sons, inc., New York, 1980.

[59] Erdodgu, E. A snapshot of geothermal energy potential and utilization in Turkey. *Renewable and Sustainable Energy Reviews* 13 (2009), pp. 2535–2543.

[60] *Solar Thermal Markets in Europe, Trends and Market Statistics 2010.* European Solar Thermal Industry Federation (ESTIF), Brussels, 2011.

[61] Fan, J., Shah, L.J., Furbo, S. Flow distribution in a solar collector panel with horizontally inclined absorber strips. *Solar Energy* 87 (2007), pp. 1501–1511.

[62] Felske, J.D. The effect of off-south orientation on the performance of flat-plate solar collectors. *Solar Energy* 20 (1978), pp. 29–36.

[63] Florides, G., Kalogirou, S. Ground heat exchangers - a review of systems, models and applications. *Renewable Energy* 32 (2007), pp. 2461–2478.

[64] Gagliano, A., Patania, F., Nocera, F., Ferlito, A., Galesi, A. Thermal performance of ventilated roofs during summer period. *Energy and Buildings* 49 (2012), pp. 611–618.

[65] Garg, V.K. *Applied Computational Fluid Dynamics*, Marcel Dekker, Inc., New York, 1998.

[66] Głuszek, A., Magiera, J. Możliwość konwersji energii słonecznej do energii cieplnej w warunkach polskich (The possibilities of the conversion of solar energy to thermal energy in Polish conditions). *Polityka Energetyczna* 11 (2008), pp. 41–49 (in Polish).

[67] Gogól, W. *Expert evidence: thermal conversion of solar energy in Polish conditions.* Polish Academy of Sciences, Committee of Thermodynamics and Combustion, Dept. 4, Warsaw, 1993 (in Polish).

[68] Gokcol, C., Dursun, B., Alboyaci, B., Sunan, E. Importance of biomass energy as alternative to other sources in Turkey. *Energy Policy* 38 (2009), pp. 424–431.

[69] Gopinathan, K.K. Solar radiation on variously oriented sloping surfaces. *Solar Energy* 47 (1991), pp. 173–179.

[70] Goswami, D.Y., Vijayaraghavan, S., Lu, S., Tamm, G. New and emerging developments in solar energy. *Solar Energy* 76 (2004), pp. 33–34.

[71] Guiavarch, A., Peuportier, B. Photovoltaic collectors efficiency according to their integration in buildings. *Solar Energy* 80 (2006), pp. 65–77.

[72] Gunerhan, H., Hepbasli, A. Determination of the optimum tilt angle of solar collectors for building applications. *Building and Environment* 42 (2007), pp. 779–783.

[73] Hasnain, S.M. Review on sustainable thermal energy storage technologies, Part I: heat storage materials and techniques. *Energy Conversion and Management* 39 (1998), pp. 1127–1138.

[74] Hassan, M.M., Beliveau, Y. Design, construction and performance prediction of integrated solar roof collectors using finite element analysis. *Construction and Building Materials* 21 (2007), pp. 1069–1078.

[75] Hassan, M.M., Beliveau, Y. Modeling of an integrated solar system. *Building and Environment* 43 (2008), pp. 804–810.

[76] Hassan, M.M. Framework for Evaluation of Active Solar Collection Systems. *Ph.D. thesis* (2003), Virginia Polytechnic Institute and State University.

[77] Henderson, D., Junaidi, H., Muneer, T., Grassie, T., Currie, J. Experimental and CFD investigation of an ICSSWH at various inclinations. *Renewable and Sustainable Energy Reviews* 11 (2007), pp. 1087–1116.

[78] Herbert, G.M.J., Iniyan, S., Sreevalsan, E., Rajapandian, S. A review of wind energy technologies. *Renewable and Sustainable Energy Reviews* 11 (2007), pp. 1117–1145.

[79] Hilmer, F., Vajen, K., Ratka, A., Ackermann, H., Fuhs, W., Melsheimer, O. Numerical solution and validation of a dynamic model of solar collectors working with varying fluid flow rate. *Solar Energy* 65 (1999), pp. 305–321.

[80] Hirunlabh, J., Wachirapuwadon, S., Pratinthong, N., Khedari, J. New configurations of a roof solar collector maximizing natural ventilation. *Building and Environment* 36 (2001), pp. 383–391.

[81] Ho, C.D., Chen, T.C. Collector efficiency improvement of recyclic double-pass sheet-and-tube solar water heaters with internal fins attached. *Renewable Energy* 33 (2008), pp. 655–664.

[82] Hollands, K.G.T., Brunger, A.P. Optimum flow rates in solar water heating systems with a counterflow exchanger. *Solar Energy* 48 (1992), pp. 15.

[83] Hottel, H.C. Performance of flat-plate energy collectors. In: Space Heating with Solar Energy. *Proc. Course Symp.* Cambridge: MIT Press, 1954.

[84] Horel, J.D., De Winter, F. *Investigations of methods to transfer heat from solar liquid-heating collectors to heat storage tanks.* Final report on US Department of Energy Contract E(04)1238, Atlas Corporation, Santa Cruz CA, 1978.

[85] Huang, H., Yan, Z. Present situation and future prospect of hydropower in China. *Renewable and Sustainable Energy Reviews* 13 (2009), pp. 1652–1656.

[86] Hyewood, H. Operating experience with solar water heating. *Journal of the Institution of Heating and Ventilation Engineers* 39 (1971), pp. 63–69.

[87] Infrared Services, Inc., http://www.infrared-thermography.com.

[88] Iordanou, G. Flat-Plate Solar Collectors for Water Heating with Improved Heat Transfer for Application in Climatic Conditions of Mediterranean Region. *Ph.D. thesis* (2009), Durham University.

[89] Isakson, P. *Solar collector model for testing and simulation.* Building Services Engineering, Royal Institute of Technology, Stockholm, Sweden, 1995.

[90] Kalogirou, S.A., Tripanagnostopoulos, Y. Hybrid PV/T solar systems for domestic hot water and electricity production. *Energy Conversion and Management* 47 (2006), pp. 3368–3382.

[91] Kalogirou, S.A., Solar thermal collectors and applications. *Progress in Energy and Combustion Science* 30 (2004), pp. 231–295.

[92] Kalogirou, S.A. *Solar Energy Engineering:Processes and Systems.* Elsevier, USA, 2009.

[93] Kalogirou, S. The potential of solar industrial process heat applications. *Applied Energy* 76 (2003), pp. 337–361.

[94] Kamminga, W. Experiences of a solar collector test method using Fourier transfer functions. *International Journal of Heat and Mass Transfer* 28 (1985), pp. 1393–1404.

[95] Kaushik, N.D., Rao, S.K. Non-convective roof pond for space heating. *Applied Energy* 12 (1982), pp. 21–36.

[96] Kemp, C.M. US Patent No. 451384, 28th April 1891.

[97] Kern, J., Harris, I. On the optimum tilt of a solar collector. *Solar Energy* 17 (1975), pp. 97–102.

[98] Key world energy statistics, International Energy Agency, Paris 2007.

[99] Kjellsson, E. Solar Collectors Combined with Ground-Source Heat Pumps in Dwellings. Analyses of System Performance. *Ph.D. thesis* (2009), Lund University.

[100] Klein, S.A., Duffie, J.A., Beckman, W.A. Transient considerations of flat-Plate solar collectors. *Transactions of ASME. Journal of Engineering for Power* 96A (1974), pp. 109.

[101] Kong, W., Wang, Z., Li, X., Li, X., Xiao, N. Theoretical analysis and experimental verification of a new dynamic test method for solar collectors. *Solar Energy* 86 (2012), pp. 398–406.

[102] Kovarik, M., Lesse, P.F. Optimal control of flow in low temperature solar heat collectors. *Solar Energy* 18 (1976), pp. 431–435.

[103] Krzaczek, M., Kowalczuk, Z. Thermal Barrier as a technique of indirect heating and cooling for residential buildings. *Energy and Buildings* 43 (2011), pp. 823–837.

[104] Kumar, S., Mullick, S.C. Wind heat transfer coefficient in solar collectors in outdoor conditions. *Solar Energy* 84 (2010), pp. 956–963.

[105] Kumar, R., Rosen, M.A. Thermal performance of integrated collector storage solar water heater with corrugated absorber surface. *Applied Thermal Engineering* 30 (2010), pp. 1764–1768.

[106] Kundu, B. Analytic method for thermal performance and optimization of an absorber plate fin having variable thermal conductivity and overall loss coefficient. *Applied Energy* 87 (2010), pp. 2243–2255.

[107] Kyoto Protocol to the United Nations Framework Convention on Climate Change, Kyoto 11 December 1997.

[108] Latała, H. Wpływ warunków solarnych na efekt pracy próżniowego i płaskiego kolektora słonecznego (The impact of solar conditions on the effect of work of vacuum tube and flat plate solar collector). *Inżynieria Rolnicza* 9 (2008), pp. 181–188 (in Polish).

[109] Launder, B.E., Spalding, D.B. Numerical Computation of Turbulent Flows. *Computer Methods in Applied Mechanics and Engineering* 3 (1974), pp. 269–289.

[110] Lewis, R.W., Nithiarasu, P., Seetharamu, K.N. *Fundamentals of the Finite Element Method for Heat and Fluid Flow*, John Wiley & Sons, Ltd, Chichester, 2004.

[111] Lewis, G. Optimum tilt of a solar collectors. *Solar and Wind Technology* 4 (1987), pp. 407.

[112] Lienhard IV, J.H., Lienhard V, J.H. *A Heat Transfer Textbook*, Phlogiston Press, Massachusetts, USA, 2004.

[113] Lof, G.O.G., Taybout, R.A. Cost of house heating with solar energy. *Solar Energy* 14 (1973), pp. 253.

[114] Lu, S.M., Li, C.M., Tang, J.C. Optimum design of natural-circulation solar-waterheater by the Taguchi method. *Energy* 28 (2008), pp. 741–750.

[115] Majumdar, S. Role of underrelaxation in momentum interpolation for calculation of flow with nonstaggered and colocated grids. *Numerical Heat Transfer* 13 (1988), pp. 125–132.

[116] Martinopoulos, G., Missirlis, D., Tsilingiridis, G., Yakinthos, K., Kyriakis, N. CFD modeling of a polymer solar collector. *Renewable Energy* 35 (2010), pp. 1499–1508.

[117] Meaburn, A., Hughes, F.M. Resonance characteristics of distributed solar collector fields. *Solar Energy* 51 (1993), pp. 215–221.

[118] Medved, S., Arkar, C., Cerne, C. A large-panel unglazed roof-integrated liquid solar collector—energy and economic evaluation. *Solar Energy* 75 (2003), pp. 455–467.

[119] Metais, B., Eckert, E.R.G. Forced, mixed, and free convection regimes. *J. Heat Transfer–Trans. ASME* 86 (1964), pp. 295–296.

[120] Minn, M.A., Ng, K.C., Khong, W.H., Melvin, T. A distributed model for a tedlar-foil flat plate solar collector. *Renewable Energy* 27 (2002), pp. 507–523.

[121] Mitchell, J.W. Heat transfer from spheres and other animal forms. *Biophysical Journal* 16 (1976), pp. 561.

[122] Mora, L., Gadgil, A.J., Wurtz, E. Comparing zonal and CFD model predictions of isothermal indoor airflows to experimental data. *Indoor Air* 13 (2003), p. 77–85.

[123] Morkovin, M.V. *Effects of Compressibility on Turbulent Flow, The Mechanics of Turbulence*, Favre, A. (ed), Gordon and Breach, New York, 1964.

[124] Munari Probst, M., Roecker, C. Towards an improved architectural quality of building integrated solar thermal systems (BIST). *Solar Energy* 81 (2007), pp. 1104–1116.

[125] Muschawek, J., Spirkl, W. Dynamic solar collector performance testing. *Solar Energy Materials Solar Cells* 30 (1993), pp. 95–105.

[126] Neale, A., Derome, D., Blocken, B., Carmeliet, J. CFD calculation of convective heat transfer coefficients and validation–Part I: Laminar flow. *Proceedings of IEA ECBCS Annex 41 working meeting,* Kyoto, Japan, 2006.

[127] Omer, A.M. Ground-source heat pumps systems and applications. *Renewable and Sustainable Energy Reviews* 12 (2008), pp. 344–371.

[128] Oszczak, W. *Kolektory słoneczne i fotoogniwa w Twoim domu (Solar collectors and photovoltaic cell in Your house).* WKŁ, Warsaw, 2012 (in Polish).

[129] Ozenger, L. A review on the experimental and analytical analysis of earth to air heat exchanger (EAHE) systems in Turkey. *Renewable and Sustainable Energy Reviews* 15 (2011), pp. 4483–4490.

[130] Ozisik, M.N., Czisik, M.N. *Finite Difference Methods in Heat Transfer.* CRC Press, 1994.

[131] Palyvos, J.A. A survey of wind convection coefficient correlations for building envelope energy systems' modeling. *Applied Thermal Engineering* 28 (2008), pp. 801–808.

[132] Patania, F., Gagliano, A., Nocera, F., Ferlito, A., Galesi, A. Thermofluid-dynamic analysis of ventilated facades. *Energy and Buildings* 42 (2010), pp. 1148–1155.

[133] Patankar, S.V. *Numerical Heat Transfer and Fluid Flow*, W.J. Minkowycz and E.M. Sparrow (eds.), Hemisphere Publishing Corporation, New York, 1980.

[134] Petit, J.R., Jouzel, J., Raynand, D., Barkov, N.I., Barnola, J.M., Basile, I. et al. Climate and atmospheric history of the past 420.000 years from the Vostok ice core in Antartica. *Nature* 399 (1999), pp. 429–436.

[135] Pinel, P., Cruickshank, C.A., Beausoleil-Morrison, I., Wills, A. A review of available methods for seasonal storage of solar thermal energy in residential applications. *Renewable and Sustainable Energy Reviews* 15 (2011), pp. 3341–3359.

[136] PN-EN ISO 6946:2008, Building Components and Building Elements, Thermal Resistance and Thermal Transmittance, Calculation Method, 2008 (in polish).

[137] PN-EN ISO 15927-4, Hygrothermal Performance of Buildings – Calculation and Presentation of Climatic Data – Part 4, Data for Assessing the Annual Energy for Cooling and Heating Systems, Warsaw, 2007 (in Polish).

[138] PN-B-02025, Calculation of energy use for heating in residential buildings and buildings of collective habitation, 2001 (in Polish).

[139] Pogorzelski, J. *Fizyka Budowli (Thermal Physics of Buildings*). PWN, Łódz, 1976 (in Polish).

[140] Pogorzelski, J. *Budownictwo ogólne tom II Fizyka Budowli, rozdział IV (Fundamentals of Buildings, Vol. 2: Thermal Physics of Buildings, Chapter 4).* Klemm, P. (editor), Arkady, Warszawa, 2009 (in Polish).

[141] Rhie, C.M., Chow, W.L. A Numerical Study of the Turbulent Flow Past an Isolated Airfoil with Trailing Edge Separation. *AIAA* 82 (1982).

[142] Rozporządzenie Ministra Infrastruktury z dnia 6 listopada 2008 r. w sprawie metodologii obliczania charakterystyki energetycznej budynku stanowiącej samodzielną całość techniczno-użytkowa oraz sposobu sporządzania i wzorów świadectw ich charakterystyki energetycznej, Dz.U. 2008 nr 201 poz. 1240,

(Ordinance of The Polish Minister of Infrastructure of 6 November 2008 containing detailed methodology for calculating energy performance certificates, in Polish).

[143] Qi, Q., Deng, S., Jiang, Y. A simulation study on a solar heat pump heating system with seasonal latent heat storage. *Solar Energy* 82 (2008), pp. 669–675.

[144] Quaschning V. *Understanding Renewable Energy Systems.* Earthscan, London, 2005.

[145] Schmidt, T., Mangold, D., Muller-Steinhagen, H. Seasonal thermal energy storage in Germany. *Proceedings of the ISES Solar World Congress*, Göteborg, Sweden, 2003.

[146] Schmidt, T., Mangold, D., Muller-Steinhagen, H. Central solar heating plants with seasonal storage in Germany. *Solar Energy* 76 (2004), pp. 165–174.

[147] Schnieders, J. Comparison of the energy yield predictions of stationary and dynamic solar collector models and the models' accuracy in the description of a vacuum tube collector. *Solar Energy* 61 (1997), pp. 179–190.

[148] Selmi, M., Al-Khawaja, M.J., Marafia, A. Validation of CFD simulation for flat plate solar energy collector. *Renewable Energy* 33 (2008), pp. 383–387.

[149] Sharples, S., Charlesworth, P.S. Full-scale measurements of wind-induced convective heat transfer from a roof-mounted flat plate solar collector. *Solar Energy* 62 (1998), pp. 69–77.

[150] Singh, J., Panesar, B.S., Sharma, S.K. Energy potential through agricultural biomass using geographical information system - A case study of Punjab. *Biomass and Bioenergy* 32 (2009), pp. 301–307.

[151] Singh, H., Saini, R.P., Saini, J.S. A review on packed bed solar energy storage systems. *Renewable and Sustainable Energy Reviews* 14 (2010), pp. 1059–1069.

[152] Smil, V. *Energy At The Crossroads: Global Perspectives And Uncertainties.* Massachusetts Institute of Technology, 2003.

[153] Smith, C. History of Solar Energy: Revisiting Solar Power's Past. *Technology Review* 98 (1995), pp. 38–47.

[154] Smolec, W. *Fototermiczna konwersja energii slonecznej (Photothermal conversion of solar energy).* PWN, Warsaw, 2000 (in Polish).

[155] Smyth, M., Russell, J., Milanowski, T. *Solar Energy in the Winemaking Industry.* Springer, London, 2011.

[156] Solarblog&Hewalex, http://www.solarblog.pl, 2012.

[157] Soltau, H. Testing the thermal performance of uncovered solar collectors. *Solar Energy* 49 (1992), pp. 263–272.

[158] Soulayman, S.S.H. On the optimum tilt of solar absorber plates. *Renewable Energy* 1 (1991), pp. 551–554.

[159] Staniszewski, B. *Wymiana ciepła (Heat Exchange), Theoretical Fundamentals.* PWN, Warsaw, 1980 (in Polish).

[160] Statsoft, Inc., STATISTICA Version 8.0 Manual. Tulsa, OK, USA, 2008.

[161] Suehrcke, H., Peterson, E.L., Selby, N. Effect of roof solar reflectance on the building heat gain in a hot climate. *Energy and Buildings* 40 (2008), pp. 2224–2235.

[162] Szargut, J., Stanek, W. Thermo-ecological optimization of a solar collector. *Energy* 32 (2007), pp. 584–590.

[163] Tesch, K. *Mechanika płynów (Fluid Mechanics).* Wydawnictwo Politechniki Gdańskiej, Gdansk, 2008 (in Polish).

[164] The Climate Database of Typical Meteorological Year, Polish Ministry of Infrastructure, Warsaw, 2009.

[165] Thirugnanasambandam, M., Iniyan, S., Goic, R. A review of solar thermal technologies. *Renewable and Sustainable Energy Reviews* 14 (2010), pp. 312–322.

[166] Tian, L., Qin, Y. Utilization of renewable energy in architectural design. *Frontiers of Architecture and Civil Engineering in China* 1 (2007), pp. 114–122.

[167] Tonui, J.K., Tripanagnostopoulos, Y. Performance improvement of PV/T solar collectors with natural air flow operation. *Solar Energy* 82 (2008), pp. 1–12.

[168] Tripanagnostopoulos, Y., Souliotis, M., Nousia, T.H. Solar collectors with colored absorbers. *Solar Energy* 68 (2000), pp. 343–356.

[169] Tsilingiridis, G., Martinopoulos, G. Thirty years of domestic solar hot water systems use in Greece – energy and environmental benefits – future perspectives. *Renewable Energy* 35 (2010), pp. 490–497.

[170] Turgut, O., Onur, N. An experimental and three-dimensional numerical study of natural convection heat transfer between two horizontal parallel plates. *International Communications in Heat and Mass Transfer* 34 (2007), pp. 644–652.

[171] Ustawa z dnia 21 listopada 2008 r. o wspieraniu termomodernizacji i remontów, Dz. U. Nr 223, poz. 1459, (Act on Supporting Thermomodernisation and Renovation Works, dated 21 November 2008, in Polish).

[172] Van Meurs, G.A.M. Seasonal Heat Storage in The Soil. *Ph.D. thesis* (1985), Delft University of Technology.

[173] Versteeg, H.K., Malalasekera, W. *An introduction to Computational Fluid Dynamics, The Finite Volume Method,* Longman Group Ltd., Harlow, 1995.

[174] Vestlund, J., Ronnelid, M., Dalenback, J.O. Thermal performance of gas-filled flat plate solar collectors. *Solar Energy* 83 (2009), pp. 896–904.

[175] Villar, M.N., Cejudo Lopez, J.M., Dominguez Munoz, F., Rodriguez Garcia, E., Carrillo Andreas, A. Numerical 3-D heat flux simulations on flat plate solar collectors. *Solar Energy* 83 (2009), pp. 1086–1092.

[176] Villi, G., Pasut, W., De Carli, M. CFD modelling and thermal performance analysis of a wooden ventilated roof structure. *Building Simulation* 2 (2009), pp. 215–228.

[177] Weitbrecht, V., Lehmann, D., Richter, A. Flow distribution in solar collectors with laminar flow condition. *Solar Energy* 73 (2002), pp. 433–441.

[178] Wilson, M.J., Paul, M.C. Effect of mounting geometry on convection occurring under a photovoltaic panel and the corresponding efficiency using CFD. *Solar Energy* 85 (2011), pp. 2540–2550.

[179] Wiśniewski, G., Gołębiowski, S., Gryciuk, M. *Kolektory słoneczne - poradnik wykorzystania energii słonecznej (Solar collectors - handbook for solar energy use).* COIB, Warsaw, 2001 (in Polish).

[180] Wiśniewski, G., Gołębiowski, S., Gryciuk, M., Kurowski, K., Więcka, A. *Kolektory słoneczne - energia słoneczna w mieszkalnictwie, hotelarstwie i drobnym przemyśle (Solar collectors - solar energy in housing, hotels and small industry).* Dom Wydawniczy MEDIUM, Warsaw, 2008 (in Polish).

[181] Wiśniewski, S., Wiśniewski, T.S. *Wymiana ciepła (Heat Exchange).* WNT, Warsaw, 1994 (in Polish).

[182] Yakhotu, V., Orszag, S.A., Thangam, S., Gatski, T.B., Speziale, C.G. Development of turbulence models for shear flows by a double expansion technique. *Physics of Fluids A.* 7 (1992), pp. 1510–1520.

[183] Yellott, H. Utilization of sun and sky radiation for heating cooling of buildings. *ASHRAE Journal* 15 (1973), pp. 31.

[184] Yu, C.C., Heinrich, J.C. Petrov–Galerkin method for multidimensional, time dependent, convective–diffusive equations. *International Journal for Numerical Methods in Engineering* 24 (1987), pp. 2201–2215.

[185] Zawadzki, M. *Kolektory słoneczne, Pompy Ciepła - Na Tak (Solar collectors, Heat Pumps - Yes).* Polska Ekologia, Warsaw, 2003 (in Polish).

[186] Zhang, H.-F., Ge, X.-S., Ye, H., Jiao, D.-S. Heat conduction and heat storage characteristics of soils. *Applied Thermal Engineering* 27 (2007), pp. 369–373.

[187] Zhi-Sheng, L., Guo-Qiang, Z., Dong-Mei, L., Jin Zhou, Li-Juan, L., Li-Xin, L. Application and development of solar energy in building industry and its prospects in China. *Energy Policy* 35 (2007), pp. 4121–4127.

[188] Zienkiewicz, O.C., Morgan, K. *Finite elements and approximations*, John Wiley & Sons, New York, USA, 1983.

[189] 2011 Buildings Energy Data Book, U.S. Department of Energy, http://buildingsdatabook.eere.energy.gov, 2012.

Streszczenie

Praca doktorska przedstawia wyniki analizy numerycznej wydajności innowacyjnego kolektora słonecznego podczas całorocznej eksploatacji w polskich warunkach klimatycznych. Prezentowany kolektor słoneczny (ukryty kolektor słoneczny) składa sie z systemu polipropylenowych rurek z płynem umieszczonych pod pokryciem dachowym dachu wentylowanego. Ze względu na swoją strukturę oraz wykorzystane materiały ukryty kolektor słoneczny charakteryzuje się stosunkowo niskim kosztem inwestycyjnym (około 36 zł/m^2). Niski koszt inwestycji oraz brak ingerencji w wygląd zewnętrzny budynku to główne zalety w porównaniu z typowymi kolektorami słonecznymi, które sprawiają że ukryty kolektor słoneczny jest atrakcyjnym rozwiązaniem na potrzeby zasilenia niskotemperaturowych systemów grzewczych w budynkach mieszkalnych. Celem niniejszej pracy jest ocena wydajności oraz możliwości zastosowania ukrytego kolektora słonecznego na potrzeby zasilenia systemów ogrzewania bazujących na niskotemperaturowych źródłach ciepła w budynkach o niskim zapotrzebowaniu na ciepło, jak również zasilenia systemów ciepłej wody użytkowej.

Badania przebiegu procesu wymiany ciepła w ukrytym kolektorze słonecznym wykonano za pomocą symulacji numerycznych. Opracowany model numeryczny, bazujący na Metodzie Elementów Skończonych, umożliwia symulację konwekcyjnej wymiany ciepła w przepływającym płynie oraz uwzględnia wpływ zjawiska konwekcji swobodnej na intensyfikację wymiany ciepła w pustce powietrznej. W przyjętym modelu MES warstwa powietrza w pustce kolektora traktowana jest jak ciało stałe o zmiennych w czasie właściwościach ortotropowych (efektywnych wartościach współczynnika przewodzenia ciepła). Uwzględniono również zmienny w czasie wpływ oporu przejmowania ciepła na wewnętrznych i zewnętrznych powierzchniach rurek. Funkcje opisujące zmienność poszczególnych parametrów w czasie w zależności od parametrów klimatu zewnętrznego oraz masowego strumienia przepływu płynu w rurkach, mające na celu uwzględnienie konwekcyjnej wymiany ciepła w domenach płynu kolektora, wyznaczono na podstawie odrębnych stacjonarnych symulacji CFD w programie ANSYS CFX 15.0. Zastosowane podejście pozwala na wykonanie niestacjonarnej symulacji pracy kolektora w okresie typowego roku meteoro-

logicznego, która jest podstawą oceny wydajności ukrytego kolektora słonecznego. Symulacje numeryczne zostały wykonane za pomocą programu komputerowego ABAQUS v. 6.10 z wykorzystaniem zbioru istniejących oraz własnych procedur i funkcji napisanych w języku programowania FORTRAN, umożliwiających między innymi symulację rzeczywistych warunków klimatu zewnętrznego oraz modyfikację parametrów konwekcyjnej wymiany ciepła na każdym kroku czasowym symulacji. Model CFD na podstawie, którego określono funkcje parametrów konwekcyjnej wymiany ciepła został pozytywnie zwalidowany względem rozwiązań analitycznych. Dlatego też można stwierdzić, że opracowany model MES jest zbliżony do rzeczywistości.

Symulacje całorocznej pracy ukrytego kolektora słonecznego, zostały poprzedzone serią parametrycznych analiz w warunkach stacjonarnych. Uzyskane wyniki analiz parametrycznych pozwoliły na weryfikację przyjętego modelu numerycznego jak również określenie optymalnych parametrów technicznych mających na celu poprawę wydajności ukrytego kolektora słonecznego. Wyniki symulacji rocznej pracy kolektora pokazały, że zastosowanie ukrytego kolektora słonecznego w polskich warunkach klimatycznych na potrzeby zasilenia systemów ciepłej wody użytkowej może być efektywne tylko podczas wiosny i lata, w szczególności w okresie od maja do sierpnia. Szacuje się, że w tym okresie czasu ukryty kolektor słoneczny (o powierzchni odpowiadającej powierzchni dachu typowego budynku jednorodzinnego) może pokryć średnio 81 % zapotrzebowania na ciepłą wodę użytkową. Średnia roczna sprawność konwersji energii słonecznej kolektora stosowanego do zasilenia systemów ogrzewania budynku wyniosła nieco powyżej 0.09 [−], podczas gdy całkowita ilość ciepła pozyskanego w okresie od czerwca do grudnia jest ponad 3 razy mniejsza w porównaniu z płaskimi kolektorami słonecznymi dla tego samego okresu czasu. Zgodnie z oczekiwaniami, wydajność ukrytego kolektora słonecznego jest znacznie niższa w porównaniu z typowymi kolektorami słonecznymi. Niemniej jednak, ukryty kolektor słoneczny o powierzchni 60 m^2 jest w stanie pozyskać w okresie jednego roku około 3 razy więcej ciepła niż jest to wymagane do pokrycia rocznego zapotrzebowania na ogrzewanie budynku o standardzie budynku pasywnego o powierzchni ogrzewanej 250 m^2. Można zatem stwierdzić, że ukryty kolektor słoneczny może zostać wykorzystany na potrzeby zasilenia systemów ogrzewania bazujących na niskotemperaturowych źródłach ciepła przeznaczonych dla budynków mieszkalnych o niskim zapotrzebowaniu na ciepło. Uzyskane wyniki są w zgodzie z opublikowanymi wynikami eksperymentalnych badań wydajności zintegrowanych kolektorów słonecznych przeznaczonych do zasilenia niskotemperaturowych systemów grzewczych.

List of publications

Publications in journals from ISI Master Journal List (1)

1. Arendt, K., Krzaczek, M., Florczuk, J. Numerical analysis by FEM and analytical study of the dynamic thermal behavior of hollow bricks with different cavity concentration. *International Journal of Thermal Sciences* 50 (2011), pp. 1543–1553.
   (*32 punkty na liście Ministerstwa Nauki i Szkolnictwa Wyższego*)

Publications in reviewed journals (1)

1. Florczuk, J., Arendt, K. Analiza wydajności kolektora słonecznego przeznaczonego dla systemu ogrzewania budynku o niskim zapotrzebowaniu na ciepło. *Aparatura Badawcza i Dydaktyczna*, T. XV, nr 2 (2010), pp. 23–29.
   (*6 punktów na liście Ministerstwa Nauki i Szkolnictwa Wyższego*)

Project reports (4)

1. Longlife Report 2, *Development of standards, criteria, specifications*, Ed. K. Rückert, TU Berlin Publications, Berlin, 2010. (ISBN 978-3-7983-2213-4)

2. Longlife Report 3.1, *Sustainable, energy efficient and resource saving residential design*, Ed. K. Rückert, TU Berlin Publications, Berlin, 2011. (ISBN 978-3-7983-2390-2)

3. Longlife Report 3.2, *Prototype Catalogue*, Ed. K. Rückert, TU Berlin Publications, Berlin, 2011. (ISBN 978-3-7983-2391-9)

4. Longlife Report 3.3, *Pilot Projects*, Ed. K. Rückert, TU Berlin Publications, Berlin, 2011. (ISBN 978-3-7983-2392-6)